

# **Journal of Mechanics of Materials and Structures**

**Volume 13, No. 4**

**July 2018**



# JOURNAL OF MECHANICS OF MATERIALS AND STRUCTURES

[msp.org/jomms](http://msp.org/jomms)

Founded by Charles R. Steele and Marie-Louise Steele

## EDITORIAL BOARD

ADAIR R. AGUIAR	University of São Paulo at São Carlos, Brazil
KATIA BERTOLDI	Harvard University, USA
DAVIDE BIGONI	University of Trento, Italy
MAENGHYO CHO	Seoul National University, Korea
HUILING DUAN	Beijing University
YIBIN FU	Keele University, UK
IWONA JASIUK	University of Illinois at Urbana-Champaign, USA
DENNIS KOCHMANN	ETH Zurich
MITSUTOSHI KURODA	Yamagata University, Japan
CHEE W. LIM	City University of Hong Kong
ZISHUN LIU	Xi'an Jiaotong University, China
THOMAS J. PENCE	Michigan State University, USA
GIANNI ROYER-CARFAGNI	Università degli studi di Parma, Italy
DAVID STEIGMANN	University of California at Berkeley, USA
PAUL STEINMANN	Friedrich-Alexander-Universität Erlangen-Nürnberg, Germany
KENJIRO TERADA	Tohoku University, Japan

## ADVISORY BOARD

J. P. CARTER	University of Sydney, Australia
D. H. HODGES	Georgia Institute of Technology, USA
J. HUTCHINSON	Harvard University, USA
D. PAMPLONA	Universidade Católica do Rio de Janeiro, Brazil
M. B. RUBIN	Technion, Haifa, Israel

**PRODUCTION** [production@msp.org](mailto:production@msp.org)

SILVIO LEVY Scientific Editor

---

See [msp.org/jomms](http://msp.org/jomms) for submission guidelines.


---

JoMMS (ISSN 1559-3959) at Mathematical Sciences Publishers, 798 Evans Hall #6840, c/o University of California, Berkeley, CA 94720-3840, is published in 10 issues a year. The subscription price for 2018 is US \$615/year for the electronic version, and \$775/year (+\$60, if shipping outside the US) for print and electronic. Subscriptions, requests for back issues, and changes of address should be sent to MSP.

---

JoMMS peer-review and production is managed by EditFLOW® from Mathematical Sciences Publishers.

PUBLISHED BY

 **mathematical sciences publishers**  
nonprofit scientific publishing

<http://msp.org/>

© 2018 Mathematical Sciences Publishers

## **PREDICTION OF SPRINGBACK AND RESIDUAL STRESS OF A BEAM/PLATE SUBJECTED TO THREE-POINT BENDING**

QUANG KHOA DANG, PEI-LUN CHANG, SHIH-KANG KUO AND DUNG-AN WANG

A model for prediction of springback and residual stress distribution of a beam/plate subjected to three-point bending and reverse bending is developed based on a mechanical-geometrical approach. A converged solution that satisfies both the Euler–Bernoulli beam theory and the geometrical constraints is obtained by a recursive scheme. The model can be applied to bending/unbending analyses of plates when the beam bending approaches a plane strain condition. Springback and residual stress distribution of a plate is predicted quite accurately by the model as verified by finite element analyses and experiments. Accuracy of springback and residual stress prediction of the model is examined with consideration of various geometry parameters of the beam and the fulcrum/support cylinders. The goal of this investigation is to develop an accurate and efficient model to predict the profile and residual stress of plates curved by bending in the postyield range. The developed model can serve as a unit cell of a more sophisticated model for leveling analyses of metal plates as multiple rollers are involved.

### **1. Introduction**

Accurate estimation of springback and residual stress distribution of metal plates under leveling process is necessary for appropriate and efficient adjustment of the roller settings of the leveling machines. Development of an analytical model of the critical to the production process. The adjustment of the roller settings of the levelers is complicated and an efficient analytical model can assist the operators in obtaining high quality of the products. Levelers consist of rollers to deform sheet metal by alternative bending. The leveling process with multiple rollers can be viewed as a cyclic three-point bending process. An accurate three-point bending model with an efficient numerical algorithm is essential in implementing an analytical model of levelers to determine its relevant key characteristics. Three-point bending test was also designed to achieve a weight efficient structure of sandwiched beams [Li et al. 2011].

When modeling three-point bending, a beam subjected to displacements of a punch cylinder contacts the punch cylinder and two fulcrum cylinders tangentially and does not penetrate cylinder surface. Conway [1947] and Theocaris et al. [1977] investigated deflections of beams under three-point bending by elliptical integrals method. Ohtsuki [1986] analyzed large deflection bending stress of an elastic beam under three-point bending based on a Legendre–Jacobi form’s elliptic integrals. Arnautov [2005] also adopted elliptical integrals to provide a bending stress solution to the problem. Batista [2015] gave an equilibrium configuration of an elastic beam subjected to three-point bending in terms of Jacobi elliptical functions. Deflection behaviors of beams under three-point bending have also been investigated by classical beam theory [Mujika 2006; Mohyeddin and Fereidoon 2014]. These solutions of the three-point bending problems were obtained by assuming elastic behavior of the beam material. Considering material

*Keywords:* springback, residual stress, three-point bending, beam, plate.

hardening in the analyses, Hill [1950] and Gao [1994] derived solutions of pure bending of beams by assuming elastic, linear plastic material. Pure bending of a plate made of a power-law-hardening material was studied by Triantafyllidis [1980] and Zhu [2007]. Kang and Li [2009] investigated bending stress of a cantilever beam with power-law nonlinearity.

Prediction of final shape of beams/plates is a complex task in metal forming industries. Residual stress distribution of beams/plates after springback has a strong influence on their final shape. Analytical solutions for springback of beams and plates under pure bending were developed by Johnson and Yu [1981]. Lin and Hua [2000] developed an analytical method to compute large deflection and springback of a thin plate with strain hardening under four-roll bending process. Gergess and Sen [2016] derived closed form solutions of load to deformation relation and profiles of steel members under point bending. For more complex bending problems, however, numerical techniques are adopted. Sitar et al. [2015] presented a numerical procedure to compute springback of beams with asymmetric cross-sections. Zhang et al. [2007] developed a model to predict springback of sheet metals after U-bending. They applied kinematic, isotropic, and combined hardening laws in their model to account for stretching, bending, and unbending of sheet metals during the U-bending process. Chiew et al. [2016] employed a numerical modeling procedure to obtain residual stress distribution of steel members produced by three-roller bending. They proposed a residual stress model to predict residual stress distribution of the curved member. Kuwabara et al. [1996] presented an analytical model to predict the amount of springback of a sheet metal subjected to bending-unbending under tension. Given the curvatures of the sheet metal before the deformation process, they calculated the residual stress distribution and residual curvature of the sheet metal at the point of interest. Takahashi et al. [1996] performed a die bending test to verify the calculated residual curvature by Kuwabara et al. [1996]. Kuwabara et al. [1999] established a numerical analysis method for analyzing bending/unbending process of sheet metal at the point of interest. Their model incorporates a three-dimensional constitutive model and the Ziegler's kinematic hardening model.

In this investigation, a one-dimensional model of three-point bending tests capable of calculating path/curvature of beams/plates, induced stress/strain histories, and hence final residual stress distribution is developed. The stress/curvature distribution along the span of the beams/plates over the supports can be calculated by the model. This model can be extended to simulate roller leveling process, which can be approximated by a sequence of three-point bends between rollers. A phenomenological combined hardening parameter is adopted to take isotropic and kinematic hardening into account during reverse bending. In the model, support contact is incorporated into the pure bending problem of beams under three-point bending in order to obtain springback and residual stress solutions. A recursive scheme considering Euler–Bernoulli beam theory and geometrical constraints is adopted to obtain converged solutions of beams under three-point bending and reverse bending. The model with consideration of the

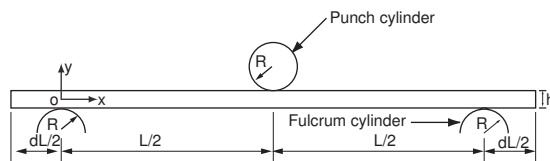


**Figure 1.** A schematic of a three-point bending test and a Cartesian coordinate system.



material strain hardening is based on proportional straining conditions. Two-dimensional, plane strain finite element analysis of beams subjected to three-point bending and reverse bending is carried out to verify the model. The analysis is performed for various displacement loadings as well as different values of radius of fulcrum cylinders. Experiments of three-point bending are performed to test the applicability of developed analytical model. Finally, discussions and conclusions are given.

## 2. Model

Besides the assumptions of Euler–Bernoulli beam theory, friction forces at the roller supports, longitudinal forces along the beam, gravity, and span shortening caused by deflection are neglected in the numerical model. Figure 1 schematically shows a three-point bending test of a beam. The beam has a length of  $L + dL$ , a thickness of  $h$  and a width of  $w$ . The overhang length of the beam is  $dL/2$ . The radius of the punch cylinder and fulcrum cylinders is  $R$ . A Cartesian coordinate system is also shown in the figure, where  $x$  represents the longitudinal direction,  $y$  represents the thickness direction, and  $z$  is the width direction of the beam. The origin of the  $y$  coordinate is at the middle of the beam as shown in the figure. Longitudinal strain  $\varepsilon_x$  can be written as

$$\varepsilon_x = -\kappa y, \quad (1)$$

where  $\varepsilon_x$  is the longitudinal strain, and  $\kappa$  represents the curvature. Large deflection of beams under three-point bending may induce significant plastic deformation in the beam material. It is critical to study the large plastic deformation of beams under three-point bending. When the beam is considered as an elastic-linear plastic material, the effective stress  $\bar{\sigma}$  is given as

$$\bar{\sigma} = \sigma_0 + E_p(\bar{\varepsilon} - \sigma_0/E), \quad (2)$$

where  $\sigma_0$  is the yield stress and  $\bar{\varepsilon}$  is the effective total strain.  $E$  and  $E_p$  are the Young's modulus and plastic modulus, respectively. Assuming the von Mises criterion and plane-strain condition apply, the stress in the width direction  $\sigma_z$  is

$$\sigma_z = \frac{1}{2}(\sigma_x + \sigma_y), \quad (3)$$

where  $\sigma_x$  and  $\sigma_y$  are the stresses in the longitudinal direction and thickness direction, respectively. Under pure bending, the stress in the thickness direction  $\sigma_y$  is negligible, and the effective stress  $\bar{\sigma}$  is

$$\bar{\sigma} = \frac{\sqrt{3}}{2}|\sigma_x|. \quad (4)$$

Assuming volume conservation and plane-strain condition apply, the effective total strain can be expressed as

$$\bar{\varepsilon} = \frac{2}{\sqrt{3}}|\varepsilon_x|. \quad (5)$$

As described by Hill [1950] and Zhu [2007], the volume conservation is needed here to solve exactly the pure bending problem of beams or plates in the elastic and plastic region. Relatively large plastic deformation is considered in this investigation. This assumption contributes to a very small fraction of error to the results. Because of symmetry, the bending moment  $M$  is given as

$$M = -2w \int_0^{h/2} \sigma_x y dy. \quad (6)$$

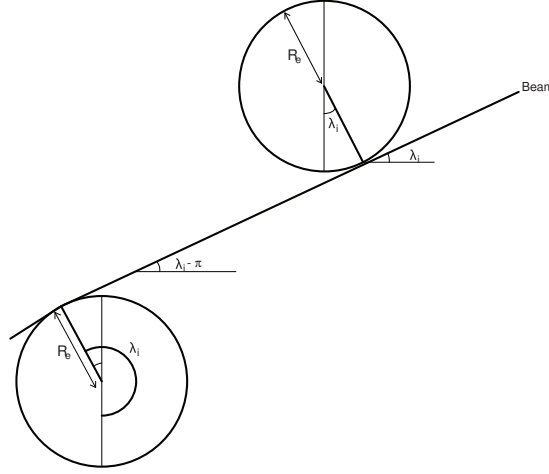


**Figure 2.** A schematic of cylinders below and above the beam.

The sign convention for the moment  $M$  and the curvature  $\kappa$  is related to the orientation of the coordinate axes.

In order to estimate the contact points at which the beam contacts with the cylinders, it is assumed that the beam contacts each cylinder tangentially as shown in Figure 2. As seen in the figure,  $R_e$  is the expanded radius of the roller and is given as

$$R_e = R + \frac{1}{2}h. \quad (7)$$

The gradient of the longitudinal axis of the beam is equal to the tangent of the contact angle  $\lambda_i$  as [Müller et al. 2013]

$$\left. \frac{dy}{dx} \right|_{x_i} = \tan \lambda_i, \quad (8)$$

where  $y(x)$  is the longitudinal axis of the beam,  $(x_i, y_i)$  is the  $i$ -th contact point, and  $\lambda_i$  is the  $i$ -th contact angle. The contact point  $(x_i, y_i)$  can be expressed as

$$x_i = x_c + R_e \sin \lambda_i, \quad y_i = y_c - R_e \cos \lambda_i, \quad (9)$$

where  $(x_c, y_c)$  is the coordinates of the center of the punch/fulcrum cylinder.

The curvature, bending moment, deflected curve of the beam, and the contact points may be determined through a recursive scheme. First, the location of the three contact points and the beam curvature  $\kappa_i$  at the  $i$ -th contact point are assumed. The bending moment  $M_i$  at the  $i$ -th contact point is computed based on (1)–(6). Neglecting weight of the beam, the bending moment at the two fulcrum cylinders can be taken as zero and it has an extreme value at the punch cylinder. The curvature of the deflected beam is estimated based on the linear distribution of the bending moment between the fulcrum cylinder and the punch cylinder. Once the curvature distribution  $\kappa(x)$  is known, the beam profile is given by

$$y(x) = \iint \kappa(x) dx + C_1 x + C_2, \quad (10)$$

parameters	value
Poisson's ratio	0.33
Young's modulus (GPa)	70.3
tensile strength (MPa)	175.1
plastic modulus (MPa)	1579

**Table 1.** Material properties for AA5052.

where the constants  $C_1$  and  $C_2$  can be determined by the contact points at the fulcrum cylinders. The recursive scheme is shown in [Figure 3](#). A converged solution of the beam profile, moment distribution, curvature distribution, and contact points that satisfies both the Euler–Bernoulli beam theory and the geometrical constraints can be obtained by the recursive scheme. The recursive scheme outlined in [Figure 3](#) is based on a procedure presented by Higo et al. [2016]. Pure bending moment/curvature equation has been used to simulate deflections of beams with elastoplastic behavior [Natarajan and Peddieson 2011]. Pandit and Srinivasan [2016] described a method to analyze large deflections of a curved beam subjected to a tip-concentrated follower load. Based on a linearly hardening model, they obtained a moment-curvature constitutive law for their bending problem.

As the punch cylinder is lifted and loses contact with the beam, the beam springs back elastically and the internal stress distribution results in a zero bending moment. Assuming no reverse yielding during unloading, the curvature after unbending  $\kappa'$  can be expressed as [Hosford and Caddell 1993]

$$\kappa' = \kappa - M/(EI), \quad (11)$$

where  $\kappa$  and  $M$  are the curvature and moment, respectively, before springback, and  $I$  is the second moment of inertia of the beam cross section.

Finite element analyses are carried out to verify the simple model for springback estimation of the beam. The commercial software ABAQUS is used in this investigation. Due to the symmetry, only the right half of the specimen is modeled. The finite element model is shown in [Figure 4](#) (top). The punch cylinder and the right fulcrum cylinder are also schematically shown in the figure. Two-dimensional plane strain 4-noded CPE4R elements are used in the model. The number of elements is 8436 in the finite element model. [Figure 4](#) (bottom) is a close up view of the mesh near the punch cylinder. The finite element mesh is made denser in the region under the punch and over the fulcrum. In ABAQUS, the “rigid surface” option is used to describe the punch cylinder and the fulcrum cylinders, and the “contact pair” option is used to describe the contact between the punch and the fulcrums with the beam. The displacement of the rigid punch is controlled in the analyses. The material properties for AA5052 aluminum alloy used in this investigation are listed in [Table 1](#). [Figure 5](#) shows a stress-strain curve for the AA5052 from tensile tests. The plastic modulus of the elastic linear plastic material behavior of the AA5052 is taken as the slope of the fitted line shown in the figure. The strain is up to 0.025 during the tensile tests. As seen in [Figure 5](#), the stress at this strain value only goes to about 200 MPa. The stress is computed by a linear extrapolation scheme for the strain higher than 0.025. The model can be applied to various metals with specified strain hardening behaviors.

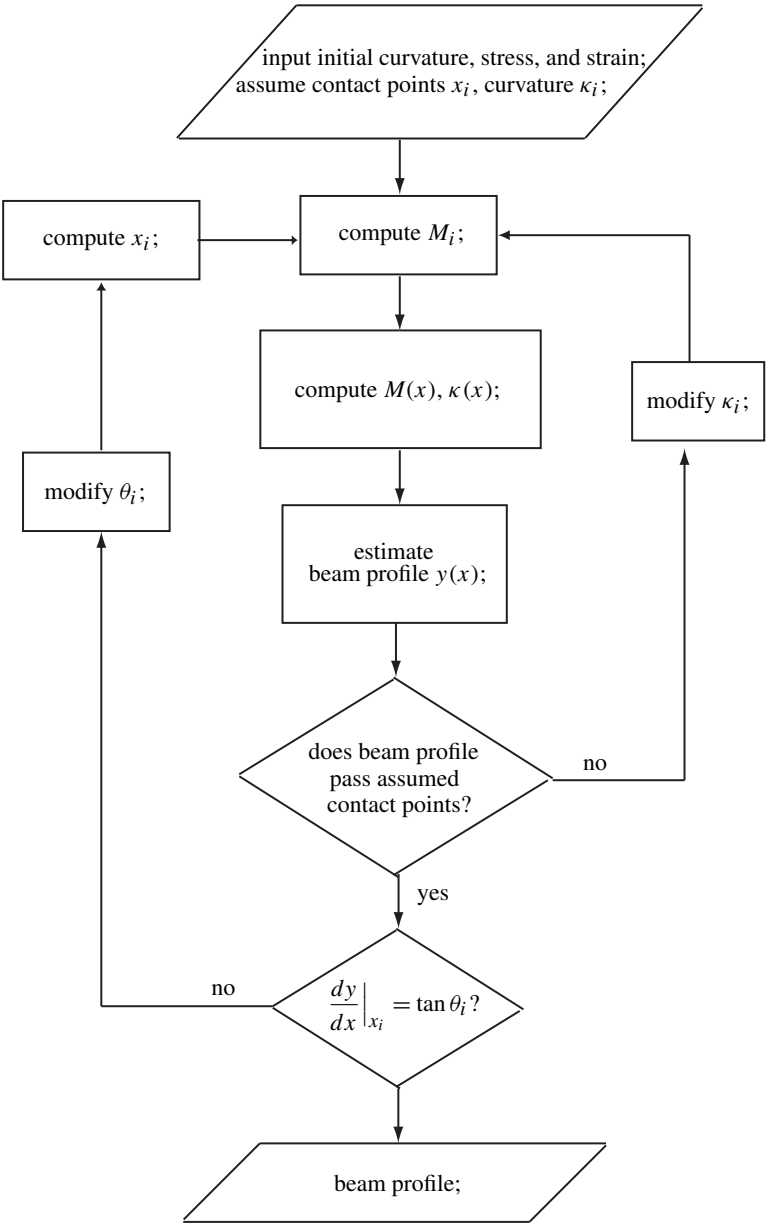


**Figure 3.** A recursive scheme.

**3. Numerical results**

The beam considered in this investigation has a length of 400 mm, a width of 100 mm, and a thickness of 6 mm. The overhang length of the beam  $dL/2$  is 60 mm. The radius of the punch cylinder and fulcrum cylinders is 1 mm. Finite element computational results are used to evaluate the applicability of the developed model. [Table 1](#) lists the material properties for the beam material, AA5052, with elastic linear



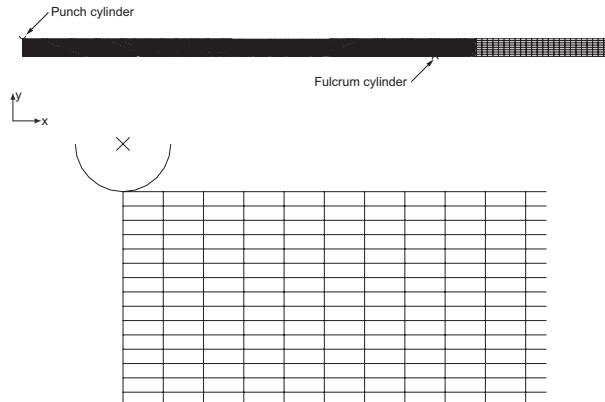


**Figure 4.** Top: a finite element model for the right half of a specimen. Bottom: a close up view of the mesh near the punch cylinder.

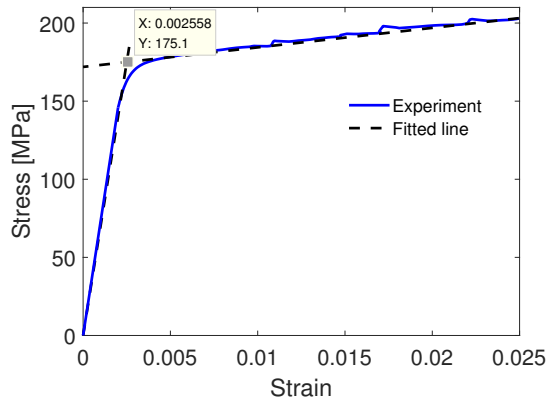


**Figure 5.** Tensile stress-strain curve for the AA5052 aluminum alloy.

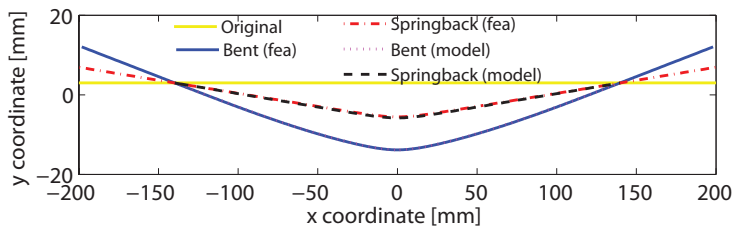


**Figure 6.** Beam profiles after bending and springback based on computational results of the model and FEA.

plastic material behavior. Computational grids of the analytical model are taken as 40 and 100 in the thickness direction and the longitudinal direction of the beam, respectively. The downward displacement of the punch cylinder is 16.81 mm.

Figure 6 shows the computational results based on the model (model) and the finite element analyses (fea). Seven contact point iterations and five contact angle iterations are required to reach a converged

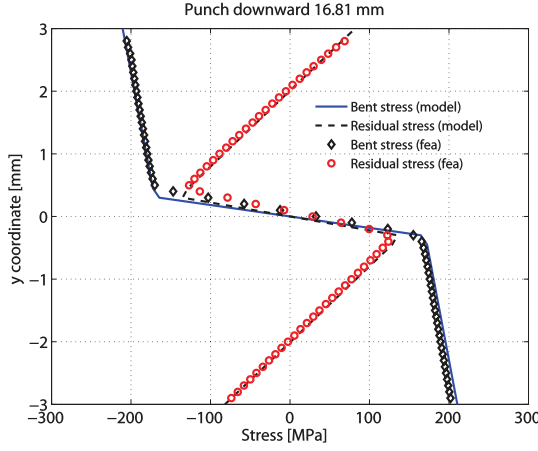


**Figure 7.** Stress distributions across beam thickness based on the model and the finite element analyses.

solution. The code based on the model takes 2.82 seconds to run on an AMD Phenom II X2 550 3.10 GHz processor. As seen in the figure, the beam profile after bending based on computational results of the model agrees with that based on the finite element analyses. The beam profile based on the model is estimated by the double integral of the curvature as in (6). The agreement between the model and the finite element analyses demonstrates the feasibility of the recursive scheme for calculation of the moment distribution and curvature distribution of the beam under three-point bending. The beam profile after springback is also shown in Figure 6. The displacements of the center of the beam due to springback based on the model and the finite element analyses are 8.02 mm and 8.28 mm, respectively. The percentage error in the springback estimation between the model and the finite element analyses is nearly 3%. The beam profile after springback predicted by the model is very close to that based on the finite element analyses.

After unloading, elastic springback occurs, and considerable residual stress results. Figure 7 shows the longitudinal stress distributions across beam thickness at the center of the beam based on the model and the finite element analyses. After bending and unloading, the stress  $\sigma_x$  based on the model agrees well with the finite element analyses. The stress distribution in the elastic region is a straight line with a slope of  $1/(\kappa E)$ . As seen in the figure, the slopes of the lines based on the model are slightly less than those based on the finite element analyses. This may be because the curvature  $\kappa$  in the model is approximated by  $\kappa \approx d^2y/dx^2$ , and the curvature of a plane curve  $y = y(x)$  is

$$\kappa = \frac{d^2y/dx^2}{(1 + (dy/dx)^2)^{3/2}}. \quad (12)$$

The applicability of the developed model for springback and residual stress distribution for beams under three-point bending is verified by the finite element analyses. The cases of plates under three-point bending can be approached by the plane strain condition considered in the derivation of the model.



**Figure 8.** A photo of a three-point bending setup for beam specimens.

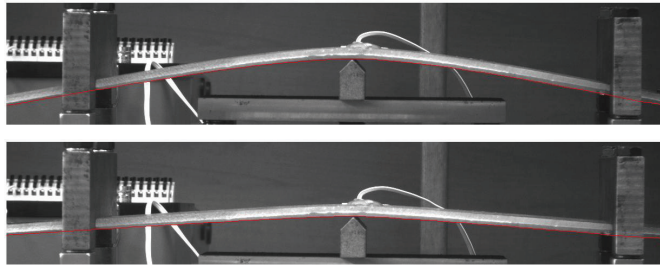


**Figure 9.** Photos of a beam specimen: after bending (top) and springback (bottom).

#### 4. Experiments and results

Specimens used in experiments were fabricated with AA5052 aluminum alloy. The material properties of AA5052 aluminum alloy are listed in [Table 1](#). The specimens were loaded in a three-point bending setup. A photo of the three-point bending setup is shown in [Figure 8](#). It is seen that the punch cylinder is placed under the specimen and can be moved upward and downward by turning a knob under the punch cylinder. The beam specimens used in this investigation have a width of 100 mm and a length of 400 mm. The thickness of the beam specimens is 6 mm. The radius of the punch cylinder and fulcrum cylinder is 1 mm. The distance  $L$  between the two fulcrums is 280 mm. The length of the two overhangs is 60 mm. The loading rate of the punch was 5 mm per minute. A video camera was used to record the deformation of the beam specimens on one side of the beam specimens. A strain gauge was attached to the top surface of the beam specimen. Loading was applied by the punch cylinder until the desired displacement of the punch was reached. The displacement of the punch was controlled by reading the output of the strain gauge. In this investigation, the displacement of the punch was set as 16.81 mm.

[Figure 9](#) (top and bottom) shows photos of a beam specimen after bending and springback, respectively. Three tests were performed and the photos of the specimen profiles were taken by the camera. [Figure 10](#) shows the beam profiles after bending and springback based on computational results of the model and the experiments. The experimental results show some discrepancies due to the alignment error of the experimental setup and sliding between the beam specimens and the punch/fulcrum cylinders. One of

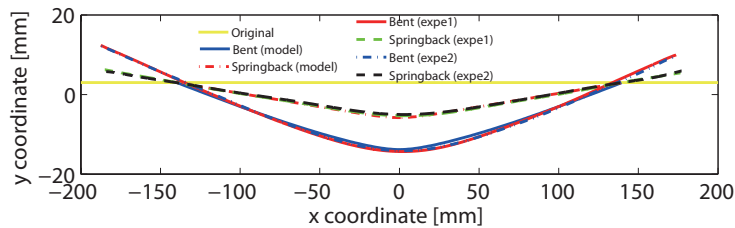


**Figure 10.** Beam profiles after bending and springback based on computational results of the model and experiments.

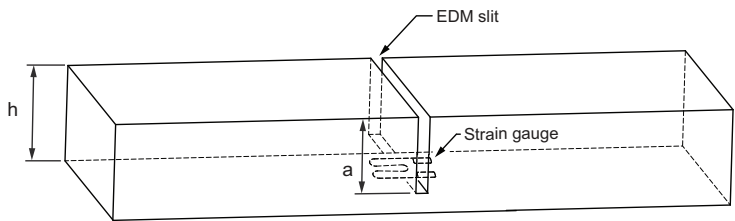


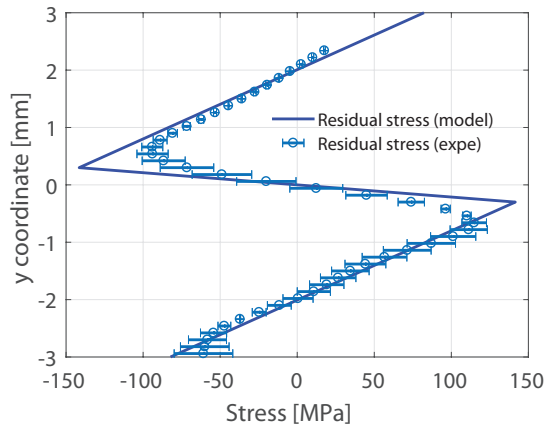
**Figure 11.** A schematic of the slitting method.

the three experimental results was discarded since it deviates from the other two experimental results in a greater amount. The average amount of springback at the center of the beam based on the two experimental results is 8.66 mm. Compared to the springback amount based on the model, 8.02 mm, the error in springback estimation of the model is 7%. This discrepancy can be accepted considering the alignment/measurement errors and sliding between specimens and punch/fulcrum cylinders during experiments.

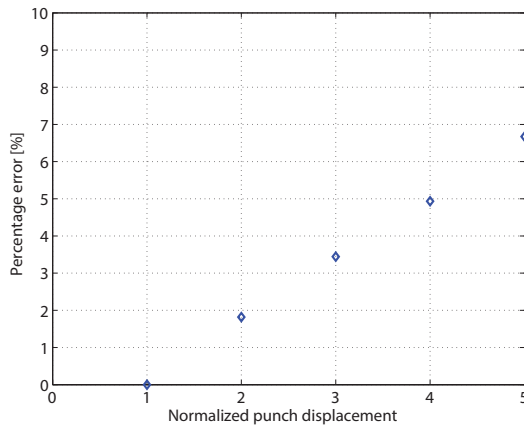
The residual stress of the bent beam was measured by a slitting method [Schajer and Prime 2006]. Figure 11 is a schematic of the slitting method. In the figure,  $a$  represents the depth of the slit. A strain gauge is attached to a surface opposite to the slit. The method is based on the principle that residual stress causes a body to deform when it is cut. The deformation is measured by strain gauges while cutting progressively through the body. The strain record allows calculation of the residual stress distribution. In this investigation, a slit was cut by electrical discharge machining (EDM) through the thickness direction at the center of the specimen to a final depth of 5.33 mm (0.89% of specimen thickness). Strain at each depth was measured by strain gauges. Residual stress results were obtained by the pulse stress function and regularization as described in Schajer and Prime [2006]. Figure 12 shows the residual stress distributions in the thickness direction at the center of the specimen based on the model and the experiment. The stress results based on the model have good agreement with the stresses measured by the slitting method.

In order to explore the feasibility of the developed model for estimation of profile and residual stress of specimens subjected to three-point bending, the effects of punch displacement on the amount of springback after unloading are examined. The values of the material constants are listed in Table 1. Figure 13 shows the error in springback as a function of the normalized punch displacement for the aluminum material. The normalized punch displacement ranges from 1 to 5. The punch displacement is normalized by the specimen thickness. The percentage error in springback is calculated by the difference





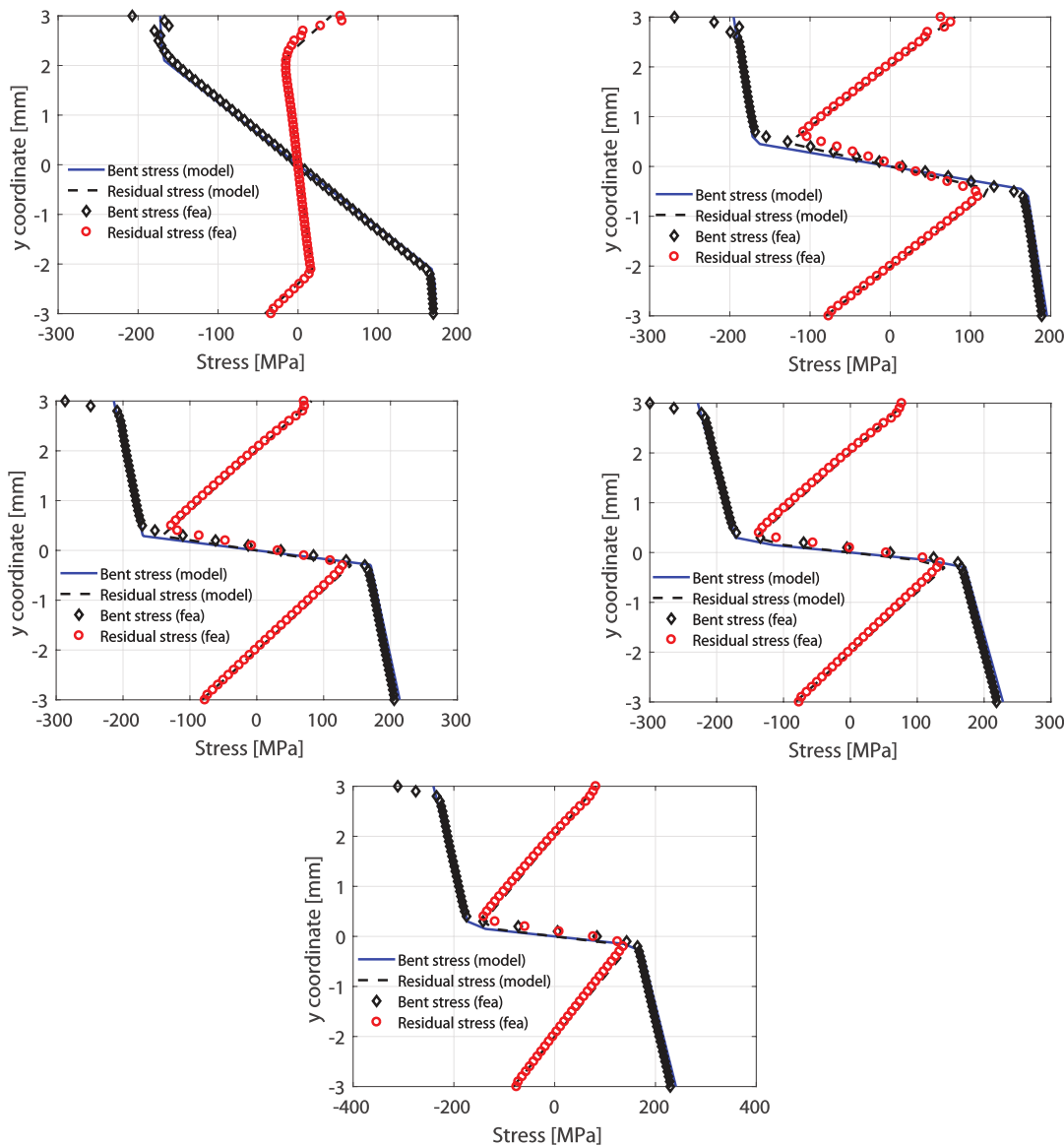
**Figure 12.** Residual distributions across beam thickness based on the model and the experiments.



**Figure 13.** Percentage error in springback as a function of the normalized punch displacement.

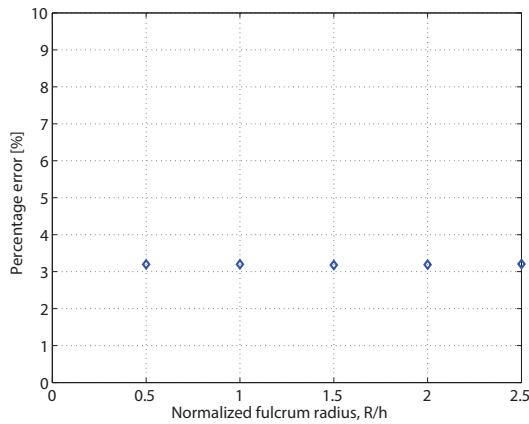
in the springback at the center of the specimen between the model and the finite element analyses divided by that of the finite element analyses. As shown in the figure, the error increases almost linearly as the normalized punch displacement increases. At the normalized punch displacement of 5, the springback amount predicted by the model has a percentage error of 6.7%.

Figure 14 shows the stress distributions at various punch displacements ranging from 6 mm to 30 mm, corresponding to the normalized punch displacements ranging from 1 to 5. Due to the pressure of the punch cylinder on the top surface of the specimen in the finite element analyses, a stress concentration region is located near the contact point at the top surface of the specimen. Therefore, the longitudinal stresses near the top surface of the specimen based on the finite element analyses are erroneous. The stress after bending and the residual stress after springback computed by the model agree with those based on the finite element analyses. The yielding fraction of the beam thickness is 31 % when the punch displacement is 6 mm. The yielding fraction reaches 90 % when the punch displacement is 30 mm. The model provides a relatively accurate estimation of the residual stress distributions under three-point bending.



**Figure 14.** Stress distributions across beam thickness based on the model and the finite element analyses at the punch displacement of 6 mm (top left), 12 mm (top right), 18 mm (center left), 24 mm (center right), and 30 mm (bottom).

The position of contact point of the specimen with the fulcrum cylinders varies as the specimen rolls over the fulcrum cylinders during three-point bending tests. When the contact points changes significantly, the position of the contact point has a major effect on the specimen profiles after springback. An analytical model should be able to model the position of the contact point accurately and efficiently. [Figure 15](#) shows the percentage error of the springback prediction of the model for different normalized radii of the fulcrum radius. The downward displacement of the punch cylinder is 16.81 mm. The fulcrum



**Figure 15.** Percentage error in springback as a function of the normalized fulcrum radius.

radius  $R$  is normalized by the specimen thickness  $h$ . The percentage error is the difference between the model prediction and computed value of the finite element analyses divided by the value of the finite element analyses and is given as a percent. For the considered  $R/h$  values of 0.5, 1, 1.5, 2, 2.5, the percentage errors are nearly 3%. When the  $R/h = 2.5$  and the downward displacement of the punch is 16.81 mm, the rotation of the beam over the fulcrum cylinders is  $8.75^\circ$ . For the  $R/h$  ratios considered, the model provides acceptable prediction of the springback of the beam under three-point bending compared to the results based on the finite element analyses.

Figure 16 and Figure 17 show the specimen's profiles and residual stress distributions, respectively, after bending and springback based on the model and the finite element analyses for various values of the normalized radius of the fulcrum cylinder. The profiles after springback and the residual stress distributions predicted by the model are in good agreement with those based on the finite element analyses. Note that the stresses near the top surface of the specimen are erroneous due to the stress concentration caused by the pressure from the punch cylinder in the finite element analyses, where the stress gets much larger than that predicted by the model.

Reverse bending has practical importance in sheet forming processes. A reverse bending process is investigated in order to verify the possibility to utilize the present model to leveling processes. Figure 18 (top) shows a setup of a three-point bending test considered in the model. The setup for reverse bending is schematically shown in Figure 18 (bottom). The curvature and deflected curve of the beam after bending and reverse bending are determined by the recursive scheme as shown in Figure 3. The curvature and stress distributions of the beam after the bending process are taken as the initial curvature and stress during the reverse bending process. Assuming isotropic hardening and using (1)–(6) and (11), the stress distributions after reverse bending and springback can be computed.

Due to the constraint of the available experimental apparatus, a reverse bending and springback experiment cannot be performed. Finite element analysis is sought to verify the deflected curve and stress distributions obtained by the model. Figure 19 (top) shows a schematic of a finite element model where two punches are in contact with the center of the beam. Two pairs of vertically aligned fulcrums are located near the left end and right end of the beam, a left pair and a right pair, respectively. Figure 19 (second row) is a schematic of the finite element model during bending. During reverse bending of

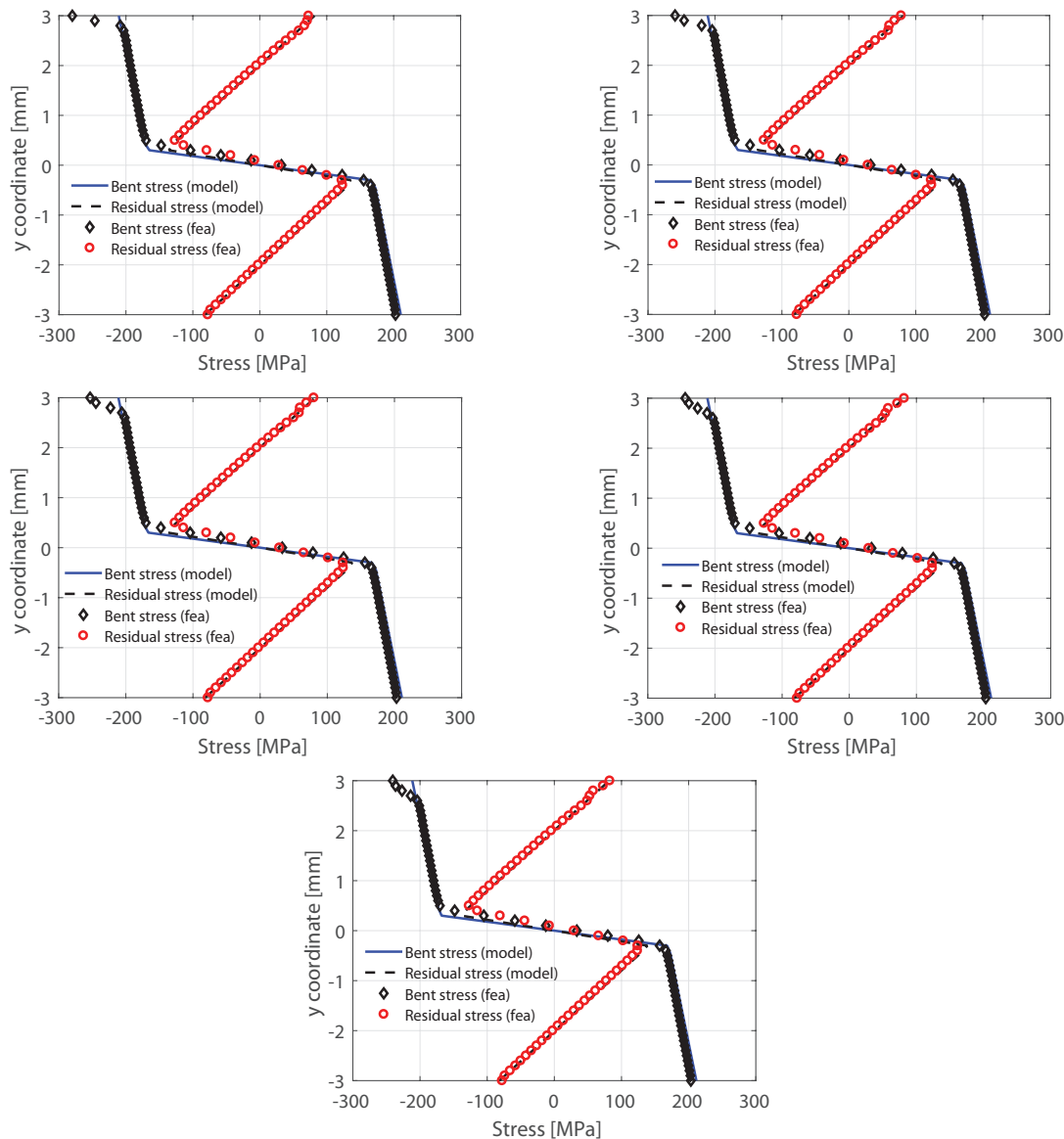


**Figure 16.** Beam profiles after bending and springback based on computational results of the model and finite element analyses at various values of the normalized radius of the fulcrum cylinder of 0.5 (top left), 1 (top right), 1.5 (center left), 2 (center right), and 2.5 (bottom).

the finite element analysis, the lower fulcrums of the left pair and the right pair and the upper punch are removed; see [Figure 19](#) (third row). The lower punch is removed for the springback analysis; see [Figure 19](#) (bottom).

In the analysis, the punch is moved downward 16.81 mm then moved upward 16.81 mm for bending and reverse bending, respectively. The radius of the punch and the fulcrum is taken as 1 mm. The beam



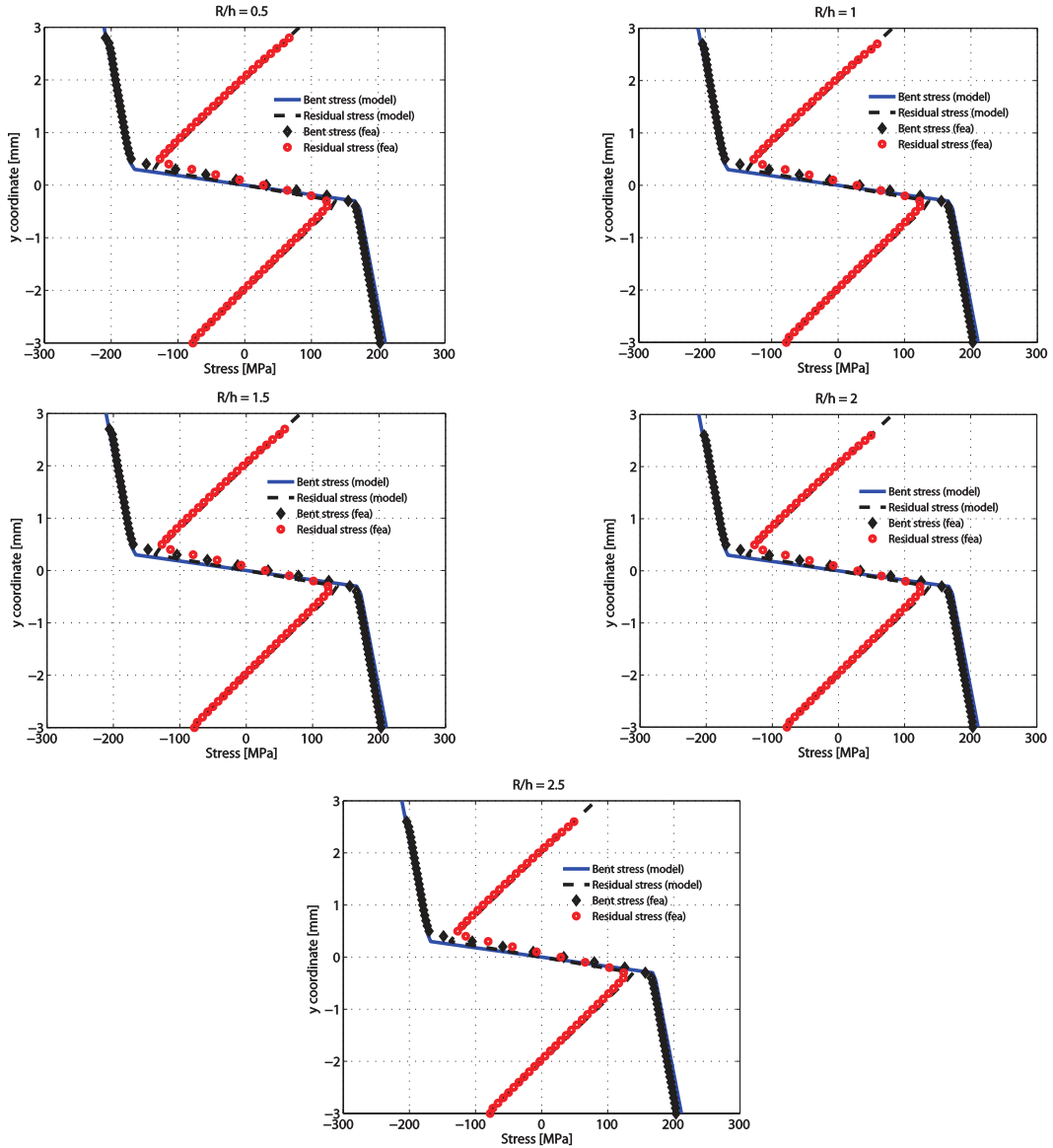


**Figure 17.** Stress distributions across beam thickness based on the model and the finite element analyses at the normalized fulcrum radius of 0.5 (top left), 1 (top right), 1.5 (center left), 2 (center right), and 2.5 (bottom).

has a length of 400 mm, a width of 100 mm and a thickness of 6 mm. Figure 20 (top) shows the meshes of the finite element model of the right half of the beam in its initial configuration. The meshes after bending, reverse bending, and springback are shown in second row, third row, and bottom of Figure 20, respectively.

Figure 21 shows the specimen's profiles after reverse bending and springback based on the model and the finite element analyses. The profiles after reverse bending and springback predicted by the model

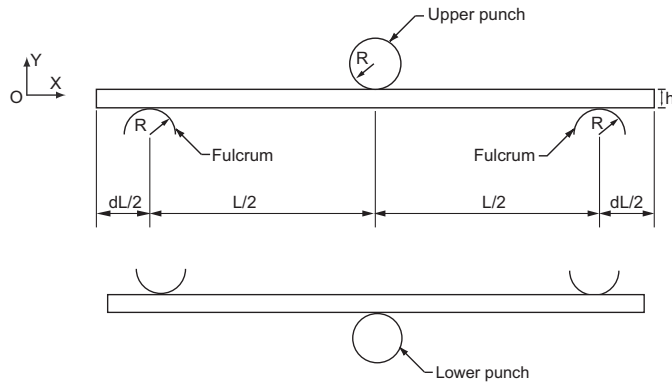


**Figure 18.** Schematics of: a three-point bending setup (top) and a three-point reverse bending setup (bottom).

are in good agreement with those based on the finite element analyses. [Figure 22](#) shows the stress distributions after reverse bending and springback based on the model and the finite element analyses. The residual stress distributions predicted by the model agree with those based on the finite element analyses.

For materials that exhibit a combined isotropic and kinematic hardening behaviors, the yield stress in reverse loading is usually lower than that in the case of continuous loading. During the three-point

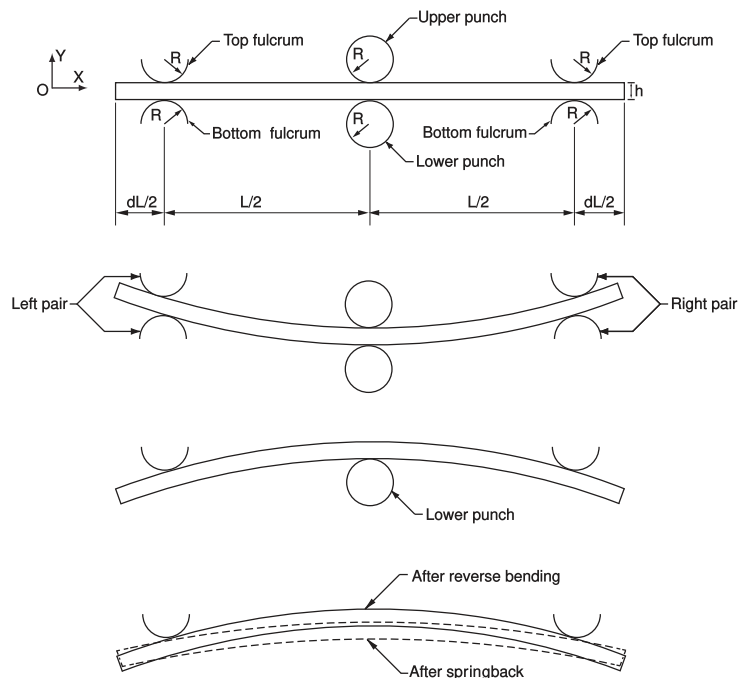


**Figure 19.** Schematics of a finite element model where two punches are in contact with the center of the beam.

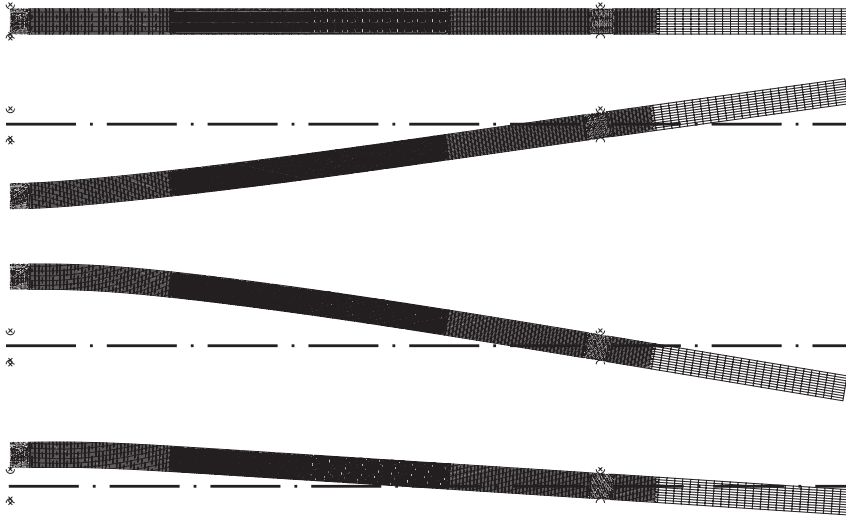


**Figure 20.** Meshes of the finite element model of the right half of the beam: in its initial configuration (top), after bending (second row), after reverse bending (third row), and after springback (bottom).

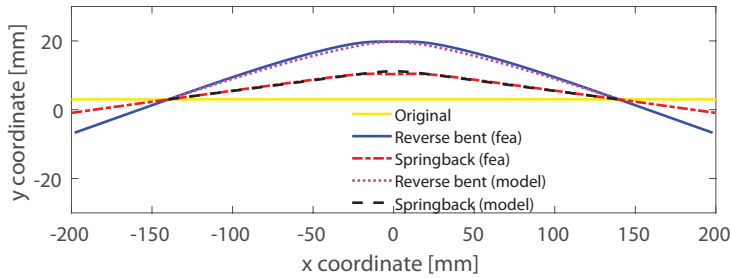


**Figure 21.** Beam profiles after reverse bending and springback based on the model and the finite element analyses.

reverse bending, the isotropic hardening model is no longer an adequate approximation. Therefore, under reverse bending, consideration of a combined hardening model is required for prediction of a realistic stress distribution and springback [Geng et al. 2002]. In order to extend the applicability of the developed model in roller leveling process, a phenomenological combined hardening parameter is adopted to take isotropic and kinematic hardening into account during reverse bending. Under reverse bending condition, change in effective stress  $\Delta\bar{\sigma}$  can be given as [Zhang et al. 2007]

$$|\Delta\bar{\sigma}| = \begin{cases} E|\Delta\bar{\epsilon}| & |\Delta\bar{\epsilon}| < |\Delta\bar{\sigma}|_{\text{lim}}/E, \\ \sigma_0 + E_p(|\Delta\bar{\epsilon}| - |\Delta\bar{\sigma}|_{\text{lim}}/E) & |\Delta\bar{\epsilon}| \geq |\Delta\bar{\sigma}|_{\text{lim}}/E, \end{cases} \quad (13)$$

where  $|\Delta\bar{\epsilon}|$  is the absolute value of the change in effective total strain from the initial loading point to the current loading point during reverse bending;  $|\Delta\bar{\sigma}|_{\text{lim}}$  is the limiting value of effective stress change

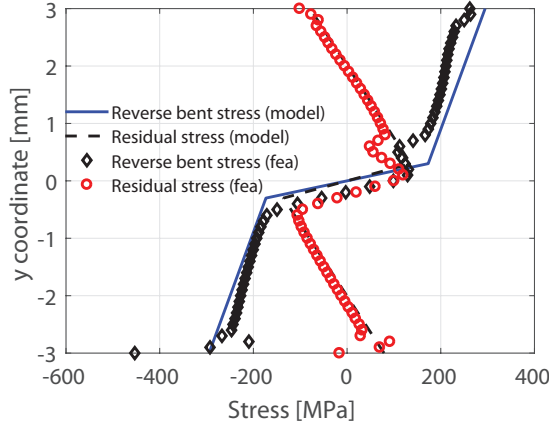


**Figure 22.** Stress distributions across beam thickness after reverse bending and spring-back based on the model and the finite element analyses.

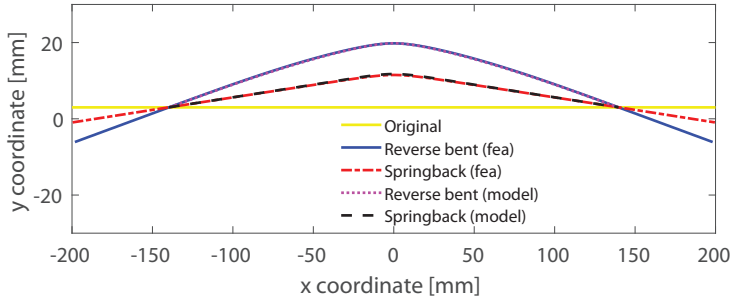


**Figure 23.** Beam profiles after reverse bending and springback based on the model and the finite element analyses for the case of kinematic hardening.

in the elastic regime after reverse bending and is written as

$$|\Delta \bar{\sigma}|_{\text{lim}} = (1 + m)|\bar{\sigma}_r| + (1 - m)(2\sigma_0 - |\bar{\sigma}_r|), \quad (14)$$

where  $|\bar{\sigma}_r|$  is the absolute value of effective stress when the reverse bending occurs and  $m$  is a combined hardening coefficient. The value of  $m$  can be taken as 1 or 0 corresponding to isotropic hardening or kinematic hardening, respectively. For combined isotropic and kinematic hardening, the value of  $m$  is between 0 and 1.

Assuming kinematic hardening during reverse bending, the feasibility of the present model for materials with kinematic hardening is investigated. Using (1)–(6), (11), and (13)–(14) with  $m = 0$ , the stress distributions after reverse bending and springback can be computed. Figure 23 shows the specimen's profiles after reverse bending and springback based on the model and the finite element analyses for the case of kinematic hardening. Good agreement is obtained between model results and finite element analyses results. Figure 24 shows the stress distributions after reverse bending and springback based on the model and the finite element analyses for the case of kinematic hardening. The stress results obtained from the model show good agreement with those based on the finite element analyses.



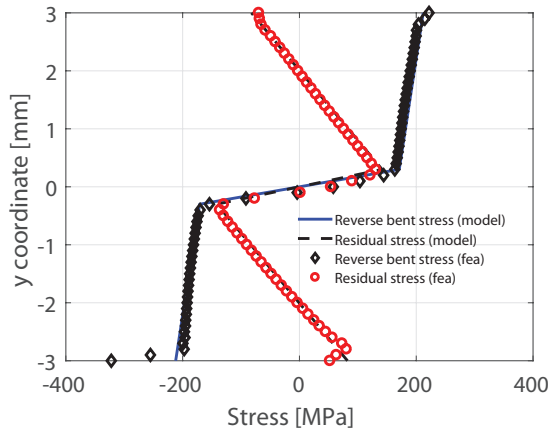


**Figure 24.** Stress distributions across beam thickness after reverse bending and springback based on the model and the finite element analyses for the case of kinematic hardening.

It is noted that the bending/unbending model presented by Kuwabara et al. [1996] can predict the residual curvature relatively accurately and their model was compared with results of finite element analyses in draw-bending processes by Hama et al. [2008]. Compared to the model presented in this investigation, Kuwabara's model is more sophisticated with the consideration of tension in bending processes and Ziegler's kinematic hardening law. The advantage of the present model is that it can calculate the residual stress and curvature distribution along the span of the beam over the supports. In the model, the deformed profile of the beam is obtained based on the curvature distribution and the combined isotropic and kinematic hardening during reverse bending is accounted for by a phenomenological combined hardening parameter. The model's prediction of the residual stress distribution and profile of the beam after bending and reverse bending is verified by experiments and finite element analyses.

## 5. Conclusions

A model for analyzing springback and residual stress distribution of beams under three-point bending is developed. Complex material hardening during bending and reverse bending can be modeled by a phenomenological combined hardening parameter in the model. The converged solutions of deflection and stress distribution of beams over the span of the supports under three-point bending and reverse bending with consideration of material plastic hardening behavior are computed very efficiently by the recursive scheme. Its feasibility to characterize the beam's profile and residual stress distribution after springback is verified by experiments and finite element analyses. The beam material is assumed to be elastic, linear plastic, and the plastic behavior of the beam is described by the von Mises yield criterion. Experimental results further confirm the accuracy of the model by comparing the experimental beam profiles and residual stress distribution after bending and springback with the results obtained by the model. Depending on the plastic behavior of the beam material, various hardening laws can be modeled and incorporated into the analytical model.

Since the multiroller leveling process of metal plates can be viewed as a series of bending/unbending of plates under three-point bending configurations, the developed model has the potential to be extended

to analyze the profile and residual stress of plates during the leveling process. Accuracy of the model for large deflection and relative large radius of fulcrum cylinders suggests that it is a reasonable building block for development of an analytical model of multiroller leveling of metal plates in steel mills.

### Acknowledgements

This work was financially supported by China Steel Corporation (contract number: 05T1D-RE004). Partial support of this work given by a grant from Ministry of Science and Technology, Taiwan (grant number: MOST 105-2221-E-005-060) is greatly appreciated. The authors would like to express their appreciation to the National Center for High-performance Computing (NCHC), Taiwan, for their assistance.

### References

- [Arnautov 2005] A. K. Arnautov, “The method of three-point bending in testing thin high-strength reinforced plastics at large deflections”, *Mech. Compos. Mater.* **41**:5 (2005), 467–476.
- [Batista 2015] M. Batista, “Large deflections of a beam subject to three-point bending”, *Int. J. Non-Linear Mech.* **69** (2015), 84–92.
- [Chiew et al. 2016] S. P. Chiew, Y. F. Jin, and C. K. Lee, “Residual stress distribution of roller bending of steel rectangular structural hollow sections”, *J. Constr. Steel Res.* **119** (2016), 85–97.
- [Conway 1947] H. D. Conway, “XCIV. The large deflection of simply supported beams”, *Lond. Edinb. Dubl. Phil. Mag. J. Sci.* **38**:287 (1947), 905–911.
- [Gao 1994] X.-L. Gao, “Finite deformation elasto-plastic solution for the pure bending problem of a wide plate of elastic linear-hardening material”, *Int. J. Solids Struct.* **31**:10 (1994), 1357–1376.
- [Geng et al. 2002] L. Geng, Y. Shen, and R. H. Wagoner, “Anisotropic hardening equations derived from reverse-bend testing”, *Int. J. Plast.* **18**:5-6 (2002), 743–767.
- [Gergess and Sen 2016] A. Gergess and R. Sen, “Curving structural steel girders by two-point bending”, *J. Constr. Steel Res.* **122** (2016), 511–519.
- [Hama et al. 2008] T. Hama, T. Nagata, C. Teodosiu, A. Makinouchi, and H. Takuda, “Finite-element simulation of springback in sheet metal forming using local interpolation for tool surfaces”, *Int. J. Mech. Sci.* **50**:2 (2008), 175–192.
- [Higo et al. 2016] T. Higo, H. Matsumoto, and S. Ogawa, “Influence of delivery-side roll position of roller leveler to plate flatness”, pp. 2129–2137 in *2016 AISTech Conference Proceedings*, 2016.
- [Hill 1950] R. Hill, *The mathematical theory of plasticity*, Oxford, Clarendon, 1950.
- [Hosford and Caddell 1993] W. F. Hosford and R. M. Caddell, *Metal forming: mechanics and metallurgy*, Prentice Hall, 1993.
- [Johnson and Yu 1981] W. Johnson and T. X. Yu, “On springback after the pure bending of beams and plates of elastic work-hardening materials, III”, *Int. J. Mech. Sci.* **23**:11 (1981), 687–695.
- [Kang and Li 2009] Y.-A. Kang and X.-F. Li, “Bending of functionally graded cantilever beam with power-law non-linearity subjected to an end force”, *Int. J. Non-Linear Mech.* **44**:6 (2009), 696–703.
- [Kuwabara et al. 1996] T. Kuwabara, S. Takahashi, and K. Ito, “Springback analysis of sheet metal subjected to bending-unbending under tension, I: Theory and results of numerical analysis”, pp. 743–746 in *Advanced Technology of Plasticity 1996: Proceedings of the 5th International Conference on Technology of Plasticity* (Columbus, Ohio), edited by T. Altan, 1996.
- [Kuwabara et al. 1999] T. Kuwabara, N. Seki, and S. Takahashi, “A rigorous numerical analysis of residual curvature of sheet metals subjected to bending-unbending under tension”, pp. 1071–1076 in *Advanced Technology of Plasticity 1999: Proceedings of the 6th International Conference on Technology of Plasticity* (Nuremberg, Germany), edited by T. Gaiger, 1999.
- [Li et al. 2011] M. Li, L. Wu, L. Ma, B. Wang, and Z. Guan, “Structural design of pyramidal truss core sandwich beams loaded in 3-point bending”, *J. Mech. Mater. Struct.* **6** (2011), 1255–1266.

- [Lin and Hua 2000] Y. H. Lin and M. Hua, “Influence of strain hardening on continuous plate roll-bending process”, *Int. J. Non-Linear Mech.* **35**:5 (2000), 883–896.
- [Mohyeddin and Fereidoon 2014] A. Mohyeddin and A. Fereidoon, “An analytical solution for the large deflection problem of Timoshenko beams under three-point bending”, *Int. J. Mech. Sci.* **78** (2014), 135–139.
- [Mujika 2006] F. Mujika, “On the difference between flexural moduli obtained by three-point and four-point bending tests”, *Polym. Test.* **25**:2 (2006), 214–220.
- [Müller et al. 2013] U. Müller, H. Krambeer, A. Wolff, A. Espina Viella, A. D. Richardson, J.-O. Perä, P. Luoto, and W. Weiberm, “Optimisation of final plate flatness by set-up coordination for subsequent manufacturing process (final plate flatness)”, Final report, EUR 25852 EN, European Commission, 2013, <https://publications.europa.eu/en/publication-detail/-/publication/24f660f1-6532-4ce5-81c7-1b60389371a9>.
- [Natarajan and Peddieson 2011] A. Natarajan and J. Peddieson, “Simulation of beam plastic forming with variable bending moments”, *Int. J. Non-Linear Mech.* **46**:1 (2011), 14–22.
- [Ohtsuki 1986] A. Ohtsuki, “An analysis of large deflections in a symmetrical three-point bending of beam”, *Bullet. JSME* **29**:253 (1986), 1988–1995.
- [Pandit and Srinivasan 2016] D. Pandit and S. M. Srinivasan, “Numerical analysis of large elasto-plastic deflection of constant curvature beam under follower load”, *Int. J. Non-Linear Mech.* **84** (2016), 46–55.
- [Schajer and Prime 2006] G. S. Schajer and M. B. Prime, “Use of inverse solutions for residual stress measurements”, *J. Eng. Mater. Technol. (ASME)* **128**:3 (2006), 375–382.
- [Sitar et al. 2015] M. Sitar, F. Kosel, and M. Brojan, “Numerical and experimental analysis of elastic–plastic pure bending and springback of beams of asymmetric cross-sections”, *Int. J. Mech. Sci.* **90** (2015), 77–88.
- [Takahashi et al. 1996] S. Takahashi, T. Kuwabara, and K. Ito, “Springback analysis of sheet metal subjected to bending–unbending under tension, II: Experimental verification”, pp. 747–750 in *Advanced Technology of Plasticity 1996: Proceedings of the 5th International Conference on Technology of Plasticity* (Columbus, Ohio), edited by T. Altan, 1996.
- [Theocaris et al. 1977] P. S. Theocaris, S. A. Paipetis, and S. Paolinelis, “Three-point bending at large deflections”, *J. Test. Eval.* **5**:6 (1977), 427–436.
- [Triantafyllidis 1980] N. Triantafyllidis, “Bifurcation phenomena in pure bending”, *J. Mech. Phys. Solids* **28**:3–4 (1980), 221–245.
- [Zhang et al. 2007] D. Zhang, Z. Cui, X. Ruan, and Y. Li, “An analytical model for predicting springback and side wall curl of sheet after U-bending”, *Comput. Mater. Sci.* **38**:4 (2007), 707–715.
- [Zhu 2007] H. X. Zhu, “Large deformation pure bending of an elastic plastic power-law-hardening wide plate: analysis and application”, *Int. J. Mech. Sci.* **49**:4 (2007), 500–514.

Received 21 May 2017. Revised 25 Sep 2018. Accepted 9 Oct 2018.

QUANG KHOA DANG: [khoadq@hcmute.edu.vn](mailto:khoadq@hcmute.edu.vn)

Graduate Institute of Precision Engineering, National Chung Hsing University, Taichung, Taiwan

PEI-LUN CHANG: [iamalan1122@yahoo.com.tw](mailto:iamalan1122@yahoo.com.tw)

Graduate Institute of Precision Engineering, National Chung Hsing University, Taichung, Taiwan

SHIH-KANG KUO: [150359@mail.csc.com.tw](mailto:150359@mail.csc.com.tw)

Iron and Steel Research and Development Department, China Steel Corporation, Kaohsiung, Taiwan

DUNG-AN WANG: [daw@dragon.nchu.edu.tw](mailto:daw@dragon.nchu.edu.tw)

Graduate Institute of Precision Engineering, National Chung Hsing University, Taichung, Taiwan



## CHARACTERIZATION OF CNT PROPERTIES USING SPACE-FRAME STRUCTURE

MUHAMMAD ARIF AND JACOB MUTHU

We studied the elastic properties of different carbon nanotubes (CNTs), i.e., pristine and defective single-wall (SWCNTs), double-wall (DWCNTs), and multiwall (MWCNTs) for zigzag and armchair configurations. CNTs atomic geometry was replicated with an equivalent space frame structure (SFS). Coordinates definition of SFS of CNTs was developed in MATLAB code and transferred to the finite element analysis (FEA) software ANSYS. The basic entity of SFS, the C-C chemical bond, was designed as a circular beam with orthotropic properties. The properties were determined by linking the energy equation of molecular mechanics to structural mechanics along with a parametric study. The van der Waals forces between intershells of DWCNTs and MWCNTs were modeled as linear elastic springs in a simplified way. The simplified model avoided the problems due to the nonlinear behavior of van der Waals forces and improved the performance of the FEA software. The effect of chirality, vacancy defects, different diameters, and number of walls on the elastic properties of CNTs were calculated, tabulated, and compared with each other. The result of the proposed SFS model with orthotropic properties was compared with other's results. The space frame structure (SFS) model is found to be better than the equivalent shell model as the defects can be placed at exact locations and a more realistic behavior can be predicted. The SFS models can developed with any type of defect, any number of walls, van der Waals force interactions, and agglomerated forms with variable geometries. These models could be directly embedded in the matrix with a designable interface region to predict tensile and torsional properties of future nanocomposites.

### 1. Introduction

The discovery of carbon nanotubes (CNTs) [Iijima 1991] has attracted immense interest in the field of high strength structural composite materials due to CNTs extraordinary mechanical properties (elastic modulus 0.5–5 TPa and tensile strength 50–200 GPa) [Qian et al. 2002; Treacy et al. 1996]. These mechanical properties made them as a potential contender for reinforcing matrices such as polymer [Muthu and Dendere 2014], ceramic [Inam et al. 2014], and metal [Tjong 2013]. Mahmoud [Shokrieh et al. 2013] and Kundalwal [Kundalwal and Ray 2014] have shown that adding a small amount of CNTs to the polymer matrix improved the mechanical, thermal, and electrical properties of the composites. Other research works [Inam et al. 2014; Sharma and Shukla 2014] have also reported that the addition of 1% CNTs increased the elastic modulus, flexural, and tensile strength of epoxy composites by 49%, 38%, and 52% respectively.

However, these experimental results are much lower than the theoretically expected values for CNT reinforced composites [Zuberi and Esat 2015]. Researchers have attributed these discrepancies between

---

*Keywords:* carbon nanotubes, numerical modeling, continuum Mechanics, finite element analysis, properties.

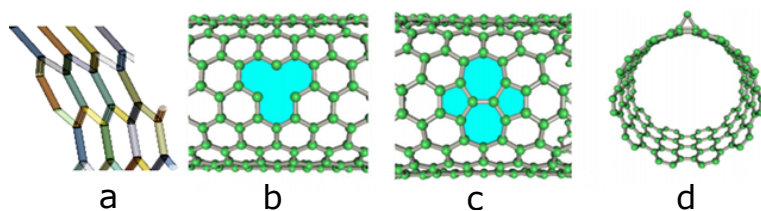


**Figure 1.** Different kinds of defects in CNTs: hexagonal arrangement (a), vacancy defect (b), Stone–Wales defect (c), adatom (d).

experimental and theoretical results to the inconsistency in CNT diameter [Nam et al. 2015], chirality (rolled up angle of graphene sheet) [Ranjbartoreh and Wang 2010], number of CNT walls [Jia et al. 2011], and defects in the CNT structure [Xiao and Hou 2006]. Different kinds of defects such as vacancy, Stone–Wales, and adatom (Figure 1) are developed in CNTs during synthesis [Tachibana 2013] and play an important role in defining their properties. Researches [Yang et al. 2016] have shown that the vacancy defects (Figure 1b) are the most influential factor in degrading the overall CNT properties. In addition, as pointed out by Popov et al. [Popov et al. 2000] that the properties of CNTs along the tube axial direction are always greater than the transverse directions (orthotropic behavior) and a similar conclusion was also drawn by Kundalwal and Kumar [Kundalwal and Kumar 2016]. Therefore, it is essential to understand the effect of the above factors (diameter, chirality, number of walls, vacancy defects, and the orthotropic behavior) on the CNTs mechanical properties, which will further be helpful in choosing suitable CNTs as composites reinforcement to obtain improved mechanical properties.

Various experimental techniques such as Raman spectroscopy, scanning electron spectroscopy, transmission electron microscopy, nanoindentation, and x-ray diffraction have been used to characterize the CNT's properties [Chabalala et al. 2011]. However, the main challenges faced with these experimental techniques are that they are either expensive or technically not feasible to obtain the nanoscale behavior of CNTs. Moreover, the conventional theoretical models such as rule of mixtures [Han et al. 2014b], effective field models [Zohdi and Wriggers 2005], and continuum mechanics models [Tserpes et al. 2008] also have limitations in predicting the behavior of CNTs at nanolength scales [Han et al. 2014b]. Hence, researchers have focused on developing molecular scale models such as molecular dynamics (MD) and molecular mechanics (MM) methods. These methods are powerful and can provide details at the molecular scale level. However, their limitations in analyzing the number of atoms, length, and time scales along with the computational cost have restricted their applications within a limited span [Han et al. 2014a].

To overcome the length scale limitations in molecular models, an equivalent continuum model (ECM) was proposed [Hernández-Pérez and Avilés 2010]. In the ECM model, the individual carbon nanotube was modeled either as a shell or as a beam with isotropic properties [Roy Chowdury et al. 2014; Hu et al. 2007]. Moreover, in these models, the hexagonal atomic structure of a CNT was completely ignored [Muc 2011] and thus resulted in exaggerated CNT properties. In addition, these models could not include the effects of vacancy defects, chirality, and van der Waals force interactions between the walls. Hence, for incorporating the CNTs atomic structure, a space frame structure (SFS) model was proposed [Ghavamian et al. 2013]. In the SFS model, the chemical bond between two carbon atoms (C–C) was modeled as a circular beam with isotropic properties in such a way that one carbon molecule was modeled using six

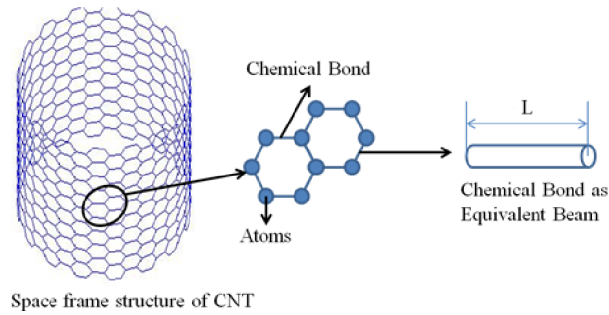


**Figure 2.** Equivalent SFS.

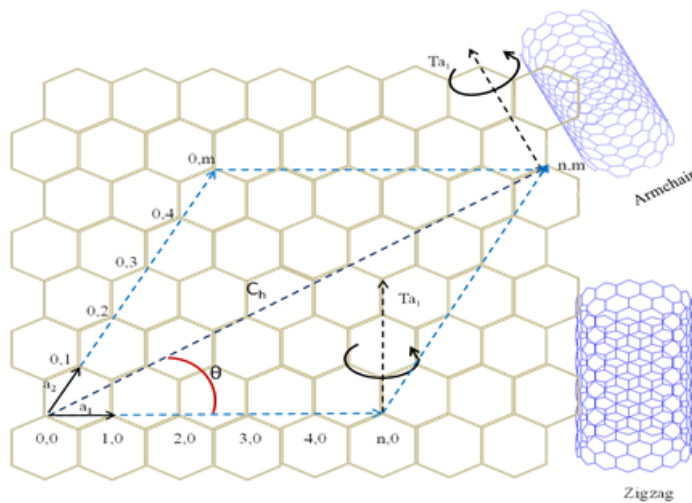


**Figure 3.** Rolling angle and chiral vector.

circular beams in a hexagonal shape, as shown in Figure 2. The chemical bond properties were obtained from both solid and molecular mechanic analysis.

However, the CNTs orthotropic properties [Muc 2010] were again ignored by the SFS model including the other important parameters as explained above. Hence the objectives of this paper were defined as to characterize the zigzag and armchair CNTs using SFS model by considering the effects of CNTs diameters, chirality, number of walls, vacancy defects, and the van der Waals interactions between the walls (double and multiwalled). In addition, this research also focused on understanding the effect of orthotropic behavior of CNTs on their properties.

## 2. Methodology for simulation

**2A. SFS modeling of CNTs.** Since CNTs are formed by rolling the graphene sheets, the parameters such as chiral angle ( $\theta$ ) and chiral vector ( $C_h$ ) define the types of CNTs such as zigzag and armchair. Figure 3 shows a schematic of chiral vector, chiral angle, and the relevant geometrical parameters.



zigzag			armchair		
$n$	$m$	diameter (Å)	$n$	$m$	diameter (Å)
7	0	5, 481	4	4	5, 424
11	0	8, 61	6	6	8, 13
14	0	10, 96	8	8	10, 84
20	0	15, 657	11	11	14, 916
28	0	21, 92	16	16	21, 696

**Table 1.** Configuration properties. Note that all MWCNTs have three walls. Furthermore, the intershell distance  $d_{s-s}$  range is 3.4 Å–3.8 Å, and the bond length  $L$  range is 1.41 Å–1.42 Å [Harik 2011].

The chiral vector ( $C_h$ ) is mathematically defined by the unit vectors  $a_1$  and  $a_2$  combined with the step integer  $n$  and  $m$ , which basically determine the chirality or twist of the nanotube:

$$\vec{C}_h = n\vec{a}_1 + m\vec{a}_2. \quad (2-1)$$

Different roll-up directions of graphene (chiral angle,  $\theta$ ) give different configurations of CNTs and are defined by

$$\theta = \sin^{-1} \left[ \frac{\sqrt{3}m}{2(n^2 + nm + m^2)} \right], \quad (2-2)$$

where  $\theta$  is the chiral angle.

Mathematically, if the step integers  $n \neq 0$  and  $m = 0$  ( $\theta = 0^\circ$ ) are set then a zigzag CNT could be defined and an armchair structure could be generated for the step integers  $n = m$  ( $\theta = 30^\circ$ ) [Rahmandoust and Öchsner 2009]. In addition, the CNTs diameters are also obtained using the step integers as

$$d = 0.783\sqrt{n^2 + nm + m^2} \quad (2-3)$$

**2B. CNTs model development.** Using the above equations, a CNT was modeled by defining its coordinates in a MATLAB code for the different types of CNTs such as zigzag, armchair, single, defective, double, and multiwall. The required chiral angle and chiral vector were obtained and given in Table 1.

A general methodology that followed for producing both zigzag or armchair configurations was that a basic unit cell (a carbon molecule) was developed along the tube circumference. At first, a single carbon molecule was divided into six equivalent triangles. The height  $h$  and half of the base  $b$  of the individual triangle were used to draw the positions of the individual carbon atoms and then the carbon molecule unit cell. The angle  $\psi$  defines the number of carbon molecules along the circumference based on the base length  $b$  with respect to the center of the CNT. Figure 4 shows the schematic of the modeling process.

The base unit cell was then extended further to obtain a base ring and then the full carbon nanotube (Figure 5). Double and multiwall CNTs were developed using the same procedure. The distance between the consecutive walls ( $d_{(s-s)}$ ) was kept at 3.4 ~ 3.8 Å [Ghavamian et al. 2013]. Figure 6 shows the double wall and multiwall CNTs modeled using the proposed procedure.

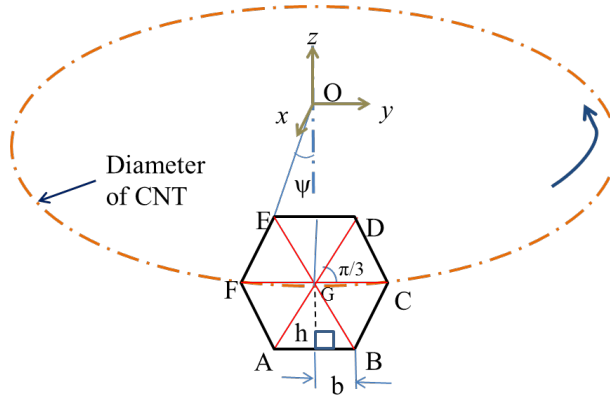


**Figure 4.** Modeling process of CNTs.

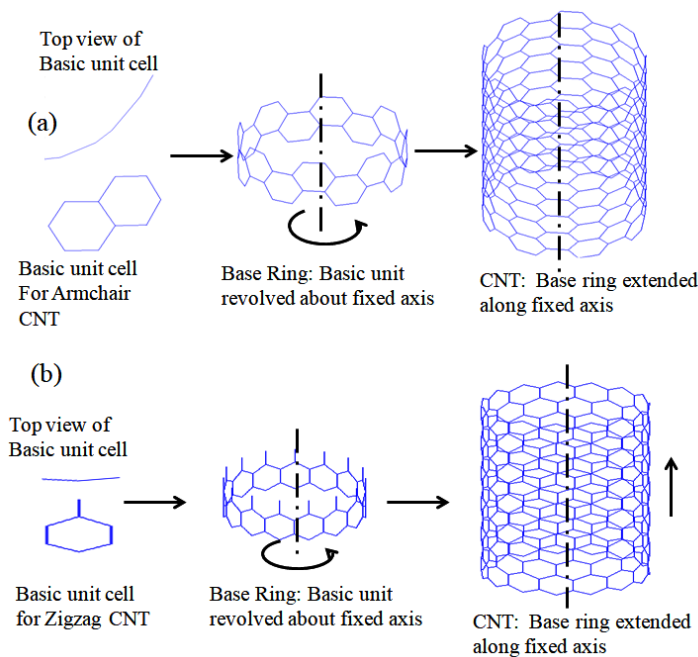


**Figure 5.** CNTs modeling process: armchair (a) and zigzag (b).

The vacancy defects were randomly generated by removing a point (carbon atom) at three different places: top, center, and bottom of the CNTs. These defects were approximately  $120^\circ$  apart from each other (Figure 7).

The macrofiles containing the CNT coordinates were transferred to ANSYS for developing an IGES-ANSYS workbench multibody CNT model. The in-built ANSYS workbench shared topology method was utilized to convert the multibody CNT SFS-model into a single part. This method joins each equivalent circular beam to the other beams through the edge joints method. Figure 8 shows the transferred ANSYS workbench CNT model developed in MATLAB. Five different diameters were used for both

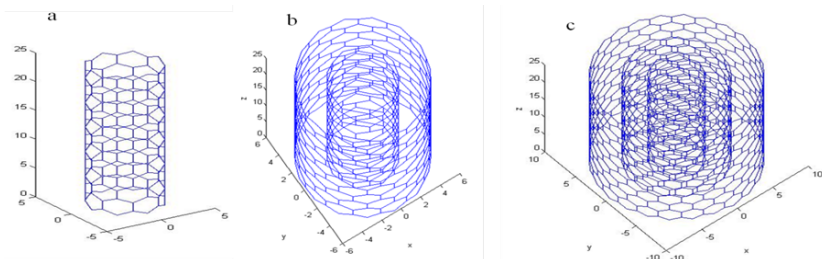


Figure 6. DWCNT and MWCNT modeling process.

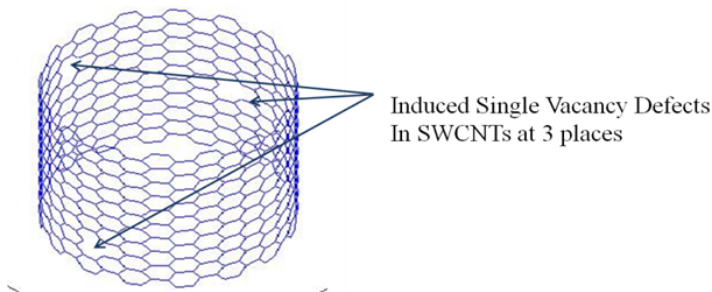


Figure 7. CNT with vacancy defects.

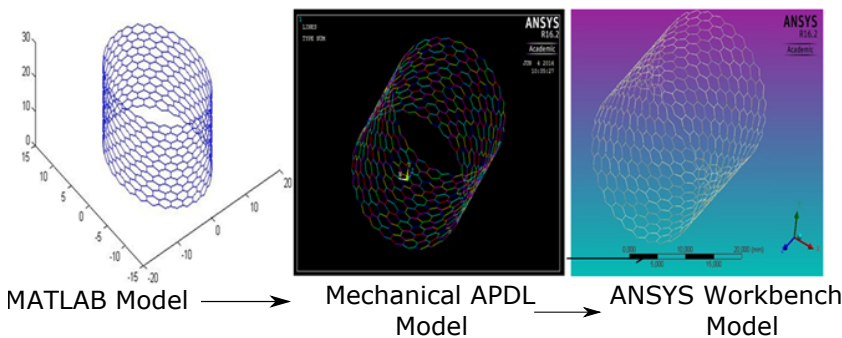
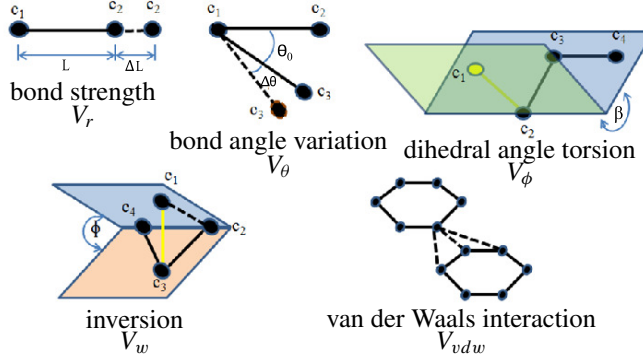


Figure 8. Equivalent SFS modeling process of CNTs.

the zigzag and armchair configurations. Pristine and defective single-walled and pristine double and multiwalled CNTs were considered for the analysis.

**2C. C-C chemical bond orthotropic properties.** The next step is to define the C-C chemical bond properties. As briefly discussed before, most of the research works have considered CNTs as an isotropic material. However, theoretical studies [Muc 2010] have shown that the CNTs behave like an orthotropic material. Hence, in this research, the orthotropic properties of CNTs were obtained by assuming orthotropic response from the individual C-C bond. Hence two different methods were used to obtain both axial and transverse response of the C-C bonds.

**2C1. C-C bond axial direction response.** The axial direction response of the C-C bond was obtained by equating the energy of the atomistic system (molecular mechanics) with the beam model (classical



**Figure 9.** Graphical representation of steric potential energy.

structural mechanics). Based on molecular mechanics, the C-C chemical bond could be expressed using steric potential energies, which gives the total potential energy ( $V_t$ ) [Rahmandoust and Öchsner 2012] of the individual C-C bond as

$$V_t = \sum V_r + \sum V_\theta + \sum V_\phi + \sum V_w + \sum V_{vdw}, \quad (2-4)$$

where  $V_r$ ,  $V_\theta$ ,  $V_\phi$ ,  $V_w$ ,  $V_{vdw}$  are the bond strength, bond angle variation, dihedral angle torsion, inversion, and interaction strain energies respectively (Figure 9).

Since the inversion and the interaction energies have very little influence on the total potential energy equation, the bond strength, bond angle variation, and dihedral angle torsion energies are only considered for the current analysis. These energies are expressed as

$$V_r = \frac{1}{2}k_r(L - L_0)^2 = \frac{1}{2}k_r(\Delta L)^2, \quad (2-5)$$

$$V_\theta = \frac{1}{2}k_\theta(\theta - \theta_0)^2 = \frac{1}{2}k_\theta(\Delta\theta)^2, \quad (2-6)$$

$$V_\phi = V_w = \frac{1}{2}k_\tau(\Delta\beta)^2. \quad (2-7)$$

Here,  $k_r$ ,  $k_\theta$ , and  $k_\tau$  are bond stretching, bond angle variation, and torsion resistance force constants, respectively;  $\Delta L$ ,  $\Delta\theta$ , and  $\Delta\beta$  are the bond stretching, bond angle variation, and angle variation of bond twist, respectively. The C-C chemical bond characteristics are assumed to be an analogue to a structural mechanics beam element (Figure 10). Here, the carbon atoms act as joints of the beam element and hence the stiffness equations associated with the structural mechanics for a beam element could be equated with the force constants of molecular mechanics to define the C-C chemical bond along the axial direction.

According to classical structural mechanics, the strain energy equations of a beam under uniform axial, bending, and torsional loads are given by

$$U_A = \frac{1}{2} \int_0^L \frac{F^2}{EA} dL = \frac{1}{2} \frac{F^2 L}{EA} = \frac{1}{2} \frac{EA}{L} \Delta L^2, \quad (2-8)$$

$$U_M = \frac{1}{2} \int_0^L \frac{M^2}{EI} dL = \frac{1}{2} \frac{M^2 L}{EI} = \frac{1}{2} \frac{EI}{L} \Delta\theta^2, \quad (2-9)$$

$$U_T = \frac{1}{2} \int_0^L \frac{T^2}{GJ} dL = \frac{1}{2} \frac{T^2 L}{GJ} = \frac{1}{2} \frac{GJ}{L} \Delta\beta^2, \quad (2-10)$$

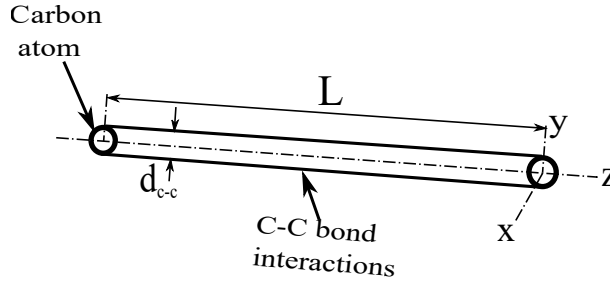


**Figure 10.** Equivalent beam model.

$k_r$	$938 \text{ kcal} \cdot \text{mol}^{-1} \cdot \text{\AA}^{-2} = 6.52 \times 10^{-7} \text{ N} \cdot \text{nm}^{-1}$
$K_\theta$	$126 \text{ kcal} \cdot \text{mol}^{-1} \cdot \text{\AA}^{-2} = 8.76 \times 10^{-10} \text{ N} \cdot \text{nm}^{-1}$
$K_\tau$	$39.986 \text{ kcal} \cdot \text{mol}^{-1} \cdot \text{\AA}^{-2} = 2.780 \times 10^{-10} \text{ N} \cdot \text{nm}^{-1}$

**Table 2.** Molecular mechanics constant values; note that the bond length  $L = 0.142 \text{ nm}$  [Tersoff and Ruoff 1994].

where  $E$  is the elastic modulus,  $A$  is the cross sectional area,  $L$  is the beam length,  $I$  is the moment of inertia,  $G$  is the polar moment of inertia,  $J$  is the polar moment of inertia,  $\theta$  is rotational angle, and  $\beta$  is relative rotation between the two ends.

By considering analogues and equating the corresponding energy equations, the relationship between structural mechanics ( $EA$ ,  $EI$ , and  $GJ$ ) and the molecular mechanics parameters ( $k_r$ ,  $k_\theta$ , and  $k_\tau$ ) are deduced as [Li and Chou 2003b]

$$k_r = \frac{EA}{L}, \quad k_\theta = \frac{EI}{L}, \quad k_\tau = \frac{GJ}{L}. \quad (2-11)$$

These above equations were used to obtain the C-C bond axial direction response. The parameters for calculating the C-C bond axial response are given in Table 2.

Using the above values, the C-C bond axial responses are calculated as

$$d_{c-c} = 4\sqrt{\frac{K_\theta}{K_r}} = 0.14660 \text{ nm}, \quad E_{zz} = \frac{(K_r)^2 L}{4\pi K_\theta} = 5.49 \text{ TPa}, \quad G_{xy} = \frac{(K_r/K_\theta) K_\tau L}{8\pi} = 0.871 \text{ TPa}.$$

**2C2. C-C bond transverse direction response.** The transverse direction responses of C-C bonds were obtained using an ANSYS parametric study. The space frame structure model of a single-wall zigzag CNT with diameter  $0.861 \text{ nm}$  was chosen along with the C-C bond axial response values previously obtained for this analysis. The parametric study was carried out by using the range of values of elastic modulus, shear modulus, and Poisson's ratio as given in Table 3. The analysis was repeated until the SFS model radius modulus was equivalent to  $650 \text{ GPa}$  [Reich et al. 2002]. Then the corresponding orthotropic properties were selected to define the transverse response of the C-C bond interactions.

The overall orthotropic response of the C-C bond is given in Table 4.

elastic modulus (GPa)		shear modulus (GPa)		Poisson's ratio		
$E_{xx}$	$E_{yy}$	$G_{xy}$	$G_{yz}$	$\gamma_{xy}$	$\gamma_{yz}$	$\gamma_{xz}$
4.5–5.5	4.5–5.5	3–8.71	3–8.71	0.1–0.25	0.1–0.25	0.1–0.25

**Table 3.** Range of values for parametric study variables.

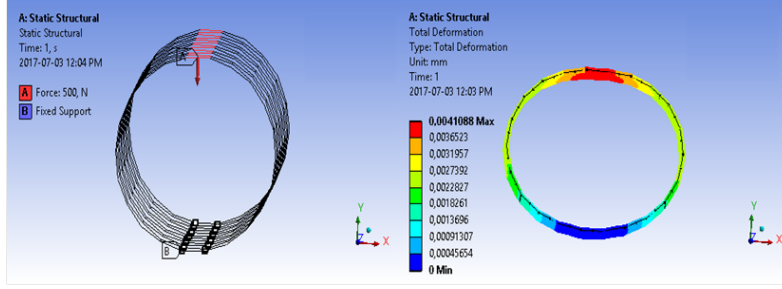


**Figure 11.** Radial test model.

modulus (GPa)			shear (GPa)		
$E_{xx}$	$E_{yy}$	$E_{zz}$	$G_{xy}$	$G_{yz}$	$G_{xz}$
523	523	5490	409	409	871

**Table 4.** Orthotropic properties of CNTs. Note that the ratio  $\gamma_{xy} = \gamma_{yz} = \gamma_{xz} = 0.1$ .

**2D. Modeling of van der Waals forces.** DWCNTs and MWCNTs contain two or more concentric shells at distances 3.4 Å to 3.8 Å from each other and interact through the van der Waals ( $F_{vdw}$ ) forces. In addition, these forces are effective within 0.85 nm range [Zuberi and Esat 2015] and the atoms which are not within the range will be coupled with the adjacent range atoms. Based on the above assumption, a single carbon atom of one shell interacts with 58 atoms of an adjacent shell (0.85 nm range) as shown in Figure 12a. Generally, the van der Waals forces are calculated using Lennard–Jones potentials [1924], given as

$$F_{(vdw)} = 4\epsilon \left[ -12 \left( \frac{\sigma}{d_{s-s}} \right)^{12} + 6 \left( \frac{\sigma}{d_{s-s}} \right)^6 \right]. \quad (2-12)$$

Ali and coworkers [Ghavamian et al. 2013] modeled the van der Waals force ( $F_{vdw}$ ) interaction between two carbon atoms as a spring with a stiffness ( $K_{\text{single C-C}}$ ) of 0.24245 N/m. However, with a large number of van der Waals interactions, modeling each interaction could lead to computational difficulties. Hence these intershell interactions were modeled as equivalent springs (Figure 12b).

Four equivalent springs at 90° intervals were inserted between two adjacent shells to model the total van der Waals force interactions. The stiffness of a single equivalent spring ( $K_{\text{eq}}$ ) was calculated from the total spring stiffness  $K_n$ . Hence,  $K_n = 58 \times K_{\text{single C-C}} \times \text{total number of atomic interactions from first shell to the second shell (TAI)}$ .

Where  $n = (\text{1st shell, 2nd shell, } \dots)$  and  $K_{\text{single C-C}}$  is the spring stiffness between two carbon atoms. The total atomic interactions (TAI) between one shell to the other were estimated by the following

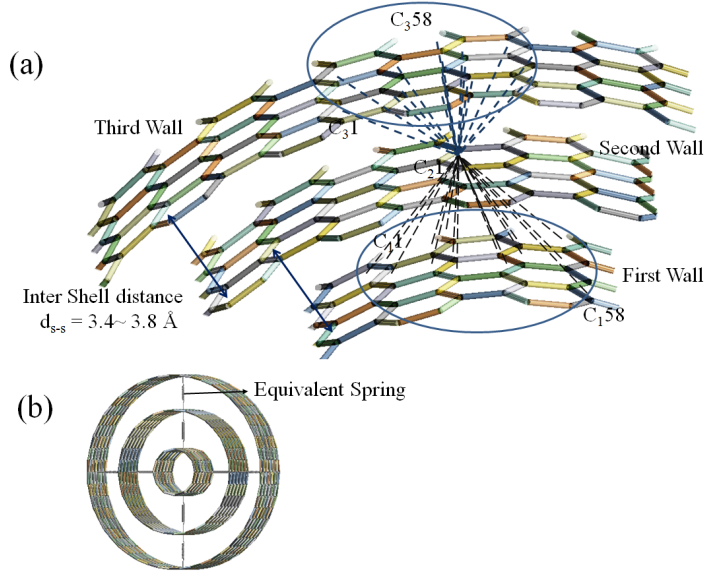


**Figure 12.** Van der Waals force interactions between different shells (a) and equivalent spring constant between shells (b).

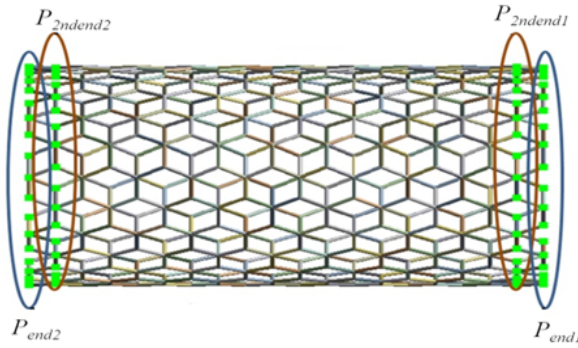


**Figure 13.** End points of CNTs.

equation:

$$TAI = P_{total} - 0.5P_{end1} - 0.5P_{end2} - 0.875P_{2ndend1} - 0.875P_{2ndend2}, \quad (2-13)$$

where  $P_{total}$  is the total number of atoms in a single shell,  $P_{end1}$  is the number of atoms in the end rows, and  $P_{2ndend1}$  is the number of atoms in second end rows (Figure 13).

Since  $P_{end1} = P_{end2}$  and  $P_{2ndend1} = P_{2ndend2}$ , the TAI equation becomes

$$TAI = P_{total} - P_{end} - 1.75P_{2ndend}.$$



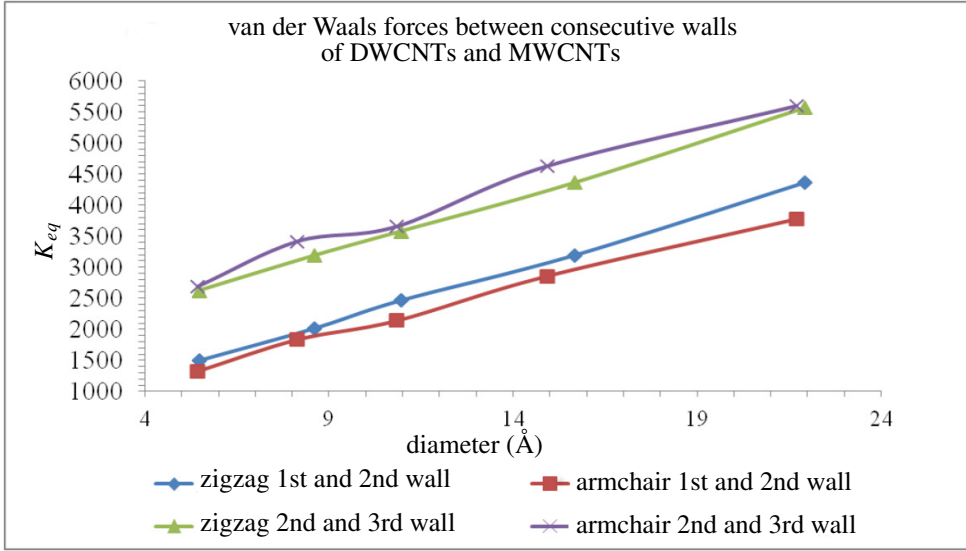


**Figure 14.** Van der Waals forces between consecutive walls.

Using the above TAI values, the total spring stiffnesses ( $K_n$ ) were obtained and then  $K_{eq}$  for the individual springs were estimated using

$$K_{eq} = \frac{K_{1stshell} + K_{2ndshell}}{S_0}, \quad (2-14)$$

where  $S_0$  is the number of springs to be inserted.

The values of equivalent spring constant  $K_{eq}$  obtained for all different CNTs are given in Table 5. Figure 14 shows that the van der Waals forces become more significant increasing diameter and increasing number of walls.

**2E. Analysis procedure.** The proposed SFS model was analyzed using the equivalent properties (EP) method for determining the CNTs properties. The equivalent properties method was defined based on the assumption that the deformation of two SFS-models could be equated when the applied load, CNT length, and area are equal. Here, the first SFS model was defined using a reference material and the second SFS was defined using the proposed orthotropic material. Based on the above definition, the CNT properties could be obtained from

$$\frac{E_{SFS-CNT}}{E_{SFS-Ref}} = \frac{\Delta L_{SFS-CNT}}{\Delta L_{SFS-Ref}}, \quad (2-15)$$

$$\frac{G_{SFS-CNT}}{G_{SFS-Ref}} = \frac{\Delta \theta_{SFS-CNT}}{\Delta \theta_{SFS-Ref}}. \quad (2-16)$$

The proposed analysis was carried out by constraining the CNT model at one end and applying a load at other end. As explained in the EP method, the C-C bond properties were assigned with a reference material and an orthotropic material individually. The first analysis was conducted with structured steel (reference material) properties of elastic modulus 200 GPa and a Poisson's ratio of 0.3. A similar analysis

zigzag (DWCNTs)

diameter (Å)	first wall				second wall				$K_{eq}$ (N/m)
	$P_{end}$	$P_{2ndend}$	total points	total working points	$P_{end}$	$P_{2ndend}$	total points	total working points	
5.481	16	16	168	124	30	30	384	302	1498
8.613	22	22	264	204	40	40	480	370	2017
10.962	28	28	336	259	46	40	552	442	2465
15.66	40	40	480	370	58	58	696	537	3189
21.924	60	60	672	507	74	74	936	733	4360

armchair (DWCNTs)

diameter (Å)	first wall				second wall				$K_{eq}$ (N/m)
	$P_{end}$	$P_{2ndend}$	total points	total working points	$P_{end}$	$P_{2ndend}$	total points	total working points	
5.424	16	16	161	117	36	36	359	260	1326
8.13	24	24	241	175	48	48	479	347	1836
0.84	32	32	321	233	52	52	519	376	2141
14.916	44	44	441	320	68	68	679	492	2855
21.696	64	64	641	465	84	84	839	608	3773

zigzag (MWCNTs)

diameter (Å)	second wall				third wall				$K_{eq}$ (N/m)
	$P_{end}$	$P_{2ndend}$	total points	total working points	$P_{end}$	$P_{2ndend}$	total points	total working points	
5.481	30	30	384	302	48	48	576	444	2623
8.613	40	40	480	370	58	58	696	537	3189
10.962	46	40	552	442	64	64	768	592	3579
15.66	58	58	696	537	76	76	912	703	4360
21.924	74	74	936	733	92	92	1104	851	5569

armchair (MWCNTs)

diameter (Å)	second wall				third wall				$K_{eq}$ (N/m)
	$P_{end}$	$P_{2ndend}$	total points	total working points	$P_{end}$	$P_{2ndend}$	total points	total working points	
5.424	36	36	359	260	56	56	560	406	2690
8.13	48	48	479	347	68	68	680	493	3418
10.84	52	52	519	376	72	72	720	522	3660
14.916	68	68	679	492	88	88	880	638	4630
21.696	84	84	839	608	104	104	1040	754	5601

**Table 5.** Equivalent spring stiffness values. For all cases,  $K_{c-c} = 0.24245$  N/m.

zig zag (SWCNT)				
diameter (Å)	elastic modulus (GPa)		shear modulus (GPa)	
	pristine	vacancy defects	pristine	vacancy defects
5.481	768.525	260.328	320.259	104.663
8.61	769.163	245.471	322.764	89.1
10.96	769.231	235.844	323.164	87.5
15.657	770.442	220.186	320.189	83.5
21.92	774.39	209.463	311.66	70.3

armchair (SWCNT)				
diameter (Å)	elastic modulus (GPa)		shear modulus (GPa)	
	pristine	vacancy defects	pristine	vacancy defects
5.424	755.213	257.637	362.658	97.8
8.13	755.149	240.937	360.011	92.9
10.84	755.659	231.113	359.075	89.0
14.916	759.881	221.317	358.563	85.0
21.696	765.583	228.005	358.125	84.0

**Table 6.** Properties of pristine SWCNTs and SWCNTs with vacancy defects (zigzag and armchair).

was again carried out by using the orthotropic properties as explained in the previous section. Then the EP method was used to obtain the overall properties of the SFS CNT-model.

### 3. Results and discussion

The analysis was carried out for obtaining the elastic properties of single, double and multiwall CNTs configurations. The results clearly showed the effect of chirality, defects, number of walls, and the C-C bond orthotropic properties on the overall CNTs properties.

**3A. Effect of chirality on the mechanical properties.** Since the chirality defines the types of CNT configurations, both zigzag and armchair were modeled and analyzed. Table 6 shows the elastic and shear modulus values of both zigzag and armchair configurations of a single-wall carbon nanotube (SWCNT).

It is evident that the elastic modulus of the zigzag configuration is higher than the armchair one. The difference between the elastic modulus of the two configurations (zigzag and armchair) decreased as the CNT's diameter increased. On the other hand, the armchair configuration has a higher shear modulus than the zigzag. It is evident from these results that the chirality of the CNT primarily affected the shear strength rather than the tensile strength.

The variations in elastic and shear modulus for both zigzag and armchair configurations are attributed to the direction of the hexagonal unit cell to the applied tensile and torsional loads. For the zigzag configuration, all six C-C bonds of a hexagonal unit have contributed towards carrying the applied load (Figure 15a), while the armchair unit cell have used only four C-C bonds for the similar types of loading (Figure 15b). Therefore the tensile strength of zigzag is higher than armchair. However, for the torsional

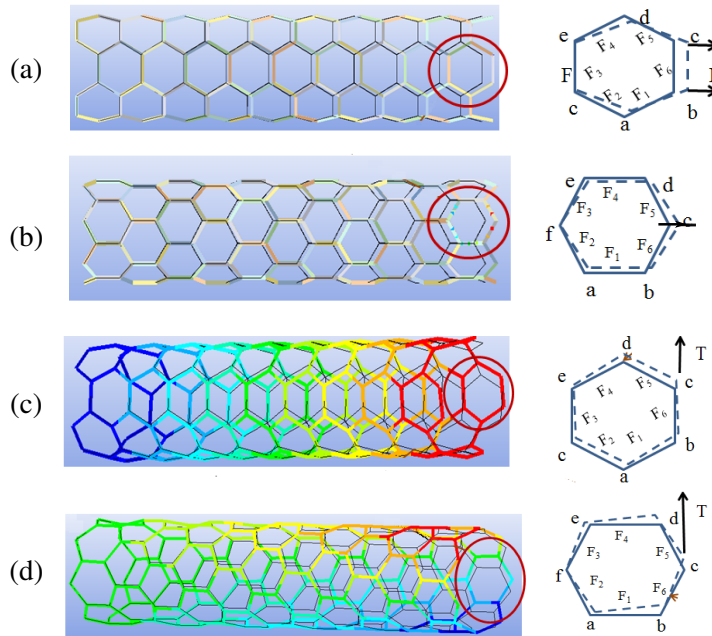


**Figure 15.** The deformation pattern of hexagonal units: armchair (a), zigzag-tensile load (b), armchair (c), and zigzag-applied moment (d).

loading, the reverse phenomenon could be seen as compared to the tensile loading (Figure 15c, d). The comparison based on chirality suggested that the zigzag SWCNTs of higher diameters could increase the properties of nanocomposites in the axial direction. For better transverse properties, armchair configurations with smaller diameters would be a better choice as a reinforcement.

The current analysis results align with the experimental values of 400 GPa to 800 GPa as given by Treacy [Treacy et al. 1996]. Further, the results are also comparable with the other numerical analysis carried out by Mohammad [Mohammadpour and Awang 2011], where they used the continuum mechanics method with nonlinear material properties and obtained the elastic properties of 881 GPa (elastic modulus) and 116 GPa (shear modulus). In addition, the molecular dynamics [Agrawal et al. 2006] results (elastic modulus 550–760 GPa for diameters in the range of 7–25 Å) for SWCNTs also align well with the SFS analysis results.

**3B. Effect of vacancy defects.** The elastic properties of both zigzag and armchair configurations of SWCNTs with vacancy defects were analyzed and their results were almost 70% lower than the corresponding pristine configurations (Table 6). In addition, the vacancy defects have shown more influence on both the elastic and shear modulus of both armchair and zigzag configurations as the diameter of the CNT was increased from 5.48 Å to 21.92 Å. The percentile decrease in CNT properties for the increase in diameter of a zigzag configuration was approximately 69.58% for the elastic modulus and 72.79% for the shear modulus. For the armchair configuration, the percentile decrease was 68.9% for the elastic modulus and 75.04% for the shear modulus, respectively (Table 7). Similar results were obtained by Ying

zigzag (SWCNT)		
diameter (Å)	elastic modulus (%)	shear modulus (%)
5.481	66.13	67.32
8.61	68.09	72.38
10.96	69.34	72.91
15.657	71.42	73.89
21.92	72.95	77.43
average	69.58	72.79

armchair (SWCNT)		
diameter (Å)	elastic modulus (%)	shear modulus (%)
5.424	65.89	73.01
8.13	68.09	74.19
10.84	69.42	75.19
14.916	70.87	76.29
21.696	70.22	76.53
average	68.9	75.04

**Table 7.** Percentile decrease of elastic and shear modulus due to vacancy defects (zigzag and armchair).

et al. [Yang et al. 2017] with elastic modulus of 270 GPa for SWCNTs with defects. Sakhaee [Sakhaee-Pour 2009] showed that the elastic and shear modulus of defective SWCNTs were 470 GPa and 160 GPa, respectively. The properties reported by these research works matched well with the results of the current research work.

It could be concluded from the results that the SWCNTs with armchair configuration with vacancy defects have shown better properties than the zigzag configuration. Moreover, the phenomenon was more significant for the diameter greater than 15 Å. From the above results, it could be pointed out that the armchair configuration with vacancy defects have shown improved properties compared to the zigzag configuration as the CNT's diameter increases.

**3C. Effect of the number of walls.** The effect of the number of walls on the CNTs properties were also analyzed using SFS CNT models. The elastic and shear modulus of both DWCNTs and MWCNTs approximately remains the same (Table 8). For the individual cases, the elastic modulus of the zigzag configuration is higher than armchair one and the armchair shear modulus is higher than the zigzag configuration. The elastic modulus varied inversely to the CNT's diameter until the value reached 15.697 Å and then the variation of elastic modulus became proportional to the CNT's diameter. The elastic modulus of DWCNT was higher at lower diameters and was gradually reduced as the CNT diameter reached 15.657 Å. Then, for further increases in diameter, the elastic modulus was increased again. For the MWCNT case, the elastic modulus values increased proportionally to the CNT's number of walls and the diameter. However, the shear modulus of both DWCNTs and MWCNTs increased as the diameter increased up to 15.697 Å, and then started to decrease with the increase in diameter.

diameter (Å)	zigzag			
	elastic modulus DWCNT (GPa)	shear modulus DWCNT (GPa)	elastic modulus MWCNT (GPa)	shear modulus MWCNT (GPa)
5.481	794.199	320.235	794.199	320.23
8.61	783.311	322.752	783.311	322.75
10.96	770.318	323.312	770.318	323.31
15.657	761.661	328.514	761.661	328.51
21.92	782.353	311.379	782.353	311.38

diameter (Å)	armchair			
	elastic modulus DWCNT (GPa)	shear modulus DWCNT (GPa)	elastic modulus MWCNT (GPa)	shear modulus MWCNT (GPa)
5.424	757.671	366.795	756.71	301.52
8.13	753.1	359.754	753.1	297.13
10.84	759.974	358.317	759.974	292.26
14.916	766.225	358.959	766.225	357.69
21.696	772.855	358.112	772.855	359.67

**Table 8.** Properties of DWCNTs and MWCNTs with zigzag and armchair CNTs.

type of CNT	diameter (Å)	elastic modulus (GPa)	shear modulus (GPa)	reference
DWCNT	10.0–30.0	1000–1100	400	[Li and Chou 2003a]
DWCNT zigzag	5.41–21.92	761–794	311–323	proposed SFS model
DWCNT armchair	5.424–21.69	753–772	358–366	
MWCNT	3.91–27.13	704	-	[Yu et al. 2000]
MWCNT	5–8	990–1029	213–228	[Sakhaee-Pour 2009]
MWCNT zigzag	5.41–21.92	761–794	310–323	proposed SFS model
MWCNT armchair	5.424–21.69	651–786	292–360	

**Table 9.** CNT elastic properties compared between the current study and other researches.

Table 9 shows a comparative analysis of results from other research works along with the current SFS model research work. It could be concluded here that the SFS structure with orthotropic C-C chemical bond could provide accurate elastic properties of both zigzag and armchair configurations for both pristine and CNTs with vacancy defects.

4. Conclusions and recommendations

In this research, the effect of chirality (zigzag and armchair), vacancy defects, and number of walls on the elastic properties of CNTs were characterized by the space frame structure method. The orthotropic properties of C-C bonds were calculated by comparing structural mechanics and molecular mechanics energy expressions along with a parametric study. A mathematical model using equivalent springs for van der Waals interactions between consecutive walls was developed to analyze their effect on DWCNTs and

MWCNTs. It has been found that the zigzag configuration elastic modulus was greater than the armchair configuration for CNTs with the same diameter. The shear modulus of the armchair configuration is greater than the zigzag configuration. Vacancy defects significantly reduced the elastic properties of SWCNTs and the effect of the vacancy defects increased as the diameter was increased further. The rate of decrease in the elastic and shear modulus of defective armchair nanotubes become insignificant as the diameter increased further. Comparatively DWCNTs have higher elastic modulus and shear modulus (average) than SWCNTs and MWCNTs for the smaller CNTs diameter range. The results shows that the SFS model elastic properties were in good agreement with the experimental and theoretical values found in the literature.

## References

- [Agrawal et al. 2006] P. M. Agrawal, B. S. Sudalayandi, L. M. Raff, and R. Komanduri, “A comparison of different methods of Young’s modulus determination for single-wall carbon nanotubes (SWCNT) using molecular dynamics (MD) simulations”, *Comput. Mater. Sci.* **38**:2 (2006), 271–281.
- [Chabalala et al. 2011] V. P. Chabalala, N. Wagner, and S. Potgieter-Vermaak, “Investigation into the evolution of char structure using Raman spectroscopy in conjunction with coal petrography, I”, *Fuel Process. Tech.* **92**:4 (2011), 750–756.
- [Ghavamian et al. 2013] A. Ghavamian, M. Rahmandoust, and A. Öchsner, “On the determination of the shear modulus of carbon nanotubes”, *Compos. B Eng.* **44**:1 (2013), 52–59.
- [Han et al. 2014a] F. Han, Y. Azdoud, and G. Lubineau, “Computational modeling of elastic properties of carbon nanotube/polymer composites with interphase regions, I: Micro-structural characterization and geometric modeling”, *Comp. Mater. Sci.* **81** (2014), 641–651.
- [Han et al. 2014b] F. Han, Y. Azdoud, and G. Lubineau, “Computational modeling of elastic properties of carbon nanotube/polymer composites with interphase regions, II: Mechanical modeling”, *Comp. Mater. Sci.* **81** (2014), 652–661.
- [Harik 2011] V. Harik, *Mechanics of carbon nanotubes*, Nanodesigns Press, Newark, DE, 2011.
- [Hernández-Pérez and Avilés 2010] A. Hernández-Pérez and F. Avilés, “Modeling the influence of interphase on the elastic properties of carbon nanotube composites”, *Comp. Mater. Sci.* **47**:4 (2010), 926–933.
- [Hu et al. 2007] N. Hu, K. Nunoya, D. Pan, T. Okabe, and H. Fukunaga, “Prediction of buckling characteristics of carbon nanotubes”, *Int. J. Solids Struct.* **44**:20 (2007), 6535–6550.
- [Iijima 1991] S. Iijima, “Helical microtubules of graphitic carbon”, *Nature* **354** (1991), 56–58.
- [Inam et al. 2014] F. Inam, A. Heaton, P. Brown, T. Peijs, and M. J. Reece, “Effects of dispersion surfactants on the properties of ceramic-carbon nanotube (CNT) nanocomposites”, *Ceram. Int.* **40**:1 (2014), 511–516.
- [Jia et al. 2011] J. Jia, J. Zhao, G. Xu, J. Di, Z. Yong, Y. Tao, C. Fang, Z. Zhang, X. Zhang, L. Zheng, and Q. Li, “A comparison of the mechanical properties of fibers spun from different carbon nanotubes”, *Carbon* **49**:4 (2011), 1333–1339.
- [Kundalwal and Kumar 2016] S. I. Kundalwal and S. Kumar, “Multiscale modeling of stress transfer in continuous microscale fiber reinforced composites with nano-engineered interphase”, *Mech. Mater.* **102** (2016), 117–131.
- [Kundalwal and Ray 2014] S. I. Kundalwal and M. C. Ray, “Improved thermoelastic coefficients of a novel short fuzzy fiber-reinforced composite with wavy carbon nanotubes”, *J. Mech. Mater. Struct.* **9**:1 (2014), 1–25.
- [Lennard-Jones 1924] J. E. Jones, “On the determination of molecular fields, I: From the variation of the viscosity of a gas with temperature”, *Proc. R. Soc. Lond. A* **106**:738 (1924), 441–462.
- [Li and Chou 2003a] C. Li and T.-W. Chou, “Elastic moduli of multi-walled carbon nanotubes and the effect of van der Waals forces”, *Compos. Sci. Technol.* **63**:11 (2003), 1517–1524.
- [Li and Chou 2003b] C. Li and T.-W. Chou, “A structural mechanics approach for the analysis of carbon nanotubes”, *Int. J. Solids Struct.* **40**:10 (2003), 2487–2499.
- [Mohammadpour and Awang 2011] E. Mohammadpour and M. Awang, “Predicting a stretching behavior of carbon nanotubes using finite element method”, pp. 374–378 in *Enabling science and nanotechnology* (Kuala Lumpur, 2010), edited by A. M. Hashim et al., AIP Conference Proc. **1341**, Amer. Inst. Physics, Melville, NY, 2011.



- [Muc 2010] A. Muc, “Design and identification methods of effective mechanical properties for carbon nanotubes”, *Mater. Des.* **31**:4 (2010), 1671–1675.
- [Muc 2011] A. Muc, “Modelling of carbon nanotubes behaviour with the use of a thin shell theory”, *J. Theor. Appl. Mech. (Warsaw)* **49**:2 (2011), 531–540.
- [Muthu and Dendere 2014] J. Muthu and C. Dendere, “Functionalized multiwall carbon nanotubes strengthened GRP hybrid composites: improved properties with optimum fiber content”, *Compos. B Eng.* **67** (2014), 84–94.
- [Nam et al. 2015] T. H. Nam, K. Goto, Y. Yamaguchi, E. V. A. Premalal, Y. Shimamura, Y. Inoue, K. Naito, and S. Ogihara, “Effects of CNT diameter on mechanical properties of aligned CNT sheets and composites”, *Compos. A Appl. Sci. Manuf.* **76** (2015), 289–298.
- [Popov et al. 2000] V. N. Popov, V. E. Van Doren, and M. Balkanski, “Elastic properties of single-walled carbon nanotubes”, *Phys. Rev. B* **61**:4 (2000), 3078–3084.
- [Qian et al. 2002] D. Qian, G. J. Wagner, W. K. Liu, M.-F. Yu, and R. S. Ruoff, “Mechanics of carbon nanotubes”, *Appl. Mech. Rev.* **55**:6 (2002), 495–533.
- [Rahmandoust and Öchsner 2009] M. Rahmandoust and A. Öchsner, “Influence of structural imperfections and doping on the mechanical properties of single-walled carbon nanotubes”, *J. Nano Res.* **6** (2009), 185–196.
- [Rahmandoust and Öchsner 2012] M. Rahmandoust and A. Öchsner, “On finite element modeling of single- and multi-walled carbon nanotubes”, *J. Nanosci. Nanotechnol.* **12**:10 (2012), 8129–8136.
- [Ranjbartoreh and Wang 2010] A. R. Ranjbartoreh and G. Wang, “Molecular dynamic investigation of mechanical properties of armchair and zigzag double-walled carbon nanotubes under various loading conditions”, *Phys. Lett. A* **374**:7 (2010), 969–974.
- [Reich et al. 2002] S. Reich, C. Thomsen, and P. Ordejón, “Elastic properties of carbon nanotubes under hydrostatic pressure”, *Phys. Rev. B* **65**:15 (2002), art. id. 153407.
- [Roy Chowdury et al. 2014] A. N. Roy Chowdury, C. M. Wang, and S. J. A. Koh, “Continuum shell model for buckling of armchair carbon nanotubes under compression or torsion”, *Int. J. Appl. Mech.* **6**:1 (2014), art. id. 145006.
- [Sakhaee-Pour 2009] A. Sakhaee-Pour, “Elastic properties of single-layered graphene sheet”, *Solid State Comm.* **149**:1–2 (2009), 91–95.
- [Sharma and Shukla 2014] K. Sharma and M. Shukla, “Three-phase carbon fiber amine functionalized carbon nanotubes epoxy composite: processing, characterisation, and multiscale modeling”, *J. Nanomater.* **2014** (2014), art. id. 837492.
- [Shokrieh et al. 2013] M. M. Shokrieh, A. Saeedi, and M. Chitsazadeh, “Mechanical properties of multi-walled carbon nanotube/polyester nanocomposites”, *J. Nanostruct. Chem.* **3**:1 (2013), art. id. 20.
- [Tachibana 2013] M. Tachibana, “Characterization of laser-induced defects and modification in carbon nanotubes by Raman spectroscopy”, pp. 31–52 in *Physical and chemical properties of carbon nanotubes*, edited by S. Suzuki, IntechOpen, London, 2013.
- [Tersoff and Ruoff 1994] J. Tersoff and R. S. Ruoff, “Structural properties of a carbon-nanotube crystal”, *Phys. Rev. Lett.* **73**:5 (1994), 676–679.
- [Tjong 2013] S. C. Tjong, “Recent progress in the development and properties of novel metal matrix nanocomposites reinforced with carbon nanotubes and graphene nanosheets”, *Mater. Sci. Eng. R* **74**:10 (2013), 281–350.
- [Treacy et al. 1996] M. M. J. Treacy, T. W. Ebbesen, and J. M. Gibson, “Exceptionally high Young’s modulus observed for individual carbon nanotubes”, *Nature* **381** (1996), 678–680.
- [Tserpes et al. 2008] K. I. Tserpes, P. Papanikos, G. Labeas, and S. G. Pantelakis, “Multi-scale modeling of tensile behavior of carbon nanotube-reinforced composites”, *Theor. Appl. Fract. Mech.* **49**:1 (2008), 51–60.
- [Xiao and Hou 2006] S. Xiao and W. Hou, “Fracture of vacancy-defected carbon nanotubes and their embedded nanocomposites”, *Phys. Rev. B* **73**:11 (2006), art. id. 115406.
- [Yang et al. 2016] L. Yang, I. Greenfeld, and H. D. Wagner, “Toughness of carbon nanotubes conforms to classic fracture mechanics”, *Sci. Adv.* **2**:2 (2016), art. id. e1500969.
- [Yang et al. 2017] Y. Yang, C. Ramirez, X. Wang, Z. Guo, A. Tokranov, R. Zhao, I. Szlufarska, J. Lou, and B. W. Sheldon, “Impact of carbon nanotube defects on fracture mechanisms in ceramic nanocomposites”, *Carbon* **115** (2017), 402–408.

- [Yu et al. 2000] M.-F. Yu, O. Lourie, M. J. Dyer, K. Moloni, T. F. Kelly, and R. S. Ruoff, “Strength and breaking mechanism of multiwalled carbon nanotubes under tensile load”, *Science* **287**:5453 (2000), 637–640.
- [Zohdi and Wriggers 2005] T. I. Zohdi and P. Wriggers, *An introduction to computational micromechanics*, Lecture Notes in Appl. and Computational Mech. **20**, Springer, 2005.
- [Zuberi and Esat 2015] M. J. S. Zuberi and V. Esat, “Investigating the mechanical properties of single walled carbon nanotube reinforced epoxy composite through finite element modelling”, *Compos. B Eng.* **71** (2015), 1–9.

Received 30 Nov 2017. Revised 8 Mar 2018. Accepted 28 May 2018.

MUHAMMAD ARIF: [engrarifjan@gmail.com](mailto:engrarifjan@gmail.com)

*School of Mechanical, Industrial and Aeronautical Engineering, University of the Witwatersrand, Johannesburg, South Africa*

JACOB MUTHU: [jacob.muthu@wits.ac.za](mailto:jacob.muthu@wits.ac.za)

*Department of Civil, Geological, and Environmental Engineering, University of Saskatchewan, Saskatoon, Canada*

and

*School of Mechanical, Industrial and Aeronautical Engineering, University of the Witwatersrand, Johannesburg, South Africa*



## ANALYTICAL APPROACH TO THE PROBLEM OF AN AUXETIC LAYER UNDER A SPATIALLY PERIODIC LOAD

HENRYK KAMIŃSKI AND PAWEŁ FRITZKOWSKI

The problem of an infinite elastic layer under a periodic load is considered. A mathematical model is formulated for the plane strain state. An analytical procedure based on the Fourier integral transformation is discussed. The displacement components are obtained as infinite sums directly via the inverse Fourier transform. Semianalytical results are presented in a nondimensional form for the case of conventional elastic materials (positive Poisson's ratio) and auxetic materials (negative Poisson's ratio). The deformation of the loaded boundary and other characteristic surfaces of the layer is analyzed, and the displacement and stress fields are demonstrated. The effect of Poisson's ratio on the system behavior is studied. The results are compared with the purely numerical solutions obtained using the finite element method.

### 1. Introduction

Nowadays, in times of advanced numerical methods and modern simulation software, the classical mathematical modeling and analytical treatment of formulated problems seem to belong to the past. Engineers and researchers almost automatically reach for powerful computer tools, even if an analytical approach could be applied easily. Beyond any doubt, most of the contemporary problems in computational mechanics are of a complex nature due to their geometry as well as the load and constraint conditions. However, often an analytical solution to a simplified model may become a strong base for further studies of more sophisticated and realistic systems.

In the field of linear elasticity, many fundamental problems have been formulated on strong assumptions. For instance, an unbounded (fully or partially) character of a domain (e.g., elastic space/plane, half-space/plane, elastic layer or strip) and/or a specific case of stress-strain state (plane stress/strain) have been considered. Such an approach has allowed for analytical treatment of the problems by means of the complex potentials method, integral transforms, Fourier series, and stress functions, etc. [Teodorescu 2013; Sadd 2004; Saada 1974; Nowacki 1970; Timoshenko and Goodier 1951].

In fact, exact solutions have significant advantages over the numerical ones. First of all, they facilitate a qualitative analysis of a given problem and enable one to draw more general conclusions. Secondly, analytical solutions play a role of a reference point for brand new or improved computational methods and algorithms. Moreover, the analytical approach may be useful for simulation studies of more complex or unconventional systems. A good example are auxetics, i.e., materials with negative Poisson's ratio. Analytical solutions to purely theoretical problems can cast new light on unusual deformation behavior of auxetic systems with numerous potential applications [Evans and Alderson 2000; Prawoto 2012; Alderson and Alderson 2007; Fritzkowski and Kamiński 2016; Sanami et al. 2014; Carneiro et al. 2013].

---

This work has been supported by 02/21/DSPB/3477 and 02/21/DSPB/3493 grants.

**Keywords:** linear elasticity, elastic layer, deformation, auxetic materials, Fourier transform, approximate methods.

It should be noted that, although auxetics have been known since the 1980s, their properties (mechanical, thermal, and others) and mechanisms of the anomalous deformation still draw attention of many researchers. However, a significant majority of the studies are based on the purely numerical approach (e.g., see [Walczak et al. 2014; Strek et al. 2010; Jopek and Strek 2015; Salit and Weller 2009]).

This paper is devoted to stress and deformation analysis of an elastic solid layer subjected to a spatially periodic load. Since a state of plane strain is assumed, the problem is reduced to a two-dimensional one. The displacement field equations are solved by a semianalytical approach, i.e., the Fourier integral transform is applied in combination with numerical evaluation of the displacement and stress components. The main aim of this work is to investigate the effect of Poisson's ratio on the behavior of the elastic system.

The paper is divided into five sections. In Section 2, a mathematical formulation of the elasticity problem is presented. The semianalytical solution procedure is presented in Section 3. Section 4, in turn, contains simulation results and discussion. Finally, some conclusions and closing remarks are provided in Section 5.

## 2. Formulation of the problem

Let us consider the elastic layer illustrated in Figure 1. The term “layer” should be understood as a part of an elastic space (infinite domain) bounded by two parallel planes at a finite distance  $h$  [Teodorescu 2013]. The upper boundary face ( $xz$ ) is subjected to a distributed normal load  $p(x)$  which is periodic along the  $x$ -axis:

$$p(x) = p(x + 2a). \quad (2-1)$$

The solid material that occupies the domain is assumed to be linearly elastic, homogeneous, and isotropic. It is characterized by shear modulus  $G$  and Poisson's ratio  $\nu$ . In the case of auxetics,  $\nu < 0$ .

Taking into account the domain and loading geometry (independent of the  $z$  coordinate), the spatial problem can be reduced to a two-dimensional formulation. The specified case falls into the category of plane strain problems, and consequently we focus on a semiinfinite planar region

$$\Omega = \begin{cases} -\infty \leq x < \infty, \\ -h \leq y \leq 0. \end{cases} \quad (2-2)$$

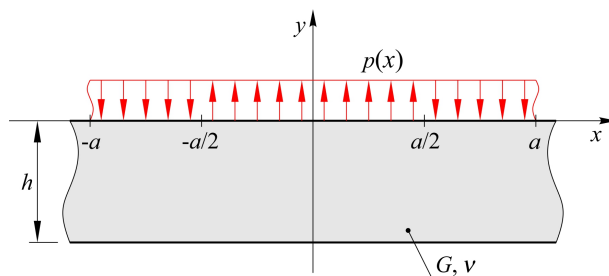


**Figure 1.** Infinite elastic layer under a periodic load.

Let  $\mathbf{u}(x, y) = [u_x, u_y]^T$  be the displacement vector. The strain-displacement relations involving only the allowable strains are given by

$$\varepsilon_x = \frac{\partial u_x}{\partial x}, \quad \varepsilon_y = \frac{\partial u_y}{\partial y}, \quad \varepsilon_{xy} = \frac{1}{2} \left( \frac{\partial u_x}{\partial y} + \frac{\partial u_y}{\partial x} \right). \quad (2-3)$$

From Hooke's law, the corresponding stress components become

$$\sigma_x = \lambda(\varepsilon_x + \varepsilon_y) + 2\mu\varepsilon_x, \quad \sigma_y = \lambda(\varepsilon_x + \varepsilon_y) + 2\mu\varepsilon_y, \quad \sigma_{xy} = 2\mu\varepsilon_{xy}, \quad (2-4)$$

where  $\lambda$  and  $\mu$  are Lamé constants, given as

$$\lambda = \frac{2G\nu}{1-2\nu}, \quad \mu = G. \quad (2-5)$$

Finally, in the case of zero body forces, the Navier–Lamé equations reduce to [Nowacki 1970; Sadd 2004]

$$\mu \nabla^2 u_x + (\lambda + \mu) \frac{\partial}{\partial x} \left( \frac{\partial u_x}{\partial x} + \frac{\partial u_y}{\partial y} \right) = 0, \quad (2-6a)$$

$$\mu \nabla^2 u_y + (\lambda + \mu) \frac{\partial}{\partial y} \left( \frac{\partial u_x}{\partial x} + \frac{\partial u_y}{\partial y} \right) = 0. \quad (2-6b)$$

Moreover, for the given problem, the unknown vector-valued function  $\mathbf{u}(x, y)$  must satisfy the following traction boundary conditions:

$$\sigma_y(x, 0) = p(x), \quad (2-7a)$$

$$\sigma_{xy}(x, 0) = 0, \quad (2-7b)$$

$$\sigma_y(x, -h) = 0, \quad (2-7c)$$

$$\sigma_{xy}(x, -h) = 0. \quad (2-7d)$$

Thus, the resulting mathematical model consists of the system of coupled partial differential equations (2-6) together with the set of boundary conditions (2-7).

### 3. Analytical solution procedure

**3.1. Transformation of the problem.** Let  $f(x)$  be a real function of a real variable  $x$ , which satisfies Dirichlet's conditions and is absolutely integrable. For further purposes, the following definition of the Fourier integral transform of  $f$  is used [Bronsztajn et al. 2004; Sneddon 1951; Teodorescu 2013]:

$$\mathcal{F}[f(x)] = \int_{-\infty}^{\infty} f(x) e^{-isx} dx, \quad (3-1)$$

where the variable  $s$  is real.

Now, let  $\tilde{u}_x$  and  $\tilde{u}_y$  denote the Fourier transforms of the displacements with respect to the  $x$ -coordinate, that is,

$$\tilde{u}_x(s, y) = \mathcal{F}_x[u_x(x, y)], \quad \tilde{u}_y(s, y) = \mathcal{F}_x[u_y(x, y)]. \quad (3-2)$$

Taking the transform of the governing equations (2-6), one can obtain

$$(\kappa - 1) \frac{\partial^2 \tilde{u}_x}{\partial y^2} + i2s \frac{\partial \tilde{u}_y}{\partial y} - s^2(\kappa + 1) \tilde{u}_x = 0, \quad (3-3a)$$

$$(\kappa + 1) \frac{\partial^2 \tilde{u}_y}{\partial y^2} + i2s \frac{\partial \tilde{u}_x}{\partial y} - s^2(\kappa - 1) \tilde{u}_y = 0, \quad (3-3b)$$

where  $\kappa$  denotes the Kolosov constant:

$$\kappa = 3 - 4\nu. \quad (3-4)$$

It should be noticed that these equations have simpler form than the original ones.

Next, consider the boundary conditions (2-7). Let  $p_b(x)$  be a basis function of the distributed load, i.e., the load over one period ( $-a \leq x \leq a$ ), so that periodic summation can be used:

$$p(x) = \sum_{k=-\infty}^{\infty} p_b(x - 2ka). \quad (3-5)$$

In the given case

$$p_b(x) = p_0 \left[ -\eta(x + a) + 2\eta\left(x + \frac{1}{2}a\right) - 2\eta\left(x - \frac{1}{2}a\right) + \eta(x - a) \right], \quad (3-6)$$

where  $p_0$  is the load intensity and  $\eta$  denotes the Heaviside step function. The Fourier transform of (3-6) is given by

$$\tilde{p}_b(s) = \frac{ip_0}{s} [e^{isa} - e^{-isa} + 2e^{isa/2} - 2e^{-isa/2}]. \quad (3-7)$$

Taking into account formula (3-5) as well as the linearity and shifting (translation) properties of the Fourier transform, for the whole periodic load applied to the infinite boundary one can write [Bronsztajn et al. 2004; Zemanian 1965]

$$\tilde{p}(s) = \tilde{p}_b(s) \sum_{k=-\infty}^{\infty} e^{-i2kas}. \quad (3-8)$$

Now, boundary conditions (2-7) can be converted to

$$\tilde{\sigma}_y(s, 0) = \tilde{p}(s), \quad (3-9a)$$

$$\tilde{\sigma}_{xy}(s, 0) = 0, \quad (3-9b)$$

$$\tilde{\sigma}_y(s, -h) = 0, \quad (3-9c)$$

$$\tilde{\sigma}_{xy}(s, -h) = 0, \quad (3-9d)$$

where

$$\tilde{\sigma}_x(s, y) = \mathcal{F}_x[\sigma_x(x, y)],$$

$$\tilde{\sigma}_y(s, y) = \mathcal{F}_x[\sigma_y(x, y)],$$

$$\tilde{\sigma}_{xy}(s, y) = \mathcal{F}_x[\sigma_{xy}(x, y)].$$

To sum up, after the transformation the boundary value problem is composed of the equilibrium equations (3-3) and associated boundary conditions (3-9).



**3.2. Solution of the transformed problem.** Due to its relatively simple form, the transformed problem can be solved in a quite conventional way. For the second-order partial differential equations (3-3), the trial solution is

$$\tilde{u}_x(s, y) = C_1 e^{ry}, \quad \tilde{u}_y(s, y) = C_2 e^{ry}, \quad (3-10)$$

where  $C_1$  and  $C_2$  are real constants, while  $r$  is generally a complex parameter to be determined. Inserting (3-10) into the homogeneous system (3-3) leads to a characteristic equation for  $r$ . There are two double roots:

$$r_{1,2} = s, \quad r_{3,4} = -s,$$

thus, the general solution is given by

$$\tilde{u}_x(s, y) = A_{11}e^{sy} + A_{12}ye^{sy} + B_{11}e^{-sy} + B_{12}ye^{-sy}, \quad (3-11a)$$

$$\tilde{u}_y(s, y) = A_{21}e^{sy} + A_{22}ye^{sy} + B_{21}e^{-sy} + B_{22}ye^{-sy}, \quad (3-11b)$$

where  $A_{ij}, B_{ij}$  (for  $i, j = 1, 2$ ) are complex constants. Substituting  $\tilde{u}_x$  and  $\tilde{u}_y$  into (3-3), one obtains

$$\alpha_{11}e^{sy} + \alpha_{12}ye^{sy} + \beta_{11}e^{-sy} + \beta_{12}ye^{-sy} = 0, \quad (3-12a)$$

$$\alpha_{21}e^{sy} + \alpha_{22}ye^{sy} + \beta_{21}e^{-sy} + \beta_{22}ye^{-sy} = 0, \quad (3-12b)$$

where  $\alpha_{ij}, \beta_{ij}$  (for  $i, j = 1, 2$ ) denote certain functions of  $s$  and  $y$ , involving the constants  $A_{ij}, B_{ij}$ . Equating to zero the coefficients  $\alpha_{ij}$  and  $\beta_{ij}$ , one can find that system (3-12) is fulfilled (for every  $s$  and  $y$ ) if

$$A_{12} = iA_{22}, \quad B_{22} = iB_{12} \quad (3-13)$$

and

$$B_{12} = -\frac{s}{\kappa}(iB_{21} + B_{11}), \quad A_{22} = -\frac{s}{\kappa}(iA_{11} + A_{21}). \quad (3-14)$$

Now, the transformed displacements with four independent constants are

$$\tilde{u}_x(s, y) = \left[ A_{11} + (A_{11} - iA_{21})\frac{sy}{\kappa} \right] e^{sy} + \left[ B_{11} - (B_{11} + iB_{21})\frac{sy}{\kappa} \right] e^{-sy}, \quad (3-15a)$$

$$\tilde{u}_y(s, y) = \left[ A_{21} - (A_{21} + iA_{11})\frac{sy}{\kappa} \right] e^{sy} + \left[ B_{21} + (B_{21} - iB_{11})\frac{sy}{\kappa} \right] e^{-sy}. \quad (3-15b)$$

The constants can be determined from the prescribed boundary conditions. Obviously, it is necessary to use relations (2-3) and (2-4) to express  $\tilde{\sigma}_y, \tilde{\sigma}_{xy}$  in terms of  $\tilde{u}_x, \tilde{u}_y$ . The traction conditions (3-9a) and (3-9b) require

$$\begin{aligned} A_{21} &= -\frac{\tilde{p}(s)e^{2hs}[4h^2s^2 - (\kappa + 1)(e^{2hs} + 2hs - 1)]}{4Gs[e^{4hs} - 2e^{2hs}(1 + 2h^2s^2) + 1]}, \\ B_{21} &= \frac{\tilde{p}(s)e^{2hs}[4h^2s^2 - (\kappa + 1)(e^{-2hs} - 2hs - 1)]}{4Gs[e^{4hs} - 2e^{2hs}(1 + 2h^2s^2) + 1]}. \end{aligned} \quad (3-16)$$

Then, conditions (3-9c) and (3-9d) lead to

$$\begin{aligned} A_{11} &= -\frac{i[2\kappa B_{21}e^{2hs} - A_{21}(4h^2s^2 + 4\kappa hs + \kappa^2 + 1)]}{4h^2s^2 - \kappa^2 + 1}, \\ B_{11} &= \frac{i[2\kappa A_{21}e^{-2hs} - B_{21}(4h^2s^2 - 4\kappa hs + \kappa^2 + 1)]}{4h^2s^2 - \kappa^2 + 1}. \end{aligned} \quad (3-17)$$

On the basis of (3-15) together with relationships (3-16) and (3-17), one can find expressions for the Fourier transforms of the displacement components:

$$\tilde{u}_x(s, y) = \frac{i\tilde{p}(s)}{4G} \frac{\phi_x(s, y)}{\psi(s, y)}, \quad \tilde{u}_y(s, y) = \frac{\tilde{p}(s)}{4G} \frac{\phi_y(s, y)}{\psi(s, y)}, \quad (3-18)$$

where

$$\begin{aligned} \phi_x(s, y) &= A_1 \sinh(sy) + A_2 \sinh(s(y + 2h)) + B_1 \cosh(sy) + B_2 \cosh(s(y + 2h)), \\ \phi_y(s, y) &= B'_1 \sinh(sy) + B'_2 \sinh(s(y + 2h)) + A'_1 \cosh(sy) + A'_2 \cosh(s(y + 2h)), \\ \psi(s, y) &= s[2h^2s^2 - \cosh(2hs) + 1], \end{aligned} \quad (3-19)$$

and

$$\begin{aligned} A_1 &= -2s(y - \kappa h + h), & A_2 &= 2sy, & A'_1 &= -2s(y + \kappa h + h), \\ B_1 &= 4hs^2(y + h) - \kappa + 1, & B_2 &= \kappa - 1, & B'_1 &= 4hs^2(y + h) + \kappa + 1, & B'_2 &= -\kappa - 1. \end{aligned}$$

These results can be subjected to the inverse Fourier transformation in order to obtain the unknown displacements  $u_x$  and  $u_y$  as well as the stresses and strains.

**3.3. Inverse transformation.** In view of the definition (3-1), the corresponding inverse Fourier transform is represented by [Bronsztejn et al. 2004; Sneddon 1951; Teodorescu 2013]

$$f(x) = \mathcal{F}^{-1}[\tilde{f}(s)] = \frac{1}{2\pi} \int_{-\infty}^{\infty} \tilde{f}(s) e^{isx} ds. \quad (3-20)$$

In computational practice, direct evaluation of the above integral is usually complicated (if possible), and therefore is rarely conducted. However, this approach can be used in the case under investigation.

It is clear from (3-18) that the complexity of the inversion procedure is mainly affected by the form of the image function  $\tilde{p}(s)$ . To simplify the calculations, Poisson's summation formula is applied [Zemanian 1965]:

$$\sum_{k=-\infty}^{\infty} e^{iks} = 2\pi \sum_{k=-\infty}^{\infty} \delta(s - 2\pi k), \quad (3-21)$$

where  $\delta$  denotes the Dirac delta function. Hence, the expression (3-8) can be written alternatively as

$$\tilde{p}(s) = \frac{\pi}{a} \tilde{p}_b(s) \sum_{k=-\infty}^{\infty} \delta\left(s - \frac{\pi k}{a}\right). \quad (3-22)$$

According to the general definition (3-20), the inverse Fourier transforms of (3-18) are

$$u_x(x, y) = \frac{1}{2\pi} \int_{-\infty}^{\infty} \frac{i\tilde{p}(s)}{4G} \frac{\phi_x(s, y)}{\psi(s, y)} e^{isx} ds, \quad u_y(x, y) = \frac{1}{2\pi} \int_{-\infty}^{\infty} \frac{\tilde{p}(s)}{4G} \frac{\phi_y(s, y)}{\psi(s, y)} e^{isx} ds. \quad (3-23)$$

Substituting (3-22) into (3-23), converting (3-7) to trigonometric form, and taking into account the sifting property of the Dirac delta leads to the following result:

$$u_x(x, y) = \frac{2ip_0}{Ga} \sum_{k=-\infty}^{\infty} \sin^3\left(\frac{1}{4}as_k\right) \cos\left(\frac{1}{4}as_k\right) \frac{\phi_x(s_k, y)}{s_k \psi(s_k, y)} e^{is_k x}, \quad (3-24a)$$

$$u_y(x, y) = \frac{2p_0}{Ga} \sum_{k=-\infty}^{\infty} \sin^3\left(\frac{1}{4}as_k\right) \cos\left(\frac{1}{4}as_k\right) \frac{\phi_y(s_k, y)}{s_k \psi(s_k, y)} e^{is_k x}, \quad (3-24b)$$

where  $s_k = \pi k/a$ . Finally, after some manipulations and observations, one can find

$$u_x(x, y) = \frac{p_0}{Ga} \sum_{k=1}^{\infty} (-1)^k \sin(s'_k x) \frac{\phi_x(s'_k, y)}{s'_k \psi(s'_k, y)}, \quad (3-25a)$$

$$u_y(x, y) = -\frac{p_0}{Ga} \sum_{k=1}^{\infty} (-1)^k \cos(s'_k x) \frac{\phi_y(s'_k, y)}{s'_k \psi(s'_k, y)}, \quad (3-25b)$$

where  $s'_k = s_{2k-1} = \pi(2k-1)/a$ . The displacements can be used to determine the strain and stress components by means of the relations (2-3) and (2-4).

For example, the full form of the  $k$ -th term for the horizontal displacement is

$$u_{xk} = \frac{(-1)^k p_0 \sin(s'_k x)}{Gas_k'^2 [2h^2 s_k'^2 - \cosh(2hs'_k) + 1]} \left[ -2s'_k(y - \kappa h + h) \sinh(s'_k y) + 2s'_k y \sinh(s'_k(y + 2h)) \right. \\ \left. + (4hs_k'^2(y + h) - \kappa + 1) \cosh(s'_k y) + (\kappa - 1) \cosh(s'_k(y + 2h)) \right]. \quad (3-26)$$

Similarly, the  $k$ -th term for the normal stress  $\sigma_x$ , for instance, can be written as

$$\sigma_{xk} = \frac{4(-1)^k p_0 \cos(s'_k x)}{as_k'^2 [2h^2 s_k'^2 - \cosh(2hs'_k) + 1]} \left[ -s'_k(y - 2h) \sinh(s'_k y) + s'_k y \sinh(s'_k(y + 2h)) \right. \\ \left. + (2hs_k'^2(y + h) - 1) \cosh(s'_k y) + \cosh(s'_k(y + 2h)) \right]. \quad (3-27)$$

As can be seen from the sample analytical results, the expressions for the displacement components naturally involve Poisson's ratio  $\nu$  (via the constant  $\kappa$ ), while the stress field is independent of the parameter.

## 4. Simulation results

**4.1. Semianalytical results.** The results reported below have been obtained for the special case when  $a/h = 1$ . For natural reasons, in numerical computations the infinite sums in formulae (3-25) are truncated to a finite number of terms:

$$u_x(x, y) \approx \sum_{k=1}^n u_{xk}, \quad u_y(x, y) \approx \sum_{k=1}^n u_{yk}. \quad (4-1)$$

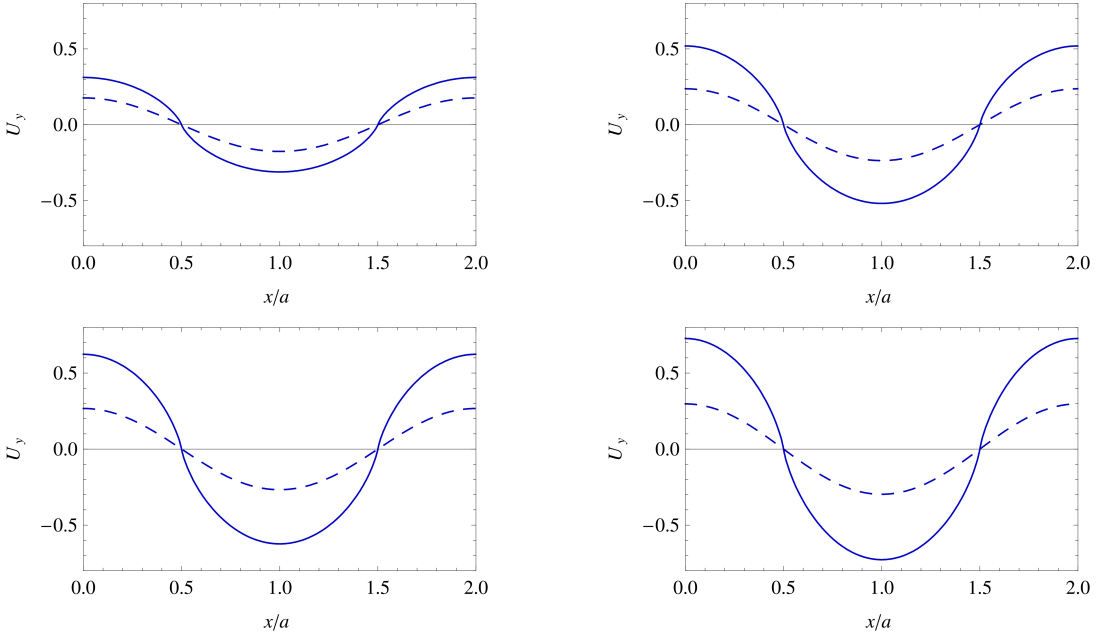


**Figure 2.** Vertical displacement of the loaded surface (solid) and the midsurface (dashed) for various values of Poisson's ratio. Top left:  $\nu = 0.25$ . Top right:  $\nu = -0.25$ . Bottom left:  $\nu = -0.5$ . Bottom right:  $\nu = -0.75$ . Results obtained for  $n = 50$ .

Moreover, the results have a nondimensional form. More precisely, the dimensionless displacements are introduced as

$$U_x(x, y) = \frac{G}{p_0 a} u_x(x, y), \quad U_y(x, y) = \frac{G}{p_0 a} u_y(x, y). \quad (4-2)$$

Analogously, the following nondimensional stresses are defined as

$$S_x(x, y) = \frac{1}{p_0} \sigma_x(x, y), \quad S_y(x, y) = \frac{1}{p_0} \sigma_y(x, y), \quad S_{xy}(x, y) = \frac{1}{p_0} \sigma_{xy}(x, y). \quad (4-3)$$

Let us start with a displacement analysis of the layer. In [Figure 2](#) the vertical displacements  $U_y$  of the loaded surface ( $y = 0$ ) and the midsurface ( $y = -h/2$ ) for  $0 \leq x \leq 2a$  are presented for various values of Poisson's ratio. For ease of comparison, all the graphs have equal axis scales. The deformation behavior is intuitively reasonable and qualitatively identical in each case. The maximum absolute values,  $\max |U_y|$ , occur at  $x = ka$  for  $k = 0, 1, 2, \dots$ , i.e., in the middle of each subinterval of the upward or downward load. As can be seen, the values grow with decreasingly lower  $\nu$ . The surfaces have zero displacement at  $x = (2k - 1)a$  for  $k = 1, 2, \dots$ , where the load changes its direction.

Similar plots for the horizontal displacement are shown in [Figure 3](#). Now, the maximum absolute values,  $\max |U_x|$ , arise at  $x = (2k - 1)a$  for  $k = 1, 2, \dots$ , while zero values can be observed at  $x = ka$  for  $k = 0, 1, 2, \dots$ . However, the displacements of the midsurface are much smaller, and a change of sign occurs as Poisson's ratio is decreased.

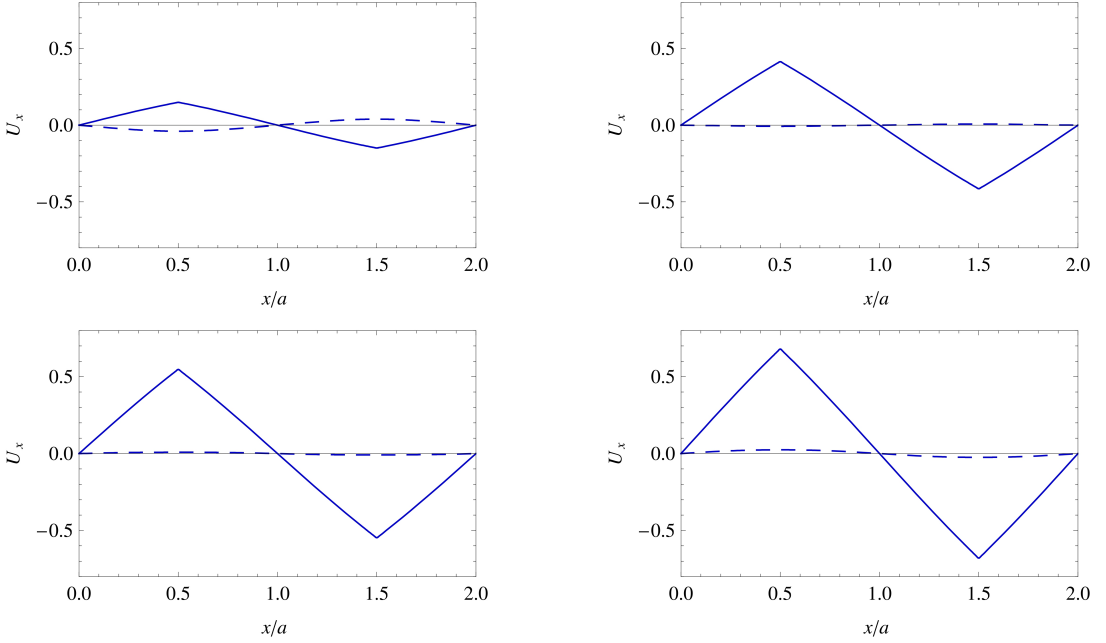


**Figure 3.** Horizontal displacement of the loaded surface (solid) and the midsurface (dashed) for various values of Poisson's ratio. Top left:  $\nu = 0.25$ . Top right:  $\nu = -0.25$ . Bottom left:  $\nu = -0.5$ . Bottom right:  $\nu = -0.75$ . Results obtained for  $n = 50$ .

To give a more systematic insight into changes of the displacements when  $\nu$  is varied, the following quantities are used:

$$U_y^{\max} = U_y|_{x=0}, \quad U_x^{\max} = U_x|_{x=a/2}$$

The functions  $U_y^{\max}(\nu)$  and  $U_x^{\max}(\nu)$  related to the top-, mid- and bottom-surface of the layer are presented in Figure 4. As can be seen, the maximum vertical displacement for all the surfaces is always positive and increases linearly with decreasing Poisson's ratio. The character of  $U_x^{\max}$  is also linear. However, the midsurface has near zero displacement, while in case of the bottom-surface the displacement is negative and it decreases with decreasing  $\nu$ .

The discussed results have been obtained for  $n = 50$ . This number of terms of the analytical solution ensures a good approximation of the layer displacements. The maximal values  $U_y^{\max}$  in the function of  $n$  for selected values of Poisson's ratio are plotted in Figure 5. As can be seen, the results converge rapidly, and for  $n > 50$  there are no significant deviations in  $U_y^{\max}$ . It should be noted that over the whole analyzed range ( $10 \leq n \leq 200$ ) the displacement values differ by less than 0.15%.

Let us turn to an overall look at the displacement field. Figure 6 shows the distribution of the horizontal and vertical displacements (scaled by a factor of  $10^2$ ) within an elementary cell of the layer:  $\langle 0, 2a \rangle \times \langle -h, 0 \rangle$ , for three values of Poisson's ratio:  $\nu = 0.25$ ,  $\nu = -0.25$  and  $\nu = -0.5$ . When it comes to  $U_x$ , there are two types of zero isolines: vertical (at  $x = a$ ) and approximately horizontal. Position of the latter one is affected by  $\nu$ . In the case of a conventional material ( $\nu > 0$ ), one can observe an evident disproportion between the area above and below the contour of zero value. In the distribution of  $U_y$ , there

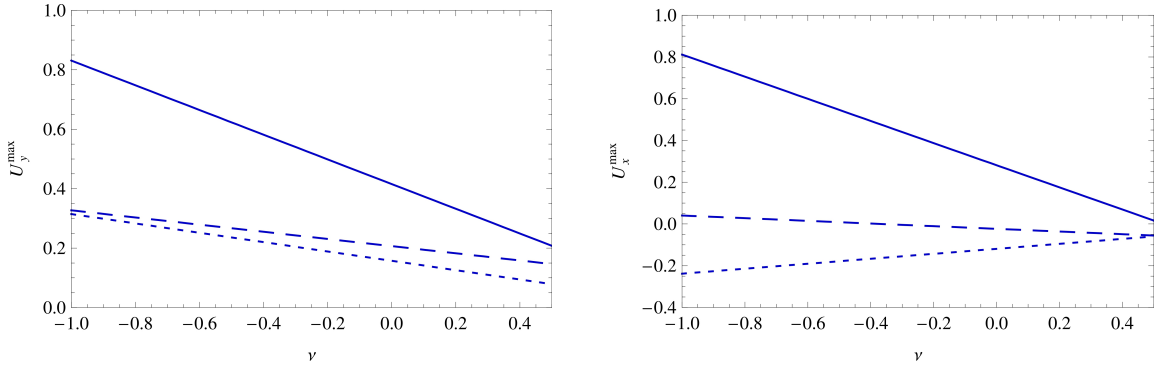


**Figure 4.** Maximal vertical (left) and horizontal (right) displacements versus Poisson's ratio for the surfaces at  $y = 0$  (solid),  $y = -h/2$  (dashed), and  $y = -h$  (dotted). Results obtained for  $n = 50$ .

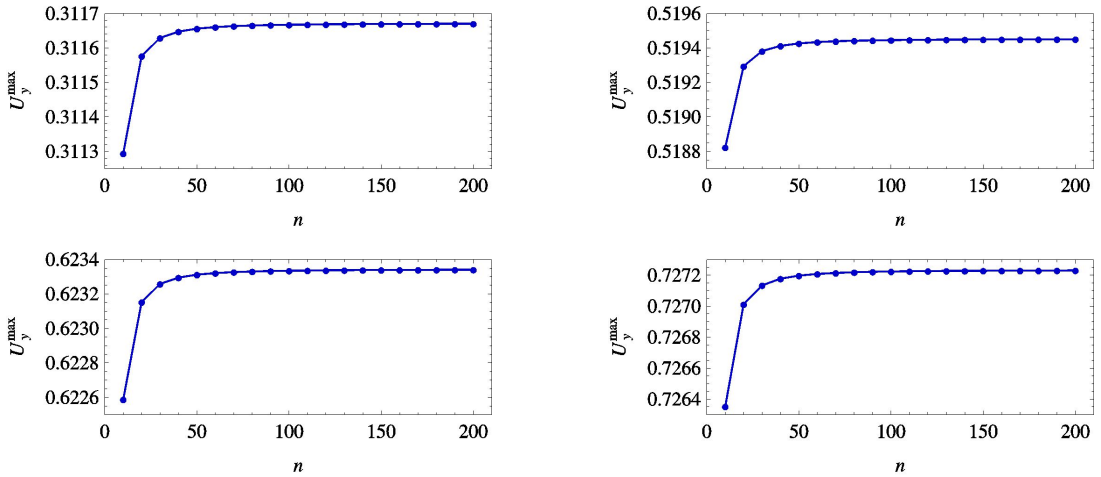


**Figure 5.** Approximated value of the maximal vertical displacement versus the number of summed terms of the analytical solution for various values of Poisson's ratio. Top left:  $\nu = 0.25$ . Top right:  $\nu = -0.25$ . Bottom left:  $\nu = -0.5$ . Bottom right:  $\nu = -0.75$ .

are only vertical zero isolines (at  $x = a/2$  and  $x = 3a/2$ ). Some differences arise in their neighborhood: the nearby contours become increasingly barrel-shaped as Poisson's ratio is decreased.

The longitudinal displacement ( $U_x$ ) of the cell through its thickness is plotted in Figure 7. More precisely, the curves that represent the layer cross-sectional deplanation at  $x = a/4$  (or  $x = 3a/4$ ) and  $x = a/2$  are presented for selected values of Poisson's ratio. As can be seen from Figure 3 and Figure 6,  $U_x(x, y) = 0$  for every  $y$  at  $x = 0$ ,  $x = a$ ,  $x = 2a$ . The displacement profiles at  $x = 5a/4$  (or  $x = 7a/4$ ) and  $x = 3a/2$ , in turn, are mirror images of the respective curves for  $x = a/4$  (or  $x = 3a/4$ ) and  $x = a/2$  about the central transverse axis  $x = a$ .

Although the displacements increase with decreasing  $\nu$  (see Figure 3), all the curves intersect at one point. Its location can be found based on (3-26). Since the second and the next terms of the series (4-1) decay strongly, they are negligible compared with the first term. Now, for two arbitrary values of the

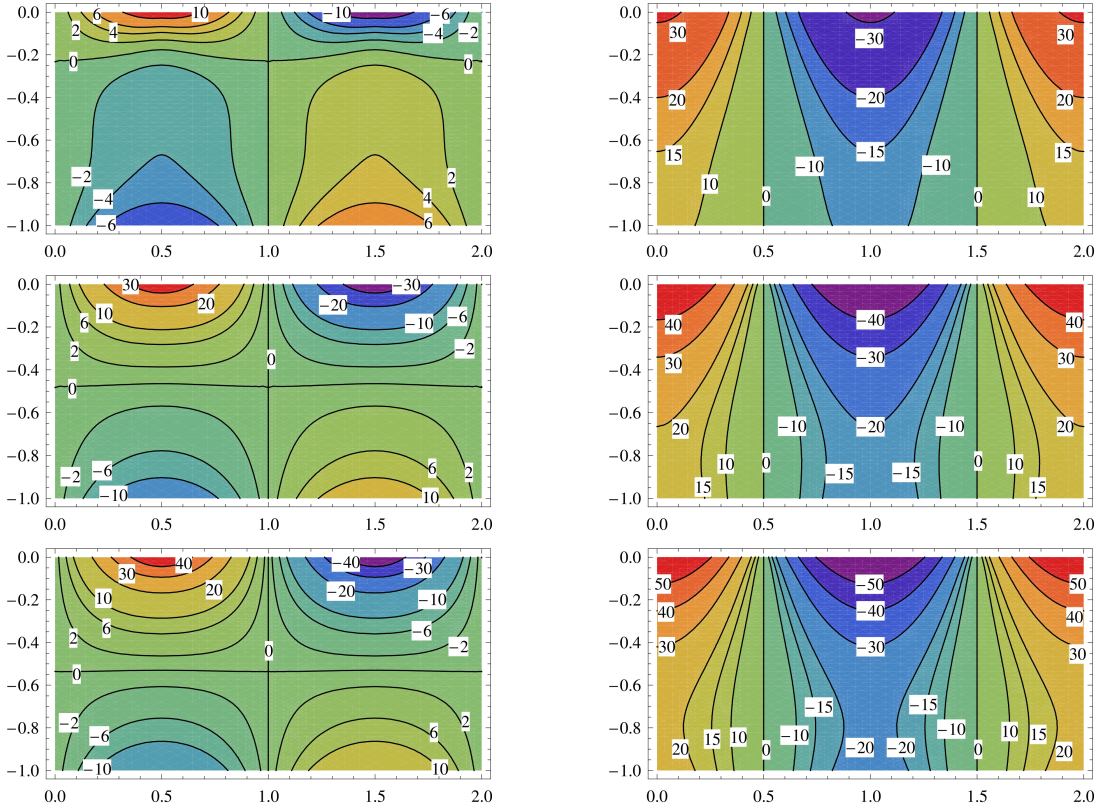


**Figure 6.** Displacement distribution in a rectangular cell—horizontal displacement  $U_x \times 10^2$  (left column) and vertical displacement  $U_y \times 10^2$  (right column). Top row:  $\nu = 0.25$ . Middle row:  $\nu = -0.25$ . Bottom row:  $\nu = -0.5$ .

Kolosov constant,  $\kappa_1$  and  $\kappa_2$ , the displacements  $u_x \approx u_{x1}$  (for every  $x$ ) are equal if

$$2\pi h \sinh\left(\pi \frac{y}{a}\right) - a \cosh\left(\pi \frac{y}{a}\right) + a \cosh\left(\pi \frac{y+2h}{a}\right) = 0. \quad (4-4)$$

In the special case when  $h = a$ , the solution of the transcendental equation is

$$y = \frac{a}{2\pi} \ln\left(\frac{2\pi + 1 - e^{-2\pi}}{2\pi - 1 + e^{2\pi}}\right) \approx -0.686a, \quad (4-5)$$

which can be treated as a sufficiently accurate approximation of the intersection point. Needless to say, the vertical location is independent of both  $x$  and  $\nu$ .

When it comes to the point of zero longitudinal displacement ( $U_x = 0$ ), it moves down as  $\nu$  is decreased. Because the point corresponds to the nearly horizontal zero isoline mentioned before (see Figure 6, left column), its  $y$ -position is similar over the whole range  $0 \leq x \leq a$  (see Figure 7). Using again the first term of the series solution, the average horizontal displacement can be defined as

$$u_x^{(\text{avg})} = \frac{1}{a} \int_0^a u_{x1} dx. \quad (4-6)$$

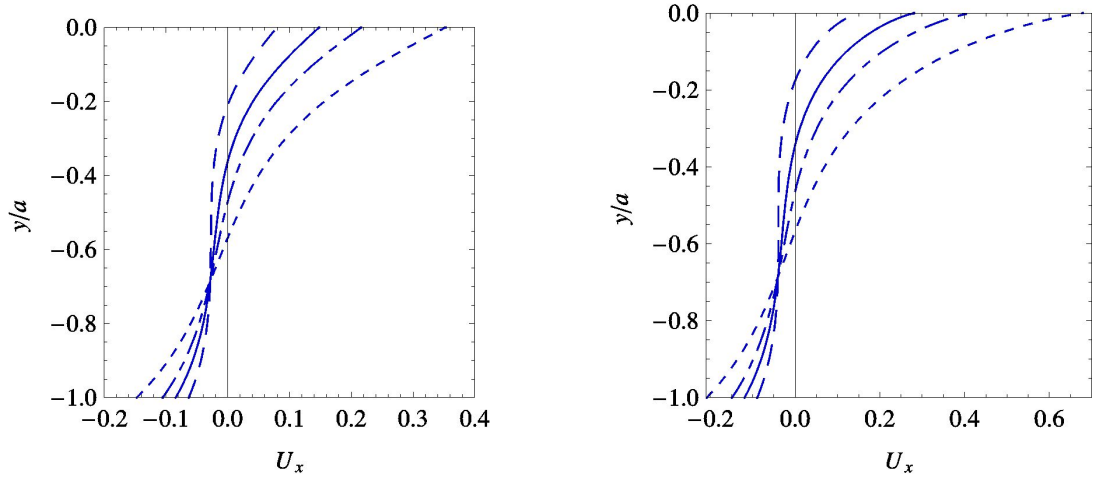


**Figure 7.** Deplanation of the layer cross-section for  $\nu = 0.25$  (dashed),  $\nu = 0$  (solid),  $\nu = -0.25$  (dot-dashed), and  $\nu = -0.75$  (dotted). Left:  $x = a/4$  and  $x = 3a/4$ . Right:  $x = a/2$ .

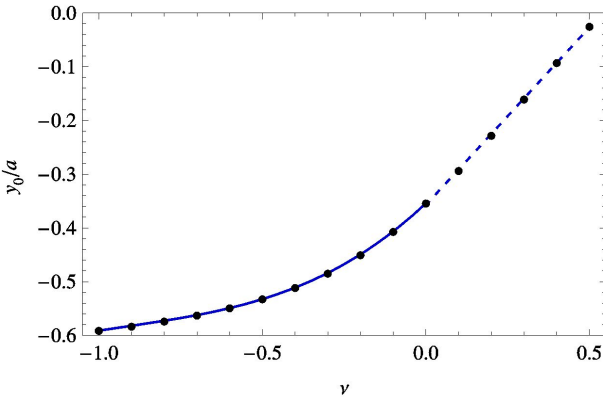


**Figure 8.** Vertical position of the zero average horizontal displacement versus Poisson’s ratio: approximate solutions (marks); the cubic curve (solid) and line (dotted) fitted in the least-squares sense.

Now, the algebraic equation  $u_x^{(\text{avg})}(y) = 0$  can be solved numerically to find the approximate (averaged) vertical position  $y_0$  of the zero point (zero isoline) for  $0 \leq x \leq a$  (and  $a \leq x \leq 2a$ ). The solutions for varying Poisson’s ratio within the range  $-1 \leq \nu \leq 0.5$  (with the step  $\Delta \nu = 0.1$ ) are shown in Figure 8. This discrete dependence  $y_0(\nu)$  can be approximated, for example, by the standard polynomial curve fitting in a least-square sense. Here, two subintervals have been considered separately, related to nonauxetic and auxetic materials ( $0 \leq \nu \leq 0.5$  and  $-1 \leq \nu \leq 0$ ). A linear function and a cubic curve have been fitted to the data, respectively. In both cases, the root-mean-square error of the approximations is less than 1% (about 0.22% and 0.47%). It can be concluded that the characteristics become “softer” in the auxetic range, i.e., the value  $y_0$  drops increasingly slower as Poisson’s ratio tends to  $-1$ .



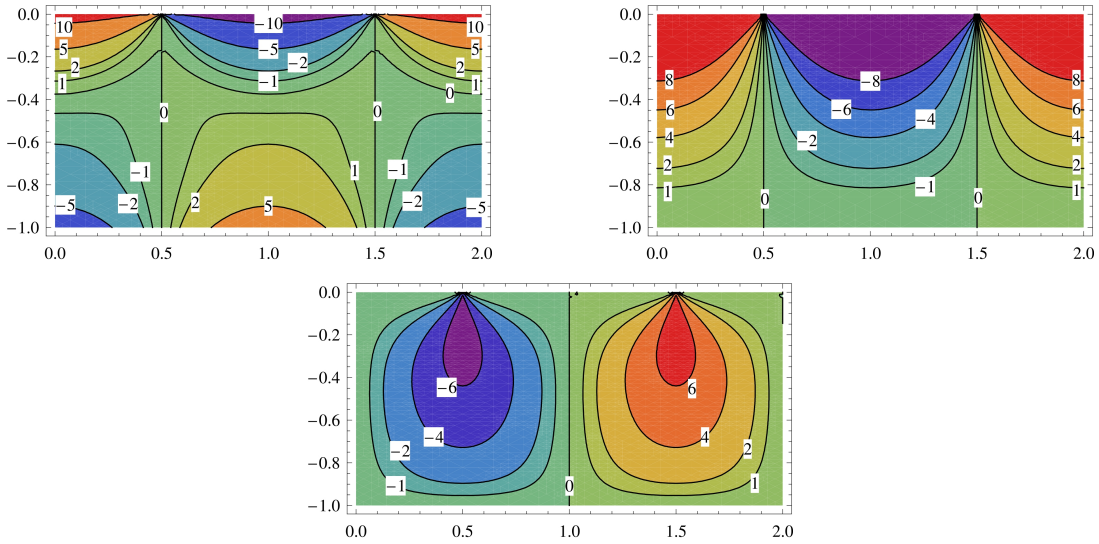


**Figure 9.** Stress distribution in a rectangular cell. Left: normal stress  $S_x \times 10$ . Right: normal stress  $S_y \times 10$ . Bottom: shear stress  $S_{xy} \times 10$ .

Distributions of normal stress  $S_x$ ,  $S_y$  and shear stress  $S_{xy}$  (all scaled by a factor of 10) are presented in [Figure 9](#). Note that the quantities are independent of  $\nu$ , according to the remark on [\(3-26\)](#) and [\(3-27\)](#). As can be seen, the vertical contours of zero normal stresses correspond to zero contours of  $U_y$ . In the case of shear stress, in turn, the zero isoline coincides with the one for  $U_x = 0$ .

The lack of dependence of the stress field on Poisson's ratio may seem curious. The problem has been considered within the classical linear elasticity framework, for the whole (thermodynamically admissible) range of  $\nu$ . Thus, one can state that  $S_x$ ,  $S_y$ ,  $S_{xy}$  are always the same, identical for both the auxetic and conventional materials (homogeneous and isotropic in each case). However, such a solution is not so unusual: results of this nature can arise within linear elasticity [[Timoshenko and Goodier 1951](#); [Timoshenko 1930](#); [Ventsel and Krauthammer 2001](#); [Boresi et al. 1993](#)]. For instance, the analyzed elastic layer problem may be confronted with the case of cylindrical bending of a rectangular plate (finite or infinite). Thus, consider a clamped-clamped thin plate of length  $a$  in the  $x$ -direction and infinitely long in the  $z$ -direction ( $xz$  is the middle plane), subjected to a uniform transverse load  $p = \text{constant}$  (upward or downward). It is well known that an expression for the plate deflection  $u_y(x)$  would include Poisson's ratio (via the flexural rigidity), while the normal stress  $\sigma_x$  would be free of this elastic constant. Obviously, the classical thin plate theory further assumes that  $\sigma_y = \sigma_{yz} = 0$  (plane stress relative to the  $xz$ -plane), which is too strong a constraint not consistent with our formulation. But even if the stress components  $\sigma_y$ ,  $\sigma_{yz}$  are approximately determined through the use of the differential equations of equilibrium (against Kirchhoff's assumptions), they also are not influenced by  $\nu$  [[Ventsel and Krauthammer 2001](#); [Boresi et al. 1993](#); [Jaeger 1964](#); [Szilard 2004](#)].

**4.2. FEM results.** Exact solutions, achievable for simple geometry and load cases, are often used to assess accuracy and efficiency of new or modified numerical techniques. Vice versa, a well-established computer method can be applied in order to validate newly developed analytical solutions. Unarguably,

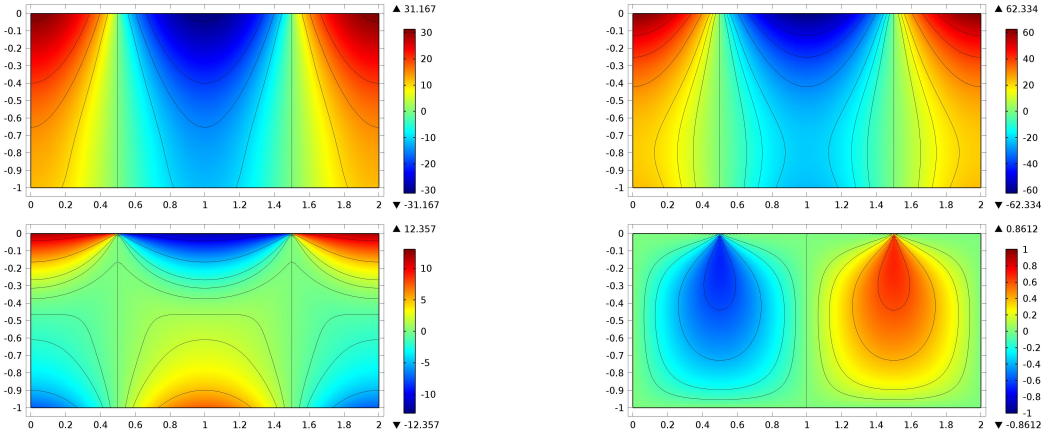


**Figure 10.** FEM results for a rectangular cell. Top left:  $U_y \times 10^2$  for  $\nu = 0.25$ . Top right:  $U_y \times 10^2$  for  $\nu = -0.5$ . Bottom left:  $S_x \times 10$ . Bottom right:  $S_{xy} \times 10$ .

the finite element method (FEM) is one of the most common approaches to modeling and simulation in science and engineering, including solid mechanics. For example, FEM-based reference results were used in [Walczak et al. 2014; Fritzowski and Kamiński 2016] to examine exact solutions or numerical solutions obtained via meshless methods. Similarly, comparative simulations have been conducted for the present case, by means of COMSOL Multiphysics software.

Due to the spatial periodicity of the layer, the linear static analysis is focused on a finite-sized domain, i.e., the rectangular cell:

$$\widehat{\Omega} = \begin{cases} 0 \leq x \leq 2a, \\ -h \leq y \leq 0. \end{cases} \quad (4-7)$$

Apart from boundary conditions (2-7a) and (2-7c), the following ones are imposed on the left and right edges (roller supports):

$$u_x(0, y) = 0, \quad u_x(2a, y) = 0. \quad (4-8)$$

Moreover, two pointwise displacement conditions are introduced as

$$u_y\left(\frac{1}{2}a, 0\right) = 0, \quad u_y\left(\frac{3}{2}a, 0\right) = 0. \quad (4-9)$$

On the one hand, these assumptions can be concluded from the semianalytical results. On the other hand, such a behavior of the loaded surface is a natural consequence of the fact that the resultant of the distributed load on the periodic cell is zero.

A uniform rectangular mesh is generated in the entire domain (a swept mesh). The quadratic quadrilateral finite elements are used. The presented results have been obtained for  $n_e = 5000$  finite elements ( $100 \times 50$ ) and  $n_{\text{dof}} = 40602$  degrees of freedom.

The distribution of displacement  $U_y$  and stress  $S_x$  obtained numerically for  $\nu = 0.25$  and  $\nu = -0.5$  are shown in Figure 10. Thus, the graphs can be compared to the ones in Figure 6, top row and bottom row, and Figure 9, left and bottom. For convenience, the same isolines have been included in the FEM-based plots. As can be seen, the displacement and stress fields provided by two different methods are in very

$\nu$		0.49	0.25	0	-0.25	-0.5	-0.75	-0.99
$U_y^{\max}$	semianalytical	0.2119	0.3117	0.4155	0.5194	0.6233	0.7272	0.8269
	FEM	0.2119	0.3117	0.4156	0.5195	0.6233	0.7272	0.8270
$U_x^{\max}$	semianalytical	0.0215	0.1488	0.2814	0.4140	0.5466	0.6792	0.8064
	FEM	0.0210	0.1484	0.2809	0.4133	0.5457	0.6779	0.8048

**Table 1.** Semianalytical vs. FEM results: maximal displacements.

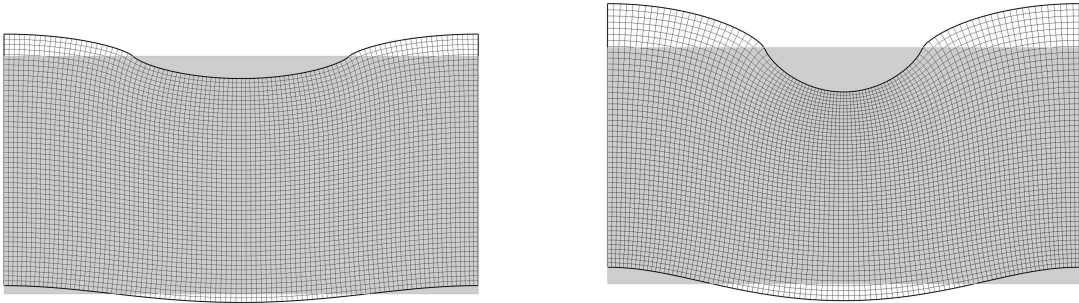


**Figure 11.** FEM results — deformation of a rectangular cell. Left:  $\nu = 0.25$ . Right:  $\nu = -0.5$ .

close agreement with each other. Table 1 contains the maximal displacements  $U_y^{\max}$  and  $U_x^{\max}$  obtained with FEM ( $n_{\text{dof}} = 40602$ ) and the semianalytical procedure ( $n = 50$ ). It turns out that the values are almost identical.

Deformation of the rectangular cell for  $\nu = 0.25$  and  $\nu = -0.5$  (drawn at the same scale) can be observed in Figure 11. In full accordance with the analytical results depicted in Figure 4, vertical displacements within the cell increase with decreasing Poisson's ratio.

## 5. Conclusions

In this paper, elastic deformation of an infinite layer under a periodic load has been considered. The semibounded character of the domain allows for an analytical treatment of the problem. The displacements of the loaded surface and other surfaces of the layer have been presented and discussed. Moreover, the distributions of the displacements as well as the normal and shear stresses in the periodic cell of the domain have been presented. The effect of Poisson's ratio on the system behavior has been analyzed.

Although the Fourier integral transform has been applied, evaluation of the inverse transforms for the displacements and stresses does not require numerical computation of residues, as for example in the case of elastic quarter-space [Fritzowski and Kamiński 2016]. The analytical solution is represented by an infinite single series of relatively simple form. The results indicate quite fast convergence of these series. Furthermore, they are in high agreement with the purely numerical solutions obtained by means of the finite element method (FEM).

It has been demonstrated that the horizontal and vertical displacements of the layer surface grow (in absolute value) with decreasing  $\nu$  at constant  $G$ . In the studied case, the relationship between the system response and Poisson's ratio turns out to be linear. Hence, in the context of contact mechanics, e.g., when

a rigid punch is pressed against an elastic material, one can expect that the indentation depth will be higher for auxetics than for conventional solids. Such behavior seems to contradict the effect of practical importance, highlighted by many authors: the indentation resistance increases with the auxeticity of the material [Sanami et al. 2014; Greaves et al. 2011; Carneiro et al. 2013]. However, in the mathematical description of deformable solids, Young's modulus and Poisson's ratio ( $E$ ,  $\nu$ ) are usually employed instead of shear modulus and Poisson's ratio ( $G$ ,  $\nu$ ). When the latter pair is used (as in this paper), the conclusions of a physical nature can change: the application of more auxetic materials (at constant shear modulus) does not necessarily suppress the deformation [Lim 2015]. So, the selection of elastic constants is crucial, and must not be ignored or underestimated by engineers and researchers.

The horizontal displacements of the layer through its thickness have been analyzed carefully. It has been shown that all the deplanation profiles for various values of  $\nu$  have a common point. Location of the zero point (zero average longitudinal displacement), in turn, is strongly affected by Poisson's ratio. As  $\nu$  is lowered, the vertical position decreases linearly in the conventional range, and in a cubic manner in the auxetic range. The stress components for the system, in turn, are independent of Poisson's ratio.

The presented semianalytical approach and the results can be a benchmark for future research on, for example, periodic cell structures made of conventional and auxetic materials.

## References

- [Alderson and Alderson 2007] A. Alderson and K. L. Alderson, "Auxetic materials", *Proc. Inst. Mech. Eng. G, J. Aerosp. Eng.* **221**:4 (2007), 565–575.
- [Boresi et al. 1993] A. Boresi, R. Schmidt, and O. Sidebottom, *Advanced mechanics of materials*, 5th ed., Wiley, New York, 1993.
- [Bronsztajn et al. 2004] I. N. Bronsztajn, K. A. Siemiendiajew, G. Musiol, and H. Mühlig, *Nowoczesne kompendium matematyki*, PWN, Warszawa, 2004.
- [Carneiro et al. 2013] V. H. Carneiro, J. Meireles, and H. Puga, "Auxetic materials: a review", *Mater. Sci. (Poland)* **31**:4 (2013), 561–571.
- [Evans and Alderson 2000] K. Evans and K. Alderson, "Auxetic materials: the positive side of being negative", *Eng. Sci. Educ. J.* **9**:4 (2000), 148–154.
- [Fritzowski and Kamiński 2016] P. Fritzowski and H. Kamiński, "Stress and displacement analysis of an auxetic quarter-plane under a concentrated force", *J. Mech. Mater. Struct.* **11**:1 (2016), 3–22.
- [Greaves et al. 2011] G. N. Greaves, A. L. Greer, R. S. Lakes, and T. Rouxel, "Poisson's ratio and modern materials", *Nat. Mater.* **10** (2011), 823–837.
- [Jaeger 1964] L. Jaeger, *Elementary theory of elastic plates*, Pergamon, Oxford, 1964.
- [Jopek and Strek 2015] H. Jopek and T. Strek, "Thermal and structural dependence of auxetic properties of composite materials", *Phys. Status Solidi B* **252**:7 (2015), 1551–1558.
- [Lim 2015] T. Lim, *Auxetic materials and structures*, Springer, 2015.
- [Nowacki 1970] W. Nowacki, *Teoria niesymetrycznej sprężystości*, PWN, Warsaw, 1970.
- [Prawoto 2012] Y. Prawoto, "Seeing auxetic materials from the mechanics point of view: a structural review on the negative Poisson's ratio", *Comput. Mater. Sci.* **58** (2012), 140–153.
- [Saada 1974] A. S. Saada, *Elasticity: theory and applications*, Pergamon Unified Engineering Series **16**, Pergamon, New York, 1974.
- [Sadd 2004] M. H. Sadd, *Elasticity: theory, applications, and numerics*, Elsevier, Amsterdam, 2004.
- [Salit and Weller 2009] V. Salit and T. Weller, "On the feasibility of introducing auxetic behavior into thin-walled structures", *Acta Mater.* **57**:1 (2009), 125–135.

- [Sanami et al. 2014] M. Sanami, N. Ravirala, K. Alderson, and A. Alderson, “Auxetic materials for sports applications”, *Procedia Eng.* **72** (2014), 453–458.
- [Sneddon 1951] I. N. Sneddon, *Fourier transforms*, McGraw-Hill, New York, 1951.
- [Strek et al. 2010] T. Strek, B. Maruszewski, A. Pozniak, and K. Wojciechowski, “Computational modelling of auxetics”, pp. 265–284 in *Finite element analysis*, edited by D. Moratal, Intech, Rijeka, Croatia, 2010.
- [Szilard 2004] R. Szilard, *Theories and applications of plate analysis: classical, numerical and engineering methods*, Wiley, Hoboken, NJ, 2004.
- [Teodorescu 2013] P. P. Teodorescu, *Treatise on classical elasticity: theory and related problems*, Springer, 2013.
- [Timoshenko 1930] S. P. Timoshenko, *Strength of materials, II: Advanced theory and problems*, Van Nostrand, New York, 1930.
- [Timoshenko and Goodier 1951] S. Timoshenko and J. N. Goodier, *Theory of elasticity*, 2nd ed., McGraw-Hill, New York, 1951.
- [Ventsel and Krauthammer 2001] E. Ventsel and T. Krauthammer, *Thin plates and shells: theory, analysis, and applications*, CRC Press, Boca Raton, FL, 2001.
- [Walczak et al. 2014] T. Walczak, G. Sypniewska-Kamińska, B. T. Maruszewski, and K. W. Wojciechowski, “Mesh versus meshless method of elastic displacement determination in a common and an auxetic material”, *Phys. Status Solidi B* **251**:11 (2014), 2225–2232.
- [Zemanian 1965] A. H. Zemanian, *Distribution theory and transform analysis: an introduction to generalized functions, with applications*, McGraw-Hill, New York, 1965.

Received 16 Jan 2018. Revised 26 Jul 2018. Accepted 19 Aug 2018.

HENRYK KAMIŃSKI: [henryk.kaminski@put.poznan.pl](mailto:henryk.kaminski@put.poznan.pl)

*Institute of Applied Mechanics, Poznan University of Technology, Poznan, Poland*

PAWEŁ FRITZKOWSKI: [pawel.fritzkowski@put.poznan.pl](mailto:pawel.fritzkowski@put.poznan.pl)

*Institute of Applied Mechanics, Poznan University of Technology, Poznan, Poland*



# STABILITY AND NONPLANAR POSTBUCKLING BEHAVIOR OF CURRENT-CARRYING MICROWIRES IN A LONGITUDINAL MAGNETIC FIELD

YUANZHUO HONG, LIN WANG AND HU-LIANG DAI

The stability and nonplanar buckling problem of current-carrying microwires in the presence of longitudinal magnetic field are investigated by accounting for the nonlinearities resulted from the axial elongation of the microwire's centerline. Based on the Euler–Bernoulli beam theory, modified couple stress theory, and Hamilton's principle, the nonlinear governing equations of the nonplanar motions of the microwire are derived. By application of Galerkin's approach, the nonplanar dynamic responses are evaluated for both clamped-clamped and pinned-pinned boundary conditions. The effects of dimensionless material length scale parameter, compressive load, magnetic field force, and slenderness ratio on the nonplanar buckling instability and the postbuckling configuration are discussed in detail. The obtained results show that the nonplanar buckling instability of microwires occurs when the magnetic field force becomes sufficiently large and the postbuckling configuration depends on the magnitude of magnetic field force, slenderness ratio, and initial conditions. The material length scale parameter can stabilize the microwire. Moreover, the stability boundaries for the magnetic field parameter and compressive load are analyzed, showing that an expected critical value of magnetic field parameter may be achieved by choosing a suitable compressive load as a trigger of automatic devices. Interestingly, it is found that the presence of an axial compressive load has no effect on the postbuckling shape, although it can destabilize the microwire system and amplify the postbuckling amplitude.

## 1. Introduction

With the flourish of nanomaterials and nanotechnology [Lee et al. 2013; Tao et al. 2010; Atashbar and Singamaneni 2005; McFarland and Colton 2005], miniaturization is becoming one of the main features in microelectromechanical systems (MEMS) and microelectronic devices [Lee et al. 2008; Li et al. 2007; Luo et al. 2006; Pauzauskie and Yang 2006; Singh 2009]. For that reason, many scientific researchers have paid great attention to the mechanical behaviors of micro/nano structures. In many practical applications, microstructures may be subjected to various physical fields, such as a magnetic field, electric field, or fluid flow. It has been experimentally observed in the scale of micrometers that strong small-length scale effects may occur in both nonmetallic and metallic materials [McFarland and Colton 2005; Fleck et al. 1994; Stölken and Evans 1998]. Namely, the mechanical properties of microscale structures may depend on their geometrical size. Obviously, such size-dependent properties cannot be classical/conventional continuum mechanics theories. Some experimental results [McFarland and Colton 2005; Fleck et al. 1994; Stölken and Evans 1998] showed that with the decrease of structural

Lin Wang is the corresponding author.

**Keywords:** nonplanar postbuckling configuration, microwire carrying electric current, modified couple stress theory, longitudinal magnetic field, buckling instability.



characteristic size, the effective stiffness of microscale structures generally becomes higher than that predicted by using the classical continuum mechanics theories, i.e., the error between the experimental result and the result from classical continuum mechanics theories might be remarkable in some cases. Therefore, several nonclassical continuum theories have been established, such as the nonlocal elasticity theory [Wang 2009; Wang et al. 2006; Chang and Yeh 2014], surface elasticity theory [Kiani 2014a; He and Lilley 2008], strain gradient elasticity theory [Ebrahimi and Barati 2017a], and couple stress theory [Yang et al. 2002; Mindlin and Tiersten 1962].

According to the nonlocal elasticity theory, the stress state at a given point is assumed to depend on the strain state of itself and its neighborhood [Wang et al. 2006]. The surface elasticity theory presumes that the surface energy cannot be ignored, and with the increase of ratio between surface/interface area and volume, the effect of surface layer may play a significant role in predicting the mechanical behavior of nanoscale structures [Wang 2009]. The couple stress theory is originally developed by Mindlin and Tiersten [1962] and further modified by Yang et al. [2002]. In the modified couple stress theory, not only the classical normal and shear stresses, but also the couple stresses, which are related to the deformation via a new material constant called the material length scale parameter, have been taken into account. So far, many researchers have utilized the modified couple stress theory to describe the size effect of microstructures [Tsias 2009; Dai et al. 2015; Dehrouyeh-Semnani et al. 2015; Mohammadabadi et al. 2015].

In the framework of the above nonclassical continuum theories, there were a few studies focused on the mechanical behavior of carbon nanotubes in magnetic fields [Kiani 2014c; Arani et al. 2015; Wang et al. 2016]. In the presence of a magnetic field, the Lorentz force generated by the induced current needs to be taken into account in some cases. For instance, Kiani [2014c] investigated the instability of a single-walled carbon nanotube (SWCNT) subjected to a three-dimensional (3D) magnetic field and obtained the critical transverse magnetic field at which buckling instability of the SWCNT occurs. Arani et al. [2015] studied the nonlinear vibration of two coupled nanotubes conveying fluid under a two-dimensional (2D) magnetic field, showing that the effect of a transverse magnetic field on the stability of CNTs is more obvious than that of a longitudinal magnetic field. More recently, Wang et al. [2016] studied the natural frequency and stability of fluid-conveying carbon nanotubes in a longitudinal magnetic field, and they found that the magnetic field can increase the critical flow velocity for flutter instability.

In addition, there were some studies associated with the vibration characteristics of micro/nano-beams acted upon by magnetic fields [Chang 2016; Ebrahimi and Barati 2016; 2017b]. For instance, Chang [2016] analyzed the effect of a magnetic field on the frequency of nonlinear nanobeams based on nonlocal elasticity theory and found that the magnetic force decreases the frequency and hence the nonlocal parameter can destabilize the nanobeam. Ebrahimi and Barati [2016] established a dynamical model of thermo-piezo-electrically actuated nanobeams under a magnetic field. On the basis of nonlocal strain gradient theory, Ebrahimi and Barati [2017b] investigated the flexural wave propagation of functionally graded (FG) nanobeams in a longitudinal magnetic field. It was shown that the wave propagation characteristics of FG nanobeams depend on various parameters including material graduation, magnetic field intensity, and length scale parameter.

In the past years, several investigations have been carried out regarding the dynamics of micro/nano-wires carrying electric current in the presence of magnetic fields [Kiani 2014a; 2015a; Wang et al. 2015]. In the dynamical model of current-carrying micro/nano-wires under magnetic fields, the induced current for the change of magnetic flux was assumed to be negligible if compared with the initial current. Hence,



the Lorentz force produced by the exerted magnetic field and initial current is the key factor needed to be accounted for.

Reviewing the studies on instability and vibration of magnetically affected micro/nano-wires carrying electric current, Kiani [2014a] studied the forced vibration of current-carrying nanowires (CCNW) in a longitudinal magnetic field accounting for both surface energy and nonlocal size effects. The influence of excitation frequency, magnetic force and small scale parameter on the maximum magnitude of transverse displacements of the CCNW was discussed. Using surface elasticity theory and considering the effect of longitudinal magnetic field, Keivan also investigated the column buckling of doubly parallel slender CCNW [Kiani 2016], and the free vibration and instability of a single CCNW modeled by a string [Kiani 2014b] or by an Euler–Bernoulli beam [Kiani 2015a]. The work of Kiani [2015b] was concerned with the vibration and buckling instability of pretensioned CCNWs acted upon by a suddenly applied 3D magnetic field. Using the differential quadrature method, Wang et al. [2015] calculated the natural frequency and buckling shapes of current-carrying microwires (CCMW) immersed in a longitudinal magnetic field. It was shown that both first- and second-mode buckling instabilities of microwires with clamped-clamped ends might occur when the magnetic field parameter becomes sufficiently large.

Amongst the valuable studies reviewed above, most researchers employed linear analytical models to analyze the dynamical system of magnetically affected CCNWs/CCMWs. However, some key questions associated with nonlinear phenomena cannot be answered excepted by nonlinear theory. For example, when a magnetically affected CCMW is buckled, the original straight equilibrium has become unstable and any motions actually would take place about the new nontrivial equilibrium points. In such a case, the postbuckling behavior must be assessed in the framework of nonlinear theories. Therefore, it is instructive for us to develop nonlinear analytical models for investigating the nonlinear postbuckling behaviors of CCMWs/CCNWs acted upon by magnetic fields.

In the present study, using the modified couple stress theory proposed by Yang et al. [2002], a nonlinear analytical model for magnetically affected CCMWs is developed to explore the microwire's dynamical behavior. Using Hamilton's principle, the nonplanar governing equations are derived by significantly accounting for the nonlinearity associated with the axial extension of the microwire when lateral displacements occur. The main feature of this analytical model is that it is capable of predicting the nonplanar configuration of the CCMW during buckling. The partial differential equations were discretized by Galerkin's approach and the resultant ordinary differential equations (ODE) were further solved via a fourth-order Runge–Kutta method. The effects of slenderness ratio, magnetic field force, axial compressive load, material length scale parameter, and initial conditions on the instability and nonplanar postbuckling configurations are evaluated, interestingly showing that the postbuckling shape of CCMWs is sensitive to the magnetic field parameter as well as the initial conditions employed.

## 2. Definition, assumption, and modeling of the problem

Consider a straight elastic microwire of length  $L$  illustrated in Figure 1. The microwire is immersed in a longitudinal magnetic field  $\mathbf{B}$  and a constant electric current  $\mathbf{I}$  is flowing through it. It is assumed that the microwire is slender enough such that the microwire can be modeled by a Euler–Bernoulli microbeam of density  $\rho$ , circular cross-sectional area  $A$ , and classical flexural rigidity  $EI$ . The effects of gravity are neglected while the axial extension of the microwire's centerline is taken into account. The initial

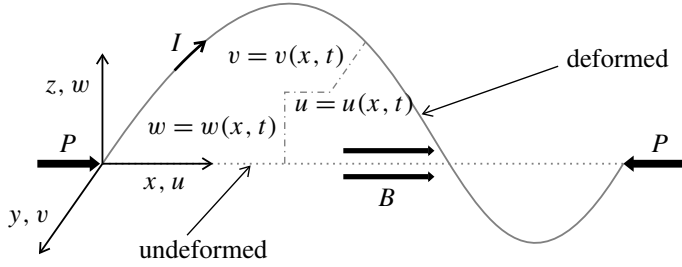


**Figure 1.** Schematic of a current-carrying microwire in a longitudinal magnetic field.

stress of the microwire may be nonzero due to the action of a given axial compressive load  $P$ . In the following analysis, using the rectangular Cartesian coordinate system  $(x, y, z)$  shown in Figure 1, the  $x$ -axis is assumed to be coincident with the centroidal axis of the undeformed microwire. The microwire may deflect along the  $y$ -axis and the  $z$ -axis, as shown in Figure 1.

According to the modified couple stress theory [Yang et al. 2002], the relation between the deviatoric part of the coupled stress tensor  $m_{ij}$  and the symmetric curvature tensor  $x_{ij}$  is given by

$$m_{ij} = 2l^2 G x_{ij}, \quad (1)$$

where  $G$  and  $l$  represent the shear modulus and the material length scale parameter respectively. By referring to the derivation of Mojahedi and Rahaeifard [2016], the nonzero components of the symmetric curvature tensor can be written as

$$x_{xy} = x_{yx} = -\frac{1}{2} \frac{\partial^2 w}{\partial x^2}, \quad x_{xz} = x_{zx} = -\frac{1}{2} \frac{\partial^2 v}{\partial x^2}. \quad (2)$$

Substituting (2) into (1), one has

$$m_{xy} = m_{yx} = -Gl^2 \frac{\partial^2 w}{\partial x^2}, \quad m_{xz} = m_{zx} = -Gl^2 \frac{\partial^2 v}{\partial x^2}. \quad (3)$$

As shown in Figure 1, the components of the displacement vector of the point  $(x, 0, 0)$  on the centroidal axis can be described as  $u = u(x, t)$ ,  $v = v(x, t)$ , and  $w = w(x, t)$ . According to the Euler–Bernoulli beam theory, the displacement field can be written as

$$u_1(x, y, z, t) = u(x, t) - z \frac{\partial w(x, t)}{\partial x} - y \frac{\partial v(x, t)}{\partial x}, \quad u_2 = v(x, t), \quad u_3 = w(x, t), \quad (4)$$

where  $u_1$ ,  $u_2$ , and  $u_3$  are, respectively, the  $x$ -,  $y$ -, and  $z$ -components of the displacement vector  $\mathbf{u}$  of a point  $(x, y, z)$  on a beam cross-section.

The initial axial strain induced by the axial compressive load can be written as

$$\varepsilon_0 = -\frac{P}{EA}. \quad (5)$$

The axial strain caused by the beam's deformation can be obtained by the von-Kármán relation and is given by

$$\varepsilon_1 = \frac{\partial u_1}{\partial x} + \frac{1}{2} \left( \frac{\partial w}{\partial x} \right)^2 + \frac{1}{2} \left( \frac{\partial v}{\partial x} \right)^2 = \frac{\partial u}{\partial x} - z \frac{\partial^2 w}{\partial x^2} - y \frac{\partial^2 v}{\partial x^2} + \frac{1}{2} \left( \frac{\partial w}{\partial x} \right)^2 + \frac{1}{2} \left( \frac{\partial v}{\partial x} \right)^2. \quad (6)$$

It is assumed that the effect of motions on the initial axial strain could be neglected for small deformations. Thus, the total axial strain of the microwire is obtained as

$$\varepsilon_x = -\frac{P}{EA} + \frac{\partial u}{\partial x} - z \frac{\partial^2 w}{\partial x^2} - y \frac{\partial^2 v}{\partial x^2} + \frac{1}{2} \left( \frac{\partial w}{\partial x} \right)^2 + \frac{1}{2} \left( \frac{\partial v}{\partial x} \right)^2, \quad (7)$$

and the axial stress can be written as

$$\sigma_x = E \left[ -\frac{P}{EA} + \frac{\partial u}{\partial x} - z \frac{\partial^2 w}{\partial x^2} - y \frac{\partial^2 v}{\partial x^2} + \frac{1}{2} \left( \frac{\partial w}{\partial x} \right)^2 + \frac{1}{2} \left( \frac{\partial v}{\partial x} \right)^2 \right]. \quad (8)$$

Now the total strain energy in the microwire can be expressed as

$$V = \frac{1}{2} \int_L \iint_A (\sigma_x \varepsilon_x + m_{xy} x_{xy} + m_{yx} x_{yx} + m_{xz} x_{xz} + m_{zx} x_{zx}) dA dx. \quad (9)$$

Substituting (2), (3), (7), and (8) into (9), one obtains

$$V = \frac{1}{2} \int_L \iint_A \left\{ E \left[ -\frac{P}{EA} + \frac{\partial u}{\partial x} - z \frac{\partial^2 w}{\partial x^2} - y \frac{\partial^2 v}{\partial x^2} + \frac{1}{2} \left( \frac{\partial w}{\partial x} \right)^2 + \frac{1}{2} \left( \frac{\partial v}{\partial x} \right)^2 \right]^2 + Gl^2 \left( \frac{\partial^2 w}{\partial x^2} \right)^2 + Gl^2 \left( \frac{\partial^2 v}{\partial x^2} \right)^2 \right\} dA dx. \quad (10)$$

The kinetic energy of the microwire is given by

$$T = \frac{1}{2} \rho A \int_0^L \left[ \left( \frac{\partial u}{\partial t} \right)^2 + \left( \frac{\partial v}{\partial t} \right)^2 + \left( \frac{\partial w}{\partial t} \right)^2 \right] dx, \quad (11)$$

where the components of the velocity vector of the point  $(x, 0, 0)$  on the centroidal axis are utilized to determine the kinetic energy of the system.

On the basis of Lorentz's formula, the CCMW immersed in a magnetic field would be subjected to a Lorentz force. For small deformations,  $\mathbf{I} = I_0(1 + \partial u / \partial x) \mathbf{e}_x + I_0(\partial w / \partial x) \mathbf{e}_y + I_0(\partial v / \partial x) \mathbf{e}_z$  is the electric current vector with amplitude  $I_0$ . According to the derivation of He and Lilley [2008], the Lorentz force per unit length of the microwire immersed in a longitudinal magnetic field can be evaluated by

$$\mathbf{f}_m = \mathbf{I} \times \mathbf{B} = B_0 I_0 \left( 0 \mathbf{e}_x, \frac{\partial w}{\partial x} \mathbf{e}_y, -\frac{\partial v}{\partial x} \mathbf{e}_z \right), \quad (12)$$

where  $\mathbf{e}_x$ ,  $\mathbf{e}_y$ , and  $\mathbf{e}_z$  represent the unit vectors associated with  $x$ -,  $y$ -, and  $z$ -axes, respectively;  $B_0$  is the magnitude of the magnetic induction vector  $\mathbf{B}$ . It is noted that an induced current may be generated because of the electromagnetic induction, yielding an additional magnetic force. According to derivation of Narendar et al. [2012], one obtains the additional magnetic forces along the  $z$ - and  $y$ -axes are  $\eta A H_x^2 \partial^2 w / \partial x^2$  and  $\eta A H_x^2 \partial^2 v / \partial x^2$ , respectively, where  $\eta$  is the magnetic field permeability and  $H_x$  is the magnetic flux vector with amplitude  $H_x$  in the  $x$  direction. In this paper, the microwire is considered to be nonferromagnetic. For nonferromagnetic materials (e.g., copper or silver), the magnetic field permeability  $\eta$  is approximately to be  $4\pi \times 10^{-7}$  H/m and the magnetic field intensity  $H_x$  is approximately equal to the magnetic induction  $\mathbf{B}$ . In this case, the Lorentz force plays a major role. Thus the effect of the additional magnetic force will be neglected in this work.

Then, the variation of the virtual work resulted from the Lorentz's force is given by

$$\delta W = BI_0 \int_0^L \left( \frac{\partial w}{\partial x} \delta v - \frac{\partial v}{\partial x} \delta w \right) dx. \quad (13)$$

According to Hamilton's principle, one has

$$\int_{t_1}^{t_2} (\delta V - \delta T - \delta W) dt = 0. \quad (14)$$

Substituting (10), (11), and (13) into (14) and considering the pinned-pinned or clamped-clamped boundary conditions of the microwire, the nonplanar version of the governing equations of the microwire carrying current in a longitudinal magnetic field takes the form

$$\rho A \frac{\partial^2 u}{\partial t^2} - EA \frac{\partial^2 u}{\partial x^2} - EA \frac{\partial v}{\partial x} \frac{\partial^2 v}{\partial x^2} - EA \frac{\partial w}{\partial x} \frac{\partial^2 w}{\partial x^2} = 0, \quad (15a)$$

$$\begin{aligned} \rho A \frac{\partial^2 v}{\partial t^2} + (AGI^2 + EI) \frac{\partial^4 v}{\partial x^4} + EA \left[ \frac{P}{EA} - \frac{\partial u}{\partial x} - \frac{1}{2} \left( \frac{\partial w}{\partial x} \right)^2 - \frac{3}{2} \left( \frac{\partial v}{\partial x} \right)^2 \right] \frac{\partial^2 v}{\partial x^2} \\ - EA \left( \frac{\partial^2 u}{\partial x^2} + \frac{\partial w}{\partial x} \frac{\partial^2 w}{\partial x^2} \right) \frac{\partial v}{\partial x} = BI_0 \frac{\partial w}{\partial x}, \end{aligned} \quad (15b)$$

$$\begin{aligned} \rho A \frac{\partial^2 w}{\partial t^2} + (AGI^2 + EI) \frac{\partial^4 w}{\partial x^4} + EA \left[ \frac{P}{EA} - \frac{\partial u}{\partial x} - \frac{1}{2} \left( \frac{\partial v}{\partial x} \right)^2 - \frac{3}{2} \left( \frac{\partial w}{\partial x} \right)^2 \right] \frac{\partial^2 w}{\partial x^2} \\ - EA \left( \frac{\partial^2 u}{\partial x^2} + \frac{\partial v}{\partial x} \frac{\partial^2 v}{\partial x^2} \right) \frac{\partial w}{\partial x} = -BI_0 \frac{\partial v}{\partial x}. \end{aligned} \quad (15c)$$

From (15), it is seen that the distributed Lorentz force is not constant but actually depends upon the deformed configuration of the microwire. When we consider the interaction between the magnetic field and microwire, it is also assumed that there is no coupling at the material level but only through the Lorentz force, which is applied as a body force in (15b) and (15c).

In consideration of no distributed axial load, the longitudinal inertia could be neglected [Kahrobaiyan et al. 2011] and (15a) can be reduced to the following form

$$-EA \frac{\partial^2 u}{\partial x^2} - EA \frac{\partial v}{\partial x} \frac{\partial^2 v}{\partial x^2} - EA \frac{\partial w}{\partial x} \frac{\partial^2 w}{\partial x^2} = 0, \quad (16)$$

namely,

$$-\frac{\partial^2 u}{\partial x^2} = \frac{1}{2} \left\{ \frac{\partial}{\partial x} \left[ \left( \frac{\partial v}{\partial x} \right)^2 + \left( \frac{\partial w}{\partial x} \right)^2 \right] \right\}. \quad (17)$$

Carrying out two integrations of (17) and applying the corresponding boundary conditions, one obtains

$$u = -\frac{1}{2} \int_0^x \left[ \left( \frac{\partial v}{\partial x} \right)^2 + \left( \frac{\partial w}{\partial x} \right)^2 \right] dx + \frac{x}{2L} \int_0^L \left[ \left( \frac{\partial v}{\partial x} \right)^2 + \left( \frac{\partial w}{\partial x} \right)^2 \right] dx. \quad (18)$$

Substituting (18) into (15b) and (15c), the governing equations of the microwire can be simplified to two-dimensional forms, as follows:

$$(AGl^2 + EI) \frac{\partial^4 v}{\partial x^4} + EA \left[ \frac{P}{EA} - \frac{C}{2L} \right] \frac{\partial^2 v}{\partial x^2} + \rho A \frac{\partial^2 v}{\partial t^2} = BI_0 \frac{\partial w}{\partial x}, \quad (19a)$$

$$(AGl^2 + EI) \frac{\partial^4 w}{\partial x^4} + EA \left[ \frac{P}{EA} - \frac{C}{2L} \right] \frac{\partial^2 w}{\partial x^2} + \rho A \frac{\partial^2 w}{\partial t^2} = -BI_0 \frac{\partial v}{\partial x}, \quad (19b)$$

where the parameter  $C$  represents the axial elongation of the centroidal axis and is defined by

$$C = \int_0^L \left[ \left( \frac{\partial v}{\partial x} \right)^2 + \left( \frac{\partial w}{\partial x} \right)^2 \right] dx. \quad (20)$$

The resultant equations may be rendered dimensionless through the use of

$$\xi = \frac{x}{L}, \quad \bar{v} = \frac{v}{L}, \quad \bar{w} = \frac{w}{L}, \quad \tau = \left[ \frac{EI}{\rho A} \right]^{1/2} \frac{t}{L^2}. \quad (21)$$

The dimensionless equations are

$$(\mu + 1) \frac{\partial^4 \bar{v}}{\partial \xi^4} + (p - \alpha c) \frac{\partial^2 \bar{v}}{\partial \xi^2} - \alpha^{3/2} f_I \frac{\partial \bar{w}}{\partial \xi} + \frac{\partial^2 \bar{v}}{\partial \tau^2} = 0, \quad (22a)$$

$$(\mu + 1) \frac{\partial^4 \bar{w}}{\partial \xi^4} + (p - \alpha c) \frac{\partial^2 \bar{w}}{\partial \xi^2} + \alpha^{3/2} f_I \frac{\partial \bar{v}}{\partial \xi} + \frac{\partial^2 \bar{w}}{\partial \tau^2} = 0, \quad (22b)$$

where several other dimensionless parameters are defined by

$$\mu = \frac{AGl^2}{EI}, \quad p = \frac{PL^2}{EI}, \quad f_I = \frac{2\sqrt{2} BI_0}{E\pi D}, \quad \alpha = \frac{AL^2}{2I} = 8 \left( \frac{L}{D} \right)^2, \quad c = \int_0^1 \left[ \left( \frac{\partial \bar{v}}{\partial \xi} \right)^2 + \left( \frac{\partial \bar{w}}{\partial \xi} \right)^2 \right] d\xi. \quad (23)$$

The various dimensionless parameters in (23) denote, respectively, the dimensionless material length scale parameter, dimensionless compressive load, dimensionless magnetic force, dimensionless parameter associated with slenderness ratio, and dimensionless axial elongation of the centerline. In the following analysis, the effects of the first four dimensionless parameters appearing in (23) on the stability and nonplanar buckling of the microwire will be discussed in detail.

In the case of a clamped-clamped microwire carrying current, the dimensionless boundary conditions to be satisfied are as follows:

$$\bar{v}(0, \tau) = \bar{v}(1, \tau) = 0, \quad \frac{\partial \bar{v}(0, \tau)}{\partial \xi} = \frac{\partial \bar{v}(1, \tau)}{\partial \xi} = 0, \quad (24a)$$

$$\bar{w}(0, \tau) = \bar{w}(1, \tau) = 0, \quad \frac{\partial \bar{w}(0, \tau)}{\partial \xi} = \frac{\partial \bar{w}(1, \tau)}{\partial \xi} = 0. \quad (24b)$$

The dimensionless boundary conditions for a pinned-pinned microwire may be written in a similar way:

$$\bar{v}(0, \tau) = \bar{v}(1, \tau) = 0, \quad \frac{\partial^2 \bar{v}(0, \tau)}{\partial \xi^2} = \frac{\partial^2 \bar{v}(1, \tau)}{\partial \xi^2} = 0, \quad (25a)$$

$$\bar{w}(0, \tau) = \bar{w}(1, \tau) = 0, \quad \frac{\partial^2 \bar{w}(0, \tau)}{\partial \xi^2} = \frac{\partial^2 \bar{w}(1, \tau)}{\partial \xi^2} = 0. \quad (25b)$$

### 3. Solutions based on Galerkin's approach

In this section, the Galerkin's approach is applied to transform the governing equations from partial differential equations (PDEs) to ordinary differential equations (ODEs). The resultant ODEs will be further solved by using a fourth-order Runge–Kutta (R–K) method. For the sake of eliminating the effects of initial conditions on the transient responses and achieving steady buckling deformation of the microwire, an additional damping term is added to the governing equations; thus, we have

$$(\mu + 1) \frac{\partial^4 \bar{v}}{\partial \xi^4} + (p - \alpha c) \frac{\partial^2 \bar{v}}{\partial \xi^2} - \alpha^{3/2} f_I \frac{\partial \bar{w}}{\partial \xi} + \frac{\partial^2 \bar{v}}{\partial \tau^2} + \gamma \frac{\partial \bar{v}}{\partial \tau} = 0, \quad (26a)$$

$$(\mu + 1) \frac{\partial^4 \bar{w}}{\partial \xi^4} + (p - \alpha c) \frac{\partial^2 \bar{w}}{\partial \xi^2} + \alpha^{3/2} f_I \frac{\partial \bar{v}}{\partial \xi} + \frac{\partial^2 \bar{w}}{\partial \tau^2} + \gamma \frac{\partial \bar{w}}{\partial \tau} = 0, \quad (26b)$$

where  $\gamma$  is a dimensionless damping coefficient. It should be explained that the additional damping term cannot affect the postbuckling configuration of the current-carrying microwire. In what follows, the damping coefficient of  $\gamma = 1$  is adopted for the purpose of obtaining fast convergence speed.

According to the Galerkin's approach, the dimensionless lateral displacements of the microwire may be expressed as

$$\bar{v}(\xi, \tau) = \sum_{n=1}^N \phi_n(\xi) q_{vn}(\tau), \quad (27a)$$

$$\bar{w}(\xi, \tau) = \sum_{n=1}^N \phi_n(\xi) q_{wn}(\tau), \quad (27b)$$

where  $N$  is the number of considered modes and  $\phi_n(\xi)$  is the  $n$ -th mode function of an Euler–Bernoulli beam with corresponding boundary conditions;  $q_{vn}(\tau)$  and  $q_{wn}(\tau)$  are the two generalized coordinates of the discretized system. It is presumed that the approximate expansion of series (27) may be reliable at a suitably high value of  $N$ .

Substituting (27a) and (27b) into (26a) and (26b), one obtains the following set of nonlinear algebraic equations:

$$\begin{bmatrix} \mathbf{K}^{vv}(\tau) & \mathbf{K}^{vw} \\ \mathbf{K}^{wv} & \mathbf{K}^{ww}(\tau) \end{bmatrix} \begin{Bmatrix} \mathbf{q}_v \\ \mathbf{q}_w \end{Bmatrix} + \begin{Bmatrix} \ddot{\mathbf{q}}_v \\ \ddot{\mathbf{q}}_w \end{Bmatrix} + \gamma \begin{Bmatrix} \dot{\mathbf{q}}_v \\ \dot{\mathbf{q}}_w \end{Bmatrix} = 0, \quad (28)$$

where single and double dots denote first- and second-order derivatives with respect to the dimensionless

time  $\tau$ . In (28), several vectors and matrices are defined by

$$\mathbf{q}_v = \begin{Bmatrix} q_{v1}(\tau) \\ \vdots \\ q_{vN}(\tau) \end{Bmatrix}, \quad \mathbf{q}_w = \begin{Bmatrix} q_{w1}(\tau) \\ \vdots \\ q_{wN}(\tau) \end{Bmatrix}, \quad (29a)$$

$$\mathbf{K}_{mn}^{vv}(\tau) = \mathbf{K}_{mn}^{ww}(\tau) = (\mu + 1)\lambda_m^4 \delta_{mn} + \eta(\tau) \mathbf{c}_{mn}, \quad (29b)$$

$$\mathbf{K}_{mn}^{vw} = -f_I \mathbf{b}_{mn}, \quad (29c)$$

$$\mathbf{K}_{mn}^{wv} = f_I \mathbf{b}_{mn}. \quad (29d)$$

The values of  $\mathbf{b}_{mn}$ ,  $\mathbf{c}_{mn}$ , and  $\lambda_n$ , which are related to the boundary conditions of the microwire, may be evaluated in closed form by defining the following set of constants:

$$\mathbf{b}_{mn} = \int_0^1 \phi_m(\xi) \phi_n'(\xi) d\xi, \quad \mathbf{c}_{mn} = \int_0^1 \phi_m(\xi) \phi_n''(\xi) d\xi. \quad (30)$$

For clamped-clamped boundary conditions, we have

$$\lambda_1 = 4.7300, \quad \lambda_2 = 7.8532, \quad \lambda_n \approx (n + \frac{1}{2})\pi \quad (n = 3, 4, 5, \dots), \quad (31a)$$

$$\phi_n(\xi) = \cos(\lambda_n \xi) - \cosh(\lambda_n \xi) - \frac{\cos(\lambda) - \cosh(\lambda_n)}{\sin(\lambda_n) - \sinh(\lambda_n)} [\sin(\lambda_n \xi) - \sinh(\lambda_n \xi)]. \quad (31b)$$

For pinned-pinned boundary conditions, one has

$$\lambda_n = n\pi \quad (n = 1, 2, 3, \dots), \quad (32a)$$

$$\phi_n(\xi) = \sqrt{2} \sin(\lambda_n \xi). \quad (32b)$$

It should be noted that the dimensionless parameter  $\eta(\tau)$  in (29b) represents the equivalent axial compression  $p$  determined by the initial axial compression and the time-varying axial elongation  $c(\tau)$ , i.e.,

$$\eta(\tau) = p - ac(\tau), \quad (33)$$

$$c(\tau) = \int_0^1 \left\{ \left[ \sum_{n=1}^N \phi_n'(\xi) q_{vn}(\tau) \right]^2 + \left[ \sum_{n=1}^N \phi_n'(\xi) q_{wn}(\tau) \right]^2 \right\} d\xi. \quad (34)$$

In order to apply the Runge–Kutta method, we define two new vectors as follows

$$\mathbf{q} = \begin{Bmatrix} \mathbf{q}_v \\ \mathbf{q}_w \end{Bmatrix}, \quad \mathbf{Q} = \begin{Bmatrix} \dot{\mathbf{q}} \\ \mathbf{q} \end{Bmatrix}. \quad (35)$$

Then one obtains

$$\dot{\mathbf{Q}} = F(\tau, \mathbf{Q}) = \begin{bmatrix} -\gamma \times [\mathbf{I}] & -[\mathbf{K}] \\ [\mathbf{I}] & [\mathbf{0}] \end{bmatrix} \begin{Bmatrix} \{\dot{\mathbf{q}}\} \\ \{\mathbf{q}\} \end{Bmatrix}, \quad (36)$$

where  $[\mathbf{I}]$  is a unit diagonal matrix and  $[\mathbf{0}]$  is a zero element matrix.

By use of the fourth-order Runge–Kutta method, the dynamic responses of the CCMW immersed in a longitudinal magnetic field may be calculated. Selecting a set of system parameters defined in (23), one

can analyze the effects of slenderness ratio, magnetic force, axial compression and material length scale parameter on the stability and nonplanar postbuckling behaviors of the microwire.

#### 4. Validity of the developed nonlinear model and proposed computational procedure

It is noted that, due to the presence of Lorentz's force, (26) could not be solved analytically. In the case of  $f_I = 0$ , however, the exact solutions for the postbuckling amplitudes of a microwire under axial compression are available [Nayfeh and Emam 2008]. In this section, first, numerical simulations based on (26) are performed in order to check the validity of the developed nonlinear model and proposed computational procedure. For that purpose, the postbuckling configuration of an axially loaded microbeam in the absence of magnetic fields is numerically calculated and compared to that obtained analytically.

In the case of  $\mu = 0$  and  $f_I = 0$ , (26) is reduced to the buckling problem of a classical Euler–Bernoulli beam subjected to a compressive load. The governing equation for the planar deflection of the microwire becomes

$$\psi^{iv}(\xi) + p\psi''(\xi) - \alpha\psi'' \int_0^1 \psi'^2(\xi) d\xi = 0. \quad (37a)$$

Now consider a simply-supported beam with an axial compressive load of  $p = 10\pi^2$ . In this case, the analytical solution for the buckling configuration is given by [Sun et al. 2017]

$$\psi_1(\xi) = \pm \frac{3\sqrt{2\alpha}}{\alpha} \sin(\pi\xi). \quad (37b)$$

As seen in Figure 2, compared with the analytical solution of (37b), our numerical results for the buckling amplitude of the microwire achieve low relative error below 0.01% for  $N > 4$ , thus demonstrating the validation and accuracy of the Runge–Kutta procedure. Synthesizing both the accuracy and computational efficiency, therefore,  $N = 5$  will be chosen for the following calculations.

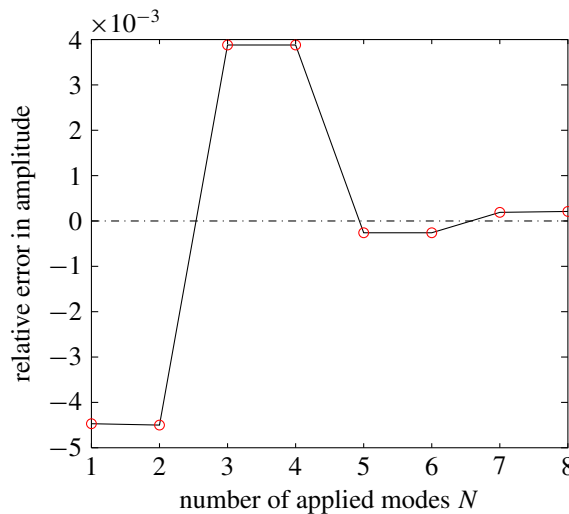


**Figure 2.** The relative error of numerical results for postbuckling amplitude as a function of the truncated mode number  $N$  for  $\mu = 0$ ,  $f_I = 0$ ,  $\alpha = 800$ , and  $p = 10\pi^2$ .



## 5. Results and discussion

This section examines the nonlinear behavior of the CCMW employing the nonlinear model developed in Section 2. More specifically, the postbuckling amplitudes of the microwire are examined in Section 5.1, for different values of  $\alpha$  and  $f_I$ . The effect of initial conditions on the postbuckling configurations (amplitude and shape) of the microwire is analyzed in Section 5.2. The influence of magnetic field parameter on the postbuckling configurations of the microwire is discussed in Section 5.3. Section 5.4 evaluates the effect of material length scale parameter on the stability and postbuckling amplitudes of the microwire. In Section 5.5, the effect of axial compressive load on the postbuckling configuration is studied.

**5.1. Postbuckling amplitudes of the microwire for various  $\alpha$  and  $f_I$ .** The microwire's stability and postbuckling amplitude are examined by setting  $\mu = 0.1$  and  $p = 0$ , and varying the value of  $\alpha$ . To observe the stability evolution of the microwire, the dimensionless magnetic force  $f_I$  is successively increased.

Figure 3 shows the buckling responses of the microwire through plots of the transverse amplitudes as a function of  $f_I$ , for clamped-clamped or pinned-pinned boundary conditions. The results are obtained for a microwire with  $\alpha = 800, 1200, 1600$ , or  $2000$ . In Figure 3, the transverse amplitudes of the microwire are denoted as  $\max(\sqrt{\bar{v}(\xi, \tau)^2 + \bar{w}(\xi, \tau)^2})$ . From this figure, one may find that the buckling instability of a clamped-clamped microwire occurs at  $f_{Ic} \approx 0.0192, 0.0104, 0.0068$ , and  $0.0048$  for four different values of  $\alpha$  ( $\alpha = 800, 1200, 1600$ , and  $2000$ ), respectively. For a pinned-pinned microwire, the buckling instability occurs at  $f_{Ic} \approx 0.0069, 0.0038, 0.0024$ , and  $0.0018$  for  $\alpha = 800, 1200, 1600$ , and  $2000$ , respectively. Since  $f_{Ic}$  represents the onset value of dimensionless magnetic force for buckling instability, it is termed as the critical magnetic force. Thus, by changing the value of  $\alpha$  and maintaining other system parameters unchanged, the slenderness ratio parameter  $\alpha$  is found to have significant effect on the critical magnetic force and hence the postbuckling amplitudes of the microwire. The evolution of postbuckling amplitudes as a function of  $\alpha$  is in accord with one's common experience. Based on further calculations, it is found that at the onset of buckling instability, we have  $\alpha^{3/2} f_{Ic} \approx 433.7$  for clamped-clamped ends and  $\alpha^{3/2} f_{Ic} \approx 157.1$  for pinned-pinned ends. For a given set of boundary conditions, therefore, the combined parameter  $\alpha^{3/2} f_I$  may be viewed as an essential index for examining the stability of CCMW acted upon by a longitudinal magnetic field. In the following discussion, we define  $\alpha^{3/2} f_I$  as a new magnetic field parameter.

**5.2. Postbuckling configurations for various initial conditions.** The results shown in Figure 3 were concerned with the transverse amplitudes of the microwire. Some calculations for the postbuckling shapes of the microwire are further conducted here. In our numerical calculations, it is noted that the initial conditions can significantly affect the final postbuckling shapes of the microwire. This trend may be the most interesting finding in this work. Some typical results are plotted in Figure 4 and Figure 5, where the dimensionless magnetic field parameter  $\alpha^{3/2} f_I$  remains unchanged while the value of  $\alpha$  is varied. In Figure 4, the initial conditions for calculations were chosen as

$$\dot{q}_v(0) = \dot{q}_w(0) = \{0, 0, 0, 0, 0\}, \quad q_v(0) = q_w(0) = \{a, 0, 0, 0, 0\}, \quad (38)$$

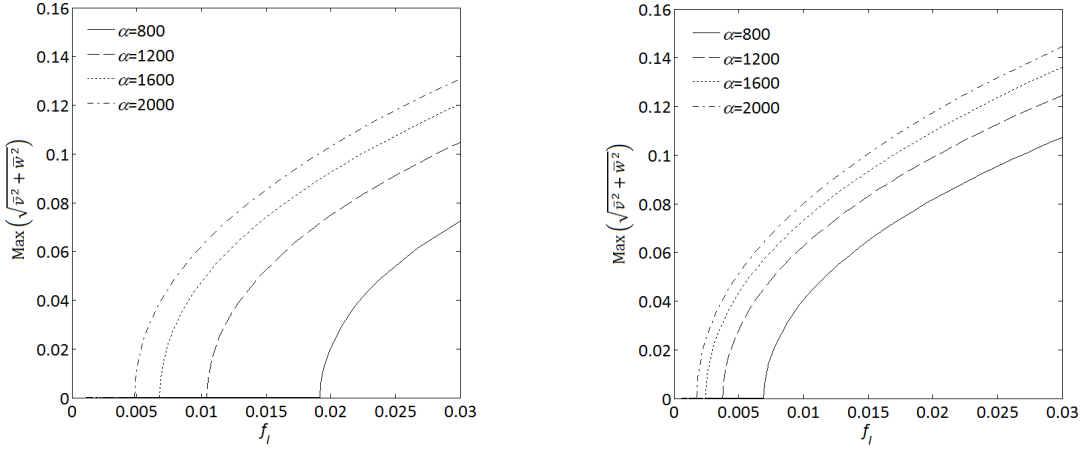


**Figure 3.** The maximum transverse amplitudes of the microwire as a function of the dimensionless magnetic force  $f_I$ , for  $\mu = 0.1$ ,  $p = 0$ , and various values of  $\alpha$ : for clamped-clamped boundary conditions (left), and for pinned-pinned boundary conditions (right).

where  $a$  is a given constant and is fixed to be 0.001 in our calculations. In Figure 5, however, another set of initial conditions were used:

$$\dot{\mathbf{q}}_v(0) = \dot{\mathbf{q}}_w(0) = \{0, 0, 0, 0, 0\}, \quad \mathbf{q}_v(0) = \{a, 0, 0, 0, 0\}, \quad \mathbf{q}_w(0) = \{0, a, 0, 0, 0\}. \quad (39)$$

As shown by the results of Figure 4 and Figure 5, for a given set of system parameters, the buckling shapes in the  $x$ - $o$ - $y$  and  $x$ - $o$ - $z$  planes are different from each other. Interestingly, the postbuckling shapes depend on the combined parameter  $\alpha^{3/2} f_I$  and the buckling amplitudes are affected by the slenderness ratio parameter  $\alpha$ . Moreover, the postbuckling configurations shown in Figure 4 (left column) (or Figure 4, right column) contain both first-mode and second-mode components of a beam with clamped-clamped (or pinned-pinned) boundary conditions. As shown by the results of Figure 5, however, the postbuckling shapes for  $v$  in  $x$ - $o$ - $y$  plane and  $w$  in  $x$ - $o$ - $z$  plane mainly contains the first-mode and second-mode components, respectively.

More extensive calculations have been done for several other possible types of initial conditions. The results are presented in Figure 6 for clamped-clamped boundary conditions and in Figure 7 for pinned-pinned boundary conditions. From the results of Figure 6 and Figure 7, it is observed that the postbuckling shapes of the microwire are strongly dependent on the initial conditions used. For a set of given initial conditions, the buckling shape for  $v$  in the  $x$ - $o$ - $y$  plane may mainly contain the first-mode component of a clamped-clamped beam. For other initial conditions, however, it may be mainly associated with the second-mode component. To the authors' knowledge, this strong dependence of postbuckling shapes on the initial conditions is a relatively new finding for CCNWs and has not been reported previously.

An alternative, perhaps easier-to-understand form of the results of Figure 6 and Figure 7, is represented in a cylindrical coordinate, as shown in Figure 8 and Figure 9. In these two figures, the radius  $r$  and angle  $\theta$ , respectively, denote the minimum distance from the deformed microwire to the  $x$ -axis and the minimum clockwise rotation angle from vector  $\{v \mathbf{e}_y, w \mathbf{e}_z\}$  to the unit vector  $\mathbf{e}_y$ . From Figure 8

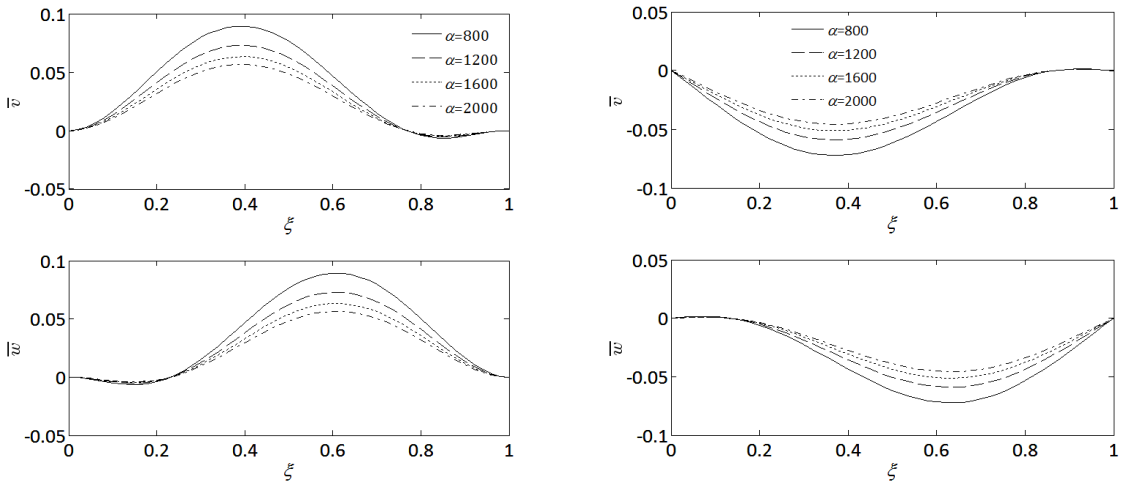


**Figure 4.** The postbuckling shapes of the microwire in the  $x$ - $o$ - $y$  and  $x$ - $o$ - $z$  planes for  $\mu = 0.1$ ,  $p = 0$ , and various values of  $\alpha$ , for: clamped-clamped boundary conditions with  $\alpha^{3/2} f_I = 1000$  (left column), and pinned-pinned boundary conditions with  $\alpha^{3/2} f_I = 500$ ; the initial conditions of (38) were chosen for all calculations (right column).

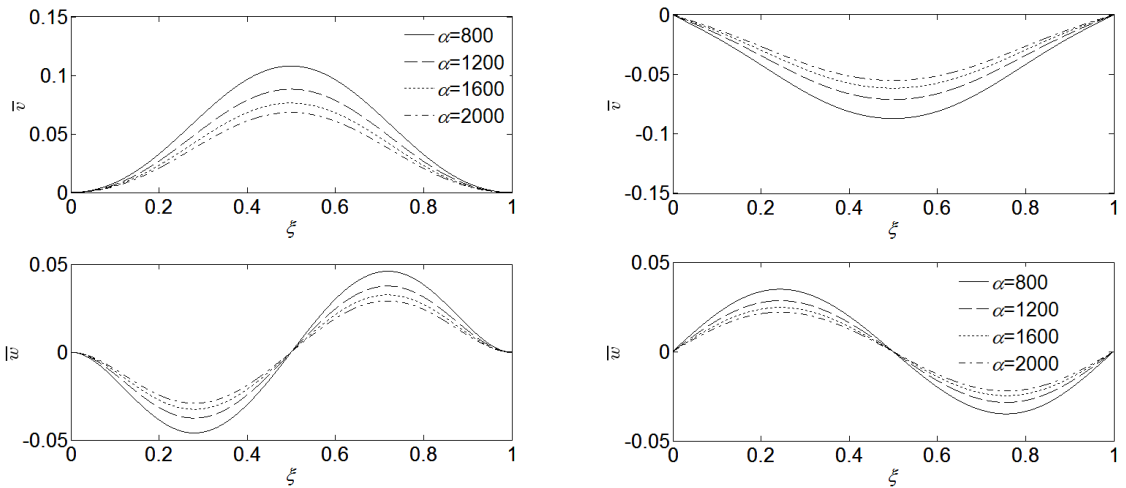


**Figure 5.** The postbuckling shapes of the microwire in the  $x$ - $o$ - $y$  and  $x$ - $o$ - $z$  planes for  $\mu = 0.1$ ,  $p = 0$ , and various values of  $\alpha$ , for: clamped-clamped boundary conditions with  $\alpha^{3/2} f_I = 1000$  (left column), and pinned-pinned boundary conditions with  $\alpha^{3/2} f_I = 500$ ; the initial conditions of (39) were chosen for all calculations (right column).

and Figure 9, one can observe two obvious but important features. First, the dimensionless radius  $r$  for a fixed  $\xi$  is identical for various different initial conditions, for either clamped-clamped or pinned-pinned boundary conditions. This implies that initial conditions have no effect on the “overall” nonplanar amplitudes of the CCMW. However, initial conditions can affect the spatial shapes of the microwire, as

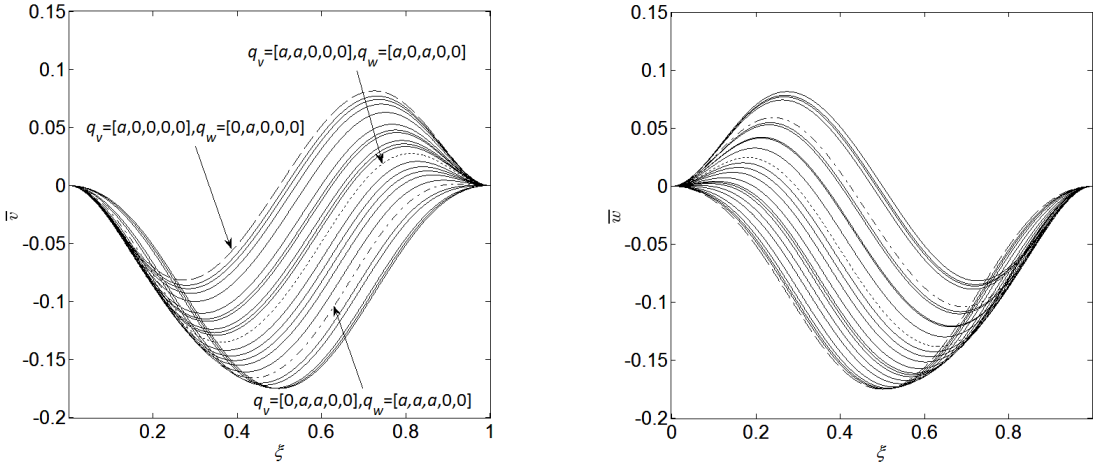


**Figure 6.** The postbuckling shapes of the microwire with clamped-clamped ends for different initial conditions:  $\mu = 0.1$ ,  $p = 0$ ,  $\alpha^{3/2} f_I = 2000$ , and  $\alpha = 800$ .

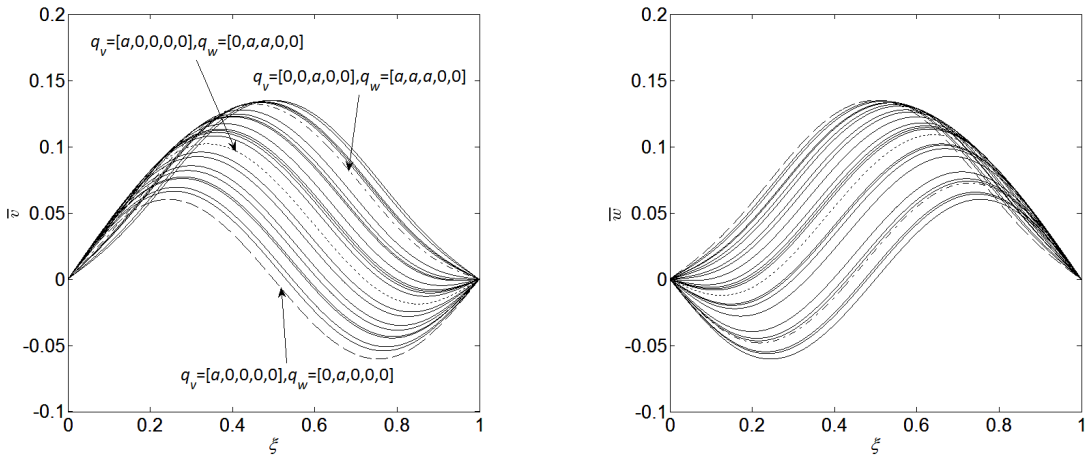


**Figure 7.** The postbuckling shapes of the microwire with pinned-pinned ends for different initial conditions:  $\mu = 0.1$ ,  $p = 0$ ,  $\alpha^{3/2} f_I = 1000$ , and  $\alpha = 800$ .

may be observed in [Figure 8](#), right, and [Figure 9](#), right. Second, the total relative rotation angles of clamped-clamped microwire and pinned-pinned microwire are 150 and 120 degrees respectively, which are independent of initial conditions.

To explain the strong dependence of postbuckling shapes on initial conditions, let us analyze the eigenvectors of the stiffness matrix  $[\mathbf{K}]$  in (8). For a given set of system parameters, extensive calculations showed that the dimensionless axial elongation of the microwire's centerline do not change for various initial conditions. This means that the stiffness matrix  $[\mathbf{K}]$  does not change. Putting the value of

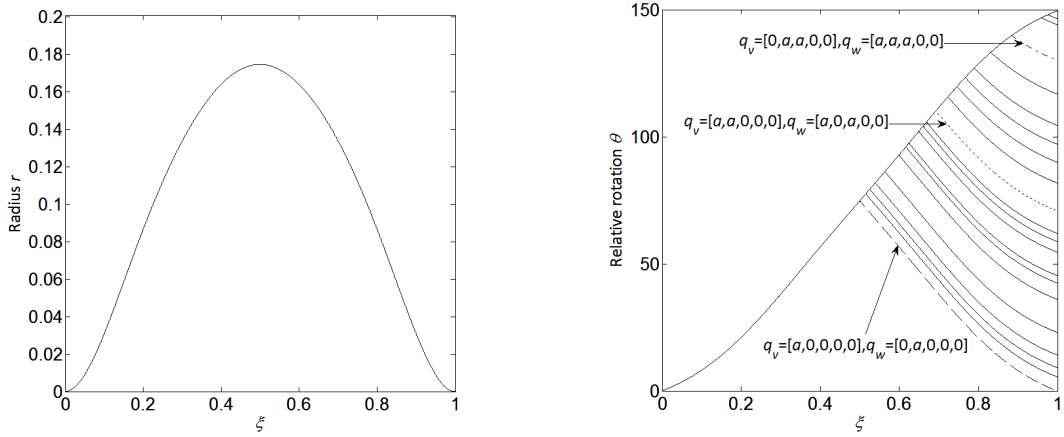


**Figure 8.** The postbuckling configurations of a clamped-clamped microwire shown in a cylindrical coordinate system for different initial conditions and  $\mu = 0.1$ ,  $p = 0$ ,  $\alpha^{3/2} f_I = 2000$ , and  $\alpha = 800$ .

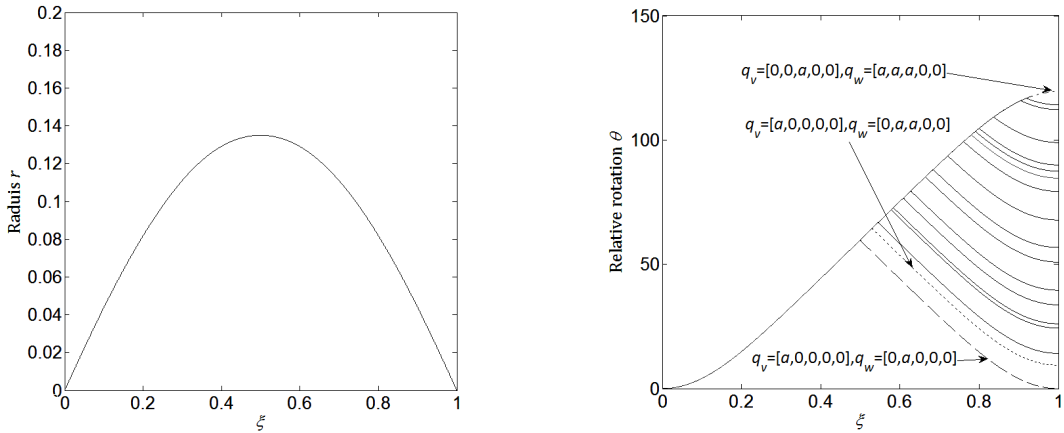


**Figure 9.** The postbuckling configurations of a pinned-pinned microwire shown in a cylindrical coordinate system, for different initial conditions and  $\mu = 0.1$ ,  $p = 0$ ,  $\alpha^{3/2} f_I = 1000$ , and  $\alpha = 800$ .

dimensionless axial elongation of the centerline into the stiffness matrix  $[K]$ , one has

$$\begin{bmatrix} K^{vv} & K^{vw} \\ K^{wv} & K^{ww} \end{bmatrix} \begin{Bmatrix} q_v \\ q_w \end{Bmatrix} = 0. \quad (40)$$

It is assumed that a particular nontrivial solution of (40) may be expressed as

$$\begin{Bmatrix} q_v \\ q_w \end{Bmatrix} = \begin{Bmatrix} X_1 \\ X_2 \end{Bmatrix}. \quad (41)$$

Bearing in mind the expression of (29), one has

$$\mathbf{K}^{vv} = \mathbf{K}^{ww}, \quad \mathbf{K}^{vw} = -\mathbf{K}^{wv}. \quad (42)$$

It is noted that, therefore, another particular solution satisfying (40) can be written as

$$\begin{Bmatrix} \mathbf{q}_v \\ \mathbf{q}_w \end{Bmatrix} = \begin{Bmatrix} \mathbf{X}_2 \\ -\mathbf{X}_1 \end{Bmatrix}. \quad (43)$$

Thus, it follows from (41) and (43) that there may exist infinite kinds of possible solutions to (28). This implies that infinite kinds of postbuckling shapes may occur, mainly determined by the chosen initial conditions. Indeed, the feature of kaleidoscopic postbuckling shapes is due to the antisymmetry of the stiffness matrix  $[\mathbf{K}]$ . This new feature for nonplanar microwires has not been detected in previous studies of microwires under buckling in a single plane.

In fact, the initial displacement conditions may be viewed as an initial disturbance for the microwire. From this point of view, a set of initial velocity conditions may be also employed as an initial disturbance.

**5.3. Effect of magnetic field parameter on the postbuckling configurations.** The main results obtained, plotted in Figures 10–12, show that the magnetic field parameter may, sometimes, affect the postbuckling configurations of the microwire. In Figure 10 and Figure 11, four values of magnetic field parameter have been chosen for calculations for clamped-clamped or pinned-pinned boundary conditions. With initial conditions defined by (39), it is clear that the magnetic field parameter does not have visible effect on the postbuckling shape of the microwire. With initial conditions of (38), however, it is seen that the effect of magnetic field parameter on the postbuckling shape is obvious. For example, the results of Figure 10 (right) show that with increasing magnetic field parameter, the buckling shape of  $w$  in the  $x$ - $o$ - $z$  plane contains more and more second-mode components of a clamped-clamped beam. Similar trends may be found for pinned-pinned boundary conditions.

In addition, it is found that the buckling instability cannot appear in higher-order modes (e.g., the third mode), even if the magnetic field parameter becomes sufficiently large.

More extensive calculations have produced the results of Figure 12, where the initial conditions of (38) were utilized, for either clamped-clamped or pinned-pinned boundary conditions. In Figure 12 (left or right), twenty different values of magnetic field parameter were selected for calculations, thus producing twenty curves in each figure. Only the configurations of  $v$  have been plotted for clarity. It should be stated that the results of postbuckling amplitudes shown in Figure 12 have been normalized for the purpose of intuitive comparison. From Figure 12 (left and right), it is clearly seen that, with the increase of magnetic field parameter, the postbuckling configuration evolves from the first-mode shape to a hybrid shapes of both first and second modes.

Strictly speaking, the displacement  $v$  (or  $w$ ) would contain contributions of all the modes according to the basic idea of the Galerkin's approach. However, the contributions of higher-order modes are not pronounced, as demonstrated in Figure 13, in which the proportions of the lowest four modes for determining the displacement of  $v$  have been quantitatively shown. It is observed that the microwire's displacement is mainly associated with the first and second modes. With the increase of magnetic field parameter, the first-mode contribution becomes smaller while the second-mode contribution becomes larger.

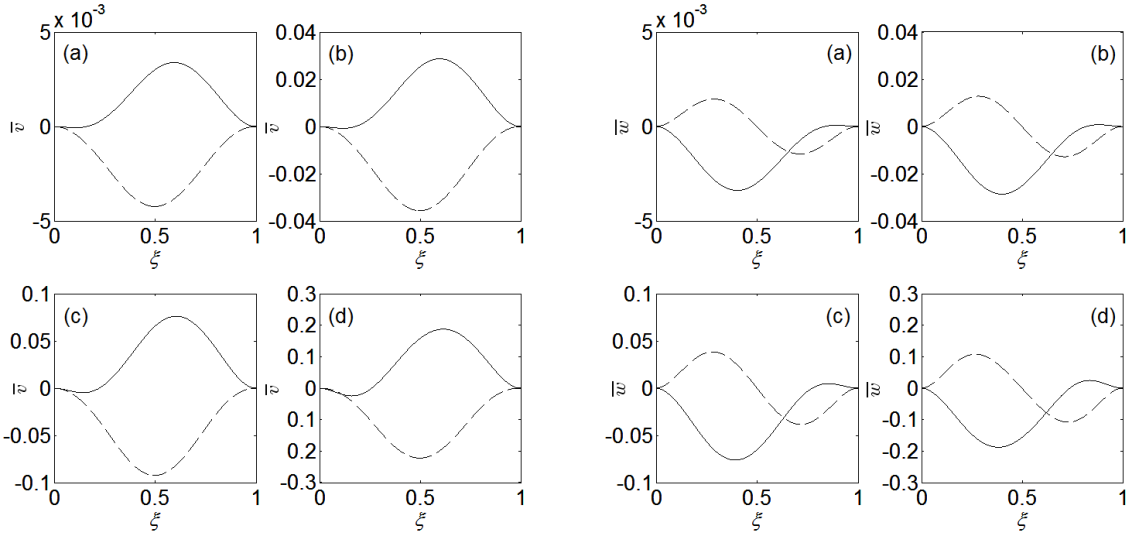


**Figure 10.** The evolution of postbuckling shapes of clamped-clamped microwires with increasing magnetic field parameter for  $\mu = 0.1$ ,  $p = 0$ , and  $\alpha = 800$ : (a)  $\alpha^{3/2} f_I = 435$ , (b)  $\alpha^{3/2} f_I = 495$ , (c)  $\alpha^{3/2} f_I = 900$ , (d)  $\alpha^{3/2} f_I = 3300$ . Solid lines indicate results where initial conditions were from (38), and dashed lines indicate results where initial conditions were from (39).

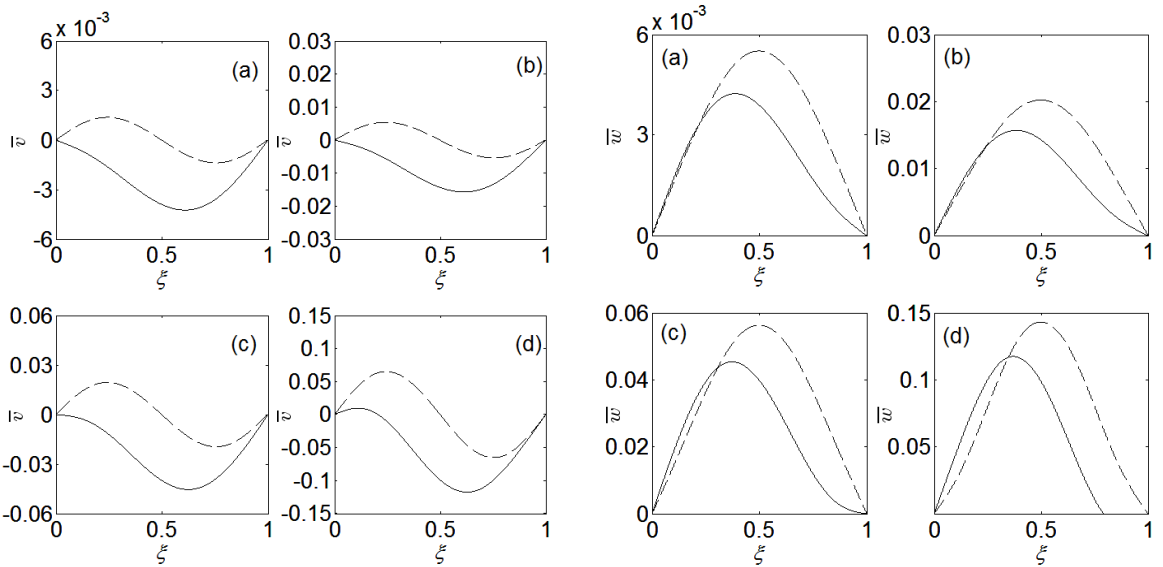


**Figure 11.** The evolution of postbuckling shapes of pinned-pinned microwires with increasing magnetic field parameter for  $\mu = 0.1$ ,  $p = 0$ , and  $\alpha = 800$ : (a)  $\alpha^{3/2} f_I = 158$ , (b)  $\alpha^{3/2} f_I = 176$ , (c)  $\alpha^{3/2} f_I = 308$ , (d)  $\alpha^{3/2} f_I = 1155$ ; Solid lines indicate results where initial conditions were from (38), and dashed lines indicate results where initial conditions were from (39).

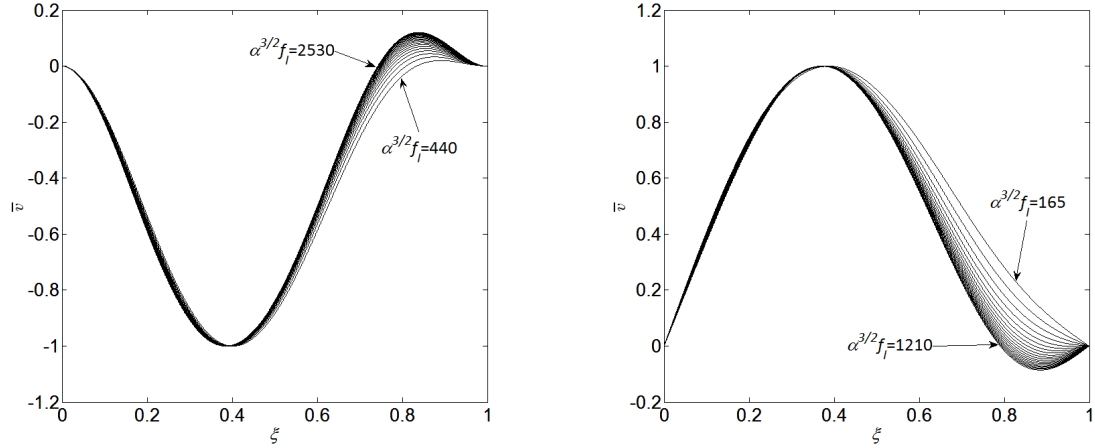


**Figure 12.** The effect of magnetic field parameter on the postbuckling shapes of  $v$  for  $\mu = 0.1$ ,  $p = 0$ , and  $\alpha = 800$ : clamped-clamped boundary conditions (left) and pinned-pinned boundary conditions (right).

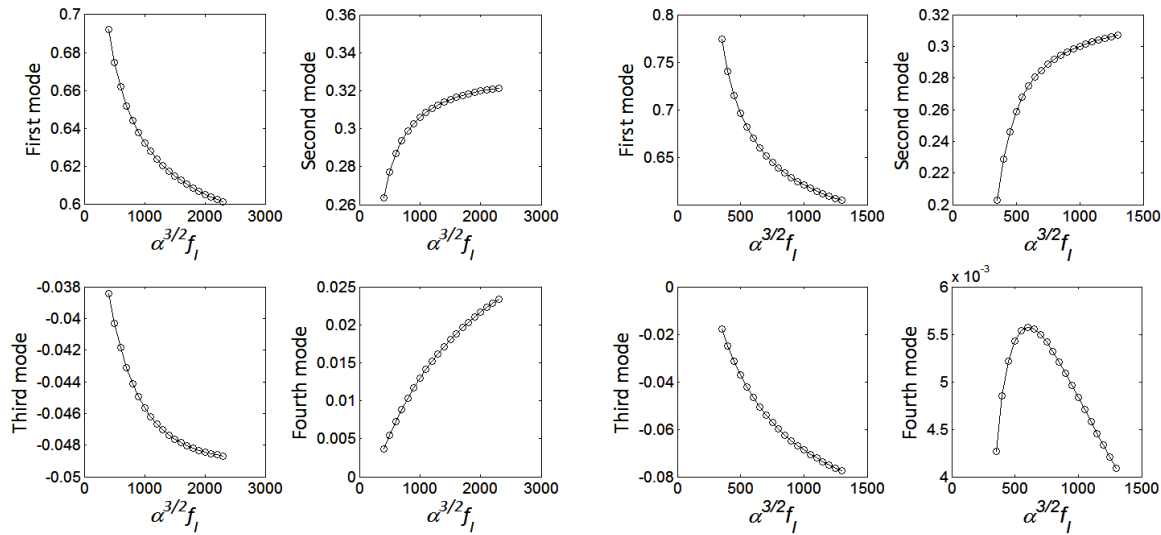


**Figure 13.** The proportions of the lowest four modes for various magnetic field parameters and  $\mu = 0.1$ ,  $p = 0$ , and  $\alpha = 800$ : clamped-clamped boundary conditions (left) and pinned-pinned boundary conditions (right).

**5.4. Effect of material length scale parameter on the stability boundaries.** The stability problem of a slender beam has been investigated by many researchers. In particular, the exact solution of postbuckling configurations of beams has been obtained by Nayfeh and his coworkers [Nayfeh and Emam 2008]. In this section, the stability boundaries of the CCMW under both axial compression and magnetic force are studied, for various values of dimensionless material length scale parameter  $\mu$ , to show the effect of  $\mu$  on the buckling behaviors of the microwire. Typical results with  $\alpha = 800$  are shown in Figure 14



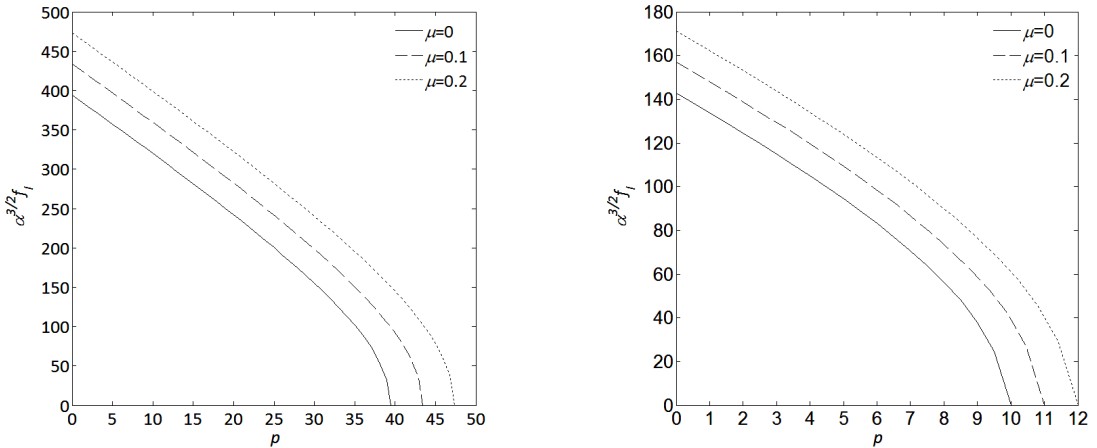


**Figure 14.** The stability boundaries for  $\alpha = 800$  and  $\mu = 0, 0.1$ , and  $0.2$  for clamped-clamped and (left) and pinned-pinned boundary conditions (right).

and Figure 15, for both clamped-clamped and pinned-pinned boundary conditions. The dimensionless material length scale parameter is chosen to be  $\mu = 0, 0.1$ , and  $0.2$  for calculations.

The results given in Figure 14 show the stability boundaries for  $\mu = 0, 0.1$ , and  $0.2$ . From Figure 14, it is noted that the critical magnetic field parameter is  $\alpha^{3/2} f_{lc} \approx 394.3$  for  $p = 0$  and  $\mu = 0$ , which is in accordance with the linear result of Wang et al. [2015] for microwires with clamped-clamped ends. It is obviously seen that the material length scale parameter can stabilize the microwire system while both the magnetic field parameter and axial compression would destabilize the microwire. When the magnetic field parameter and axial compression are small and locate below the stability boundary, the microwire is stable. If, however, the magnetic field parameter and axial compression are large and locate beyond the stability boundary, the microwire is buckled. Utilizing the critical buckling curves shown in Figure 14, an expected critical value of magnetic field parameter may be achieved by choosing a suitable compressive load as a trigger of automatic devices.

Based on the nonlinear governing equations of (26), the maximum amplitudes of lateral displacements ( $\max[\sqrt{\bar{v}(\xi, \tau)^2 + \bar{w}(\xi, \tau)^2}]$ ) are plotted in Figure 15. It is observed that the material length scale can decrease the buckling amplitudes of the microwire, again, indicating that the material length scale parameter plays a stabilizing effect on the microwire system.

**5.5. Effect of axial compression on the postbuckling configurations.** The effect of axial compression on the postbuckling configurations of the microwire can be seen in Figure 16, where the parameters were chosen as  $\mu = 0.1$ ,  $\alpha^{3/2} f_l = 1000$ , and  $\alpha = 800$ . The initial conditions defined by (38) were used for calculations. An interesting feature of Figure 16 is that the axial compression does not affect the postbuckling shapes at all, although it does affect the postbuckling amplitudes of the microwire. This implies that the main role of an axial compression is to promote the occurrence of buckling instability and change the postbuckling amplitude of the microwire. Thus, even if the axial compression is sufficiently large, the postbuckling configuration (shape) is still dominated by the first-order mode or the second-order mode. In fact, higher modes can only slightly affect the postbuckling configuration of the microwire.

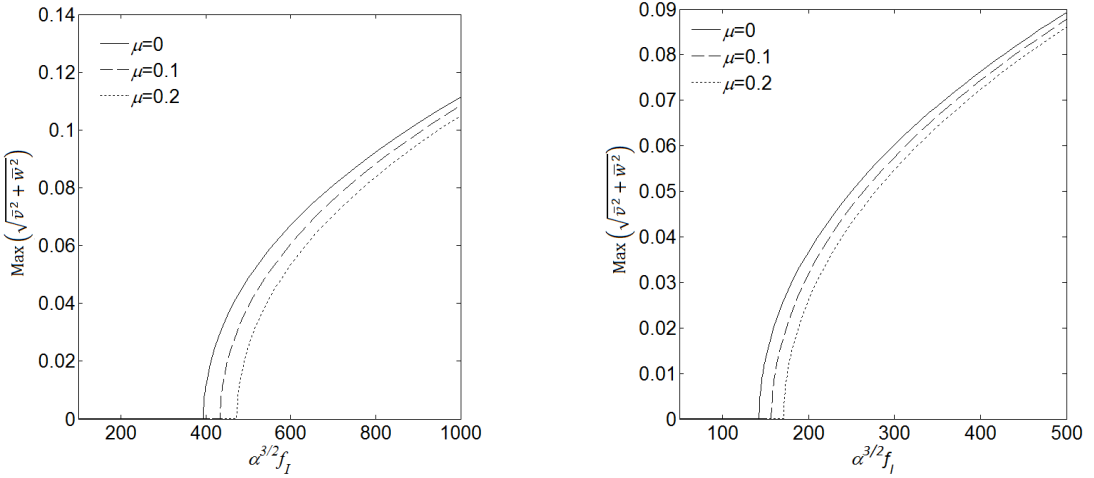


**Figure 15.** The maximum amplitude of lateral displacements as a function of the dimensionless magnetic field parameter for  $\alpha = 800$ ,  $p = 0$  and three different values of  $\mu$  for clamped-clamped and (left) and pinned-pinned boundary conditions (right).

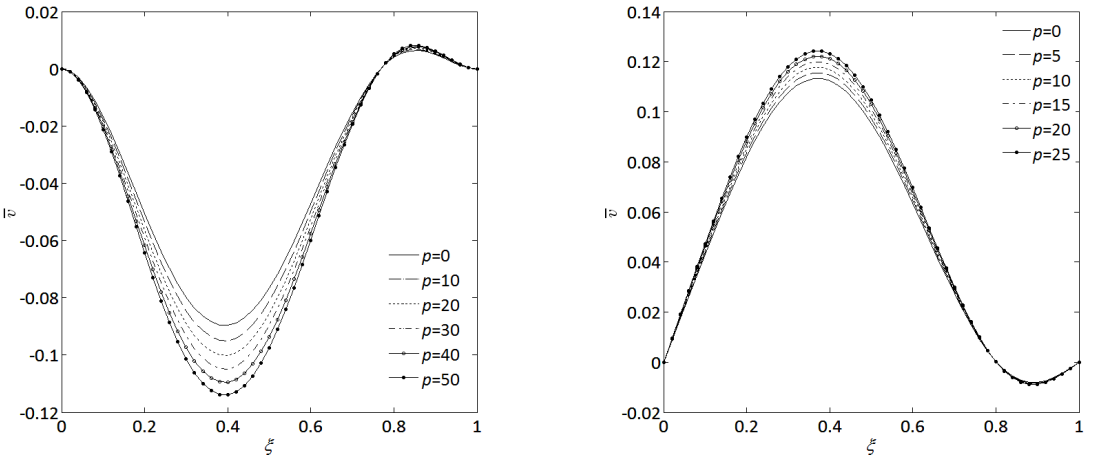


**Figure 16.** The evolution of postbuckling configurations of the microwire with increasing axial compression for  $\mu = 0.1$ ,  $\alpha = 800$ , and  $\alpha^{3/2} f_I = 1000$ : with clamped-clamped boundary conditions (left), and with pinned-pinned boundary conditions; all results were obtained using initial conditions of (38) (right).

Before leaving Section 5, it should be mentioned that the stability and postbuckling response of the microwire were not analyzed from the point of view of energy, although the governing equations were derived from Hamilton's principle. In the above analysis, the postbuckling responses and critical loads were evaluated by numerically solving (26). The connection with energy of the system in the pre- and post-buckling responses may be another interesting topic for the system of current-carrying microwires. This needs more extensive analysis in the future.

## 6. Conclusions

This paper studies the stability and nonplanar postbuckling of a current-carrying microwire subjected to a longitudinal magnetic field, by taking into account the geometric nonlinearities caused by the axial elongation of the microwire's centerline. Based on the Euler–Bernoulli beam assumptions, the modified couple stress theory and Hamilton's principle, the dimensionless version of nonplanar nonlinear equations of the microwire is derived. Using the Galerkin's approach and a fourth-order Runge–Kutta method, numerical results for both clamped-clamped and pinned-pinned boundary conditions are obtained. The effects of several dimensionless parameters associated with slenderness ratio, magnetic field, compressive load, and material length scale on the nonplanar buckling and postbuckling configurations are analyzed. Among others, some major conclusions are summarized as follows:

The slenderness ratio parameter  $\alpha$  has an obvious effect on the stability and the postbuckling amplitude of the microwire. The most interesting result obtained is that the nonplanar postbuckling shapes of the microwire under a longitudinal magnetic field may change when the initial conditions were varied, indicating that the nontrivial equilibria are sensitive to the initial conditions used for calculations. The dependence of postbuckling shapes on initial conditions makes it difficult to accurately determine the final postbuckling configurations of the microwires in practice. It is also expected that such high sensitivity of postbuckling configurations to initial conditions can be validated experimentally in the future. If such sensitivity is physically true, then how to minimize or control such a sensitivity is another interesting topic. In addition, one may also envision that some other methods such as a stochastic approach, or perhaps a statistical method can help understand such a sensitivity further.

The influence of magnetic field parameter on the postbuckling shapes is found to be remarkable in many cases. With the increase of magnetic field parameter, the postbuckling configurations are mostly associated with the first- and second-mode components, and the proportion of the second-mode component becomes larger while the proportion of the first-mode component decreases. In all cases, the proportion of higher-order modes (e.g., third or fourth modes) is low and may be neglected.

The effect of material length scale parameter on the stability and postbuckling amplitude of the microwire may be foreseen using one's experience. With the increase of dimensionless material length scale parameter, the microwire becomes more stable. For a buckled microwire, the postbuckling amplitude would decrease with increasing material length scale parameter.

Finally, it is found that the axial compressive load has an obvious effect on the postbuckling amplitude while it does not affect the postbuckling shape of the microwire. Moreover, the presence of an axial compression may reduce the threshold value of the magnetic field parameter for buckling instability.

## Acknowledgment

This work is supported by the National Natural Science Foundation of China (No. 11572133).

## References

- [Arani et al. 2015] A. G. Arani, P. Dashti, S. Amir, and M. Yousefi, "Nonlinear vibration of coupled nano- and microstructures conveying fluid based on Timoshenko beam model under two-dimensional magnetic field", *Acta Mech.* **226**:8 (2015), 2729–2760.

- [Atashbar and Singamaneni 2005] M. Z. Atashbar and S. Singamaneni, “Room temperature gas sensor based on metallic nanowires”, *Sens. Actuator B Chem.* **111-112** (2005), 13–21.
- [Chang 2016] T.-P. Chang, “Nonlinear free vibration analysis of nanobeams under magnetic field based on nonlocal elasticity theory”, *J. Vibroeng.* **18**:3 (2016), 1912–1919.
- [Chang and Yeh 2014] T.-P. Chang and Q.-J. Yeh, “Nonlinear free vibration of nanobeams subjected to magnetic field based on nonlocal elasticity theory”, in *International Conference of Scientific Computing '14*, edited by H. R. Arabnia et al., 2014.
- [Dai et al. 2015] H. L. Dai, Y. K. Wang, and L. Wang, “Nonlinear dynamics of cantilevered microbeams based on modified couple stress theory”, *Int. J. Eng. Sci.* **94** (2015), 103–112.
- [Dehrouyeh-Semnani et al. 2015] A. M. Dehrouyeh-Semnani, M. Dehrouyeh, M. Torabi-Kafshgari, and M. Nikkhah-Bahrami, “An investigation into size-dependent vibration damping characteristics of functionally graded viscoelastically damped sandwich microbeams”, *Int. J. Eng. Sci.* **96** (2015), 68–85.
- [Ebrahimi and Barati 2016] F. Ebrahimi and M. R. Barati, “Dynamic modeling of a thermo-piezo-electrically actuated nanosize beam subjected to a magnetic field”, *Appl. Phys. A Mater. Sci. Process.* **122** (2016), 451.
- [Ebrahimi and Barati 2017a] F. Ebrahimi and M. R. Barati, “Flexural wave propagation analysis of embedded S-FGM nanobeams under longitudinal magnetic field based on nonlocal strain gradient theory”, *AJSE* **42**:5 (2017), 1715–1726.
- [Ebrahimi and Barati 2017b] F. Ebrahimi and M. R. Barati, “Flexural wave propagation analysis of embedded S-FGM nanobeams under longitudinal magnetic field based on nonlocal strain gradient theory”, *AJSE* **42**:5 (2017), 1715–1726.
- [Fleck et al. 1994] N. A. Fleck, G. M. Muller, M. F. Ashby, and J. W. Hutchinson, “Strain gradient plasticity: theory and experiment”, *Acta Metall. Mater.* **24**:2 (1994), 475–487.
- [He and Lilley 2008] J. He and C. M. Lilley, “Surface stress effect on bending resonance of nanowires with different boundary conditions”, *Appl. Phys. Lett.* **93** (2008), 263108.
- [Kahrobaian et al. 2011] M. H. Kahrobaian, M. Asghari, M. Rahaeifard, and M. T. Ahmadian, “A nonlinear strain gradient beam formulation”, *Int. J. Eng. Sci.* **49**:11 (2011), 1256–1267.
- [Kiani 2014a] K. Kiani, “Forced vibrations of a current-carrying nanowire in a longitudinal magnetic field accounting for both surface energy and size effects”, *Physica E* **63** (2014), 27–35.
- [Kiani 2014b] K. Kiani, “Surface effect on free transverse vibrations and dynamic instability of current-carrying nanowires in the presence of a longitudinal magnetic field”, *Phys. Lett. A* **378**:26-27 (2014), 1834–1840.
- [Kiani 2014c] K. Kiani, “Vibration and instability of a single-walled carbon nanotube in a three-dimensional magnetic field”, *J. Phys. Chem. Solids* **75**:1 (2014), 15–22.
- [Kiani 2015a] K. Kiani, “Axial buckling analysis of a slender current-carrying nanowire acted upon by a magnetic field using the surface energy approach”, *J. Phys. D Appl. Phys.* **48**:24 (2015), 245302.
- [Kiani 2015b] K. Kiani, “Vibrations and instability of pretensioned current-carrying nanowires acted upon by a suddenly applied three-dimensional magnetic field”, *Mater. Chem. Phys* **162** (2015), 531–541.
- [Kiani 2016] K. Kiani, “Column buckling of doubly parallel slender nanowires carrying electric current acted upon by a magnetic field”, *J. Phys. Chem. Solids* **95** (2016), 89–97.
- [Lee et al. 2008] J.-Y. Lee, S. T. Connor, Y. Cui, and P. Peumans, “Solution-processed metal nanowire mesh transparent electrodes”, *Nano Lett.* **8**:2 (2008), 689–692.
- [Lee et al. 2013] J.-H. Lee, H.-S. Shin, Y.-J. Noh, S.-I. Na, and H.-K. Kim, “Brush painting of transparent PEDOT/Ag nanowire/PEDOT multilayer electrodes for flexible organic solar cells”, *Sol. Energy Mater. Sol. Cells* **114** (2013), 15–23.
- [Li et al. 2007] Q. Li, S.-M. Koo, M. D. Edelstein, J. S. Suehle, and C. A. Richter, “Silicon nanowire electromechanical switches for logic device application”, *Nanotechnology* **18**:31 (2007), 315202.
- [Luo et al. 2006] L. Luo, Y. Zhang, S. S. Mao, and L. Lin, “Fabrication and characterization of ZnO nanowires based UV photodiodes”, *Sens. Actuators A Phys.* **127**:2 (2006), 201–206.
- [McFarland and Colton 2005] A. W. McFarland and J. S. Colton, “Role of material microstructure in plate stiffness with relevance to microcantilever sensors”, *J. Micromech. Microeng.* **15**:5 (2005), 1060.
- [Mindlin and Tiersten 1962] R. D. Mindlin and H. F. Tiersten, “Effects of couple-stresses in linear elasticity”, *Arch. Ration. Mech. Anal.* **11**:1 (1962), 415–448.

- [Mohammadabadi et al. 2015] M. Mohammadabadi, A. R. Daneshmehr, and M. Homayounfar, “Size-dependent thermal buckling analysis of micro composite laminated beams using modified couple stress theory”, *Int. J. Eng. Sci.* **92** (2015), 47–62.
- [Mojahedi and Rahaeifard 2016] M. Mojahedi and M. Rahaeifard, “A size-dependent model for coupled 3D deformations of nonlinear microbridges”, *Int. J. Eng. Sci.* **100** (2016), 171–182.
- [Narendar et al. 2012] S. Narendar, S. S. Gupta, and S. Gopalakrishnan, “Wave propagation in single-walled carbon nanotube under longitudinal magnetic field using nonlocal Euler–Bernoulli beam theory”, *Appl. Math. Model.* **36**:9 (2012), 4529–4538.
- [Nayfeh and Emam 2008] A. H. Nayfeh and S. A. Emam, “Exact solution and stability of postbuckling configurations of beams”, *Nonlinear Dyn.* **54**:4 (2008), 395–408.
- [Pauzauskie and Yang 2006] P. J. Pauzauskie and P. Yang, “Nanowire photonics”, *Mater. Today* **9**:10 (2006), 36–45.
- [Singh 2009] M. R. Singh, “Photonic transistors made from metallic photonic quantum wires”, *Microelectron. J.* **40** (2009), 749–752.
- [Stölken and Evans 1998] J. S. Stölken and A. G. Evans, “A microbend test method for measuring the plasticity length scale”, *Acta Mater.* **46**:1 (1998), 5109–5115.
- [Sun et al. 2017] X.-P. Sun, Y.-Z. Hong, H.-L. Dai, and L. Wang, “Nonlinear frequency analysis of buckled nanobeams in the presence of longitudinal magnetic field”, *Acta Mech. Solida Sin.* **30**:5 (2017), 465–473.
- [Tao et al. 2010] R.-H. Tao, J.-M. Wu, H.-X. Xue, X.-M. Song, X. Pan, X.-Q. Fang, X.-D. Fang, and S.-Y. Dai, “A novel approach to titania nanowire arrays as photoanodes of back-illuminated dye-sensitized solar cells”, *J. Power Sources* **195**:9 (2010), 2989–2995.
- [Tsiatas 2009] G. C. Tsiatas, “A new Kirchhoff plate model based on a modified couple stress theory”, *Int. J. Solids Struct.* **46**:13 (2009), 2757–2764.
- [Wang 2009] L. Wang, “Vibration and instability analysis of tubular nano- and micro-beams conveying fluid using nonlocal elastic theory”, *Physica E* **41**:10 (2009), 1835–1840.
- [Wang et al. 2006] C. M. Wang, Y. Y. Zhang, S. S. Ramesh, and S. Kitipornchai, “Buckling analysis of micro- and nano-rods/tubes based on nonlocal Timoshenko beam theory”, *J. Phys. D Appl. Phys.* **39**:17 (2006), 3904.
- [Wang et al. 2015] L. Wang, W.-B. Liu, and H.-L. Dai, “Dynamics and instability of current-carrying microbeams in a longitudinal magnetic field”, *Physica E* **66** (2015), 87–92.
- [Wang et al. 2016] L. Wang, Y. Hong, H. Dai, and Q. Ni, “Natural frequency and stability tuning of cantilevered CNTs conveying fluid in magnetic field”, *Acta Mech. Solida Sin.* **29**:6 (2016), 567–576.
- [Yang et al. 2002] F. Yang, A. C. M. Chong, D. C. C. Lam, and P. Tong, “Couple stress based strain gradient theory for elasticity”, *Int. J. Solids Struct.* **39**:10 (2002), 2731–2743.

Received 22 Feb 2018. Revised 24 Jul 2018. Accepted 30 Jul 2018.

YUANZHUO HONG: [hyzlink@qq.com](mailto:hyzlink@qq.com)

Department of Mechanics, Huazhong University of Science and Technology, Wuhan, China

and

Hubei Key Laboratory for Engineering Structural Analysis and Safety Assessment, Wuhan, China

LIN WANG: [wanglindds@hust.edu.cn](mailto:wanglindds@hust.edu.cn)

Department of Mechanics, Huazhong University of Science and Technology, Wuhan, China

and

Hubei Key Laboratory for Engineering Structural Analysis and Safety Assessment, Wuhan, China

HU-LIANG DAI: [daihulianglx@hust.edu.cn](mailto:daihulianglx@hust.edu.cn)

Department of Mechanics, Huazhong University of Science and Technology, Wuhan, China

and

Hubei Key Laboratory for Engineering Structural Analysis and Safety Assessment, Wuhan, China



# THREE-DIMENSIONAL TREFFTZ COMPUTATIONAL GRAINS FOR THE MICROMECHANICAL MODELING OF HETEROGENEOUS MEDIA WITH COATED SPHERICAL INCLUSIONS

GUANNAN WANG, LEITING DONG, JUNBO WANG AND SATYA N. ATLURI

Three-dimensional computational grains based on the Trefftz method (TCGs) are developed to directly model the micromechanical behavior of heterogeneous materials with coated spherical inclusions. Each TCG is polyhedral in geometry and contains three phases: an inclusion, the surrounded coating (or interphase) and the matrix. By satisfying the 3D Navier's equations exactly, the internal displacement and stress fields within the TCGs are expressed in terms of the Papkovitch–Neuber (P–N) solutions, in which spherical harmonics are employed to further express the P–N potentials. Further, the Wachspres coordinates are adopted to represent the polyhedral-surface displacements that are considered as nodal shape functions, in order to enforce the compatibility of deformations between two TCGs. Two techniques are developed to derive the local stiffness matrix of the TCGs: one is directly using the multi-field boundary variational principle (MFBVP) while the other is first applying the collocation technique for the continuity conditions within and among the grains and then employing a primal-field boundary variational principle (PFBVP). The local stress distributions at the interfaces between the 3 phases, as well as the effective homogenized material properties generated by the direct micromechanical simulations using the TCGs, are compared to other available analytical and numerical results in the literature, and good agreement is always obtained. The material and geometrical parameters of the coatings/interphases are varied to test their influence on the homogenized and localized responses of the heterogeneous media. Finally, the periodic boundary conditions are applied to the representative volume elements (RVEs) that contain one or more TCGs to model the heterogeneous materials directly.

## 1. Introduction

Heterogeneous materials reinforced with spherical-shaped inclusions have been widely applied in the aviation industry and the automobile industry due to their higher property-to-volume ratios relative to the monoclinic materials. In recent years, the effect of the interfaces between the inclusions and the matrices in particle-filled composites has received increasing attention because of the need to tailor the composite materials to meet specific requirements. Thus a good understanding of interfacial effects in composites, and establishing effective and highly efficient numerical models, when coatings/interfaces are considered, will be beneficial for the design and development of coated particulate composites.

Various classical micromechanical models were generalized to study the coated particulate composites. For example, the initial composite spherical assemblage (CSA) model proposed by Hashin [1962] was generalized to the three-phase domain to study the elastic moduli of coated particulate composites [Qiu

Leiting Dong is the corresponding author.

**Keywords:** Trefftz computational grains, heterogeneous materials, coated spherical inclusions, Papkovitch–Neuber solutions, spherical harmonics, variational principles, collocation technique, periodic boundary conditions.



and Weng 1991; Herve and Zaoui 1993] or mineral materials [Nguyen et al. 2011]. The (generalized) self-consistent scheme (GSCS) was also employed to study the multiphase heterogeneous materials [Cherkaoui et al. 1994; Quang and He 2007]; The Mori–Tanaka (M–T) model was modified to calculate the properties of composites reinforced with uniformly distributed particles with interphases [Jiang et al. 2009]. The classical semi-analytical homogenization techniques largely provide the currently available tools, and even provide explicit expressions in the analysis of coated particulate composites, and thus have gained wide acceptance within the communities of mechanics and materials. However, most of these models are based on the assumption of the mean-field homogenization which only predicts accurate effective properties but cannot effectively recover the local inter-phase stress distributions, which are essentially important in the prediction of the possible failures and damages in the lifetime of heterogeneous materials.

Compared to the classical homogenization techniques, the simple finite-element (FE) methods can overcome the disadvantages mentioned above. The finite element method [Marur 2004; Liu et al. 2005; Tsui et al. 2006; Zhang et al. 2007; Jiang et al. 2008] has been widely used in investigating various aspects of particulate composites with coatings/interfaces, including computing the homogenized moduli, local stress concentrations, damage, and strengthening. However, the disadvantages of these simple finite elements are also well-known, such as unsatisfactory performance in problems which involve constraints (shear/membrane/incompressibility locking), low convergence rates for problems which are of singular nature (stress concentration problems and fracture mechanics problems), difficulty to satisfy higher-order continuity requirements (plates and shells), sensitivity to mesh distortion, etc. In order to capture the stress field accurately, the usual finite element methods involve extensive and laborious mesh generation, and very fine meshes involving large computational costs. Taking Figure 1, left, as an example [Chen et al. 2016; 2017], a total of 3952 hexahedron linear elements are adopted to discretize a single grain with an inclusion. If an RVE of a heterogeneous composite has to be modeled, with say a hundred or thousand grains, to not only generate effective properties but also capture the stress concentrations at the interfaces of inhomogeneities, the usual finite element method becomes almost impossible to be applied without using very high-performance super computers. Some other numerical techniques were also proposed to improve the stability and accuracy of the FE methods in micromechanical modeling of complex microstructures, for instance, fast Fourier transforms (FFT) [Moulinec and Suquet 1998; Michel et al. 2000], extended finite element method (XFEM) [Yvonnet et al. 2011; Zhu et al. 2011], etc.

In order to effectively reduce the computational efforts without sacrificing the accuracy, the concept of Trefftz computational grains (TCGs) was developed by Dong and Atluri [2012c; 2012b; 2012a], and Bishay and Atluri [2013; 2014; 2015; Bishay et al. 2014] used radial basis functions as well as Trefftz formulation based computational grains for multi-functional composites. Instead of applying the simple finite element discretization of the microstructures, an arbitrarily shaped TCG composed of fiber/coating/matrix constituents is treated as a “super” element (Figure 1, right), whose internal displacement and traction fields are represented by the Trefftz solutions. Based on the Trefftz concept [Qin 2005] of using the complete analytical solutions which satisfy the Navier’s equations of elasticity, the development of the highly accurate and efficient two- and three-dimensional polyhedral computational grains was achieved. It should be noted that the idea of the VCFEM was initially proposed to investigate the particle reinforced composites [Ghosh et al. 1995; Moorthy and Ghosh 1998] in the 2D cases. However, the VCFEM developed in [Ghosh et al. 1995; Moorthy and Ghosh 1998] was based on the hybrid-stress finite element method, with both domain and boundary integrations for each Voronoi



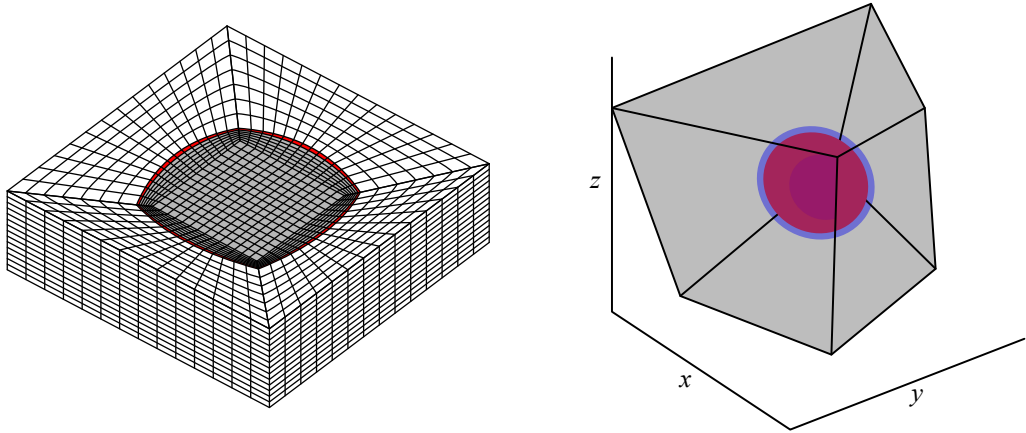


**Figure 1.** Left: the usual FE mesh discretization of spherical particulate composites [Chen et al. 2016; 2017]. Right: a single polyhedral Trefftz computational grain (TCG) with three phases.

element, and adopted incomplete stress functions (in the hybrid stress finite element method), leading to the inefficient computational efforts and highly inaccurate internal and interfacial stress distributions. The new version of the TCGs [Dong and Atluri 2012a; 2012b; 2012c] differ from the hybrid stress VCFEM in [Ghosh et al. 1995; Moorthy and Ghosh 1998] in the following ways 1) a complete Trefftz trial displacement solution is assumed in the TCG by satisfying both the equilibrium and compatibility conditions a priori; 2) only boundary integrals are involved in the newly developed TCG, ensuring its better accuracy and efficiency in the micromechanical computations. All of these characteristics prove that the Trefftz computational grains are reliable tools in generating both effective properties as well as the inter-phase local stress field distributions in the micromechanics of heterogeneous materials.

Based on the framework established by Dong and Atluri [2012a; 2012b; 2012c], the Trefftz computational grains (TCGs) are generalized in this paper, for the micromechanical modeling of heterogeneous materials reinforced with coated particles (or particles with interphases). By avoiding the large-scale mesh discretization of a microstructure within the normal FE framework, each arbitrarily shaped TCG in the present situation is composed of a particulate inclusion, a coating/interphase and the surrounding matrix phase, Figure 1, right. The trial displacement solutions of each constituent are obtained by employing Papkovitch–Neuber (P–N) solutions [Lurie 2005], in which the P–N potentials are further represented by the spherical harmonics. Two approaches are then used to develop the local stiffness matrix of the TCGs: First, a multi-field boundary variational principle is proposed to enforce continuities between adjacent constituents and TCGs, as well as the external boundary conditions, if any; Second, the collocation technique [Dong and Atluri 2012b; 2012c; Wang et al. 2018] is applied to satisfy the interfacial continuity conditions, while a primal-field boundary variational principle is employed to satisfy the interphase continuities and the boundary conditions, a technique which we name as CPFVBP. Both approaches generate accurate predictions as compared to the currently available semi-analytical and numerical results. Finally, an easy implementation of periodic boundary conditions (PBCs) is achieved on the representative volume elements by surface-to-surface constraint scheme.

The remainder of the paper is organized as follows: [Section 2](#) solves the displacement fields in each constituent of a TCG in terms of the P–N solutions and develops the local stiffness matrix of the TCGs. [Section 3](#) validates the homogenized moduli and local inter-phase stress distributions through comparing with the CSA and detailed fine-mesh FE results. The influence of the coatings/interphases on the various properties of composites materials is thoroughly investigated in [Section 4](#). Finally, the effects of the periodic boundary conditions on the RVEs are studied in [Section 5](#). [Section 6](#) concludes this contribution.

## 2. Development of polyhedral Trefftz computational grains (TCGs) with coated spherical inclusions/voids

**2.1. Boundary displacement field for a polyhedral TCG.** For an arbitrarily polyhedral-shaped TCG in the 3D space, each surface is a polygon, [Figure 1](#), right. Constructing an inter-TCG compatible displacement on the boundary of the polyhedral element is not as simple as that for the 2D version. One way of doing this is to use barycentric coordinates as nodal shape functions on each polygonal face of the 3D TCGs.

Consider a polygonal face  $V_n$  with  $n$  nodes  $\mathbf{x}^1, \mathbf{x}^2, \dots, \mathbf{x}^n$ , within barycentric coordinates, denoted as  $\lambda_i$  ( $i = 1, 2, \dots, n$ ). The coordinates  $\lambda_i$  depend only on the position vector  $\mathbf{x}^i$ . To obtain a good performance of a TCG, we only consider barycentric coordinates that satisfy the following properties:

1. Being nonnegative:  $\lambda_i \geq 0$  in the polygon  $V_n$ .
2. Smoothness:  $\lambda_i$  is at least  $C^1$  continuous in the polygon  $V_n$ .
3. Linearity along each edge that composes the polygon  $V_n$ .
4. Linear completeness: For any linear function  $f(\mathbf{x})$ , the equation  $f(\mathbf{x}) = \sum_{i=1}^n f(\mathbf{x}^i) \lambda_i$  holds.
5. Partition of unity:  $\sum_{i=1}^n \lambda_i \equiv 1$ .
6. Dirac delta property:  $\lambda_i(\mathbf{x}^j) = \delta_{ij}$ .

Among the many barycentric coordinates that satisfy these conditions, Wachspress coordinate is the most simple and efficient [[Wachspress 1975](#)].

A point  $\mathbf{x} \in V_n$  within the polygon is determined in terms of two parameters:  $B_i$  as the area of the triangle with the vertices of  $\mathbf{x}^{i-1}$ ,  $\mathbf{x}^i$  and  $\mathbf{x}^{i+1}$ , and  $A_i(\mathbf{x})$  as the area of the triangle with vertices of  $\mathbf{x}$ ,  $\mathbf{x}^i$  and  $\mathbf{x}^{i+1}$ , [Figure 2](#). Thus, the Wachspress coordinate of the point  $\mathbf{x}$  can be written as

$$\lambda_i(\mathbf{x}) = \frac{w_i(\mathbf{x})}{\sum_{j=1}^n w_j(\mathbf{x})}, \quad (1)$$

wherein the weight function is defined as

$$w_i(\mathbf{x}) = \frac{B_i(\mathbf{x}^{i-1}, \mathbf{x}^i, \mathbf{x}^{i+1})}{A_{i-1}(\mathbf{x}^{i-1}, \mathbf{x}^i, \mathbf{x}) A_i(\mathbf{x}^i, \mathbf{x}^{i+1}, \mathbf{x})}. \quad (2)$$

The inter-TCG compatible displacement field is therefore expressed in terms of the nodal shape functions for the polygonal surface vertices and the nodal displacements in the Cartesian coordinates:

$$\tilde{u}_i(\mathbf{x}) = \sum_{k=1}^n \lambda_k(\mathbf{x}) u_i(\mathbf{x}^k) \quad \mathbf{x} \in V_n, V_n \subset \partial\Omega^e, \quad (3)$$

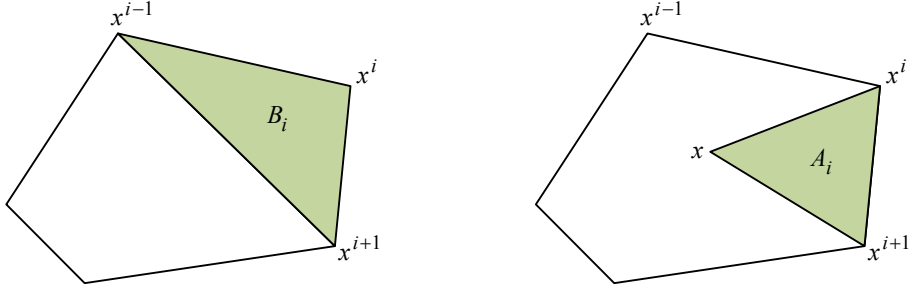


**Figure 2.** Definition of Wachspress coordinates on each surface of a polyhedron.

where  $\partial\Omega^e$  denotes the surface of each TCG.

**2.2. The governing equations of linear elasticity for each phase of the TCGs.** As shown in Figure 3, the solutions of the 3D linear elasticity for the matrix and inclusion phases should satisfy the equilibrium equations, strain-displacement compatibilities, as well as the constitutive relations in each element  $\Omega^e$ :

$$\sigma_{ij,j}^k + f_i^k = 0, \quad (4)$$

$$\varepsilon_{ij}^k = \frac{1}{2}(u_{i,j}^k + u_{j,i}^k), \quad (5)$$

$$\sigma_{ij}^k = \lambda^k \varepsilon_{mm}^k \delta_{ij} + 2\mu^k \varepsilon_{ij}^k, \quad (6)$$

where the superscript  $k = m, c, p$  denotes the matrix, the coating and the inclusion (particle) phases,  $u_i^k$ ,  $\varepsilon_{ij}^k$ ,  $\sigma_{ij}^k$  are the displacement, strain and stress components,  $f_i^k$  is the body force, which is neglected in this situation, and Here,  $\lambda^k$  and  $\mu^k$  are the Lamé constants of each phase.

At the interfaces between the constituents within each TCG, the displacement continuities and traction reciprocities can be written as

$$u_i^m = u_i^c \quad \text{at } \partial\Omega_c^e, \quad (7)$$

$$-n_j \sigma_{ij}^m + n_j \sigma_{ij}^c = 0 \quad \text{at } \partial\Omega_c^e, \quad (8)$$

$$u_i^c = u_i^p \quad \text{at } \partial\Omega_p^e, \quad (9)$$

$$-n_j \sigma_{ij}^c + n_j \sigma_{ij}^p = 0 \quad \text{at } \partial\Omega_p^e, \quad (10)$$

where  $\partial\Omega_c^e$  and  $\partial\Omega_p^e$  are the outer surfaces of the coating and inclusion phases, respectively. The external boundary conditions for each TCG can be written as

$$u_i^m = \bar{u}_i \quad \text{at } S_u^e, \quad (11)$$

$$n_j \sigma_{ij}^m = \bar{t}_i \quad \text{at } S_t^e, \quad (12)$$

$$(n_j \sigma_{ij}^m)^+ + (n_j \sigma_{ij}^m)^- = 0 \quad \text{at } \rho^e, \quad (13)$$

where  $S_u^e$ ,  $S_t^e$  and  $\rho^e$  are displacement, traction and other boundaries of the domain  $\Omega^e$ , respectively, and  $\partial\Omega^e = S_u^e \cup S_t^e \cup \rho^e$ .  $\bar{u}_i$ ,  $\bar{t}_i$  are the prescribed boundary displacement and traction components when they exist.

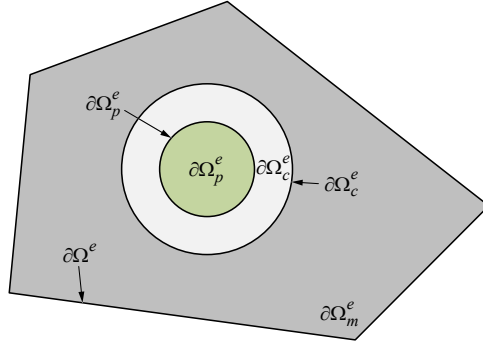


**Figure 3.** A polyhedral Trefftz computational grain and its nomenclature.

**2.3. Papkovitch–Neuber solutions as the trial internal displacement fields within each TCG.** Navier’s equation can be derived from (4)–(6):

$$(\lambda^k + \mu^k) u_{j,ji}^k + \mu^k \Delta u_i^k = 0. \quad (14)$$

Solving the displacement components directly from (14) is a rather difficult task. Papkovitch [1932] and Neuber [1934] suggested that the solutions can be represented in the forms of harmonic functions:

$$\mathbf{u}^k = \frac{4(1 - \nu^k) \mathbf{B}^k - \nabla(\mathbf{R} \cdot \mathbf{B}^k + B_0^k)}{2\mu^k}, \quad (15)$$

where  $B_0^k$  and  $\mathbf{B}_k = [B_1^k \ B_2^k \ B_3^k]^T$  are scalar and vector harmonic functions.  $\mathbf{R}$  is the position vector.  $\mu^k$  is the shear modulus of the  $k$ -th constituent.

The number of independent harmonic functions in (15) is more than the number of independent displacement components. Therefore, it is desired to keep only three of the four harmonic functions. Thus, by dropping  $B_0^k$  we have the following solution:

$$\mathbf{u}^k = \frac{4(1 - \nu^k) \mathbf{B}^k - \nabla \mathbf{R} \cdot \mathbf{B}^k}{2\mu^k}. \quad (16)$$

The general solution of (16) is complete for an infinite domain external to a closed surface. However, for a simply-connected domain, equation (16) is only complete when  $\nu \neq 0.25$ . M. G. Slobodiansky proved that, by expressing  $B_0^k$  as a specific function of  $\mathbf{B}^k$ , the derived general solution of (14) is complete for a simply-connected domain with any valid Poisson’s ratio:

$$\mathbf{u}^k = \frac{4(1 - \nu^k) \mathbf{B}^k + \mathbf{R} \cdot \nabla \mathbf{B}^k - \mathbf{R} \nabla \cdot \mathbf{B}^k}{2\mu^k}. \quad (17)$$

The harmonic vector  $\mathbf{B}$  needs to be further expressed using the special functions to define various domain surfaces. To accommodate the spherical inclusion and its coating, spherical harmonics are adopted and introduced in the next section.

**2.4. Spherical harmonics.** Consider a point with Cartesian coordinates  $x_1, x_2, x_3$  and the corresponding spherical coordinates  $q^1 = R, q^2 = \theta, q^3 = \varphi$  having the following relationship:

$$x_1 = R \sin \theta \cos \varphi, \quad x_2 = R \sin \theta \sin \varphi, \quad x_3 = R \cos \theta. \quad (18)$$

From (18), we have

$$\begin{aligned} \frac{\partial x_1}{\partial R} &= \sin \theta \cos \varphi, & \frac{\partial x_1}{\partial \theta} &= R \cos \theta \cos \varphi, & \frac{\partial x_1}{\partial \varphi} &= -R \sin \theta \sin \varphi, \\ \frac{\partial x_2}{\partial R} &= \sin \theta \sin \varphi, & \frac{\partial x_2}{\partial \theta} &= R \cos \theta \sin \varphi, & \frac{\partial x_2}{\partial \varphi} &= R \sin \theta \cos \varphi, \\ \frac{\partial x_3}{\partial R} &= \cos \theta, & \frac{\partial x_3}{\partial \theta} &= -R \sin \theta, & \frac{\partial x_3}{\partial \varphi} &= 0, \end{aligned} \quad (19)$$

and

$$\frac{\partial q^s}{\partial x_k} = \frac{1}{H_s^2} \frac{\partial x_k}{\partial q^s}, \quad \frac{\partial \mathbf{R}}{\partial q^r} \cdot \frac{\partial \mathbf{R}}{\partial q^s} = \delta_{rs} H_r H_s, \quad (20)$$

where

$$H_1 = H_R = 1, \quad H_2 = H_\theta = R, \quad H_3 = H_\varphi = R \sin \theta, \quad (21)$$

are called Lamé's coefficients. By defining a set of orthonormal base vectors of the spherical coordinate system:

$$\mathbf{g}_r = \frac{1}{H_r} \frac{\partial \mathbf{R}}{\partial q^r}, \quad (22)$$

we have

$$\begin{aligned} \frac{\partial \mathbf{g}_R}{\partial R} &= 0, & \frac{\partial \mathbf{g}_R}{\partial \theta} &= \mathbf{g}_\theta, & \frac{\partial \mathbf{g}_R}{\partial \varphi} &= \mathbf{g}_\varphi \sin \theta, \\ \frac{\partial \mathbf{g}_\theta}{\partial R} &= 0, & \frac{\partial \mathbf{g}_\theta}{\partial \theta} &= -\mathbf{g}_R, & \frac{\partial \mathbf{g}_\theta}{\partial \varphi} &= \mathbf{g}_\varphi \cos \theta, \\ \frac{\partial \mathbf{g}_\varphi}{\partial R} &= 0, & \frac{\partial \mathbf{g}_\varphi}{\partial \theta} &= 0, & \frac{\partial \mathbf{g}_\varphi}{\partial \varphi} &= -(\mathbf{g}_R \sin \theta + \mathbf{g}_\theta \cos \theta). \end{aligned} \quad (23)$$

Therefore, the Laplace operator of a scalar  $f$  has the following form:

$$\begin{aligned} \nabla^2 f &= \nabla \cdot \nabla f = \frac{1}{H_r} \mathbf{g}_r \frac{\partial}{\partial q_r} \cdot \frac{1}{H_s} \mathbf{g}_s \frac{\partial f}{\partial q_s} \\ &= \frac{1}{R} \left[ \frac{\partial}{\partial R} R^2 \frac{\partial f}{\partial R} + \frac{\partial}{\partial \xi} (1 - \xi^2) \frac{\partial f}{\partial \xi} + \frac{1}{1 - \xi^2} \frac{\partial f}{\partial \lambda^2} \right], \end{aligned} \quad (24)$$

where the new variable  $\xi = \cos \theta$  is introduced. By assuming that  $f = L(R) M(\xi) N(\varphi)$  and using  $k^2$  and  $n(n+1)$  as separating constants, it can be shown that  $L, M, N$  satisfy the following equations:

$$N''(\varphi) + k^2 N(\varphi) = 0, \quad (25)$$

$$[(1 - \xi^2) M'(\xi)]' + \left[ n(n+1) - \frac{k^2}{1 - \xi^2} \right] M(\xi) = 0, \quad (26)$$

$$[R^2 L'(R)]' - n(n+1) L(R) = 0. \quad (27)$$

Equation (25) leads to particular solutions  $\cos k\varphi$  and  $\sin k\varphi$  for a nonnegative integer  $k$ , because of the periodicity of  $N(\varphi)$ . Equation (26), which is clearly the associated Legendre's differential equation, leads to the associated Legendre's functions of the first and the second kinds, where only the associated Legendre's functions of the first kind are valid for constructing  $M(\xi)$ . Denoting them as  $P_n^k(\xi)$ , we have

$$P_n^k(\xi) = (-1)^k (1 - \xi^2)^{k/2} \frac{d^k}{d\xi^k} P_n(\xi), \quad P_n(\xi) = \frac{1}{2^{2n} n!} \left[ \frac{d^n}{d\xi^n} (\xi^2 - 1)^n \right]. \quad (28)$$

The product of  $M(\xi)N(\varphi)$  are called spherical surface harmonics, and can be normalized to be

$$\begin{aligned} Y_n^k(\theta, \varphi) &= \sqrt{\frac{2n+1}{4\pi} \frac{(n-k)!}{(n+k)!}} P_n^k(\cos(\theta)) e^{ik\varphi} \\ &= \sqrt{\frac{2n+1}{4\pi} \frac{(n-k)!}{(n+k)!}} P_n^k(\cos(\theta)) [\cos(k\varphi) + i \sin(k\varphi)] \\ &= Y C_n^k(\theta, \varphi) + i Y S_n^k(\theta, \varphi), \end{aligned} \quad (29)$$

such that

$$\int_0^{2\pi} \int_0^\pi Y_n^k(\theta, \varphi) \bar{Y}_{n'}^{k'}(\theta, \varphi) \sin \theta d\theta d\varphi = \delta_{kk'} \delta_{nn'}. \quad (30)$$

Finally, equation (27) leads to particular solutions  $R^n$  and  $R^{-(m+1)}$ . For different problems, different forms of  $L(R)$  should be used, which leads to different forms of spherical harmonics. For the internal problem of a sphere, only  $R^n$  is valid.  $f$  can be expanded as

$$f_p = \sum_{n=0}^{\infty} R^n \left\{ a_0^j Y C_0^0(\theta, \varphi) + \sum_{j=1}^n [a_n^j Y C_n^j(\theta, \varphi) + b_n^j Y S_n^j(\theta, \varphi)] \right\}. \quad (31)$$

For external problems in an infinite domain, only  $R^{-(m+1)}$  is valid,  $f$  can be expanded as

$$f_k = \sum_{m=0}^{\infty} R^{-(m+1)} \left\{ c_0^j Y C_0^0(\theta, \varphi) + \sum_{j=1}^m [c_m^j Y C_m^j(\theta, \varphi) + d_m^j Y S_m^j(\theta, \varphi)] \right\}, \quad (32)$$

where  $a_n^j$ ,  $b_n^j$ ,  $c_m^j$  and  $d_m^j$  are the unknown coefficients that can be solved through their implementations into the elasticity solutions and variational principles. The numbers of the unknown coefficients depend on the harmonic terms employed in the calculations, which are further dependent on the complexity of the problems.

As is mentioned in [Liu 2007a; 2007b], the above trial functions will lead to ill-conditioned systems of equations when being applied in the Trefftz method to numerically solve a boundary value problem. Thus, the characteristic lengths are introduced to scale the equations (31) and (32) [Dong and Atluri 2012b; 2012c; Liu 2007a; 2007b] to better condition the relevant matrices that arise in the Trefftz method.

For a specific domain of interest, two characteristic lengths  $R_{\text{non}}$  and  $R_{\text{sig}}$  are defined, which are respectively the maximum and minimum values of the radial distance  $R$  of points where boundary conditions are specified. Therefore,  $(R/R_{\text{non}})^n$  and  $(R_{\text{sig}}/R)^{-(m+1)}$  is confined between 0 and 1 for any positive

integers  $n$  and  $m$ . Harmonics are therefore scaled as

$$f_p = \sum_{n=0}^{\infty} \left( \frac{R}{R_{\text{non}}} \right)^n \left\{ a_0^0 Y C_0^0(\theta, \varphi) + \sum_{j=1}^n [a_n^j Y C_n^j(\theta, \varphi) + b_n^j Y S_n^j(\theta, \varphi)] \right\}, \quad (33)$$

$$f_k = \sum_{m=0}^{\infty} \left( \frac{R}{R_{\text{sig}}} \right)^{-(m+1)} \left\{ c_0^0 Y C_0^0(\theta, \varphi) + \sum_{j=1}^m [c_m^j Y C_m^j(\theta, \varphi) + d_m^j Y S_m^j(\theta, \varphi)] \right\}. \quad (34)$$

**2.5. Trefftz trial displacement fields.** For an element with an inclusion as well as the coating of spherical geometries, the displacement field in the inclusion can be derived by substituting the nonsingular harmonics, equation (33) into (17):

$$\mathbf{u}^p = [4(1 - \nu^p) \mathbf{B}^{pi} + \mathbf{R} \cdot \nabla \mathbf{B}^{pi} - \mathbf{R} \nabla \cdot \mathbf{B}^{pi}] / (2\mu^p). \quad (35)$$

The displacement fields in the matrix and the coating phases are the summation of  $\mathbf{u}^{ki}$  (the nonsingular part) and  $\mathbf{u}^{ke}$  (the singular part, with the singularity being located at the center of the inclusion).  $\mathbf{u}^{ki}$  can be derived by substituting (33) into (17), and  $\mathbf{u}^{ke}$  can be derived by substituting (34) into (16):

$$\begin{aligned} \mathbf{u}^k &= \mathbf{u}^{ki} + \mathbf{u}^{ke} \quad (k = m, c), \\ \mathbf{u}^{ki} &= [4(1 - \nu^k) \mathbf{B}^{ki} + \mathbf{R} \cdot \nabla \mathbf{B}^{ki} - \mathbf{R} \nabla \cdot \mathbf{B}^{ki}] / (2\mu^k), \\ \mathbf{u}^{ke} &= [4(1 - \nu^k) \mathbf{B}^{ke} - \nabla \mathbf{R} \cdot \mathbf{B}^{ke}] / (2\mu^k). \end{aligned} \quad (36)$$

A more detailed illustration is given in [Dong and Atluri 2012b]. The expressions of strains and stresses can be then calculated by using *Wolfram Mathematica 8.0*, and are too complicated to be explicitly presented here. To obtain the converged results in this presentation, we let  $n = 3$  for the nonsingular solution of the particulate phase, equation (35), and  $n = 4, m = 3$  for the elastic solutions of the coating and matrix phases, equation (36).

**2.6. TCGs through the multi-field boundary variational principle.** The four-field energy functional of the 3-phase Trefftz computational grains can be expressed for an elastic coated particulate reinforced heterogeneous media:

$$\begin{aligned} \pi(\tilde{u}_i^m, u_i^m, u_i^c, u_i^p) &= \sum_e \left\{ \int_{\partial\Omega^e + \partial\Omega_c^e} -\frac{1}{2} t_i^m u_i^m dS + \int_{\partial\Omega^e} t_i^m \tilde{u}_i^m dS + \int_{\partial\Omega_c^e} t_i^m u_i^c dS \right\} \\ &+ \sum_e \int_{\partial\Omega_c^e + \partial\Omega_p^e} \frac{1}{2} t_i^c u_i^c dS + \sum_e \left\{ \int_{\partial\Omega_p^e} -\frac{1}{2} t_i^p u_i^p dS + \int_{\partial\Omega_p^e} t_i^p u_i^c dS \right\} - \int_{S_i} \bar{t}_i \tilde{u}_i dS, \end{aligned} \quad (37)$$

where the matrix strain energy, coating strain energy, inclusion strain energy, as well as the work done by external force are included. A first variation of the functional in (37) yields the Euler–Lagrange equations expressed in (7)–(13).

By assuming the displacement and stress fields in the vector forms:

$$\tilde{\mathbf{u}}_m = \tilde{\mathbf{N}} \mathbf{q} \quad \text{at } \partial\Omega^e \quad (38)$$

$$\mathbf{u}_m = \mathbf{N}_m \boldsymbol{\alpha} \quad \text{in } \Omega_m^e \quad (39a)$$

$$\mathbf{t}_m = \mathbf{R}_m \boldsymbol{\alpha} \quad \text{at } \partial\Omega^e, \partial\Omega_c^e \quad (39b)$$

$$\mathbf{u}_c = \mathbf{N}_c \boldsymbol{\beta} \quad \text{in } \Omega_c^e \quad (40a)$$

$$\mathbf{t}_c = \mathbf{R}_c \boldsymbol{\beta} \quad \text{at } \partial\Omega_c^e, \partial\Omega_p^e \quad (40b)$$

$$\mathbf{u}_p = \mathbf{N}_p \boldsymbol{\gamma} \quad \text{in } \Omega_p^e \quad (41a)$$

$$\mathbf{t}_p = \mathbf{R}_p \boldsymbol{\gamma} \quad \text{at } \partial\Omega_p^e \quad (41b)$$

and substituting them into (37), the finite element equations can be deduced by making the first variation:

$$\delta \begin{Bmatrix} \mathbf{q} \\ \boldsymbol{\beta} \end{Bmatrix}^T \begin{bmatrix} \mathbf{G}_{\alpha q}^T \mathbf{H}_{\alpha\alpha}^{-1} \mathbf{G}_{\alpha q} & \mathbf{G}_{\alpha q}^T \mathbf{H}_{\alpha\alpha}^{-1} \mathbf{G}_{\alpha\beta} \\ \mathbf{G}_{\alpha\beta}^T \mathbf{H}_{\alpha\alpha}^{-1} \mathbf{G}_{\alpha q} & \mathbf{G}_{\alpha\beta}^T \mathbf{H}_{\alpha\alpha}^{-1} \mathbf{G}_{\alpha\beta} + \mathbf{H}_{\beta\beta} + \mathbf{G}_{\beta\gamma}^T \mathbf{H}_{\gamma\gamma}^{-1} \mathbf{G}_{\beta\gamma} \end{bmatrix} \begin{Bmatrix} \mathbf{q} \\ \boldsymbol{\beta} \end{Bmatrix} = \delta \begin{Bmatrix} \mathbf{q} \\ \boldsymbol{\beta} \end{Bmatrix}^T \begin{Bmatrix} \mathbf{Q} \\ \mathbf{0} \end{Bmatrix}, \quad (42)$$

where  $\boldsymbol{\alpha}$  and  $\boldsymbol{\gamma}$  are eliminated in the above equation and expressed in terms of  $\boldsymbol{\beta}$  and  $\mathbf{q}$ , and

$$\begin{aligned} \mathbf{H}_{\alpha\alpha} &= \int_{\partial\Omega^e + \partial\Omega_c^e} \mathbf{R}_m^T \mathbf{N}_m dS, \quad \mathbf{H}_{\beta\beta} = \int_{\partial\Omega_c^e + \partial\Omega_p^e} \mathbf{R}_c^T \mathbf{N}_c dS, \quad \mathbf{H}_{\gamma\gamma} = \int_{\partial\Omega_p^e} \mathbf{R}_p^T \mathbf{N}_p dS, \\ \mathbf{G}_{\alpha\beta} &= \int_{\partial\Omega_c^e} \mathbf{R}_m^T \mathbf{N}_c dS, \quad \mathbf{G}_{\alpha q} = \int_{\partial\Omega^e} \mathbf{R}_m^T \tilde{\mathbf{N}} dS, \quad \mathbf{G}_{\beta\gamma} = \int_{\partial\Omega_p^e} \mathbf{R}_c^T \mathbf{N}_p dS, \quad \mathbf{Q} = \int_{\partial\Omega^e} \tilde{\mathbf{N}}^T \bar{\mathbf{t}} dS. \end{aligned}$$

By defining  $\mathbf{k}_{qq} = \mathbf{G}_{\alpha q}^T \mathbf{H}_{\alpha\alpha}^{-1} \mathbf{G}_{\alpha q}$ ,  $\mathbf{k}_{q\beta} = \mathbf{G}_{\alpha q}^T \mathbf{H}_{\alpha\alpha}^{-1} \mathbf{G}_{\alpha\beta}$  and  $\mathbf{k}_{\beta\beta} = \mathbf{G}_{\alpha\beta}^T \mathbf{H}_{\alpha\alpha}^{-1} \mathbf{G}_{\alpha\beta} + \mathbf{H}_{\beta\beta} + \mathbf{G}_{\beta\gamma}^T \mathbf{H}_{\gamma\gamma}^{-1} \mathbf{G}_{\beta\gamma}$ , the local stiffness matrix of a TCG is

$$\mathbf{k}_{\text{local}} = \mathbf{k}_{qq} - \mathbf{k}_{q\beta} \mathbf{k}_{\beta\beta}^{-1} \mathbf{k}_{q\beta}^T, \quad (43)$$

with the vectors of unknown coefficients in terms of the nodal displacement field:

$$\begin{aligned} \boldsymbol{\alpha} &= \mathbf{H}_{\alpha\alpha}^{-1} (\mathbf{G}_{\alpha q} - \mathbf{G}_{\alpha\beta} \mathbf{k}_{\beta\beta}^{-1} \mathbf{k}_{q\beta}^T) \mathbf{q}, \\ \boldsymbol{\beta} &= -\mathbf{k}_{\beta\beta}^{-1} \mathbf{k}_{q\beta}^T \mathbf{q}, \\ \boldsymbol{\gamma} &= -\mathbf{H}_{\gamma\gamma}^{-1} \mathbf{G}_{\beta\gamma} \mathbf{k}_{\beta\beta}^{-1} \mathbf{k}_{q\beta}^T \mathbf{q}. \end{aligned} \quad (44)$$

It should be noted that the six rigid-body modes in the field expressions should be eliminated for the application of MFBVP but not for the CPFVBVP. By displaying the displacement and stress expressions in matrix forms, the following three modes only make contributions to the total resultant forces at the source point and should be taken out:

$$\mathbf{c}_0^0 = \{1 \ 0 \ 0\}^T, \quad \mathbf{c}_1^0 = \{0 \ 1 \ 0\}^T, \quad \mathbf{c}_2^0 = \{0 \ 0 \ 1\}^T, \quad (45)$$



while the following modes need to be eliminated because they only contribute to the total resultant moments at the source point:

$$\begin{aligned} c_1^0 &= \{1 \ 0 \ 0\}^T, & c_1^1 &= \{0 \ 0 \ \sqrt{2}\}^T, \\ c_1^0 &= \{0 \ 1 \ 0\}^T, & c_1^1 &= \{0 \ \sqrt{2} \ 0\}^T, \\ c_1^0 &= \{0 \ 1 \ 0\}^T, & d_1^1 &= \{-1 \ 0 \ 0\}^T. \end{aligned} \quad (46)$$

**2.7. TCGs through collocation and the primal-field boundary variational principle.** An alternative to the MFBVP is employing a collocation technique for the internal displacement continuity and traction reciprocity conditions between adjacent constituents and applying the primal field boundary variational principle for the inter-element conditions.

By using collocation technique, a certain number of collocation points are usually uniformly distributed along the interfaces of heterogeneities  $\partial\Omega_c^e$ ,  $\partial\Omega_p^e$  as well as the boundary of the elements  $\partial\Omega^e$ . The coordinates of the collocation points are denoted as follows:  $x_i^{mh} \in \partial\Omega^e$ ,  $h = 1, 2, \dots$ ;  $x_i^{ck} \in \partial\Omega_c^e$ ,  $k = 1, 2, \dots$ ; and  $x_i^{pl} \in \partial\Omega_p^e$ ,  $l = 1, 2, \dots$ .

For a TCG with a coated elastic inclusion, the conditions of displacement continuities and traction reciprocities are applied at the local collocation points of the interfaces between adjacent constituents:

$$\begin{aligned} u_i^m(x_j^{ck}, \alpha) &= u_i^c(x_j^{ck}, \beta), & x_j^{ck} &\in \partial\Omega_c^e, \\ wt_i^m(x_j^{ck}, \alpha) + wt_i^c(x_j^{ck}, \beta) &= 0, & x_j^{ck} &\in \partial\Omega_c^e, \end{aligned} \quad (47)$$

$$\begin{aligned} u_i^c(x_j^{pl}, \beta) &= u_i^p(x_j^{pl}, \gamma), & x_j^{pl} &\in \partial\Omega_p^e, \\ wt_i^c(x_j^{pl}, \beta) + wt_i^p(x_j^{pl}, \gamma) &= 0, & x_j^{pl} &\in \partial\Omega_p^e, \end{aligned} \quad (48)$$

as well as the relationship between internal displacements and nodal functions:

$$u_i^m(x_j^{mh}, \alpha) = \tilde{u}_i(x_j^{mh}, q) \quad x_j^{mh} \in \partial\Omega^e, \quad (49)$$

where the parameter “ $w$ ” is used to balance the displacement and traction equations, avoiding the effect of the material properties on the discrepancy of the magnitude. In this situation  $w = 1/(2\mu_c)$ .

From the above relations, a system of equations can be easily set up for the unknown coefficients of different phases:

$$A_{\alpha q}^e \alpha = B_{\alpha q}^e q, \quad A_{\alpha\beta}^e \alpha = B_{\alpha\beta}^e \beta, \quad A_{\beta\gamma}^e \beta = B_{\beta\gamma}^e \gamma, \quad (50)$$

which yield to a system of equations as following:

$$\begin{bmatrix} A_{\alpha\beta}^e & -B_{\alpha\beta}^e & \mathbf{0} \\ \mathbf{0} & A_{\beta\gamma}^e & -B_{\beta\gamma}^e \\ A_{\alpha q}^e & \mathbf{0} & \mathbf{0} \end{bmatrix} \begin{Bmatrix} \alpha \\ \beta \\ \gamma \end{Bmatrix} = \begin{bmatrix} \mathbf{0} \\ \mathbf{0} \\ B_{\alpha q}^{eT} \end{bmatrix}^T q. \quad (51)$$

	$E$ (GPa)	$\nu$
Al <sub>2</sub> O <sub>3</sub> Particle	390.0	0.24
SiC Coating	413.6	0.17
Al Matrix	74	0.33

**Table 1.** The material properties of a TCG composed of Al<sub>2</sub>O<sub>3</sub>/SiC/Al.

After relating the trial internal displacement expressions with nodal shape function of each TCG, a primal-field boundary variational principle is then introduced to derive the local stiffness matrix:

$$\pi_4(u_i) = \sum_e \left\{ \int_{\partial\Omega^e} \frac{1}{2} t_i u_i dS - \int_{S_f^e} \bar{t}_i u_i dS \right\}. \quad (52)$$

Substituting the displacement expressions into the above functional and making the first variation lead to

$$\sum_e (\delta \mathbf{q}^T \mathbf{C}_{\alpha q}^T \mathbf{M}_{\alpha\alpha}^{-1} \mathbf{C}_{\alpha q} \mathbf{q} - \delta \mathbf{q}^T \mathbf{Q}) = 0, \quad (53)$$

in which  $\mathbf{M}_{\alpha\alpha} = \int_{\partial\Omega^e} \mathbf{R}_m^T \mathbf{N}_m dS$ .

**Remarks:** Using MFBVP is plagued by LBB conditions because of the Lagrange multipliers involved [Babuška 1973; Brezzi 1974; Punch and Atluri 1984; Rubinstein et al. 1983], while CPFBVP avoids the LBB violation by introducing the collocation technique. In addition, only one matrix  $\mathbf{M}_{\alpha\alpha}$  is integrated in the CPFBVP, while several matrices are evaluated in the MFBVP. Thus, the CPFBVP should be more computationally efficient than the MFBVP, which is also proved by the following numerical examples.

### 3. Numerical validations

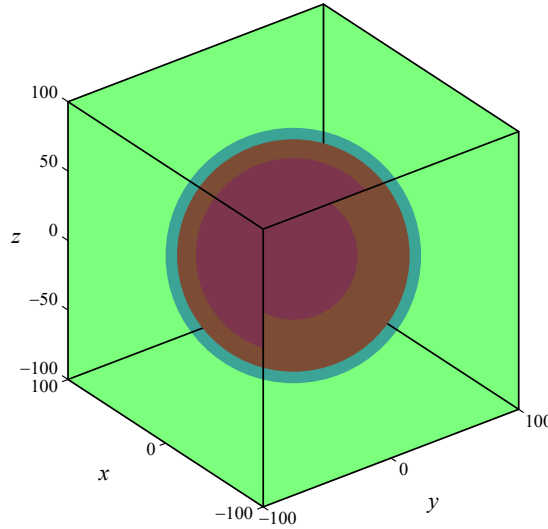
**3.1. Condition numbers.** As is introduced in the previous section, the characteristic parameters  $R_{\text{non}}$  and  $R_{\text{sig}}$  are introduced to scale the T-Trefftz trial functions. The magnitudes of  $R_{\text{non}}$  and  $R_{\text{sig}}$  are determined by the geometries of the investigated domains. Here we study the effect of the characteristic parameters on the condition numbers of the coefficient matrices involved in the calculations. In this example, a TCG with the material properties listed in Table 1 is investigated; see Figure 4. The dimensions of the TCG are  $L \times W \times H = 200 \times 200 \times 200 \mu\text{m}^3$ , and the outer radii of inclusion and coating are  $R_p = 72.56 \mu\text{m}$  and  $R_c = 79.82 \mu\text{m}$ , respectively. Tables 2 and 3 list the condition numbers of the inverted matrices in both MFBVP and CPFBVP, with or without introducing  $R_{\text{non}}$  and  $R_{\text{sig}}$ . It can be easily observed that when the characteristic parameters are not adopted ( $R_{\text{non}} = 1$  and  $R_{\text{sig}} = 1$ ), the condition numbers are too large to generate accurate results. The usage of  $R_{\text{non}}$  and  $R_{\text{sig}}$  can significantly reduce the condition numbers and guarantee calculation precision.

**3.2. Patch test.** The one-element patch test is conducted in this section. The same element is considered with same geometrical parameters and material properties listed in Table 1; see Figure 4. A uniform loading is applied to the right face ( $y = 100 \mu\text{m}$ ), while the essential boundary conditions are applied at the left face ( $y = -100 \mu\text{m}$ ). The exact solutions for the deformation of a homogeneous cube can be

Matrix	Without $R_{\text{non}}, R_{\text{sig}}$	With $R_{\text{non}}, R_{\text{sig}}$
$\mathbf{H}_{\alpha\alpha}$	$3.819 \times 10^{31}$	$1.678 \times 10^2$
$\mathbf{H}_{\gamma\gamma}$	$2.094 \times 10^{10}$	$0.991 \times 10^2$

**Table 2.** Condition numbers of the matrices of (42) used in MFBVP.

Matrix	Without $R_{\text{non}}, R_{\text{sig}}$	With $R_{\text{non}}, R_{\text{sig}}$
$\mathbf{M}_{\alpha\alpha}$	$4.593 \times 10^{33}$	$7.605 \times 10^4$

**Table 3.** Condition numbers of the matrix of (53) used in CPFVBVP.**Figure 4.** A TCG used to generate the condition numbers and patch test.

expressed as:

$$u_1 = -\frac{p\nu}{E}x_1, \quad u_2 = \frac{p}{E}x_2, \quad u_3 = -\frac{p\nu}{E}x_3, \quad (54)$$

which are compared with the numerical nodal displacement  $\mathbf{q}$  on the right face, and the error is defined as

$$\Delta = \frac{\|\mathbf{q} - \mathbf{q}^{\text{exact}}\|}{\|\mathbf{q}^{\text{exact}}\|}. \quad (55)$$

The errors generated by MFBVP and CPFVBVP are  $1.737 \times 10^{-6}$  and  $1.827 \times 10^{-4}$ , respectively, indicating both approaches obtain results with high accuracy. The execution time of the MFBVP and CPFVBVP to generate the local stiffness matrix of the TCG is 29.351 s and 6.51 s, respectively. The execution time of the MFBVP is a bit longer because the MFBVP involves more matrices to be integrated.

**3.3. Homogenized material properties and localized interphase stress distributions.** In order to validate the present theory in the micromechanical modeling of composites reinforced with coated particles,

$(R_c - R_p)/R_p$	CSA (GPa)	CPFBVP (GPa)	errors	MFBVP (GPa)	errors
Homogeneous	72.55	72.55	0.00%	72.55	0.00%
0	79.77	80.39	0.78%	79.81	0.05%
0.1	82.12	82.69	0.69%	82.17	0.06%
0.3	88.70	89.40	0.79%	88.89	0.21%
0.5	98.90	99.11	0.21%	99.27	0.37%

**Table 4.** Homogenized bulk modulus generated by the TCG and CSA models for various thicknesses of the coating.

both the homogenized bulk moduli as well as the local interphase stress distributions generated by the TCGs are compared with the composite sphere assemblage (CSA) model. The detailed derivation of CSA model is illustrated in the [Appendix](#).

A TCG with the dimension of  $L \times W \times H = 200 \times 200 \times 200 \mu\text{m}^3$  is used in this case and the particulate volume fraction is 10%. The material properties of the three constituents are listed in [Table 1](#). For a better test of the TCG, the thickness of the coating is varied for comparison. Both MFBVP and CPFBVP are adopted to generate the bulk modulus. [Table 4](#) shows that both methods generate well-matched predictions relative to the CSA model with the maximum error of less than 1%, and MFBVP usually generates smaller errors than CPFBVP for various thicknesses.

Then the local inter-phase stress concentrations are verified against CSA model. The stress components  $\sigma_{xx}(z = 0)$ ,  $\sigma_{yy}(z = 0)$ ,  $\sigma_{xy}(z = 0)$  at the inner radius of coating ( $R_p$ ) and the inner radius of the matrix ( $R_c$ ) are thoroughly compared in [Figures 5 and 6](#). Both MFBVP and CPFBVP agree well with the CSA results at the interface between the coating and matrix, while CPFBVP generates slightly offset results at the interface between the particle and coating relative to the other two methods.

Finally, the homogenized moduli are generated for a TCG with hard core/soft shell system, which has extensive applications in various structures [[Xu et al. 2014a; 2014b](#)]. In the present situation, the Young’s modulus and bulk modulus generated by CPFBVP are compared with a very fine-mesh FEM [[Tsui et al. 2001](#)] and the CSA model, respectively. [Figure 7](#) compares the generated homogenized moduli with material properties listed in [Table 5](#). Three sets of thickness parameters are used for the comparison. Since the glass bead and Polycarbonate matrix are connected by a weak interphase, the overall moduli are decreased as the thickness of coating increases. It can be easily observed that the overall moduli computed by the TCGs are in good agreement with both the very detailed FE and the CSA results.

It should be pointed out that the CSA model usually generates reasonably accurate bulk modulus and only the upper and lower bounds of the Young’s modulus for coated particulate composites. In addition, the phase-to-phase interaction is ignored within the model’s assumptions, leading to inaccurate interphase stress fields for composites with large particulate volume fractions. Those concerns are alleviated in the TCGs, which adopt complete Trefftz solutions to calculate the effective properties and also recover exactly the local field concentrations at the interfaces of inhomogeneities. What’s more, the effect of the locations of the particulates is also considered in the present technique, which cannot be easily captured by most of the existing methods.

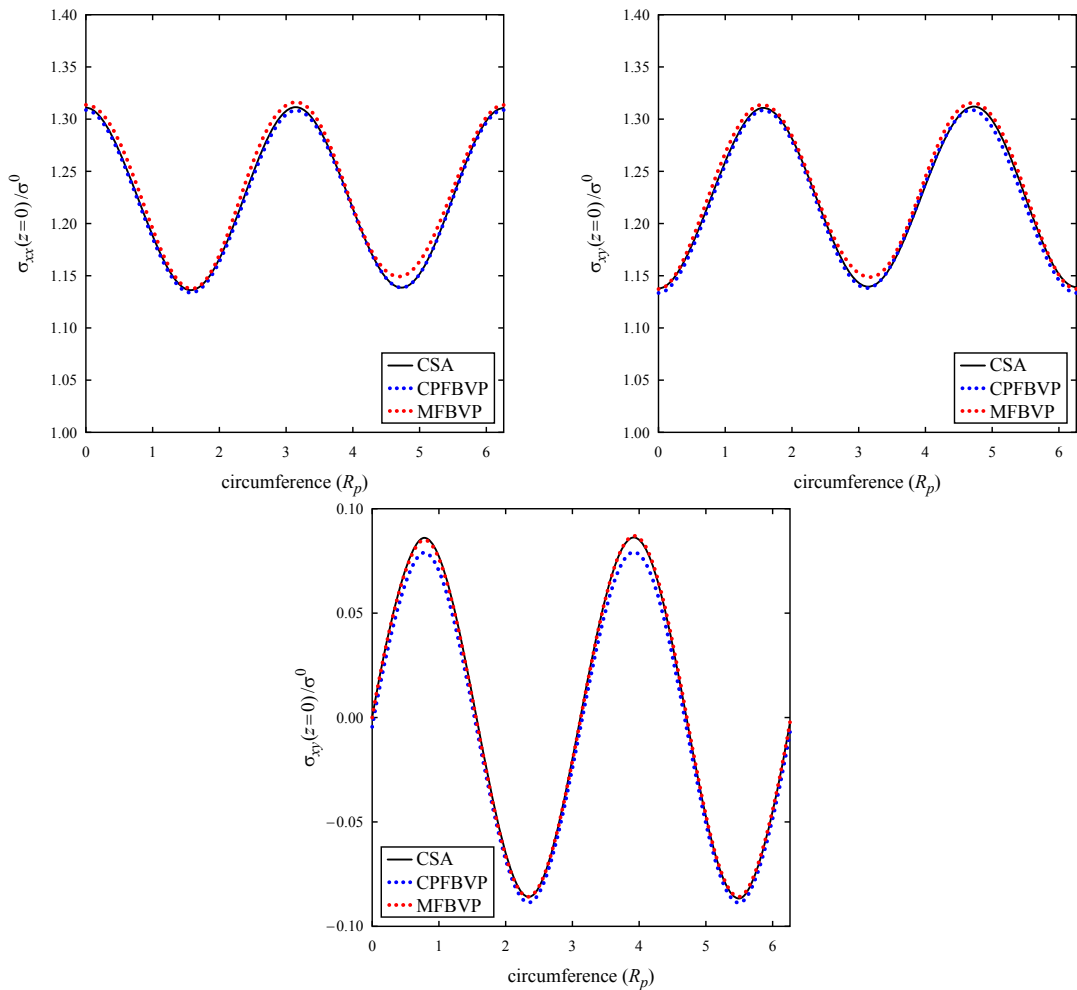


**Figure 5.** Variations of the three components  $\sigma_{xx}(z = 0)$ ,  $\sigma_{yy}(z = 0)$ ,  $\sigma_{xy}(z = 0)$  at the inner radius of the coating  $R_p$ .

	$E$ (GPa)	$\nu$
4 $\mu$ m Glass bead	70.0	0.22
Coating	0.50	0.30
Polycarbonate Matrix	2.28	0.38

**Table 5.** The material properties of a TCG with hard core/soft shell system.

#### 4. Numerical studies

In the last section, the accuracy of the TCG is validated by generating the effective properties as well as the localized interphase stresses in composites with coated particles. In this section, we employ the TCGs

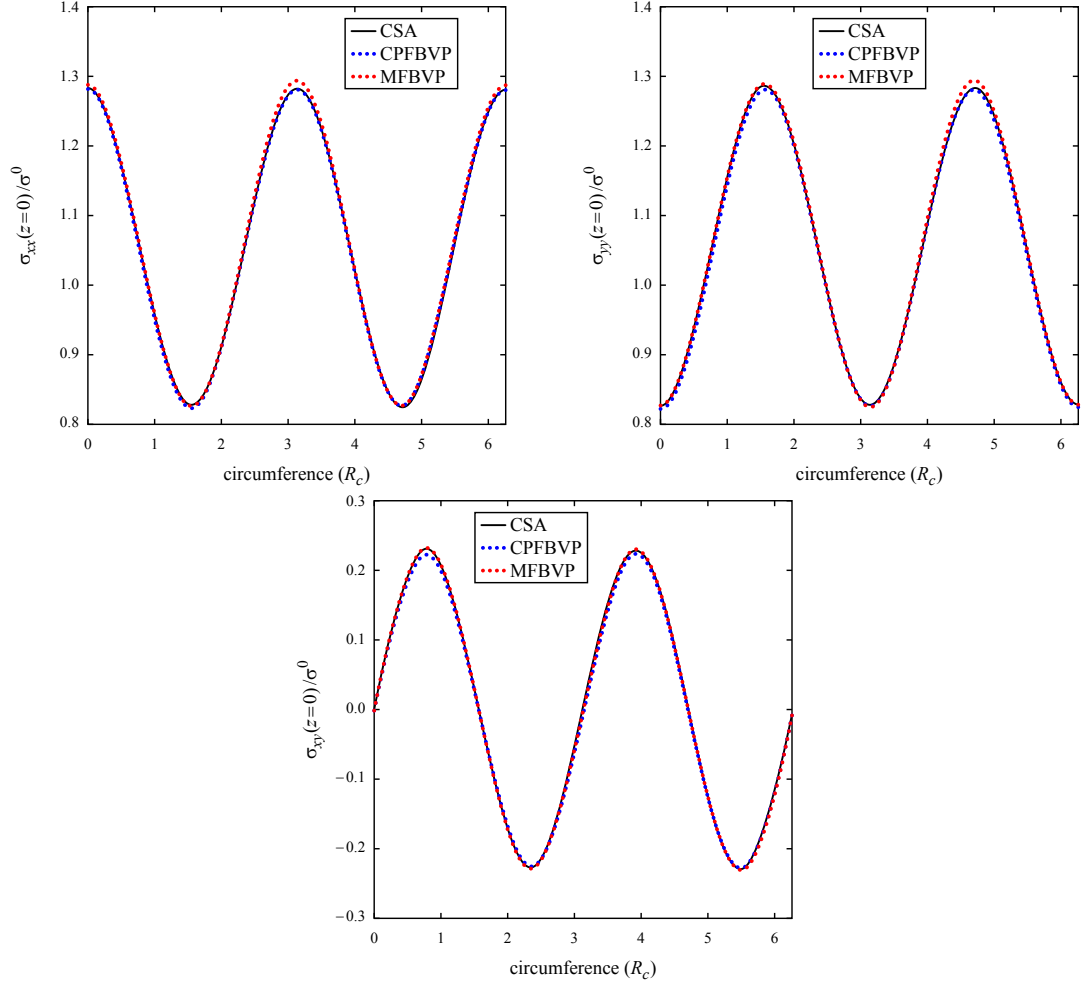


**Figure 6.** Variations of the three components  $\sigma_{xx}(z = 0)$ ,  $\sigma_{yy}(z = 0)$ ,  $\sigma_{xy}(z = 0)$  at the inner radius of matrix  $R_c$ .

to study the effect of coatings/interphases on the micromechanical behavior of composite materials. The  $\text{Al}_2\text{O}_3/\text{Al}$  particle/matrix system is adopted in this section, while the material properties and thickness of coating/interphase are varied.

**4.1. Effective properties.** In this example, A TCG is still employed with the dimensions of  $L \times W \times H = 200 \times 200 \times 200 \mu\text{m}^3$  and the particle volume fraction of 0.2. The Young’s modulus of the coating varies from 0 to 1000 GPa, and the ratio of thickness of the coating to the radius of the particle varies from 0 to 0.1. The homogenized moduli of the composite materials are illustrated in Figure 8. It can be easily observed that the homogenized moduli increase with the increase of the coating’s moduli and thickness ( $E_c/E_m \geq 1$ ). In addition, for a smaller magnitude of coating’s material properties, the homogenized moduli of composites are very small no matter which thickness is adopted. This is due to the fact that

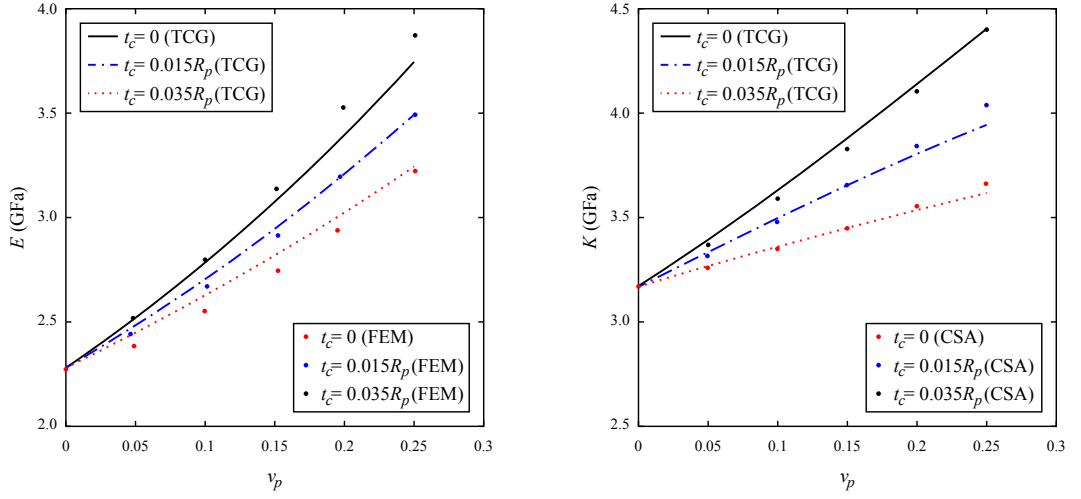


**Figure 7.** Comparison of (left) Young's moduli  $E$  and (right) bulk moduli  $K$  computed by using the TCGs, against the very fine-mesh FE and CSA results, respectively, for glass bead/polycarbonate composite with coatings of different thicknesses.

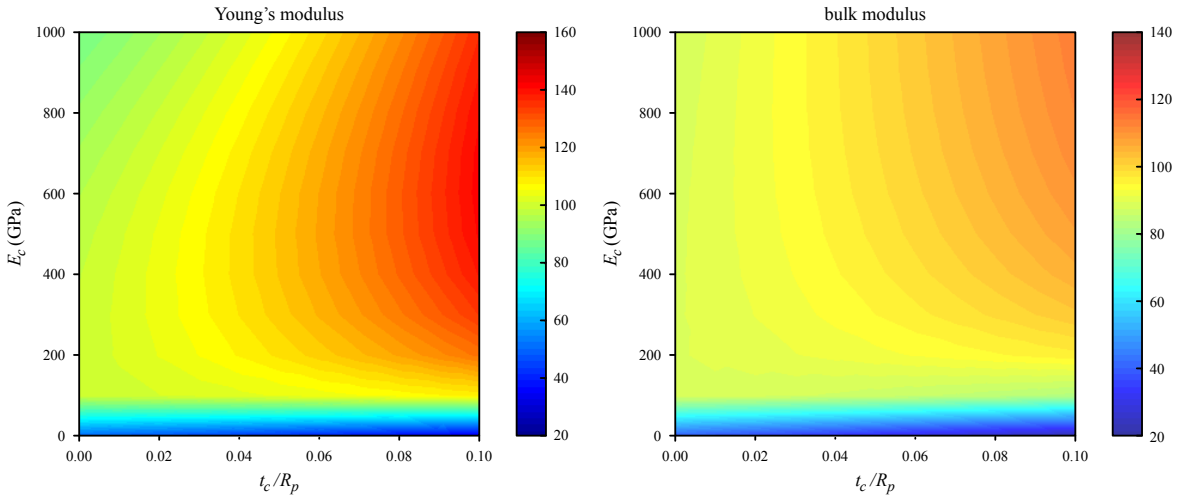


**Figure 8.** The effects of Young's modulus and thickness of the coating on the effective (left) Young's modulus and (right) bulk modulus of the composite.

the connection between fiber/matrix is very weak and the particle/coating domains can be treated as porosities.

**4.2. Local interphase stress concentrations.** The coating system plays an important role in the stress transfer between the constituents [Wang and Pindera 2016a]. Thus, herein the stress concentrations are studied by still tailoring the properties of the coatings. The definition of the stress concentration factor is  $SCF = \sigma_{\theta\theta}/\sigma_{yy}^0$  in this situation. According to the transformations between the spherical and Cartesian

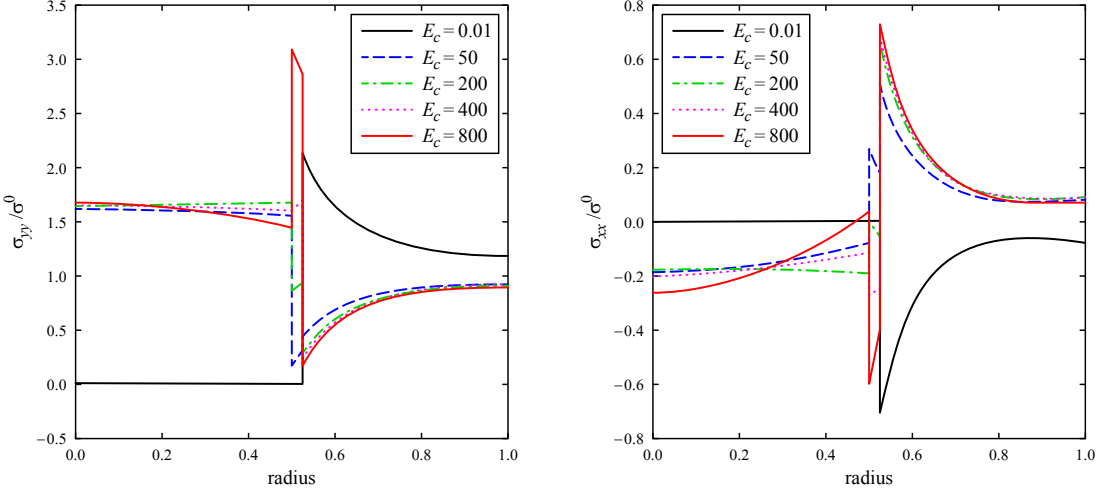


**Figure 9.** The effect of Young's modulus of the coating on the stress components  $\sigma_{yy}(\theta = 0, \varphi = 0)$  and  $\sigma_{xx}(\theta = \pi/2, \varphi = 0)$ .

coordinates,  $\sigma_{\theta\theta} = \sigma_{yy}(\theta = 0, \varphi = 0)$  and  $\sigma_{\theta\theta} = \sigma_{xx}(\theta = \pi/2, \varphi = 0)$ ,  $\text{SCF} = \sigma_{yy}/\sigma_{yy}^0$  at  $\theta = 0, \varphi = 0$  locations and  $\text{SCF} = \sigma_{xx}/\sigma_{yy}^0$  at  $\theta = \pi/2, \varphi = 0$  locations.

The effect of the Young's modulus of the coating is firstly generated in Figure 9 by fixing its thickness as  $t_c/R_p = 0.05$ . The radius of the spherical particle is of one-quarter length of the TCG. The Young's modulus of the coating is varied from 0.01 GPa to 800 GPa. It can be easily observed that the largest SCFs occur at the interface between the coating and matrix. As is already mentioned before, when the coating has a low elastic modulus (0.01 GPa), the particle and coating can be treated as a porosity domain, and the corresponding stresses are essentially zeros (solid black line). When the modulus increases from 50 GPa to 800 GPa, the stress  $\sigma_{yy}$  at zero degree within the particle domain maintains within a narrow range of variations. Meanwhile,  $\sigma_{yy}/\sigma_{yy}^0$  increases dramatically (from about 0.17 to over 3.09) in the coating domain, and then reduces and stabilizes at around 0.18 in the matrix phase. Conversely, the other component  $\sigma_{xx}/\sigma_{yy}^0$  increases and stabilizes when  $E_c$  is larger than a certain amount, and shows more variations in the particle domain.

In contrast to the Young's modulus of the coating, the thickness of the coating plays a less important role in affecting the stress distributions, as illustrated in Figure 10. The magnitudes of the stresses barely change for different thicknesses. It should be noted that the SiC properties are used for the coating (Table 4) in this situation.

## 5. Implementation of periodic boundary conditions

To apply the periodic boundary conditions, the classical methods [Miehe and Koch 2002; Wang and Pindera 2016b] usually enforce the same values for the degrees of freedom of matching nodes on two opposite RVE sides. Thus, it requires a periodic mesh, which has the same mesh distribution on two opposite parts of the RVE boundary. However, the mesh of a TCG is generally nonperiodic so that the classical



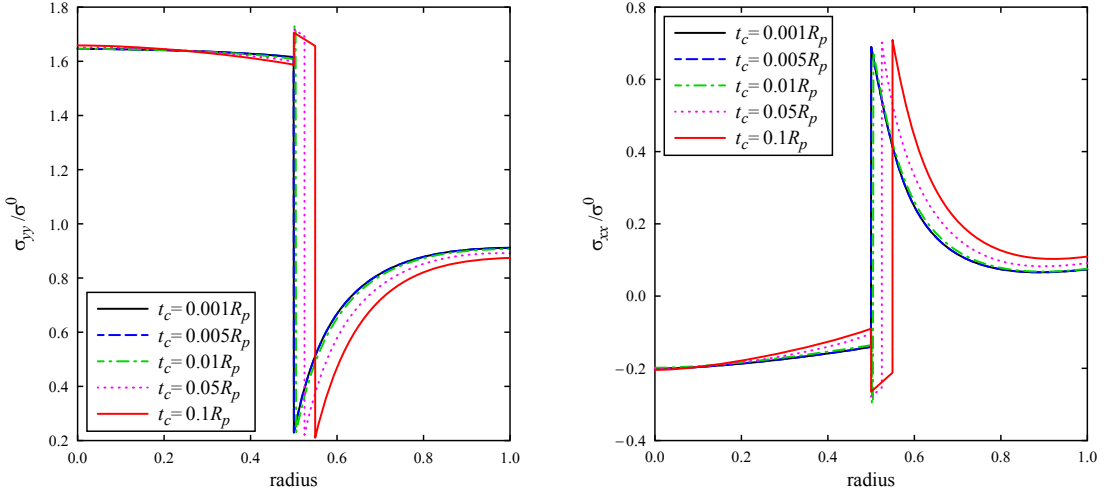


**Figure 10.** The effect of thickness of the coating on the stress components  $\sigma_{yy}(\theta = 0, \varphi = 0)$  and  $\sigma_{xx}(\theta = \pi/2, \varphi = 0)$ .

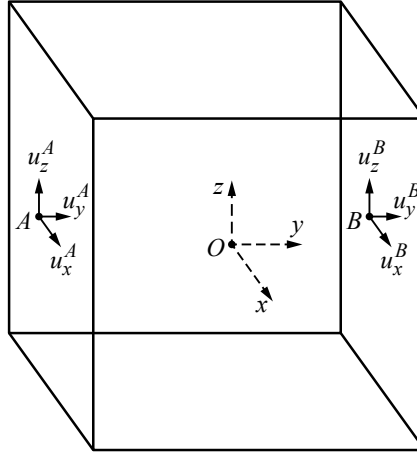


**Figure 11.** An RVE enforced with periodic displacement boundary conditions.

method cannot be directly employed. In this study, we developed a simple methodology to enforce periodic displacement boundary conditions on one RVE based on the surface-to-surface constraint scheme.

Figure 11 is a simple RVE with the origin point “O” located at the center. The point “A” is the mirror image of the point “B” relative to the original point. According to the reflectional symmetries with the reference to the  $y = 0$  plane, the displacement components between “A” and “B” points should have the following relations [Drago and Pindera 2007]:

$$u_x^B - u_x^A = \bar{\varepsilon}_{xi} \cdot L_i, \quad u_y^B - u_y^A = \bar{\varepsilon}_{yi} \cdot L_i, \quad u_z^B - u_z^A = \bar{\varepsilon}_{zi} \cdot L_i, \quad (56)$$

where  $i = x, y, z$ .  $\bar{\varepsilon}_{ij}$  is the macroscopic strain component and  $L_i$  is the dimension of the microstructure. Similar relations are applied to each pair of the symmetric points at the boundaries of the RVE.

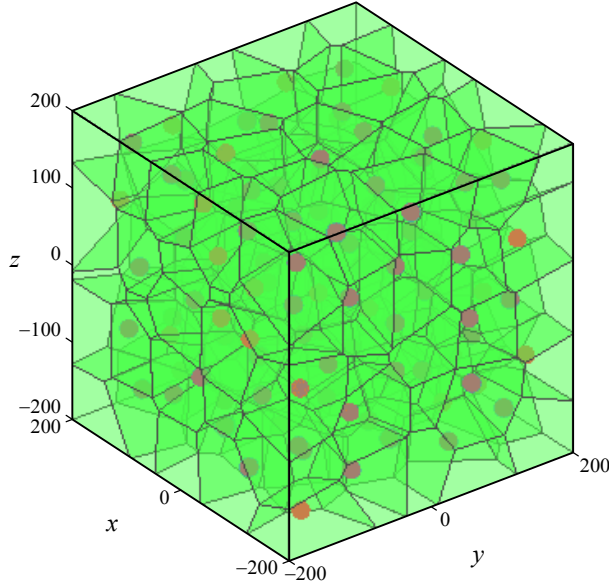


**Figure 12.** An RVE of 125 TCGs with the particle volume fraction of 1%.

Next an RVE including 125 coated spherical particles is considered in Figure 12, each particle is embedded within one TCG. The coating thickness is only 1% of the radius of the particle.

In a 3D RVE, the boundary points are composed of points on the six different faces, which are denoted as  $p_i^+$  or  $p_i^-$  ( $i = x, y, z$ ), where “+” and “−” signs stand for the positive and negative sides of the domain. Thus, the periodic boundary conditions are expressed as:

$$\begin{aligned} \mathbf{u}(p_x^+) - \mathbf{N}(p_x^-) \mathbf{u}(p_x^-) &= \bar{\mathbf{e}} \cdot L_x, \\ \mathbf{u}(p_y^+) - \mathbf{N}(p_y^-) \mathbf{u}(p_y^-) &= \bar{\mathbf{e}} \cdot L_y, \\ \mathbf{u}(p_z^+) - \mathbf{N}(p_z^-) \mathbf{u}(p_z^-) &= \bar{\mathbf{e}} \cdot L_z, \end{aligned} \quad (57)$$

where  $\mathbf{u}$  is the displacement vector and  $\bar{\mathbf{e}}$  is the applied macroscopic strain.  $L_x, L_y, L_z$  are the dimensions of the RVE in the Cartesian coordinate.  $\mathbf{N}$  is the interpolation function. After assembling the local stiffness matrices and equivalent nodal forces, the periodic boundary conditions can be directly enforced to the final global equations as essential boundary conditions, where all the nodal points at the boundaries of the RVE are involved. Equation (57) is applied at every boundary point on each face of RVE against its counterpart on the opposite face. For two points of the opposite faces which are exactly well matched, the periodic boundary conditions are easy to be applied by setting  $\mathbf{N} = 1$ ; while a point on one face which doesn't have the matched point on the other face, we locate the matched location, search the points close to this location, and apply the periodic conditions at those points using interpolations within the Wachspress coordinates [Dong and Atluri 2012b]. By validating the boundary conditions, we calculate the effective moduli by applying 1% macroscopic strain in the  $y$ -direction. Table 6 lists the generated results by assigning homogenous matrix properties (listed in Table 1) to the composite constituents, where the results perfectly recover the material properties of the matrix in the former case. In addition,

Material properties	$E$ (GPa)	$\nu$
Homogeneous (matrix)	73.926	0.330
Composites	75.090	0.329

**Table 6.** Calculated effective properties by the RVE with 125 TCGs with different constituent properties.

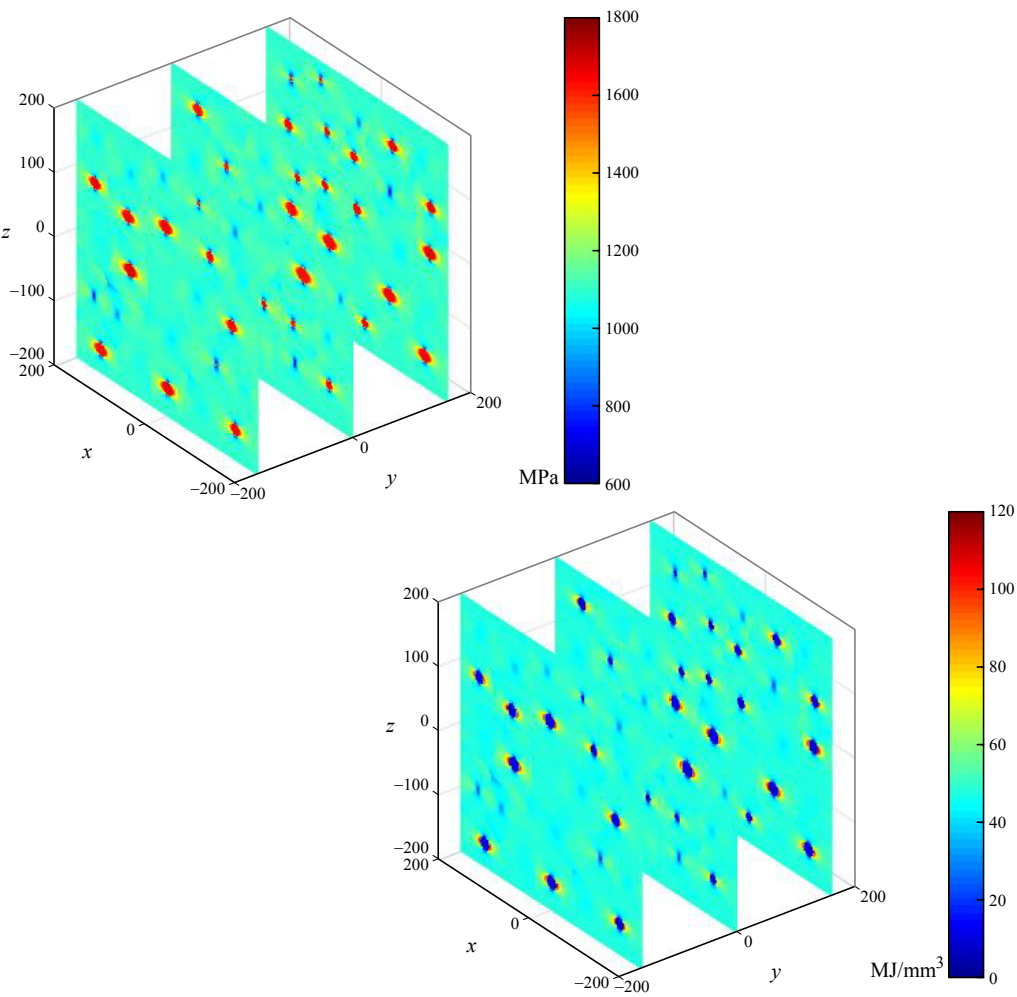


**Figure 13.** Distributions of (top) maximum principal stress (Unit: MPa) and (bottom) strain energy density (Unit: MJ/mm<sup>3</sup>) in the RVE containing 125 coated particles.

the local field distributions are illustrated in [Figure 13](#), where three cross-sections of the domain are focused upon. The principal stresses and energy densities are presented, and the concentrations always appear at the interfaces of the constituents, which help to identify the possible failure modes in the three-phase composite materials.

## 6. Conclusions

A Trefftz computational grain is developed based on the Voronoi Cell framework for the direct micromechanical modeling of heterogeneous materials reinforced with coated particulate inclusions. In order to dramatically reduce the mesh discretization effort as well as the computational effort, each TCG is treated as a three-phase particle/coating/matrix grain, wherein the exact internal displacement field is assumed in terms of the P–N solutions that are further represented by the spherical harmonics. Two approaches are adopted to set up the local stiffness matrix of TCGs, where the MFBVP implements the continuity and boundary conditions through Lagrange multipliers, while the CPFBVP uses the collocation technique for continuity conditions and a primal variational principle for the boundary condition implementation. Both approaches generate accurate homogenized moduli as well as exact local interphase stress distributions, with good agreement to the very fine-mesh FE technique and the CSA model. The effects of the material properties as well as the thickness of the coating system on the effective properties and localized stress concentrations are also examined for the TCGs, where the former parameters play more important roles than the latter one in altering the response of composite materials. Finally, an easy implementation of periodic boundary conditions is applied on the RVEs through the surface-to-surface constraints of displacement field on the opposite faces. The developed TCGs provide accurate and efficient computational tools in the direct modeling of the micromechanical behavior of the particulate composites reinforced with coatings/interphases, which cannot be easily competed by the off-the-shelf FE packages and classical models.

**Appendix: Derivation of CSA model.** The only existing Navier's equation for all the three phases is

$$\frac{d^2 u_r^{(k)}}{dr^2} + \frac{2}{r} \frac{du_r^{(k)}}{dr} - \frac{2u_r^{(k)}}{r^2} = 0 \quad (k = p, c, m), \quad (\text{A1})$$

which yields the displacement expression:

$$u_r^{(k)} = A^{(k)} r + B^{(k)} / r^2, \quad u_\theta^{(k)} = u_\varphi^{(k)} = 0. \quad (\text{A2})$$

Through the strain-displacement and stress-strain relations, the stress components can be expressed as

$$\begin{aligned} \sigma_{rr}^{(k)} &= 3K^{(k)} A^{(k)} - 4G^{(k)} B^{(k)} / r^3, \\ \sigma_{\theta\theta}^{(k)} &= 3K^{(k)} A^{(k)} + 2G^{(k)} B^{(k)} / r^3, \\ \sigma_{\varphi\varphi}^{(k)} &= 3K^{(k)} A^{(k)} + 2G^{(k)} B^{(k)} / r^3, \end{aligned} \quad (\text{A3})$$

where  $K$  and  $G$  are bulk and shear modulus of each phase. It should be noted that  $B^{(p)} = 0$  since the displacements or stresses should be bounded at the origin of the particle phase. Beyond what is discussed above, the continuity conditions between the adjacent constituents are applied:

$$\begin{aligned} u_r^{(p)}(r=a) &= u_r^{(c)}(r=a) \Rightarrow A^{(p)} a = A^{(c)} a + B^{(c)} / a^2, \\ \sigma_{rr}^{(p)}(r=a) &= \sigma_{rr}^{(c)}(r=a) \Rightarrow 3K^{(p)} A^{(p)} = 3K^{(c)} A^{(c)} - 4G^{(c)} B^{(c)} / a^3, \end{aligned} \quad (\text{A4})$$

$$\begin{aligned} u_r^{(c)}(r=b) &= u_r^{(m)}(r=b) \Rightarrow A^{(c)} b + B^{(c)} / b^2 = A^{(m)} b + B^{(m)} / b^2, \\ \sigma_{rr}^{(c)}(r=b) &= \sigma_{rr}^{(m)}(r=b) \Rightarrow 3K^{(c)} A^{(c)} - 4G^{(c)} B^{(c)} / b^3 = 3K^{(m)} A^{(m)} - 4G^{(m)} B^{(m)} / b^3. \end{aligned} \quad (\text{A5})$$

In addition, a homogeneous surface stress loading  $\sigma^0$  is applied at the outermost radius ( $r = c$ ) to calculate the bulk modulus, and

$$\sigma_{rr}^{(m)}(r = c) = \sigma^0 \Rightarrow 3K^{(m)}A^{(m)} - 4G^{(m)}B^{(m)}/c^3 = \sigma^0. \quad (\text{A6})$$

Thus, five equations are established for the five unknowns  $A^{(p)}$ ,  $A^{(c)}$ ,  $B^{(c)}$ ,  $A^{(m)}$ ,  $B^{(m)}$ , and finally, through the definition of bulk modulus:

$$K^* = \frac{\sigma_{rr}^{(m)}(r = c)}{u_r^{(m)}(r = c)/c}. \quad (\text{A7})$$

The replacement scheme is also used by Qiu and Weng [1991] to obtain the exact expression of the homogenized bulk modulus for the three-phase composites, which is also programmed to validate the above equations.

### Acknowledgement

The authors gratefully acknowledge the support for the work provided by Texas Tech University. Support from the National Natural Science Foundation of China (grant No. 11502069) and the National Key Research and Development Program of China (No. 2017YFA0207800) is thankfully acknowledged.

### References

- [Babuška 1973] I. Babuška, “The finite element method with Lagrange multipliers”, *Numer. Math.* **20**:3 (1973), 179–192.
- [Bishay and Atluri 2013] P. L. Bishay and S. N. Atluri, “2D and 3D multiphysics Voronoi cells based on radial basis functions, for Direct Mesoscale Numerical Simulation (DMNS) of the switching phenomena in ferroelectric polycrystalline materials”, *CMC: Comput. Mater. Con.* **33**:1 (2013), 19–62.
- [Bishay and Atluri 2014] P. L. Bishay and S. N. Atluri, “Trefftz-Lekhnitskii Grains (TLGs) for Efficient Direct Numerical Simulation (DNS) of the micro/meso mechanics of porous piezoelectric materials”, *Comput. Mater. Sci.* **83** (2014), 235–249.
- [Bishay and Atluri 2015] P. L. Bishay and S. N. Atluri, “Computational Piezo-Grains (CPGs) for a highly-efficient micromechanical modeling of heterogeneous piezoelectric-piezomagnetic composites”, *Eur. J. Mech. A Solids* **53** (2015), 311–328.
- [Bishay et al. 2014] P. L. Bishay, A. Alotaibi, and S. N. Atluri, “Multi-Region Trefftz Collocation Grains (MTCGs) for modeling piezoelectric composites and porous materials in direct and inverse problems”, *J. Mech. Mater. Struct.* **9**:3 (2014), 287–312.
- [Brezzi 1974] F. Brezzi, “On the existence, uniqueness and approximation of saddle-point problems arising from Lagrange multipliers”, *ESAIM: Math. Model. Numer. Anal.* **8** (1974), 129–151.
- [Chen et al. 2016] Q. Chen, X. Chen, Z. Zhai, and Z. Yang, “A new and general formulation of three-dimensional finite-volume micromechanics for particulate reinforced composites with viscoplastic phases”, *Compos. B Eng.* **85** (2016), 216–232.
- [Chen et al. 2017] Q. Chen, G. Wang, X. Chen, and J. Geng, “Finite-volume homogenization of elastic/viscoelastic periodic materials”, *Compos. Struct.* **182** (2017), 457–470.
- [Cherkaoui et al. 1994] M. Cherkaoui, H. Sabar, and M. Berveiller, “Micromechanics approach of the coated inclusion problem and applications to composite materials”, *J. Eng. Mater. Technol. (ASME)* **116**:3 (1994), 274–278.
- [Dong and Atluri 2012a] L. Dong and S. N. Atluri, “Trefftz Voronoi cells with elastic/rigid inclusions or voids for micromechanical analysis of composite and porous materials”, *Comput. Model. Eng. Sci.* **83**:2 (2012), 183–220.
- [Dong and Atluri 2012b] L. Dong and S. N. Atluri, “Development of 3D Trefftz Voronoi cells with/without spherical voids &/or elastic/rigid inclusions for micromechanical modeling of heterogeneous materials”, *CMC: Comput. Mater. Con.* **29**:2 (2012), 169–212.
- [Dong and Atluri 2012c] L. Dong and S. N. Atluri, “Development of 3D Trefftz Voronoi cells with ellipsoidal voids &/or elastic/rigid inclusions for micromechanical modeling of heterogeneous materials”, *CMC: Comput. Mater. Con.* **30**:1 (2012), 31–81.

- [Drago and Pindera 2007] A. Drago and M.-J. Pindera, “Micro-macromechanical analysis of heterogeneous materials: Macroscopically homogeneous vs periodic microstructures”, *Compos. Sci. Technol.* **67**:6 (2007), 1243–1263.
- [Ghosh et al. 1995] S. Ghosh, K. Lee, and S. Moorthy, “Multiple scale analysis of heterogeneous elastic structures using homogenization theory and voronoi cell finite element method”, *Int. J. Solids Struct.* **32**:1 (1995), 27–62.
- [Hashin 1962] Z. Hashin, “The elastic moduli of heterogeneous materials”, *J. Appl. Mech. (ASME)* **29** (1962), 143–150.
- [Herve and Zaoui 1993] E. Herve and A. Zaoui, “*n*-Layered inclusion-based micromechanical modelling”, *Int. J. Eng. Sci.* **31**:1 (1993), 1–10.
- [Jiang et al. 2008] Y. Jiang, W. Guo, and H. Yang, “Numerical studies on the effective shear modulus of particle reinforced composites with an inhomogeneous inter-phase”, *Comput. Mater. Sci.* **43**:4 (2008), 724–731.
- [Jiang et al. 2009] Y. Jiang, K. Tohgo, and Y. Shimamura, “A micro-mechanics model for composites reinforced by regularly distributed particles with an inhomogeneous interphase”, *Comput. Mater. Sci.* **46**:2 (2009), 507–515.
- [Liu 2007a] C.-S. Liu, “A modified Trefftz method for two-dimensional Laplace equations considering the domain’s characteristic length”, *Comput. Model. Eng. Sci.* **21**:1 (2007), 53–65.
- [Liu 2007b] C.-S. Liu, “An effectively modified direct Trefftz method for 2D potential problems considering the domain’s characteristic length”, *Eng. Anal. Bound. Elem.* **31**:12 (2007), 983–993.
- [Liu et al. 2005] D. S. Liu, C. Y. Chen, and D. Y. Chiou, “3-D Modeling of a composite material reinforced with multiple thickly coated particles using the infinite element method”, *Comput. Model. Eng. Sci.* **9**:2 (2005), 179–191.
- [Lurie 2005] A. I. Lurie, *Theory of elasticity*, 4th ed., Springer, 2005.
- [Marur 2004] P. R. Marur, “Estimation of effective elastic properties and interface stress concentrations in particulate composites by unit cell methods”, *Acta Mater.* **52**:5 (2004), 1263–1270.
- [Michel et al. 2000] J. C. Michel, H. Moulinec, and P. Suquet, “A computational method based on augmented Lagrangians and fast Fourier transforms for composites with high contrast”, *Comput. Model. Eng. Sci.* **1**:2 (2000), 79–88.
- [Miehe and Koch 2002] C. Miehe and A. Koch, “Computational micro-to-macro transitions of discretized microstructures undergoing small strains”, *Arch. Appl. Mech.* **72**:4-5 (2002), 300–317.
- [Moorthy and Ghosh 1998] S. Moorthy and S. Ghosh, “A Voronoi Cell finite element model for particle cracking in elastic-plastic composite materials”, *Comput. Methods Appl. Mech. Eng.* **151**:3 (1998), 377–400.
- [Moulinec and Suquet 1998] H. Moulinec and P. Suquet, “A numerical method for computing the overall response of nonlinear composites with complex microstructure”, *Comput. Methods Appl. Mech. Eng.* **157**:1 (1998), 69–94.
- [Neuber 1934] H. Neuber, “Ein neuer Ansatz zur Lösung räumlicher Probleme der Elastizitätstheorie”, *J. Appl. Math. Mech.* **14**:4 (1934), 203–212.
- [Nguyen et al. 2011] N. B. Nguyen, A. Giraud, and D. Grgic, “A composite sphere assemblage model for porous oolitic rocks”, *Int. J. Rock Mech. Min.* **48**:6 (2011), 909–921.
- [Papkovish 1932] P. F. Papkovish, “Solution Générale des équations différentielles fondamentales d’élasticité exprimée par trois fonctions harmoniques”, *C. R. Math. Acad. Sci. Paris* **195** (1932), 513–515.
- [Punch and Atluri 1984] E. F. Punch and S. N. Atluri, “Development and testing of stable, invariant, isoparametric curvilinear 2- and 3-D hybrid-stress elements”, *Comput. Methods Appl. Mech. Eng.* **47**:3 (1984), 331–356.
- [Qin 2005] Q.-H. Qin, “Trefftz finite element method and its applications”, *Appl. Mech. Rev. (ASME)* **58** (2005), 316–337.
- [Qiu and Weng 1991] Y. P. Qiu and G. J. Weng, “Elastic moduli of thickly coated particle and fiber-reinforced composites”, *J. Appl. Mech. (ASME)* **58** (1991), 388–398.
- [Quang and He 2007] H. L. Quang and Q.-C. He, “A one-parameter generalized self-consistent model for isotropic multiphase composites”, *Int. J. Solids Struct.* **44**:21 (2007), 6805–6825.
- [Rubinstein et al. 1983] R. Rubinstein, E. F. Punch, and S. N. Atluri, “An analysis of, and remedies for, kinematic modes in hybrid-stress finite elements: selection of stable, invariant stress fields”, *Comput. Methods Appl. Mech. Eng.* **38**:1 (1983), 63–92.
- [Tsui et al. 2001] C. P. Tsui, C. Y. Tang, and T. C. Lee, “Finite element analysis of polymer composites filled by interphase coated particles”, *J. Mater. Process. Technol.* **117**:1 (2001), 105–110.

- [Tsui et al. 2006] C. P. Tsui, D. Z. Chen, C. Y. Tang, P. S. Uskokovic, J. P. Fan, and X. L. Xie, “Prediction for debonding damage process and effective elastic properties of glass-bead-filled modified polyphenylene oxide”, *Compos. Sci. Technol.* **66**:11 (2006), 1521–1531.
- [Wachspress 1975] E. Wachspress, *A rational finite element basis*, Academic Press, New York, 1975.
- [Wang and Pindera 2016a] G. Wang and M.-J. Pindera, “Locally-exact homogenization of unidirectional composites with coated or hollow reinforcement”, *Mater. Des.* **93** (2016), 514–528.
- [Wang and Pindera 2016b] G. Wang and M.-J. Pindera, “On boundary condition implementation via variational principle in elasticity-based homogenization”, *J. Appl. Mech. (ASME)* **83**:10 (2016), 101008.
- [Wang et al. 2018] G. Wang, L. Dong, and S. N. Atluri, “A Trefftz collocation method (TCM) for three-dimensional linear elasticity by using the Papkovitch-Neuber solutions with cylindrical harmonics”, *Eng. Anal. Bound. Elem.* **88** (2018), 93–103.
- [Xu et al. 2014a] W. Xu, H. Chen, W. Chen, and L. Jiang, “Prediction of transport behaviors of particulate composites considering microstructures of soft interfacial layers around ellipsoidal aggregate particles”, *Soft Matter* **20** (2014), 627–638.
- [Xu et al. 2014b] W. Xu, W. Chen, and H. Chen, “Modeling of soft interfacial volume fraction in composite materials with complex convex particles”, *J. Chem. Phys.* **140** (2014), 034704.
- [Yvonnet et al. 2011] J. Yvonnet, Q.-C. He, Q.-Z. Zhu, and J.-F. Shao, “A general and efficient computational procedure for modelling the Kapitza thermal resistance based on XFEM”, *Comput. Mater. Sci.* **50**:4 (2011), 1220–1224.
- [Zhang et al. 2007] W. X. Zhang, L. X. Li, and T. J. Wang, “Interphase effect on the strengthening behavior of particle-reinforced metal matrix composites”, *Comput. Mater. Sci.* **41**:2 (2007), 145–155.
- [Zhu et al. 2011] Q.-Z. Zhu, S.-T. Gu, J. Yvonnet, J.-F. Shao, and Q.-C. He, “Three-dimensional numerical modelling by XFEM of spring-layer imperfect curved interfaces with applications to linearly elastic composite materials”, *Int. J. Numer. Methods Eng.* **88**:4 (2011), 307–328.

Received 25 Mar 2018. Revised 4 Jul 2018. Accepted 25 Jul 2018.

GUANNAN WANG: [gw5qv@virginia.edu](mailto:gw5qv@virginia.edu)

Center for Advanced Research in the Engineering Sciences, Texas Tech University, Lubbock, TX, United States

and

Department of Mechanical Engineering, Texas Tech University, Lubbock, TX, United States

LEITING DONG: [ltdong@buaa.edu.cn](mailto:ltdong@buaa.edu.cn)

School of Aeronautic Science and Engineering, Beihang University, Beijing, China

JUNBO WANG: [junbowang@outlook.com](mailto:junbowang@outlook.com)

School of Aeronautic Science and Engineering, Beihang University, Beijing, China

SATYA N. ATLURI: [snatluri.ttu@gmail.com](mailto:snatluri.ttu@gmail.com)

Center for Advanced Research in the Engineering Sciences, Texas Tech University, Lubbock, TX, United States

and

Department of Mechanical Engineering, Texas Tech University, Lubbock, TX, United States





## UNIFORM STRESS RESULTANTS INSIDE TWO NONELLIPTICAL INHOMOGENEITIES IN ISOTROPIC LAMINATED PLATES

XU WANG, LIANG CHEN AND PETER SCHIAVONE

We use complex variable methods to establish two sets of specific conditions which ensure the existence of uniform and hydrostatic internal membrane stress resultants and bending moments inside two through-thickness nonelliptical elastic inhomogeneities embedded in an infinite isotropic laminated Kirchhoff plate subjected to uniform remote membrane stress resultants and bending moments. These conditions can be interpreted as restrictions on the remote membrane stress resultants and bending moments for the given material and geometric parameters. We show that when these conditions are met, explicit expressions are available for the uniform stress resultants inside the two inhomogeneities and the constant hoop stress resultants on the matrix side along the two interfaces.

### 1. Introduction

Establishing uniformity of stresses inside multiple elastic inhomogeneities is both a fascinating and challenging area of study which continues to attract considerable attention in the literature (see, for example, [Kang et al. 2008](#); [Liu 2008](#); [Wang 2012](#); [Wang and Schiavone 2016](#); [Dai et al. 2015](#); [2016](#)). The majority of these investigations although confined to planar elasticity, antiplane elasticity, or conductivity have generated ideas and procedures which lend themselves well to other areas which play an equally important role in the engineering sciences. One such area concerns the analysis of laminated plate structures which are used extensively in mechanical, civil, aviation, and aerospace applications. A simple and elegant complex variable formulation, originally presented by Beom and Earmme [\[1998\]](#), was recently developed by Wang and Zhou [\[2014\]](#) to tackle the coupled stretching and bending deformations of isotropic laminated plates within the context of the celebrated Kirchhoff plate theory [\[Timoshenko and Woinowsky-Krieger 1959; Reddy 1997\]](#).

In this paper, we adopt the complex variable formulation of Wang and Zhou [\[2014\]](#) and the conformal mapping in Wang [\[2012\]](#) to study the coupled stretching and bending deformations of an infinite isotropic laminated plate in which there are embedded two through-thickness nonelliptical elastic inhomogeneities when the surrounding (plate) matrix is subjected to uniform remote membrane stress resultants and bending moments. The internal stress resultants (here, internal membrane stress resultants and bending moments for the plate) inside the two inhomogeneities are uniform and hydrostatic when either a set of three or two conditions on the remote loading is satisfied for the given material and geometric parameters. In addition, the hoop membrane stress resultant and hoop bending moment on the matrix side are uniformly distributed along the two inhomogeneity-matrix interfaces and the two inhomogeneities also satisfy the “harmonic field condition” of Bjorkman and Richards [\[1976\]](#). In contrast to previous results

*Keywords:* isotropic laminated plate, uniform stress resultants, complex variable method, conformal mapping.

in [Wang 2012; Wang and Schiavone 2016], the coefficient  $\Lambda$  appearing in the mapping function should be determined through the solution of a generalized eigenvalue problem for two  $2 \times 2$  real symmetric matrices. Both cases of when the two real symmetric matrices are either proportional or nonproportional to each other have been discussed in detail.

## 2. Complex variable formulation for isotropic laminated plates

In this section, we review the complex variable formulation for an isotropic laminated plate. Consider an undeformed plate of uniform thickness  $h$  in a Cartesian coordinate system  $\{x_i\}$  ( $i = 1, 2, 3$ ) with its reference plane (not the midplane) at  $x_3 = 0$ . The plate is composed of an isotropic, linearly elastic material which can be inhomogeneous in the thickness direction. In what follows, Greek and Latin indices take the values 1, 2 and 1, 2, 3, respectively and we sum over repeated indices.

The displacement field in the Kirchhoff plate theory is assumed to take the form

$$\tilde{u}_\alpha(x_i) = u_\alpha + x_3 \vartheta_\alpha, \quad \tilde{u}_3(x_i) = w, \quad (1)$$

where the two in-plane displacements  $u_\alpha$ , the deflection  $w$ , and the slopes  $\vartheta_\alpha = -w_{,\alpha}$  on the reference plane are all independent of  $x_3$ .

The coordinate system is chosen judiciously so that the two in-plane displacements and the deflection on the reference plane are *decoupled* in the equilibrium equations [Beom and Earmme 1998]. We introduce the integral operator  $Q(\cdots) = \int_{-h_0}^{h-h_0} (\cdots) dx_3$  in which  $h_0$  is the distance between the reference plane and the lower surface of the plate. Accordingly, the membrane stress resultants and bending moments defined by  $N_{\alpha\beta} = Q\sigma_{\alpha\beta}$ ,  $M_{\alpha\beta} = Qx_3\sigma_{\alpha\beta}$  (with  $\sigma_{\alpha\beta}$  being the in-plane stress components), the transverse shearing forces  $\Re_\beta = M_{\alpha\beta,\alpha}$ , in-plane displacements, deflection, and slopes on the reference plane of the plate as well as the four stress functions  $\varphi_\alpha$  and  $\eta_\alpha$  can be expressed concisely in terms of four analytic functions  $\phi(z)$ ,  $\psi(z)$ ,  $\Phi(z)$ , and  $\Psi(z)$  of the complex variable  $z = x_1 + ix_2$  as [Beom and Earmme 1998; Wang and Zhou 2014]

$$N_{11} + N_{22} = 4 \operatorname{Re}\{\phi'(z) + B\Phi'(z)\}, \quad (2)$$

$$N_{22} - N_{11} + 2iN_{12} = 2[\bar{z}\phi''(z) + \psi'(z) + B\bar{z}\Phi''(z) + B\Psi'(z)],$$

$$M_{11} + M_{22} = 4D(1 + \nu^D) \operatorname{Re}\{\Phi'(z)\} + \frac{B(\kappa^A - 1)}{\mu} \operatorname{Re}\{\phi'(z)\},$$

$$M_{22} - M_{11} + 2iM_{12} = -2D(1 - \nu^D)[\bar{z}\Phi''(z) + \Psi'(z)] - \frac{B}{\mu}[\bar{z}\phi''(z) + \psi'(z)], \quad (3)$$

$$\Re_1 - i\Re_2 = 4D\Phi''(z) + \frac{B(\kappa^A + 1)}{2\mu}\phi''(z),$$

$$2\mu(u_1 + iu_2) = \kappa^A\phi(z) - \overline{z\phi'(z)} - \overline{\psi(z)},$$

$$\vartheta_1 + i\vartheta_2 = \Phi(z) + \overline{z\Phi'(z)} + \overline{\Psi(z)}, \quad w = -\operatorname{Re}\{\bar{z}\Phi(z) + \gamma(z)\},$$

$$\varphi_1 + i\varphi_2 = i[\phi(z) + \overline{z\phi'(z)} + \overline{\psi(z)}] + iB[\Phi(z) + \overline{z\Phi'(z)} + \overline{\Psi(z)}], \quad (4)$$

$$\eta_1 + i\eta_2 = iD(1 - \nu^D)[\kappa^D\Phi(z) - \overline{z\Phi'(z)} - \overline{\Psi(z)}] + i\frac{B}{2\mu}[\kappa^A\phi(z) - \overline{z\phi'(z)} - \overline{\psi(z)}],$$

in which  $\Psi(z) = \gamma'(z)$ , and

$$\begin{aligned} \mu &= \frac{1}{2}(A_{11} - A_{12}), \quad B = B_{12}, \quad D = D_{11}, \quad \nu^A = \frac{A_{12}}{A_{11}}, \quad \nu^D = \frac{D_{12}}{D_{11}}, \\ \kappa^A &= \frac{3A_{11} - A_{12}}{A_{11} + A_{12}} = \frac{3 - \nu^A}{1 + \nu^A}, \quad \kappa^D = \frac{3D_{11} + D_{12}}{D_{11} - D_{12}} = \frac{3 + \nu^D}{1 - \nu^D}, \end{aligned} \quad (5)$$

with  $A_{ij} = QC_{ij}$ ,  $B_{ij} = Qx_3C_{ij}$ , and  $D_{ij} = Qx_3^2C_{ij}$  ( $ij = 11, 12$ ). The parameters  $C_{11}$  and  $C_{12}$  can be expressed in terms of the Young's modulus  $E = E(x_3)$  and Poisson's ratio  $\nu = \nu(x_3)$  of the plate as  $C_{11} = E/(1 - \nu^2)$  and  $C_{12} = \nu E/(1 - \nu^2)$ . The distance  $h_0$  is determined as  $h_0 = \int_0^h X_3 C_{11} dX_3 / \int_0^h C_{11} dX_3$  with  $X_3 = x_3 + h_0$  being the vertical coordinate of the given point from the lower surface of the plate.

In addition, the membrane stress resultants, bending moments, transverse shearing forces, and modified Kirchhoff transverse shearing forces  $V_1 = \mathfrak{R}_1 + M_{12,2}$  and  $V_2 = \mathfrak{R}_2 + M_{21,1}$  (which apply exclusively to free edges), can be expressed in terms of the four stress functions  $\varphi_\alpha$  and  $\eta_\alpha$  [Cheng and Reddy 2002] as

$$N_{\alpha\beta} = -\epsilon_{\beta\omega} \varphi_{\alpha,\omega}, \quad M_{\alpha\beta} = -\epsilon_{\beta\omega} \eta_{\alpha,\omega} - \frac{1}{2} \epsilon_{\alpha\beta} \eta_{\omega,\omega}, \quad \mathfrak{R}_\alpha = -\frac{1}{2} \epsilon_{\alpha\beta} \eta_{\omega,\omega\beta}, \quad V_\alpha = -\epsilon_{\alpha\omega} \eta_{\omega,\omega\omega}, \quad (6)$$

with  $\epsilon_{\alpha\beta}$  denoting the components of the two-dimensional permutation tensor.

In a new coordinate system  $\{\hat{x}_i\}$  ( $i = 1, 2, 3$ ) in which  $\hat{x}_3 = 0$  lies on an arbitrary plane parallel to the reference plane and  $\hat{x}_\alpha = x_\alpha$ , the in-plane displacements  $\hat{u}_\alpha$  and slopes  $\hat{\vartheta}_\alpha$  on  $\hat{x}_3 = 0$  and the stress functions  $\hat{\varphi}_\alpha$  and  $\hat{\eta}_\alpha$  in the new coordinate system can be given quite simply as

$$\begin{aligned} \hat{\vartheta}_1 + i\hat{\vartheta}_2 &= \vartheta_1 + i\vartheta_2, \quad \hat{u}_1 + i\hat{u}_2 = u_1 + iu_2 - \hat{h}(\vartheta_1 + i\vartheta_2), \\ \hat{\varphi}_1 + i\hat{\varphi}_2 &= \varphi_1 + i\varphi_2, \quad \hat{\eta}_1 + i\hat{\eta}_2 = \eta_1 + i\eta_2 + \hat{h}(\varphi_1 + i\varphi_2). \end{aligned} \quad (7)$$

Here,

$$\hat{h} = h_0 - h_1, \quad (8)$$

and  $h_1$  is the distance between  $\hat{x}_3 = 0$  and the lower surface of the plate (we note that  $h_1$  is positive or negative, respectively, if  $\hat{x}_3 = 0$  is above or below the lower surface of the plate). In the new coordinate system, the stress resultants  $\hat{N}_{\alpha\beta} = \hat{Q}\sigma_{\alpha\beta}$  and  $\hat{M}_{\alpha\beta} = \hat{Q}\hat{x}_3\sigma_{\alpha\beta}$  with  $\hat{Q}(\cdots) = \int_{-h_1}^{h-h_1} (\cdots) d\hat{x}_3$ , the transverse shearing forces  $\hat{\mathfrak{R}}_\beta = \hat{M}_{\alpha\beta,\alpha}$ , and the modified Kirchhoff transverse shearing forces  $\hat{V}_1 = \hat{\mathfrak{R}}_1 + \hat{M}_{12,2}$  and  $\hat{V}_2 = \hat{\mathfrak{R}}_2 + \hat{M}_{21,1}$  can also be expressed in terms of the newly introduced stress functions  $\hat{\varphi}_\alpha$  and  $\hat{\eta}_\alpha$  as

$$\hat{N}_{\alpha\beta} = -\epsilon_{\beta\omega} \hat{\varphi}_{\alpha,\omega}, \quad \hat{M}_{\alpha\beta} = -\epsilon_{\beta\omega} \hat{\eta}_{\alpha,\omega} - \frac{1}{2} \epsilon_{\alpha\beta} \hat{\eta}_{\omega,\omega}, \quad \hat{\mathfrak{R}}_\alpha = -\frac{1}{2} \epsilon_{\alpha\beta} \hat{\eta}_{\omega,\omega\beta}, \quad \hat{V}_\alpha = -\epsilon_{\alpha\omega} \hat{\eta}_{\omega,\omega\omega}. \quad (9)$$

### 3. Uniform stress resultants inside two nonelliptical inhomogeneities

Consider an infinite isotropic laminated plate containing two through-thickness nonelliptical elastic inhomogeneities. Let  $S_1$ ,  $S_2$ , and  $S_3$  denote the left inhomogeneity, the surrounding matrix, and the right inhomogeneity, respectively, all of which are perfectly bonded through the respective left and right interfaces  $L_1$  and  $L_2$ . The matrix is subjected to uniform remote membrane stress resultants ( $N_{11}^\infty$ ,  $N_{22}^\infty$ ,  $N_{12}^\infty$ ) and bending moments ( $M_{11}^\infty$ ,  $M_{22}^\infty$ ,  $M_{12}^\infty$ ). Throughout the paper, the subscripts 1, 2, and 3 are used to identify the quantities in  $S_1$ ,  $S_2$ , and  $S_3$ , respectively. In what follows, the new coordinate system  $\{\hat{x}_i\}$  ( $i = 1, 2, 3$ ) is common to all three phases and is chosen such that  $\hat{x}_3 = 0$  is on the reference plane of the matrix.

Applying the aforementioned conditions, the corresponding boundary value problem reduces to the following system of equations in the analytic functions  $\phi(z)$ ,  $\psi(z)$ ,  $\Phi(z)$ , and  $\Psi(z)$  defined in each of  $S_1$ ,  $S_2$ , and  $S_3$ :

$$\begin{aligned} & \frac{1}{2\mu_2}[\kappa_2^A \phi_2(z) - z\overline{\phi_2'(z)} - \overline{\psi_2(z)}] \\ & \quad = \frac{1}{2\mu_1}[\kappa_1^A \phi_1(z) - z\overline{\phi_1'(z)} - \overline{\psi_1(z)}] - \hat{h}_1[\Phi_1(z) + z\overline{\Phi_1'(z)} + \overline{\Psi_1(z)}], \\ & \Phi_2(z) + z\overline{\Phi_2'(z)} + \overline{\Psi_2(z)} = \Phi_1(z) + z\overline{\Phi_1'(z)} + \overline{\Psi_1(z)}, \\ & \phi_2(z) + z\overline{\phi_2'(z)} + \overline{\psi_2(z)} + B_2[\Phi_2(z) + z\overline{\Phi_2'(z)} + \overline{\Psi_2(z)}] \\ & \quad = \phi_1(z) + z\overline{\phi_1'(z)} + \overline{\psi_1(z)} + B_1[\Phi_1(z) + z\overline{\Phi_1'(z)} + \overline{\Psi_1(z)}], \\ & \frac{B_2}{2\mu_2}[\kappa_2^A \phi_2(z) - z\overline{\phi_2'(z)} - \overline{\psi_2(z)}] + D_2(1 - \nu_2^D)[\kappa_2^D \Phi_2(z) - z\overline{\Phi_2'(z)} - \overline{\Psi_2(z)}] \\ & \quad = \frac{B_1}{2\mu_1}[\kappa_1^A \phi_1(z) - z\overline{\phi_1'(z)} - \overline{\psi_1(z)}] + D_1(1 - \nu_1^D)[\kappa_1^D \Phi_1(z) - z\overline{\Phi_1'(z)} - \overline{\Psi_1(z)}] \\ & \quad \quad + \hat{h}_1[\phi_1(z) + z\overline{\phi_1'(z)} + \overline{\psi_1(z)}] + \hat{h}_1 B_1[\Phi_1(z) + z\overline{\Phi_1'(z)} + \overline{\Psi_1(z)}], \quad z \in L_1, \quad (10a) \end{aligned}$$

$$\begin{aligned} & \frac{1}{2\mu_2}[\kappa_2^A \phi_2(z) - z\overline{\phi_2'(z)} - \overline{\psi_2(z)}] \\ & \quad = \frac{1}{2\mu_3}[\kappa_3^A \phi_3(z) - z\overline{\phi_3'(z)} - \overline{\psi_3(z)}] - \hat{h}_3[\Phi_3(z) + z\overline{\Phi_3'(z)} + \overline{\Psi_3(z)}], \\ & \Phi_2(z) + z\overline{\Phi_2'(z)} + \overline{\Psi_2(z)} = \Phi_3(z) + z\overline{\Phi_3'(z)} + \overline{\Psi_3(z)}, \\ & \phi_2(z) + z\overline{\phi_2'(z)} + \overline{\psi_2(z)} + B_2[\Phi_2(z) + z\overline{\Phi_2'(z)} + \overline{\Psi_2(z)}] \\ & \quad = \phi_3(z) + z\overline{\phi_3'(z)} + \overline{\psi_3(z)} + B_3[\Phi_3(z) + z\overline{\Phi_3'(z)} + \overline{\Psi_3(z)}], \\ & \frac{B_2}{2\mu_2}[\kappa_2^A \phi_2(z) - z\overline{\phi_2'(z)} - \overline{\psi_2(z)}] + D_2(1 - \nu_2^D)[\kappa_2^D \Phi_2(z) - z\overline{\Phi_2'(z)} - \overline{\Psi_2(z)}] \\ & \quad = \frac{B_3}{2\mu_3}[\kappa_3^A \phi_3(z) - z\overline{\phi_3'(z)} - \overline{\psi_3(z)}] + D_3(1 - \nu_3^D)[\kappa_3^D \Phi_3(z) - z\overline{\Phi_3'(z)} - \overline{\Psi_3(z)}] \\ & \quad \quad + \hat{h}_3[\phi_3(z) + z\overline{\phi_3'(z)} + \overline{\psi_3(z)}] + \hat{h}_3 B_3[\Phi_3(z) + z\overline{\Phi_3'(z)} + \overline{\Psi_3(z)}], \quad z \in L_2, \quad (10b) \end{aligned}$$

$$\begin{aligned} \phi_2(z) &\cong \delta_1 z + O(1), \quad \psi_2(z) \cong \delta_2 z + O(1), \\ \Phi_2(z) &\cong \gamma_1 z + O(1), \quad \Psi_2(z) \cong \gamma_2 z + O(1), \quad |z| \rightarrow \infty, \quad (10c) \end{aligned}$$

where

$$\begin{aligned} \delta_1 &= \frac{\mu_2 D_2(1 + \nu_2^D)(N_{11}^\infty + N_{22}^\infty) - B_2 \mu_2 (M_{11}^\infty + M_{22}^\infty)}{4\mu_2 D_2(1 + \nu_2^D) - B_2^2(\kappa_2^A - 1)}, \\ \gamma_1 &= \frac{4\mu_2 (M_{11}^\infty + M_{22}^\infty) - B_2(\kappa_2^A - 1)(N_{11}^\infty + N_{22}^\infty)}{16\mu_2 D_2(1 + \nu_2^D) - 4B_2^2(\kappa_2^A - 1)}, \\ \delta_2 &= \frac{\mu_2 D_2(1 - \nu_2^D)(N_{22}^\infty - N_{11}^\infty + 2iN_{12}^\infty) + B_2 \mu_2 (M_{22}^\infty - M_{11}^\infty + 2iM_{12}^\infty)}{2\mu_2 D_2(1 - \nu_2^D) - B_2^2}, \\ \gamma_2 &= \frac{-2\mu_2 (M_{22}^\infty - M_{11}^\infty + 2iM_{12}^\infty) - B_2(N_{22}^\infty - N_{11}^\infty + 2iN_{12}^\infty)}{4\mu_2 D_2(1 - \nu_2^D) - 2B_2^2}. \end{aligned} \quad (11)$$

We assume the matrix  $S_2$  in the  $z$ -plane is mapped onto an annulus  $1 \leq |\xi| \leq \rho^{-1/2}$  in the  $\xi$ -plane by the following conformal mapping function [Wang 2012]

$$z = \omega(\xi) = R \left[ \frac{1}{\xi - \lambda} + \frac{p}{\xi - \lambda^{-1}} + \frac{\Lambda^{-1} p}{\rho \xi - \lambda^{-1}} + \sum_{n=1}^{+\infty} (a_n \xi^n + a_{-n} \xi^{-n}) \right], \quad (12)$$

$$\xi(z) = \omega^{-1}(z), \quad 1 \leq |\xi| \leq \rho^{-1/2},$$

where  $R$  is a real scaling constant;  $\lambda$  ( $1 < \lambda < \rho^{-1/2}$ ) is a real constant;  $p$  is a complex constant;  $\Lambda$ ,  $a_n$ , and  $a_{-n}$  are unknown complex coefficients to be determined. Using the mapping function in (12), the two interfaces  $L_1$  and  $L_2$  in the  $z$ -plane are mapped onto two coaxial circles with radii 1 and  $\rho^{-1/2}$  in the  $\xi$ -plane, respectively. In addition,  $z = \infty$  is mapped to the point  $\xi = \lambda$ .

In order to ensure that the stress resultants inside the two inhomogeneities are uniform, the analytic functions defined in the two elastic inhomogeneities should take the following form:

$$\phi_1(z) = \frac{4\mu_1(\kappa_2^A + 1)[D_1(1 + v_1^D) + D_2(1 - v_2^D) + \hat{h}_1(B_1 + B_2)]X - 16\mu_1 D_2(B_1 - B_2 - 2\mu_2 \hat{h}_1)Y}{\Delta_1} z, \quad (13)$$

$$\Phi_1(z) = \frac{-(\kappa_2^A + 1)[(B_1 - B_2)(\kappa_1^A - 1) + 4\mu_1 \hat{h}_1]X + 8D_2[\mu_2(\kappa_1^A - 1) + 2\mu_1]Y}{\Delta_1} z,$$

$$\psi_1(z) = \Psi_1(z) = 0, \quad z \in S_1; \quad (13)$$

$$\phi_3(z) = \frac{4\mu_3(\kappa_2^A + 1)[D_3(1 + v_3^D) + D_2(1 - v_2^D) + \hat{h}_3(B_3 + B_2)]X - 16\mu_3 D_2(B_3 - B_2 - 2\mu_2 \hat{h}_3)Y}{\Delta_3} z,$$

$$\Phi_3(z) = \frac{-(\kappa_2^A + 1)[(B_3 - B_2)(\kappa_3^A - 1) + 4\mu_3 \hat{h}_3]X + 8D_2[\mu_2(\kappa_3^A - 1) + 2\mu_3]Y}{\Delta_3} z,$$

$$\psi_3(z) = \Psi_3(z) = 0, \quad z \in S_3; \quad (14)$$

where  $X$  and  $Y$  are two real coefficients, and

$$\begin{aligned} \Delta_1 &= 4[\mu_2(\kappa_1^A - 1) + 2\mu_1][D_1(1 + v_1^D) + D_2(1 - v_2^D) + \hat{h}_1(B_1 + B_2)] \\ &\quad - 2(B_1 - B_2 - 2\mu_2 \hat{h}_1)[(B_1 - B_2)(\kappa_1^A - 1) + 4\mu_1 \hat{h}_1], \\ \Delta_3 &= 4[\mu_2(\kappa_3^A - 1) + 2\mu_3][D_3(1 + v_3^D) + D_2(1 - v_2^D) + \hat{h}_3(B_3 + B_2)] \\ &\quad - 2(B_3 - B_2 - 2\mu_2 \hat{h}_3)[(B_3 - B_2)(\kappa_3^A - 1) + 4\mu_3 \hat{h}_3]. \end{aligned} \quad (15)$$

By enforcing continuity of displacements and stress resultants across the left interface  $L_1$  in (10a), we arrive at

$$\phi_2(\xi) = \phi_2(\omega(\xi)) = X\omega(\xi),$$

$$\Phi_2(\xi) = \Phi_2(\omega(\xi)) = Y\omega(\xi),$$

$$\begin{aligned}
\psi_2(\xi) &= \psi(\omega(\xi)) \\
&= \left\{ \frac{X}{\Delta_1} \left( 8[\mu_1(\kappa_2^A - 1) - \mu_2(\kappa_1^A - 1)][D_1(1 + v_1^D) + D_2(1 - v_2^D) + \hat{h}_1(B_1 + B_2)] \right. \right. \\
&\quad \left. \left. - 2[(\kappa_1^A - 1)(B_1 - B_2) + 4\mu_1\hat{h}_1][(\kappa_2^A - 1)(B_1 - B_2) + 4\mu_2\hat{h}_1] \right) \right. \\
&\quad \left. + \frac{Y}{\Delta_1} (16\mu_2 D_2[(\kappa_1^A - 1)(B_1 - B_2) + 4\mu_1\hat{h}_1]) \right\} \bar{\omega}\left(\frac{1}{\xi}\right), \\
\Psi_2(\xi) &= \Psi_2(\omega(\xi)) \\
&= \left\{ -\frac{X}{\Delta_1} (2(\kappa_2^A + 1)[(\kappa_1^A - 1)(B_1 - B_2) + 4\mu_1\hat{h}_1]) \right. \\
&\quad \left. - \frac{Y}{\Delta_1} \left( 8[\mu_2(\kappa_1^A - 1) + 2\mu_1][D_1(1 + v_1^D) - D_2(1 + v_2^D) + \hat{h}_1(B_1 + B_2)] \right. \right. \\
&\quad \left. \left. - 4(B_1 - B_2 - 2\mu_2\hat{h}_1)[(\kappa_1^A - 1)(B_1 - B_2) + 4\mu_1\hat{h}_1] \right) \right\} \bar{\omega}\left(\frac{1}{\xi}\right), \\
&\quad 1 \leq |\xi| \leq \rho^{-1/2}. \quad (16)
\end{aligned}$$

Similarly, by enforcing continuity of displacements and stress resultants across the right interface  $L_2$  in (10b), we arrive at

$$\begin{aligned}
\phi_2(\xi) &= X\omega(\xi), \\
\Phi_2(\xi) &= Y\omega(\xi), \\
\psi_2(\xi) &= \left\{ \frac{X}{\Delta_3} \left( 8[\mu_3(\kappa_2^A - 1) - \mu_2(\kappa_3^A - 1)][D_3(1 + v_3^D) + D_2(1 - v_2^D) + \hat{h}_3(B_3 + B_2)] \right. \right. \\
&\quad \left. \left. - 2[(\kappa_3^A - 1)(B_3 - B_2) + 4\mu_3\hat{h}_3][(\kappa_2^A - 1)(B_3 - B_2) + 4\mu_2\hat{h}_3] \right) \right. \\
&\quad \left. + \frac{Y}{\Delta_3} (16\mu_2 D_2[(\kappa_3^A - 1)(B_3 - B_2) + 4\mu_3\hat{h}_3]) \right\} \bar{\omega}\left(\frac{1}{\rho\xi}\right), \\
\Psi_2(\xi) &= \left\{ -\frac{X}{\Delta_3} 2(\kappa_2^A + 1)[(\kappa_3^A - 1)(B_3 - B_2) + 4\mu_3\hat{h}_3] \right. \\
&\quad \left. - \frac{Y}{\Delta_3} \left( 8[\mu_2(\kappa_3^A - 1) + 2\mu_3][D_3(1 + v_3^D) - D_2(1 + v_2^D) + \hat{h}_3(B_3 + B_2)] \right. \right. \\
&\quad \left. \left. - 4(B_3 - B_2 - 2\mu_2\hat{h}_3)[(\kappa_3^A - 1)(B_3 - B_2) + 4\mu_3\hat{h}_3] \right) \right\} \bar{\omega}\left(\frac{1}{\rho\xi}\right), \\
&\quad 1 \leq |\xi| \leq \rho^{-1/2}. \quad (17)
\end{aligned}$$

In order to ensure that the elastic field in the matrix is unique, the two sets of functions  $\phi_2(\xi)$ ,  $\Phi_2(\xi)$ ,  $\psi_2(\xi)$ , and  $\Psi_2(\xi)$  obtained in (16) and (17) should coincide. Consequently, we find that

$$\Lambda = \frac{c_{11}X + c_{12}Y}{d_{11}X + d_{12}Y} = \frac{c_{12}X + c_{22}Y}{d_{12}X + d_{22}Y}, \quad (18)$$

and

$$a_n = \frac{\lambda^{-n-1} + p\Lambda^{-1}\rho^n\lambda^{n+1}}{1 - \Lambda\rho^{-n}}, \quad a_{-n} = \frac{\lambda^{n-1} + p\lambda^{1-n}}{\Lambda^{-1}\rho^{-n} - 1}, \quad n = 1, 2, \dots, +\infty, \quad (19)$$

where

$$\begin{aligned}
 c_{11} &= \frac{1}{\Delta_3} \left( 4[\mu_3(\kappa_2^A - 1) - \mu_2(\kappa_3^A - 1)][D_3(1 + v_3^D) + D_2(1 - v_2^D) + \hat{h}_3(B_3 + B_2)] \right. \\
 &\quad \left. - [(\kappa_3^A - 1)(B_3 - B_2) + 4\mu_3\hat{h}_3][(\kappa_2^A - 1)(B_3 - B_2) + 4\mu_2\hat{h}_3] \right), \\
 c_{12} &= \frac{8\mu_2 D_2}{\Delta_3} [(\kappa_3^A - 1)(B_3 - B_2) + 4\mu_3\hat{h}_3], \\
 c_{22} &= \frac{16\mu_2 D_2}{\Delta_3(\kappa_2^A + 1)} \left( 2[\mu_2(\kappa_3^A - 1) + 2\mu_3][D_3(1 + v_3^D) - D_2(1 + v_2^D) + \hat{h}_3(B_3 + B_2)] \right. \\
 &\quad \left. - (B_3 - B_2 - 2\mu_2\hat{h}_3)[(\kappa_3^A - 1)(B_3 - B_2) + 4\mu_3\hat{h}_3] \right), \quad (20a)
 \end{aligned}$$

$$\begin{aligned}
 d_{11} &= \frac{1}{\Delta_1} \left( 4[\mu_1(\kappa_2^A - 1) - \mu_2(\kappa_1^A - 1)][D_1(1 + v_1^D) + D_2(1 - v_2^D) + \hat{h}_1(B_1 + B_2)] \right. \\
 &\quad \left. - [(\kappa_1^A - 1)(B_1 - B_2) + 4\mu_1\hat{h}_1][(\kappa_2^A - 1)(B_1 - B_2) + 4\mu_2\hat{h}_1] \right), \\
 d_{12} &= \frac{8\mu_2 D_2}{\Delta_1} [(\kappa_1^A - 1)(B_1 - B_2) + 4\mu_1\hat{h}_1], \\
 d_{22} &= \frac{16\mu_2 D_2}{\Delta_1(\kappa_2^A + 1)} \left( 2[\mu_2(\kappa_1^A - 1) + 2\mu_1][D_1(1 + v_1^D) - D_2(1 + v_2^D) + \hat{h}_1(B_1 + B_2)] \right. \\
 &\quad \left. - (B_1 - B_2 - 2\mu_2\hat{h}_1)[(\kappa_1^A - 1)(B_1 - B_2) + 4\mu_1\hat{h}_1] \right). \quad (20b)
 \end{aligned}$$

Equation (18) can be rewritten in the form

$$\begin{bmatrix} c_{11} & c_{12} \\ c_{12} & c_{22} \end{bmatrix} \begin{bmatrix} X \\ Y \end{bmatrix} = \Lambda \begin{bmatrix} d_{11} & d_{12} \\ d_{12} & d_{22} \end{bmatrix} \begin{bmatrix} X \\ Y \end{bmatrix}, \quad (21)$$

which is a generalized eigenvalue problem for the two  $2 \times 2$  real symmetric matrices

$$\begin{bmatrix} c_{11} & c_{12} \\ c_{12} & c_{22} \end{bmatrix} \quad \text{and} \quad \begin{bmatrix} d_{11} & d_{12} \\ d_{12} & d_{22} \end{bmatrix}, \quad (22)$$

with  $\Lambda$  the eigenvalue and  $\mathbf{v} = [X \ Y]^T$  the associated eigenvector. In what follows, we first address the case in which the above two matrices are not proportional to each other, i.e.,

$$\begin{bmatrix} c_{11} & c_{12} \\ c_{12} & c_{22} \end{bmatrix} \neq k \begin{bmatrix} d_{11} & d_{12} \\ d_{12} & d_{22} \end{bmatrix}, \quad (23)$$

where  $k$  is an arbitrary real constant.

In this case, the two eigenvalues of (21) can be determined explicitly as

$$\Lambda_{1,2} = \frac{c_{11}d_{22} + c_{22}d_{11} - 2c_{12}d_{12} \pm \sqrt{(c_{11}d_{22} - c_{22}d_{11})^2 + 4(c_{11}d_{12} - c_{12}d_{11})(c_{22}d_{12} - c_{12}d_{22})}}{2(d_{11}d_{22} - d_{12}^2)}, \quad (24)$$

and the two eigenvectors associated with the two eigenvalues are then

$$\mathbf{v}_1 = \begin{bmatrix} c_{12} - \Lambda_1 d_{12} \\ \Lambda_1 d_{11} - c_{11} \end{bmatrix}, \quad \mathbf{v}_2 = \begin{bmatrix} c_{12} - \Lambda_2 d_{12} \\ \Lambda_2 d_{11} - c_{11} \end{bmatrix}, \quad (25)$$

which implies that the two coefficients  $X$  and  $Y$  are not independent. It is necessary that the two eigenvalues  $\Lambda_1$  and  $\Lambda_2$  should be real. Consequently, it is seen from (24) that the following inequality must be satisfied:

$$(c_{11}d_{22} - c_{22}d_{11})^2 + 4(c_{11}d_{12} - c_{12}d_{11})(c_{22}d_{12} - c_{12}d_{22}) \geq 0.$$

A comparison of (16) with the asymptotic behaviors at infinity specified in (10c) leads to

$$\delta_1 = X, \quad \gamma_1 = Y, \quad \delta_2 = -2\bar{p}\lambda^2(d_{11}X + d_{12}Y), \quad \gamma_2 = \bar{p}\lambda^2 \frac{\kappa_2^A + 1}{4\mu_2 D_2}(d_{12}X + d_{22}Y). \quad (26)$$

The necessary and sufficient condition for the existence of the real coefficient  $X$  (or  $Y$ ) simultaneously satisfying the four conditions in (26) is found to be

$$\begin{aligned} & \frac{N_{22}^\infty - N_{11}^\infty + 2iN_{12}^\infty}{N_{11}^\infty + N_{22}^\infty} \\ &= \frac{\bar{p}\lambda^2}{8\mu_2 D_2 [c_{12} - \Lambda_j d_{12} + B_2(\Lambda_j d_{11} - c_{11})]} \\ & \quad \times \{8\mu_2 D_2 (c_{11}d_{12} - c_{12}d_{11}) + B_2(\kappa_2^A + 1)[c_{12}d_{12} - c_{11}d_{22} + \Lambda_j(d_{11}d_{22} - d_{12}^2)]\}, \\ & \frac{M_{11}^\infty + M_{22}^\infty}{N_{11}^\infty + N_{22}^\infty} = \frac{4\mu_2 D_2 (1 + \nu_2^D)(\Lambda_j d_{11} - c_{11}) + B_2(\kappa_2^A - 1)(c_{12} - \Lambda_j d_{12})}{4\mu_2 [c_{12} - \Lambda_j d_{12} + B_2(\Lambda_j d_{11} - c_{11})]}, \\ & \frac{M_{22}^\infty - M_{11}^\infty + 2iM_{12}^\infty}{N_{11}^\infty + N_{22}^\infty} \\ &= -\frac{\bar{p}\lambda^2}{8\mu_2 [c_{12} - \Lambda_j d_{12} + B_2(\Lambda_j d_{11} - c_{11})]} \\ & \quad \times \{(1 - \nu_2^D)(\kappa_2^A + 1)[c_{12}d_{12} - c_{11}d_{22} + \Lambda_j(d_{11}d_{22} - d_{12}^2)] + 4B_2(c_{11}d_{12} - c_{12}d_{11})\}, \\ & \quad j = 1, 2. \quad (27) \end{aligned}$$

For the given material and geometric parameters, the three conditions in (27) can be considered as restrictions on the remote loading.

The internal uniform hydrostatic stress resultants inside the two nonelliptical inhomogeneities can be expressed in terms of the two loading parameters  $\delta_1$  and  $\gamma_1$  defined in (11) as

$$N_{11} = N_{22} = f_{11}\delta_1 + f_{12}\gamma_1, \quad N_{12} = 0, \quad (28)$$

$$M_{11} = M_{22} = g_{11}\delta_1 + g_{12}\gamma_1, \quad M_{12} = 0, \quad z \in S_1,$$

$$N_{11} = N_{22} = f_{31}\delta_1 + f_{32}\gamma_1, \quad N_{12} = 0, \quad (29)$$

$$M_{11} = M_{22} = g_{31}\delta_1 + g_{32}\gamma_1, \quad M_{12} = 0, \quad z \in S_3,$$

where the eight coefficients  $f_{j1}$ ,  $f_{j2}$ ,  $g_{j1}$ ,  $g_{j2}$ ,  $j = 1, 3$  are defined by



$$\begin{aligned}
\frac{f_{j1}}{\kappa_2^A + 1} &= \frac{1}{\Delta_j} \{8\mu_j[D_j(1+v_j^D) + D_2(1-v_2^D) + \hat{h}_j(B_j + B_2)] - 2B_j[(B_j - B_2)(\kappa_j^A - 1) + 4\mu_j\hat{h}_j]\}, \\
\frac{f_{j2}}{16D_2} &= \frac{1}{\Delta_j} [B_j\mu_2(\kappa_2^A - 1) + 2B_2\mu_j + 4\mu_j\mu_2\hat{h}_j], \\
\frac{g_{j1}}{\kappa_2^A + 1} &= \frac{1}{\Delta_j} \{2B_j(\kappa_j^A - 1)[D_j(1+v_j^D) + D_2(1-v_2^D) + \hat{h}_j(B_j + B_2)] \\
&\quad - 2D_j(1+v_j^D)[(B_j - B_2)(\kappa_j^A - 1) + 4\mu_j\hat{h}_j]\}, \\
\frac{g_{j2}}{8D_2} &= \frac{1}{\Delta_j} \{2D_j(1+v_j^D)[\mu_2(\kappa_j^A - 1) + 2\mu_j] - B_j(\kappa_j^A - 1)[(B_j - B_2) - 2\mu_2\hat{h}_j]\}, \quad j = 1, 3. \quad (30)
\end{aligned}$$

It should be emphasized that, in view of (27)<sub>2</sub>,  $\delta_1$  and  $\gamma_1$  can ultimately be expressed in terms of only  $N_{11}^\infty + N_{22}^\infty$ . In addition,  $N_{11} + N_{22}$  and  $M_{11} + M_{22}$  are uniformly distributed in the matrix as

$$N_{11} + N_{22} = 4(\delta_1 + B_2\gamma_1), \quad M_{11} + M_{22} = \frac{B_2(\kappa_2^A - 1)}{\mu_2}\delta_1 + 4D_2(1+v_2^D)\gamma_1, \quad z \in S_2. \quad (31)$$

The above result implies that the two elastic inhomogeneities will not disturb the quantities  $N_{11} + N_{22}$  and  $M_{11} + M_{22}$  when inserted into the surrounding (uncut) matrix (i.e.,  $N_{11} + N_{22} = N_{11}^\infty + N_{22}^\infty$  and  $M_{11} + M_{22} = M_{11}^\infty + M_{22}^\infty$  for  $z \in S_2$ ). Thus the two elastic inhomogeneities are “harmonic” [Bjorkman and Richards 1976; 1979; Richards and Bjorkman 1980; Wang and Schiavone 2015]. In addition, it follows from (28), (29), and (31) that the hoop membrane stress resultant and hoop bending moment are constant along the two interfaces  $L_1$  and  $L_2$  on the matrix side and are given by

$$\begin{aligned}
N_{tt} &= (4 - f_{11})\delta_1 + (4B_2 - f_{12})\gamma_1, \\
M_{tt} &= \left[ \frac{B_2(\kappa_2^A - 1)}{\mu_2} - g_{11} - \hat{h}_1 f_{11} \right] \delta_1 + [4D_2(1+v_2^D) - g_{12} - \hat{h}_1 f_{12}]\gamma_1, \quad z \in L_1, \quad (32)
\end{aligned}$$

$$\begin{aligned}
N_{tt} &= (4 - f_{31})\delta_1 + (4B_2 - f_{32})\gamma_1, \\
M_{tt} &= \left[ \frac{B_2(\kappa_2^A - 1)}{\mu_2} - g_{31} - \hat{h}_3 f_{31} \right] \delta_1 + [4D_2(1+v_2^D) - g_{32} - \hat{h}_3 f_{32}]\gamma_1, \quad z \in L_2. \quad (33)
\end{aligned}$$

Next, we address the case in which the two matrices in (22) are proportional to each other, i.e.,

$$\begin{bmatrix} c_{11} & c_{12} \\ c_{12} & c_{22} \end{bmatrix} = k \begin{bmatrix} d_{11} & d_{12} \\ d_{12} & d_{22} \end{bmatrix}. \quad (34)$$

In this case, it is seen from (18) that  $\Lambda = k$ , and that the two coefficients  $X$  and  $Y$  are now independent of each other. The necessary and sufficient condition for the existence of the two real coefficients  $X$  and  $Y$  simultaneously satisfying the four conditions in (26) is quite simply derived as

$$\delta_2 = -2\bar{p}\lambda^2(d_{11}\delta_1 + d_{12}\gamma_1), \quad \gamma_2 = \bar{p}\lambda^2 \frac{\kappa_2^A + 1}{4\mu_2 D_2} (d_{12}\delta_1 + d_{22}\gamma_1), \quad (35)$$

or more explicitly

$$\begin{aligned}
N_{11}^\infty - N_{22}^\infty + 2iN_{12}^\infty &= p\lambda^2[\chi_{11}(N_{11}^\infty + N_{22}^\infty) + \chi_{12}(M_{11}^\infty + M_{22}^\infty)], \\
M_{11}^\infty - M_{22}^\infty + 2iM_{12}^\infty &= p\lambda^2[\chi_{21}(N_{11}^\infty + N_{22}^\infty) + \chi_{22}(M_{11}^\infty + M_{22}^\infty)], \quad (36)
\end{aligned}$$

with the four coefficients  $\chi_{11}$ ,  $\chi_{12}$ ,  $\chi_{21}$ , and  $\chi_{22}$  being defined by

$$\begin{aligned}
 \chi_{11} &= \frac{1}{4\mu_2 D_2 [8\mu_2 D_2 (1 + v_2^D) - 2B_2^2 (\kappa_2^A - 1)]} \\
 &\quad \times \{ 8\mu_2 D_2 [4d_{11}\mu_2 D_2 (1 + v_2^D) - d_{12}B_2 (\kappa_2^A - 1)] \\
 &\quad - B_2 (\kappa_2^A + 1) [4d_{12}\mu_2 D_2 (1 + v_2^D) - d_{22}B_2 (\kappa_2^A - 1)] \}, \\
 \chi_{12} &= \frac{8\mu_2 D_2 (d_{12} - d_{11}B_2) - B_2 (\kappa_2^A + 1) (d_{22} - d_{12}B_2)}{D_2 [8\mu_2 D_2 (1 + v_2^D) - 2B_2^2 (\kappa_2^A - 1)]}, \\
 \chi_{21} &= \frac{1}{4\mu_2 [8\mu_2 D_2 (1 + v_2^D) - 2B_2^2 (\kappa_2^A - 1)]} \\
 &\quad \times \{ (1 - v_2^D) (\kappa_2^A + 1) [4d_{12}\mu_2 D_2 (1 + v_2^D) - d_{22}B_2 (\kappa_2^A - 1)] \\
 &\quad - 4B_2 [4d_{11}\mu_2 D_2 (1 + v_2^D) - d_{12}B_2 (\kappa_2^A - 1)] \}, \\
 \chi_{22} &= \frac{(1 - v_2^D) (\kappa_2^A + 1) (d_{22} - d_{12}B_2) - 4B_2 (d_{12} - d_{11}B_2)}{8\mu_2 D_2 (1 + v_2^D) - 2B_2^2 (\kappa_2^A - 1)}. \tag{37}
 \end{aligned}$$

An example of when the two  $2 \times 2$  real symmetric matrices are proportional to each other arises when the two inhomogeneities have identical elastic properties (i.e.,  $\mu_1 = \mu_3$ ,  $D_1 = D_3$ ,  $B_1 = B_3$ ,  $v_1^A = v_3^A$ ,  $v_1^D = v_3^D$ ) and  $\hat{h}_1 = \hat{h}_3$ . In this example, we will have  $c_{11} = d_{11}$ ,  $c_{12} = d_{12}$ ,  $c_{22} = d_{22}$ . Consequently,  $\Lambda = k = 1$ . Various shapes of the two nonelliptical inhomogeneities in the case  $\Lambda = 1$  (in (12)) have been illustrated numerically in [Wang 2012].

For given material and geometric parameters, the two conditions in (36) can be considered as constraints on the remote loading. Once the two conditions in (36) are satisfied, (28) and (29) for the internal uniform hydrostatic stress resultants and (32) and (33) for the constant hoop stress resultants on the matrix side along the two interfaces remain valid for this case. Recall that now  $\delta_1$  and  $\gamma_1$  can be expressed in terms of  $N_{11}^\infty + N_{22}^\infty$  and  $M_{11}^\infty + M_{22}^\infty$  in view of the fact that  $X$  and  $Y$  are independent.

#### 4. Conclusions

We have identified the shapes of the two nonelliptical elastic inhomogeneities and the conditions leading to uniform interior stress resultants inside the two inhomogeneities. When the inequality in (23) is satisfied, two values of the real coefficient  $\Lambda$  are determined from (24) for the given material parameters of the composite plate. Three conditions on remote loading for the given material and geometric parameters are derived in (27). Once these conditions are satisfied, elementary expressions of the internal uniform hydrostatic stress resultants and constant hoop stress resultants on the matrix side along the two interfaces in terms of only  $N_{11}^\infty + N_{22}^\infty$  are presented in (28), (29), (32), and (33). When (34) is valid, a single value of  $\Lambda = k$  is found. Two conditions on remote loading for the given material and geometric parameters are derived in (36). In this case, the internal uniform hydrostatic stress resultants and constant hoop stress resultants on the matrix side along the two interfaces can be expressed in terms of both  $N_{11}^\infty + N_{22}^\infty$  and  $M_{11}^\infty + M_{22}^\infty$ .

The complex coefficients  $a_n$  and  $a_{-n}$  can be uniquely determined from (19) for given values of  $\lambda$ ,  $\rho$ ,  $p$ , and  $\Lambda$ . Consequently, the shapes of the two inhomogeneities are known. In addition, the two

inhomogeneities are “harmonic” in the sense that they satisfy the harmonic field condition of Bjorkman and Richards [1976] in that their introduction will not cause any disturbance of the fields  $N_{11} + N_{22}$  and  $M_{11} + M_{22}$  in the surrounding matrix.

### Acknowledgements

This work is supported by the National Natural Science Foundation of China (Grant No. 11272121) and through a Discovery Grant from the Natural Sciences and Engineering Research Council of Canada (Grant No: RGPIN — 2017-03716115112).

### References

- [Beom and Earmme 1998] H. G. Beom and Y. Y. Earmme, “Complex variable method for problems of a laminate composed of multiple isotropic layers”, *Int. J. Fract.* **92**:4 (1998), 305–324.
- [Bjorkman and Richards 1976] G. S. Bjorkman and R. Richards, “Harmonic holes — an inverse problem in elasticity”, *J. Appl. Mech. (ASME)* **43**:3 (1976), 414–418.
- [Bjorkman and Richards 1979] G. S. Bjorkman and R. Richards, “Harmonic holes for nonconstant fields”, *J. Appl. Mech. (ASME)* **46**:3 (1979), 573–576.
- [Cheng and Reddy 2002] Z.-Q. Cheng and J. N. Reddy, “Octet formalism for Kirchhoff anisotropic plates”, *Proc. R. Soc. Lond. A* **458**:2022 (2002), 1499–1517.
- [Dai et al. 2015] M. Dai, C.-F. Gao, and C. Q. Ru, “Uniform stress fields inside multiple inclusions in an elastic infinite plane under plane deformation”, *Proc. R. Soc. Lond. A* **471**:2177 (2015), art. id. 20140933, 23 pp.
- [Dai et al. 2016] M. Dai, P. Schiavone, and C.-F. Gao, “Uniform strain fields inside periodic inclusions incorporating interface effects in anti-plane shear”, *Acta Mech.* **227**:10 (2016), 2795–2803.
- [Kang et al. 2008] H. Kang, E. Kim, and G. W. Milton, “Inclusion pairs satisfying Eshelby’s uniformity property”, *SIAM J. Appl. Math.* **69**:2 (2008), 577–595.
- [Liu 2008] L. P. Liu, “Solutions to the Eshelby conjectures”, *Proc. R. Soc. Lond. A* **464**:2091 (2008), 573–594.
- [Reddy 1997] J. N. Reddy, *Mechanics of laminated composite plates: theory and analysis*, CRC Press, Boca Raton, FL, 1997.
- [Richards and Bjorkman 1980] R. Richards and G. S. Bjorkman, “Harmonic shapes and optimum design”, *J. Eng. Mech. Div. (ASCE)* **106**:6 (1980), 1125–1134.
- [Timoshenko and Woinowsky-Krieger 1959] S. P. Timoshenko and S. Woinowsky-Krieger, *Theory of plates and shells*, 2nd ed., McGraw-Hill, New York, 1959.
- [Wang 2012] X. Wang, “Uniform fields inside two non-elliptical inclusions”, *Math. Mech. Solids* **17**:7 (2012), 736–761.
- [Wang and Schiavone 2015] X. Wang and P. Schiavone, “Harmonic shapes in isotropic laminated plates”, *J. Mech. Mater. Struct.* **10**:3 (2015), 433–445.
- [Wang and Schiavone 2016] X. Wang and P. Schiavone, “Two inhomogeneities of irregular shape with internal uniform stress fields interacting with a screw dislocation”, *Compt. Rend. Mécaniq.* **344**:7 (2016), 532–538.
- [Wang and Zhou 2014] X. Wang and K. Zhou, “An inclusion of arbitrary shape in an infinite or semi-infinite isotropic multi-layered plate”, *Int. J. Appl. Mech.* **6**:1 (2014), 1450001.

Received 18 Apr 2018. Revised 13 Aug 2018. Accepted 18 Aug 2018.

XU WANG: [xuwang@ecust.edu.cn](mailto:xuwang@ecust.edu.cn)

School of Mechanical and Power Engineering, East China University of Science and Technology, Shanghai, China

LIANG CHEN: [liangchen5962@mail.ecust.edu.cn](mailto:liangchen5962@mail.ecust.edu.cn)

School of Mechanical and Power Engineering, East China University of Science and Technology, Shanghai, China

PETER SCHIAVONE: [p.schiavone@ualberta.ca](mailto:p.schiavone@ualberta.ca)

Department of Mechanical Engineering, University of Alberta, Edmonton, AB, Canada



# AN ANALYTICAL SOLUTION FOR HEAT FLUX DISTRIBUTION OF CYLINDRICALLY ORTHOTROPIC FIBER REINFORCED COMPOSITES WITH SURFACE EFFECT

JUNHUA XIAO, YAOLING XU AND FUCHENG ZHANG

A theoretical study is conducted on the problem of two-dimensional steady-state heat transfer of composites with cylindrically orthotropic fiber with surface effect containing isotropic core. By introducing an appropriate coordinate transformation to convert the governing differential equation into a harmonic one, an analytical solution to the heat flux fields of the cylindrically orthotropic nanofiber reinforced composites is derived based on the surface theory model. Numerical examples provide a better understanding of interesting interaction effects of composite microstructures (geometric and physical parameters of the fiber and core) in heat flux distribution. The radial and circumferential heat flux distributions in the nanocomposites are investigated. The effects of size of the fiber, thermal conductivity of the core and radius of the core on the heat flux distribution are discussed.

## 1. Introduction

Carbon fiber reinforced composites have been extensively used in modern industries including sports equipment, civil engineering, mechanical engineering, aerospace structures, defense and automobile industries [DeValve and Pitchumani 2013; Peng et al. 2017], because of their high specific strength, modulus, stiffness, low density, thermal stability, and corrosion resistance [Khan et al. 2010; Wang et al. 2012; Li et al. 2017]. Different from common fibers, carbon fibers exhibit special heterogeneity and anisotropy [Hashin 1990; Christensen 1994], that is, polyacrylonitrile based carbon fibers generally exhibit circumferential alignment of the graphite basal planes, and pitch based carbon fibers typically show radial alignment [Yan et al. 2010; Avery and Herakovich 1986; Knott and Herakovich 1991].

Thermal performance is one of the most important properties of composites in many applications as thermal protections, heat shields and heat guides [Gori and Corasaniti 2014]. In recent years, significant progress has been made in addressing the effective thermal conductivity of composites from a fundamental perspective by using theoretical, numerical and experimental methods.

The knowledge of heat flux fields is also important to understanding and predicting the thermal properties of composite in many heat conduction problems [Frankel et al. 2008; Stokes-Griffin and Compston 2016]. The heat flux distribution in composites is a basilica problem in inverse heat transfer problem [Alifanov 1994; Orlande 2011]. The following are some representative literatures in recent years. By presenting a finite element model, Rodríguez and Cabeza [1999] investigated the heat flux distribution in a composite with cylindrically orthotropic and homogeneous fiber. Using a thermomechanical cohesive zone model, Hattiangadi and Siegmund [2005] studied the distribution of total heat flux drop ahead of the crack tip across an intact interface for different values of interface conductance. Based on the

*Keywords:* surface effect, nanofiber, size dependent, heat flux, cylindrically orthotropic fiber.

conjugate gradient method, Yang and Chang [2006] estimated the heat and moisture fluxes of a double-layer annular cylinder with interface resistance. Yin et al. [2008] derived the heat flux field for a single particle embedded in a graded material by using the equivalent inclusion method. Frankel et al. [2010] presented a new heat flux-temperature integral relationship for anisotropic materials and obtained both an exact analytic solution for temperature and heat flux. Yang et al. [2010] estimated the heat flux and temperature distributions for the system composed of a multilayer composite strip and semi-infinite foundation based on the conjugate gradient method and the discrepancy principle. Yan et al. [2010] examined the effects of the existence of the core and the cylindrical orthotropy of the fiber on the heat flux at the center of the fiber. Lee et al. [2012] developed an inverse analysis for simultaneously estimating the heat fluxes at the inner and outer boundary surfaces of a functionally graded hollow circular cylinder from the knowledge of temperature measurements taken within the cylinder. Shi et al. [2013] calculated the cold wall heat flux of silica-phenolic composite exposed to heat flux environments. Yang et al. [2013] solved the inverse hyperbolic heat conduction problem in estimating the inner-wall heat flux of a hollow cylinder from the knowledge of temperature measurements taken within the medium. Rylko [2015] presented the temperature distribution and the heat flux expressed in terms of a series in the radius of ideally conducting fibers in deterministic and random composites. Gounni and Alami [2017] studied the optimal allocation of the phase change material within a composite wall for surface temperature and heat flux reduction by an experimental approach.

To the best of our knowledge, the investigation on the distribution characteristics of the heat flux fields in the nanocomposites reinforced with cylindrically orthotropic fiber has not been reported. Classical heat transfer theory does not address size effect of the fibers in composites. However, size effect of the heat properties for nanocomposites often become prominent when the size of reinforced fibers are on the order of nanometer [Györy and Márkus 2014; Machrafi 2016; Sobolev 2017]. The surface effect of nanofibers plays an important role in heat flux fields in the nanocomposites because of the high surface-to-volume ratios of this solid material. By introducing interface physical constants, Gurtin-Murdoch surface theory [Gurtin and Murdoch 1975; Gurtin and Murdoch 1978; Gurtin et al. 1998] takes into account the nanoscale microresponse in the macroscopic response of the material, which has become an effective analytical method for studying microscopic and macroscopic properties of the nanocomposites. Duan and Karihaloo [2007] prove that when the thermoelastic term is included in the constitutive relation of interface stress model, there exists an exact relation between the effective coefficient of thermal expansion and the effective elastic moduli of the heterogeneous medium. Recent research [Xiao et al. 2018] shows that the surface theory model can be applied to solve the heat transfer problem of nanofiber reinforced composites.

This work investigates the heat flux distribution of composites reinforced with cylindrically orthotropic nanofiber under two dimensional steady-state heat transfer conditions. An analytical solution to the heat flux fields in the composites is derived by using the surface theory model. The effects of the fiber size, the core thermal conductivity and the core radius on the heat flux fields are discussed.

## 2. Model and complex variable elasticity theory

Consider a cylindrically orthotropic fiber with surface effect containing isotropic core under two dimensional steady-state heat conduction as shown in Figure 1, where  $(x, y)$  denotes the Cartesian coordinates

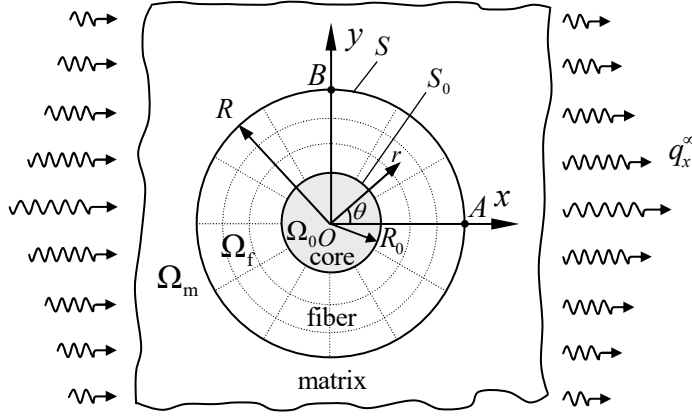


**Figure 1.** A cylindrically orthotropic fiber with surface effect containing isotropic core under far-field constant heat flux  $q_x^\infty$ .

and  $(r, \theta)$  denotes the polar coordinates. Random orientation of the graphite basal planes in the transverse plane of the fiber would result in a transversely isotropic core in the carbon fiber [Avery and Herakovich 1986; Knott and Herakovich 1991], which is shown in the Figure. The regions  $\Omega_0$ ,  $\Omega_f$ ,  $\Omega_m$  denote the isotropic fiber core, the cylindrically orthotropic nanofiber and the isotropic matrix, respectively. The contour  $S$  with a radius  $R$  denotes the interface between the fiber and the matrix, which possesses different thermal property from the fiber and the matrix. The contours  $S_0$  with a radius  $R_0$  denote the interfaces between the fiber core and the fiber. The subscripts 0, f, m denote the fiber core, the fiber and the matrix, respectively. Assuming the nanocomposites is subjected to a far-field constant heat flux  $q_x^\infty$  along the  $x$  axis. Based on the theory of Gurtin–Murdoch surface model [Gurtin and Murdoch 1975; Gurtin and Murdoch 1978; Gurtin et al. 1998], the nanofiber interface  $S$  has its own thermal property, which is regarded as a layer without thickness [Xiao et al. 2018].

The basic equation of the problem can be given as

$$\frac{\partial q_r}{\partial r} + \frac{q_r}{r} + \frac{\partial q_\theta}{r \partial \theta} = 0 \quad \text{in } \Omega_0, \Omega_f, \Omega_m, \quad (1)$$

$$\begin{bmatrix} H_r \\ H_\theta \end{bmatrix} = \begin{bmatrix} \partial T / \partial r \\ \frac{1}{r} (\partial T / \partial \theta) \end{bmatrix} \quad \text{in } \Omega_0, \Omega_f, \Omega_m, \quad (2)$$

$$\begin{Bmatrix} q_r \\ q_\theta \end{Bmatrix} = - \begin{bmatrix} k_r & 0 \\ 0 & k_\theta \end{bmatrix} \begin{Bmatrix} H_r \\ H_\theta \end{Bmatrix} \quad \text{in } \Omega_f, \quad (3)$$

$$\begin{Bmatrix} q_r \\ q_\theta \end{Bmatrix} = - \begin{bmatrix} k_i & 0 \\ 0 & k_i \end{bmatrix} \begin{Bmatrix} H_r \\ H_\theta \end{Bmatrix} \quad (i = 0, m) \quad \text{in } \Omega_0, \Omega_m, \quad (4)$$

where  $q$ ,  $H$  and  $T$  denote heat flux, temperature gradient and temperature, respectively;  $k_r$  and  $k_\theta$  are the radial and circumferential conductivities, respectively.

By substituting (2) and (3) into (1) yields the following governing differential equation:

$$\frac{\partial}{\partial r} \left( r \frac{\partial T}{\partial r} \right) + \gamma^2 \frac{1}{r} \frac{\partial^2 T}{\partial \theta^2} = 0 \quad \text{in } \Omega_f, \quad (5)$$

where  $\gamma = \sqrt{k_\theta/k_r}$ . Define a complex plane  $z$ :

$$z = x + iy = r e^{i\theta}. \quad (6)$$

In general,  $\gamma \neq 1$  (i.e.  $k_r \neq k_\theta$ ), equation (5) is not a harmonic equation. Introduce a new complex plane  $z_1$  as follows [Yan et al. 2010]

$$z_1 = r e^{i\theta_1}, \quad (7)$$

where  $\theta_1 = \theta/\gamma$ . In the  $z_1$ -plane, equation (5) is transformed into a harmonic equation:

$$\frac{\partial}{\partial r} \left( r \frac{\partial T}{\partial r} \right) + \frac{1}{r} \frac{\partial^2 T}{\partial \theta_1^2} = 0. \quad (8)$$

The transformation from the  $z$ -plane to the  $z_1$ -plane is not a conformal mapping. Introduce again a complex plane  $\zeta$  as follows

$$\zeta = z_1^\gamma = r^{\gamma-1} z. \quad (9)$$

It is a conformal mapping from  $z$ -plane to plane  $\zeta$ .

The temperature field  $T$  is a harmonic function in  $\zeta$ -plane and can be expressed as an analytical function  $\omega(\zeta)$ :

$$T = \frac{1}{2} [\omega(\zeta) + \overline{\omega(\zeta)}] = \text{Re}[\omega(\zeta)]. \quad (10)$$

Define the heat transfer rate  $\Phi$  along the arc  $\widehat{AB}$ :

$$\Phi = \frac{i}{2} \sqrt{k_r k_\theta} [\omega(\zeta) - \overline{\omega(\zeta)}]_A^B = -\sqrt{k_r k_\theta} \text{Im}[\omega(\zeta)]|_A^B. \quad (11)$$

By substituting (10) into (2) and (3), it is the following expressions are obtained that

$$\begin{cases} q_r = -\frac{\gamma}{r} k_r \text{Re}[\omega'(\zeta)\zeta] \\ q_\theta = \frac{1}{r} k_\theta \text{Im}[\omega'(\zeta)\zeta] \end{cases} \quad \text{in } \Omega_f. \quad (12)$$

Then, equation (12) can be rewritten as

$$\frac{q_r}{\gamma k_r} - i \frac{q_\theta}{k_\theta} = -\frac{1}{r} \{ \text{Re}[\omega'(\zeta)\zeta] + i \text{Im}[\omega'(\zeta)\zeta] \} = -\frac{\zeta}{r} \omega'(\zeta) \quad \text{in } \Omega_f. \quad (13)$$

When  $\gamma = 1$  (i.e.  $k_r = k_\theta = k$ ), equations (11) and (13) degenerate into the following expressions:

$$\Phi = \frac{i}{2} k [\omega(\zeta) - \overline{\omega(\zeta)}]_A^B = -k \text{Im}[\omega(\zeta)]|_A^B, \quad (14)$$

$$q_r - i q_\theta = -\frac{k}{r} \omega'(z) z, \quad (15)$$

$$q_x - i q_y = -k \omega'(z). \quad (16)$$



### 3. Exact solution to heat flux fields

On the interface  $S$ , the nonclassical heat transfer boundary conditions can be written as [Xiao et al. 2018]

$$q_r^f - q_r^m = \frac{1}{R} \frac{\partial q_\theta^S}{\partial \theta} \quad \text{on } S, \quad (17)$$

$$q_\theta^{S_1} = -k_s H_\theta^S \quad \text{on } S, \quad (18)$$

where  $k_s$  is the interface thermal constant.

For a coherent interface, the interfacial temperature gradient is equal to the associated temperature gradient in the abutting bulk materials, i.e.

$$H_\theta^S = H_\theta^f(R) = H_\theta^m(R). \quad (19)$$

Assuming the fiber-core interface  $S_0$  is perfect and the fiber-matrix interface  $S$  is imperfect, the boundary conditions at the interfaces  $S_0$  and  $S$  can be given as

$$T_0 = T_f \quad \text{on } S_0, \quad (20)$$

$$\Phi_0 = \Phi_f \quad \text{on } S_0, \quad (21)$$

$$T_f = T_m \quad \text{on } S, \quad (22)$$

$$q_r^f - q_r^m = -\frac{k_s}{R} \frac{\partial H_\theta^S}{\partial \theta} \quad \text{on } S. \quad (23)$$

In an annular region, the analytical function  $\omega(z)$  can be expanded into Laurent series [Muskhelishvili 1953]:

$$\omega(z) = a^* \ln z + \sum_{k=-\infty}^{\infty} a_k z^k, \quad (24)$$

where  $a^*$  and  $a_k$  are complex constants to be determined.

The complex potential  $\omega_0(z)$  and  $\omega_m(z)$  are expanded in  $z$ -plane and the complex potential  $\omega_f(\zeta)$  is expanded in  $\zeta$ -plane. It is seen that taking the following finite terms of the series can arrive at the exact solution:

$$\omega_0(z) = A_1 z \quad \text{in } \Omega_0, \quad (25)$$

$$\omega_f(\zeta) = B_1 \zeta + B_{-1} \frac{1}{\zeta} = B_1 r^{\gamma-1} z + \frac{B_{-1}}{r^{\gamma-1}} \frac{1}{z} \quad \text{in } \Omega_f, \quad (26)$$

$$\omega_m(z) = C_1 z + C_{-1} \frac{1}{z} \quad \text{in } \Omega_m, \quad (27)$$

where  $A_1$ ,  $B_1$ ,  $B_{-1}$ ,  $C_1$ , and  $C_{-1}$  are constants to be determined.

Substituting (27) into (16) and integrating with the far field condition  $(q_x^m - i q_y^m)|_{z \rightarrow \infty} = q_x^\infty - i q_y^\infty$ , we obtain

$$C_1 = -\frac{q_x^\infty}{k_m}. \quad (28)$$

From (20)–(23), one obtains the following expressions:

$$A_1 = B_1 R_0^{\gamma-1} + \frac{B_{-1}}{R_0^{\gamma+1}}, \quad (29)$$

$$k_0 A_1 = \sqrt{k_r k_\theta} \left( B_1 R_0^{\gamma-1} - \frac{B_{-1}}{R_0^{\gamma+1}} \right), \quad (30)$$

$$B_1 R^{\gamma-1} + \frac{B_{-1}}{R^{\gamma+1}} = C_1 + \frac{C_{-1}}{R^2}, \quad (31)$$

$$k_m \left( C_1 - \frac{C_{-1}}{R^2} \right) - \gamma k_r \left( B_1 R^{\gamma-1} - \frac{B_{-1}}{R^{\gamma+1}} \right) = \frac{k_s}{R} \left( C_1 + \frac{C_{-1}}{R^2} \right). \quad (32)$$

From (29)–(32), the coefficients  $B_1$ ,  $B_{-1}$ ,  $C_1$ , and  $C_{-1}$  can be expressed by  $A_1$  as follows:

$$B_1 = L_1 A_1 \quad B_{-1} = L_{-1} A_1 \quad C_1 = M_1 A_1 \quad C_{-1} = M_{-1} A_1, \quad (33)$$

where

$$\begin{aligned} L_1 &= \frac{R_0^{1-\gamma}}{2} \left( 1 + \frac{k_0}{\sqrt{k_r k_\theta}} \right), \\ L_{-1} &= \frac{R_0^{1+\gamma}}{2} \left( 1 - \frac{k_0}{\sqrt{k_r k_\theta}} \right), \\ M_1 &= \frac{1}{4k_m} \left[ \left( k_m + \frac{k_s}{R} + \gamma k_r \right) \left( 1 + \frac{k_0}{\sqrt{k_r k_\theta}} \right) \frac{R^{\gamma-1}}{R_0^{\gamma-1}} + \left( k_m + \frac{k_s}{R} - \gamma k_r \right) \frac{R_0^{\gamma+1}}{R^{\gamma+1}} \left( 1 - \frac{k_0}{\sqrt{k_r k_\theta}} \right) \right], \\ M_{-1} &= \frac{R^2}{4k_m} \left[ \left( k_m - \frac{k_s}{R} - \gamma k_r \right) \left( 1 + \frac{k_0}{\sqrt{k_r k_\theta}} \right) \frac{R^{\gamma-1}}{R_0^{\gamma-1}} + \left( k_m - \frac{k_s}{R} + \gamma k_r \right) \frac{R_0^{\gamma+1}}{R^{\gamma+1}} \left( 1 - \frac{k_0}{\sqrt{k_r k_\theta}} \right) \right]. \end{aligned} \quad (34)$$

From (28) and (33), it follows that

$$\begin{aligned} A_1 &= -\frac{q_x^\infty}{Q}, \\ Q &= \frac{1}{4} \left[ \left( k_m + \frac{k_s}{R} + \gamma k_r \right) \left( 1 + \frac{k_0}{\sqrt{k_r k_\theta}} \right) \frac{R^{\gamma-1}}{R_0^{\gamma-1}} + \left( k_m + \frac{k_s}{R} - \gamma k_r \right) \frac{R_0^{\gamma+1}}{R^{\gamma+1}} \left( 1 - \frac{k_0}{\sqrt{k_r k_\theta}} \right) \right]. \end{aligned} \quad (35)$$

From (12), (15), (16), (25)–(27), the overall heat flux fields in the core, fiber and matrix can be expressed as

$$\begin{Bmatrix} q_r^0 \\ q_\theta^0 \end{Bmatrix} = k_0 A_1 \begin{bmatrix} -\cos \theta \\ \sin \theta \end{bmatrix} \quad \text{in the core,} \quad (36)$$

$$\begin{Bmatrix} q_r^f \\ q_\theta^f \end{Bmatrix} = \begin{bmatrix} \gamma k_r \cos \theta \left( \frac{B_{-1}}{r^{\gamma+1}} - B_1 r^{\gamma-1} \right) \\ k_\theta \sin \theta \left( \frac{B_{-1}}{r^{\gamma+1}} + B_1 r^{\gamma-1} \right) \end{bmatrix} \quad \text{in the fiber,} \quad (37)$$

$$\begin{Bmatrix} q_r^m \\ q_\theta^m \end{Bmatrix} = k_m \begin{bmatrix} \cos \theta \left( \frac{C_{-1}}{r^2} - C_1 \right) \\ \sin \theta \left( \frac{C_{-1}}{r^2} + C_1 \right) \end{bmatrix} \quad \text{in the matrix,} \quad (38)$$

where the expression of coefficients  $A_1$ ,  $B_1$ ,  $B_{-1}$ ,  $C_1$ , and  $C_{-1}$  are shown in (33)–(35).

#### 4. Results and discussion

As an example discussion, take the carbon fiber reinforced epoxy resin as the computational object in this work. The conductivity of the epoxy resin matrix is  $k_m = 0.19 \text{ W/mK}$ . The unit of the interface thermal constant  $k_s$  is  $\text{W/K}$ . Due to the lack of research on the interface thermal constant of the nanofiber in the existing literature, it is assumed that the ration of the thermal constant of the interface to that of the matrix is a real constant  $k_s/k_m = 2 \times 10^{-10} \text{ m}$  according to the theory of surface elasticity [Xiao et al. 2018; Luo and Wang 2009].

The radial and circumferential conductivities of the cylindrically orthotropic fiber are not available and hardly measured by an experiment [Yan et al. 2010]. According to a reasonable assumption by Hasselman et al. [1993], the parameters are taken as  $k_r/k_m = 100$  and  $k_\theta/k_m = 2.4$  for a radially orthotropic fiber, and  $k_r/k_m = 2.4$  and  $k_\theta/k_m = 100$  for a circumferentially orthotropic fiber. For the convenience of comparison, choose the parameters with  $k_r/k_m = k_\theta/k_m = \sqrt{240}$  for a transversely isotropic fiber [Yan et al. 2010].

**Example 1.** The variations of the dimensionless heat fluxes along the interfaces  $S$  of the fiber are plotted in Figure 2, where  $k_m = 0.19 \text{ W/mK}$ ,  $k_s/k_m = 2 \times 10^{-10} \text{ m}$ ,  $R_0/R = 0.1$ ,  $k_0/k_m = 51.2$  and fiber radius  $R = 5 \text{ nm}$ .

With the increase in angle  $\theta$  from  $0^\circ$  to  $90^\circ$ , the radial heat flux decreases to zero gradually, while the circumferential heat flux increases from zero monotonously. It is seen that when the radial and circumferential conductivities of the fiber change, it has little effect on the radial heat flux, whereas it has a great effect on circumferential heat flux.

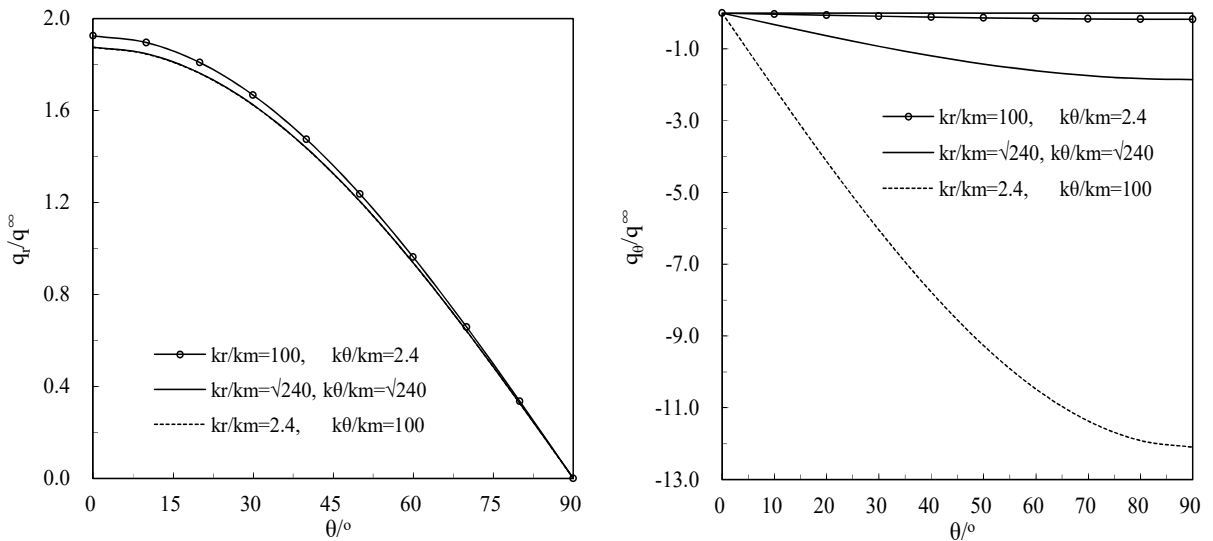


**Figure 2.** Distributions of the dimensionless heat fluxes on the interfaces  $S$  of the fiber: radial heat flux  $q_r/q_\infty$  (left) and circumferential heat flux  $q_\theta/q_\infty$  (right).

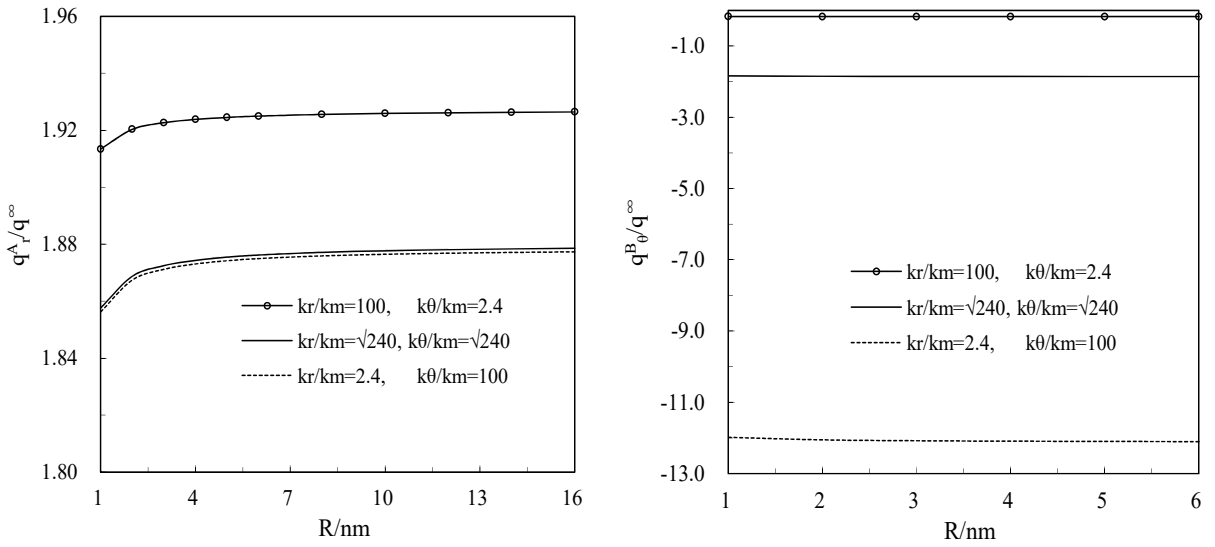


**Figure 3.** Effects of the size of the fiber on the dimensionless heat fluxes: radial heat flux  $q_r/q^\infty$  at point A (left) and circumferential heat flux  $q_\theta/q^\infty$  at point B (right).

**Example 2.** The effects of size of the fiber on the dimensionless heat fluxes at point A (maximum radial heat flux on the fiber interface as seen in Figure 2, left) and point B (maximum circumferential heat flux on the fiber interface as seen in Figure 2, right) are depicted in Figure 3, where  $k_m = 0.19 \text{ W/mK}$ ,  $k_s/k_m = 2 \times 10^{-10} \text{ m}$ ,  $R_0/R = 0.1$  and  $k_0/k_m = 51.2$ .

Figure 3 (left) shows that when the size of the fiber is at the nanometer scale, the radial heat flux at point A is size dependent, while the circumferential heat flux at point B has nothing to do with the size of the fiber.

**Example 3.** The variations of the dimensionless heat fluxes at points A and B with the nondimensional conductivity of the core  $k_0/k_m$  are plotted in Figure 4, where  $k_m = 0.19 \text{ W/mK}$ ,  $k_s/k_m = 2 \times 10^{-10} \text{ m}$ ,  $R_0/R = 0.1$  and fiber radius  $R = 5 \text{ nm}$ .

It is seen that with the increase of  $k_0/k_m$ , the influence of the conductivity of the core on the radial heat flux at point A is significant when  $k_r > k_\theta$ , while becomes slight when  $k_r < k_\theta$ . The change in the conductivity of the core has little effect on the circumferential heat flux at point B on the fiber interface.

**Example 4.** The variations in the dimensionless heat fluxes at points A and B with the nondimensional radius  $R_0/R$  of the core are plotted in Figure 5, where  $k_m = 0.19 \text{ W/mK}$ ,  $k_s/k_m = 2 \times 10^{-10} \text{ m}$ ,  $k_0/k_m = 51.2$  and fiber radius  $R = 5 \text{ nm}$ .

It is seen that the radial and circumferential heat fluxes increase monotonically when the core radius  $R_0/R$  increases gradually from 0 to 1. Figure 5 illustrates an interesting phenomenon in which the effect of the core radius on the heat fluxes depends on the cylindrical orthotropy of the fiber. If  $k_r \gg k_\theta$ , the radial heat flux at point A first increases significantly ( $R_0/R < 0.1$ ), and then slowly tend to a constant value. For the circumferential heat flux at point B, the influence of the core radius can be ignored. If  $k_r \ll k_\theta$ , the radial heat flux at point A first almost unchanged ( $R_0/R < 0.8$ ), and then drastically increases.

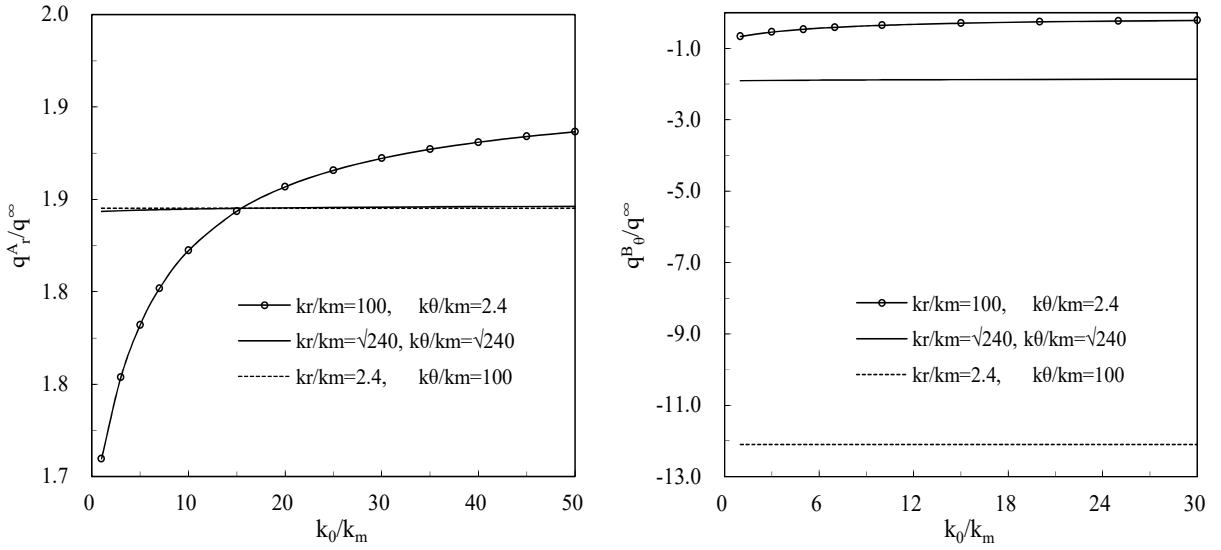


**Figure 4.** Effects of the nondimensional conductivity of the core  $k_0/k_m$  on the dimensionless heat fluxes: radial heat flux  $q_r/q^\infty$  at point A (left) and circumferential heat flux  $q_\theta/q^\infty$  at point B (right).

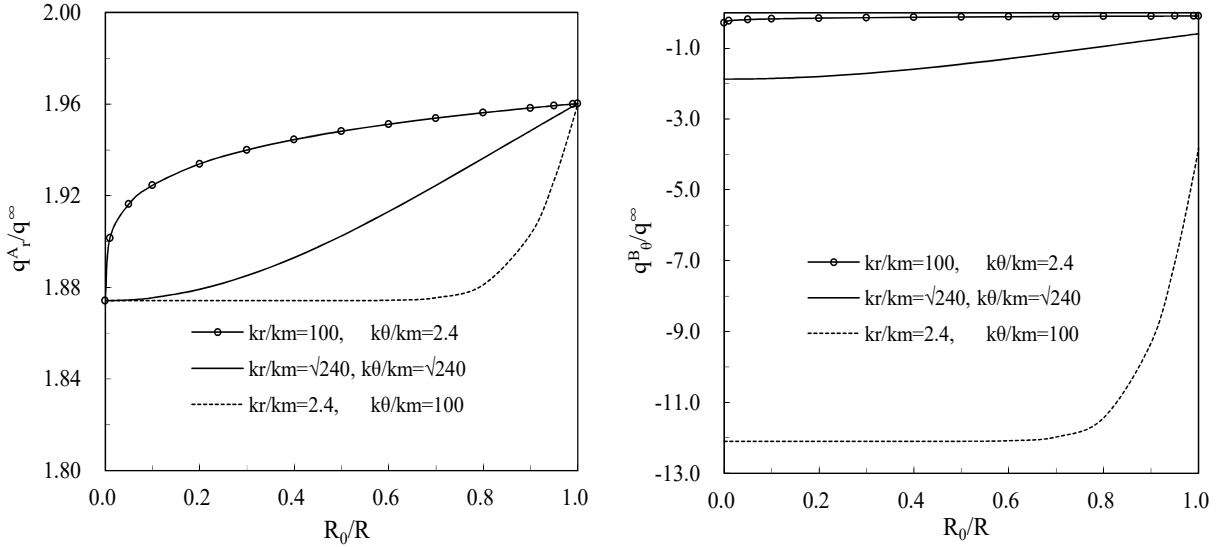


**Figure 5.** Effects of the nondimensional radius  $R_0/R$  of the core on the dimensionless heat fluxes: radial heat flux  $q_r/q^\infty$  at point A (left) and circumferential heat flux  $q_\theta/q^\infty$  at point B (right).

For the circumferential heat flux at point B, the influence of the core radius is slight when  $R_0/R < 0.8$ , but becomes significant with the increase of  $R_0/R$ .

## 5. Conclusions

The problem of composites reinforced with cylindrically orthotropic nanofiber under two-dimensional steady-state heat conduction is investigated based on the surface theory model and the theory of complex variable elasticity. An analytical solution for the heat flux fields in the nanocomposites is obtained. The effects of fiber size, core thermal conductivity and core radius on the heat flux fields are discussed. The major results are: (a) Changes in the radial and circumferential conductivities of the fiber have little effect on the radial heat flux, but have a great effect on circumferential heat flux. (b) When the size of the fiber is at the nanometer scale, the radial heat fluxes are size dependent and the circumferential heat fluxes shows size independent. (c) The influences of the core thermal conductivity and the core radius on the radial and circumferential heat flux depend on the cylindrical orthotropy of the fiber.

## Acknowledgments

This work was supported by the National Natural Science Foundation of China (11302186, 51471146) and the Hebei Province High School Top Young Talent (BJ2014058).

## References

- [Alifanov 1994] O. M. Alifanov, *Inverse heat transfer problems*, Springer, New York, 1994.
- [Avery and Herakovich 1986] W. B. Avery and C. T. Herakovich, “Effect of fiber anisotropy on thermal stresses in fibrous composites”, *J. Appl. Mech. (ASME)* **53**:4 (1986), 751–756.
- [Christensen 1994] R. M. Christensen, “Properties of carbon fibers”, *J. Mech. Phys. Solids* **42**:4 (1994), 681–695.
- [DeValve and Pitchumani 2013] C. DeValve and R. Pitchumani, “Experimental investigation of the damping enhancement in fiber-reinforced composites with carbon nanotubes”, *Carbon* **63** (2013), 71–83.
- [Duan and Karihaloo 2007] H. L. Duan and B. L. Karihaloo, “Thermo-elastic properties of heterogeneous materials with imperfect interfaces: generalized Levin’s formula and Hill’s connections”, *J. Mech. Phys. Solids* **55**:5 (2007), 1036–1052.
- [Frankel et al. 2008] J. I. Frankel, M. Keyhani, R. V. Arimilli, and J. Wu, “A new multidimensional integral relationship between heat flux and temperature for direct internal assessment of heat flux”, *Z. Angew. Math. Phys.* **59**:5 (2008), 869–888.
- [Frankel et al. 2010] J. I. Frankel, M. Keyhani, B. Elkins, and R. V. Arimilli, “A new anisotropic, two-dimensional, transient heat flux-temperature integral relationship for half-space diffusion”, *J. Appl. Math. Mech.* **90**:2 (2010), 161–170.
- [Gori and Corasaniti 2014] F. Gori and S. Corasaniti, “Effective thermal conductivity of composites”, *Int. J. Heat Mass Transf.* **77** (2014), 653–661.
- [Gounni and Alami 2017] A. Gounni and M. E. Alami, “The optimal allocation of the PCM within a composite wall for surface temperature and heat flux reduction: an experimental approach”, *Appl. Therm. Eng.* **127** (2017), 1488–1494.
- [Gurtin and Murdoch 1975] M. E. Gurtin and A. I. Murdoch, “A continuum theory of elastic material surfaces”, *Arch. Ration. Mech. Anal.* **57**:4 (1975), 291–323.
- [Gurtin and Murdoch 1978] M. E. Gurtin and A. I. Murdoch, “Surface stress in solids”, *Int. J. Solids Struct.* **14**:6 (1978), 431–440.
- [Gurtin et al. 1998] M. E. Gurtin, J. Weissmüller, and F. Larché, “A general theory of curved deformable interfaces in solids at equilibrium”, *Philos. Mag. A* **78**:5 (1998), 1093–1109.
- [Györy and Márkus 2014] E. Györy and F. Márkus, “Size dependent thermal conductivity in nano-systems”, *Thin Solid Films* **565** (2014), 89–93.
- [Hashin 1990] Z. Hashin, “Thermoelastic properties and conductivity of carbon/carbon fiber composites”, *Mech. Mater.* **8**:4 (1990), 293–308.

- [Hasselman et al. 1993] D. P. H. Hasselman, K. Y. Donaldson, and J. R. Thomas Jr, “Effective thermal conductivity of uniaxial composite with cylindrically orthotropic carbon fibers and interfacial thermal barrier”, *J. Compos. Mater.* **27**:6 (1993), 637–644.
- [Hattiangadi and Siegmund 2005] A. Hattiangadi and T. Siegmund, “A numerical study on interface crack growth under heat flux loading”, *Int. J. Solids Struct.* **42**:24–25 (2005), 6335–6355.
- [Khan et al. 2010] S. U. Khan, A. Munir, R. Hussain, and J.-K. Kim, “Fatigue damage behaviors of carbon fiber-reinforced epoxy composites containing nanoclay”, *Compos. Sci. Technol.* **70**:14 (2010), 2077–2085.
- [Knott and Herakovich 1991] T. W. Knott and C. T. Herakovich, “Effect of fiber orthotropy on effective composite properties”, *J. Compos. Mater.* **25**:6 (1991), 732–759.
- [Lee et al. 2012] H.-L. Lee, W.-J. Chang, S.-H. Sun, and Y.-C. Yang, “Estimation of temperature distributions and thermal stresses in a functionally graded hollow cylinder simultaneously subjected to inner-and-outer boundary heat fluxes”, *Compos. B Eng.* **43**:2 (2012), 786–792.
- [Li et al. 2017] Y. Li, S. Cai, and X. Huang, “Multi-scaled enhancement of damping property for carbon fiber reinforced composites”, *Compos. Sci. Technol.* **143** (2017), 89–97.
- [Luo and Wang 2009] J. Luo and X. Wang, “On the anti-plane shear of an elliptic nano inhomogeneity”, *Eur. J. Mech. A Solids* **28**:5 (2009), 926–934.
- [Machrafi 2016] H. Machrafi, “An extended thermodynamic model for size-dependent thermoelectric properties at nanometric scales: application to nanofilms, nanocomposites and thin nanocomposite films”, *Appl. Math. Model.* **40**:3 (2016), 2143–2160.
- [Muskhelishvili 1953] N. I. Muskhelishvili, *Some basic problems of the mathematical theory of elasticity*, Noordhoff, Groningen, 1953.
- [Orlande 2011] H. R. B. Orlande, “Inverse heat transfer problems”, *Head Transf. Eng.* **32**:9 (2011), 715–717.
- [Peng et al. 2017] M. Peng, Y. Zhou, G. Zhou, and H. Yao, “Triglycidyl para-aminophenol modified montmorillonites for epoxy nanocomposites and multi-scale carbon fiber reinforced composites with superior mechanical properties”, *Compos. Sci. Technol.* **148** (2017), 80–88.
- [Rodríguez and Cabeza 1999] A. C. Rodríguez and J. M. G. Cabeza, “Effect of cylindrically orthotropic carbon fibers with transversely isotropic core on effective thermal conductivity of unidirectional composites”, *J. Compos. Mater.* **33**:11 (1999), 984–1001.
- [Rylko 2015] N. Rylko, “Edge effects for heat flux in fibrous composites”, *Comput. Math. Appl.* **70**:10 (2015), 2283–2291.
- [Shi et al. 2013] S. Shi, J. Liang, and G. Lin, G. Fang, “High temperature thermomechanical behavior of silica-phenolic composite exposed to heat flux environments”, *Compos. Sci. Technol.* **87**:9 (2013), 204–209.
- [Sobolev 2017] S. L. Sobolev, “Discrete space-time model for heat conduction: application to size-dependent thermal conductivity in nano-films”, *Int. J. Heat Mass Transf.* **108** (2017), 933–939.
- [Stokes-Griffin and Compston 2016] C. M. Stokes-Griffin and P. Compston, “An inverse model for optimisation of laser heat flux distributions in an automated laser tape placement process for carbon-fibre/PEEK”, *Compos. A Appl. Sci. Manuf.* **88** (2016), 190–197.
- [Wang et al. 2012] W. G. Wang, B. L. Xiao, and Z. Y. Ma, “Evolution of interfacial nanostructures and stress states in Mg matrix composites reinforced with coated continuous carbon fibers”, *Compos. Sci. Technol.* **72**:2 (2012), 152–158.
- [Xiao et al. 2018] J. Xiao, Y. Xu, and F. Zhang, “An analytical method for predicting the effective transverse thermal conductivity of nano coated fiber composites”, *Compos. Struct.* **189** (2018), 553–559.
- [Yan et al. 2010] P. Yan, C. P. Jiang, and F. Song, “A complex variable solution of two-dimensional heat conduction of composites reinforced with periodic arrays of cylindrically orthotropic fibers”, *Comput. Mater. Sci.* **50**:2 (2010), 704–713.
- [Yang and Chang 2006] Y.-C. Yang and W.-J. Chang, “Simultaneous inverse estimation for boundary heat and moisture fluxes of a double-layer annular cylinder with interface resistance”, *Appl. Math. Comput.* **176**:2 (2006), 594–608.
- [Yang et al. 2010] Y.-C. Yang, S.-S. Chu, W.-J. Chang, and T.-S. Wu, “Estimation of heat flux and temperature distributions in a composite strip and homogeneous foundation”, *Int. Commun. Heat Mass* **37**:5 (2010), 495–500.
- [Yang et al. 2013] Y.-C. Yang, W.-L. Chen, H.-M. Chou, and J. L. L. Salazar, “Inverse hyperbolic thermoelastic analysis of a functionally graded hollow circular cylinder in estimating surface heat flux and thermal stresses”, *Int. J. Heat Mass Transf.* **60** (2013), 125–133.

[Yin et al. 2008] H. M. Yin, G. H. Paulino, W. G. Buttlar, and L. Z. Sun, “Heat flux field for one spherical inhomogeneity embedded in a functionally graded material matrix”, *Int. J. Heat Mass Transf.* **51**:11 (2008), 3018–3024.

Received 27 May 2018. Revised 2 Sep 2018. Accepted 28 Sep 2018.

JUNHUA XIAO: [xiaojunhua@ysu.edu.cn](mailto:xiaojunhua@ysu.edu.cn)

Key Laboratory of Mechanical Reliability for Heavy Equipments and Large Structures of Hebei Province, Yanshan University, Qinhuangdao 066004, China

YAOLING XU: [xylysu@163.com](mailto:xylysu@163.com)

Key Laboratory of Mechanical Reliability for Heavy Equipments and Large Structures of Hebei Province, Yanshan University, Qinhuangdao 066004, China

FUCHENG ZHANG: [zfc@ysu.edu.cn](mailto:zfc@ysu.edu.cn)

State Key Laboratory of Metastable Materials Science and Technology, Yanshan University, Qinhuangdao 066004, China



## STRAIN GRADIENT FRACTURE OF A MODE III CRACK IN AN ELASTIC LAYER ON A SUBSTRATE

JINE LI AND BAOLIN WANG

This paper studies the problem of a mode III crack in an elastic layer on a substrate under the framework of strain gradient elasticity theory. The effects of volumetric and surface strain gradient parameters on the crack tip asymptotic stress and crack shape are investigated. Due to strain gradient effect, the crack opening, the magnitude of the stress ahead of the crack tip, and the stress intensity factor are significantly higher than those in classical linear elastic fracture mechanics. More significantly, the direction of the stress ahead of the crack tip with strain gradient is opposite to that in the classical linear elastic fracture mechanics. The conventional linear elastic fracture mechanics results are recovered when the gradient parameter reduces to zero. The influence of the substrate on the fracture mechanics parameters is very significant when the strain gradient effect of the materials is considered.

### 1. Introduction

Continuum methods, being less computationally intensive, have been extensively used to investigate the macro structural behavior on theoretical as well as the empirical grounds. Classical continuum elasticity theories assume that the stresses in a material point depend only on the strain components at that point. They do not account for the contributions of strain gradients therefore can not account for size effects of materials, which are more evident when the dimensions of the structures are scaled down to the micro and nano-domains. In that case, the material microstructural length scales become comparable to the length scale of deformation field that tends to cause non-homogenous and scale/size dependent mechanical behavior [Giannakopoulos and Stamoulis 2007].

Size dependent mechanical behavior in micro-scale elements have been observed extensively in experiments [Fleck et al. 1994; Stolken 1997; Ma and Clarke 1995; McElhaney et al. 1998; Nix 1989; Poole et al. 1996; Stelmashenko et al. 1993]. Size dependence of the stiffness of the material was also confirmed by micro-cantilever experiments conducted by McFarland and Colton [2005]. It has been understood that the non-classical continuum theories such as the higher-order gradient theories and couple stress theory can interpret the scale-dependent behaviour of materials. Mindlin and Tiersten [1962], Toupin [1962], and Koiter [1964] introduced the couple stress elasticity theory, incorporating two higher order material constants to predict the size effects. The higher-order strain gradient theory was introduced by Mindlin [1965] that includes the effect of the first and second derivatives of the strain tensor on the strain energy density. Lam et al. [2003] introduced three higher-order material constants in the constitutive equations of the modified strain gradient theory. In several modern theories, the response at a certain scale is influence by a characteristic length at the lowest level [Benvenuti and Simone 2013]. This is very evident in the case of lattice system potential energy that depends on the inter-atomic distance [Kiang et al. 1998]. In

*Keywords:* Strain gradient elasticity, film-substrate structure, mode III crack, crack tip field, fracture mechanics.

order to cater for the underlying microstructure into the continuum theory, higher order strain gradient theories were presented by Mindlin and Eshel [1968].

On the other hand, strain gradient effects become important near a crack tip because of the strain singularity, particularly when the size of fracture process zone is on the order of the intrinsic material length. Over the years, a few studies related to a crack in an infinite medium were conducted based on gradient elasticity theories. The pioneering works are gradient elasticity with mode III cracking investigated by Vardoulakis et al. [1996], Exadaktylos et al. [1996], and subsequently by Exadaktylos [1998] for the mode I fracture and Exadaktylos and Vardoulakis [2001] for the scale related fracture in rock mechanics. In a series of excellent studies, Fannjiang et al. [2002], Paulino et al. [2003], and Chan et al. [2008] applied gradient elasticity theory to mode III crack problems in functionally graded materials for cracks perpendicular and parallel to the material gradation direction, respectively. Some interesting information related to dislocation based-gradient elastic fracture mechanics for the anti-plane crack problem is discussed by Mousavi and Aifantis [2005]. Karimipour and Fotuhi [2017] carried out a comprehensive study for an anti-plane infinite plane with multiple cracks. In a series of studies, Wu and his colleagues have explored the thermally induced fracture of interface crack in bi-material structures [Wu et al. 2016a], crack tip field and crack extension in functionally graded materials [Shi et al. 2014], and film/substrate structures with ferroelectric effect [Qiu et al. 2018; Wu et al. 2016b].

Furthermore, investigations of cracking of a surface layer on a substrate of different materials have its root application for ensuring the reliability of coating/substrate structures [Grosskreutz and Mcneilt 1969; Kim and Nairn 2000]. Fracture mechanics analysis of such problem has attracted interests from numerous researchers including world-class scientist in the field (e.g., Hutchinson et al. 1987; Schulze and Erdogan 1998). So far, fracture mechanics of strain gradient materials have been limited to an infinite medium so that the only length parameter is the crack size. Strain gradient fracture of layered composite materials, however, is very rare. Therefore, this paper investigates the problem of an anti-plane (mode III) crack in an elastic layer on a substrate. The crack opening displacements, the stress at the crack tip front and the stress intensity factors are shown graphically. Many observations different from those of the conventional linear elastic fracture mechanics are observed.

## 2. Anti-plane deformation with strain gradient effects

This paper considers a cracked strain gradient layer on a substrate of different material as shown in Figure 1. The crack has length  $2a$  and is at the interface of two strain gradient layers of heights  $h_1$  and  $h_2$ , respectively. We consider the anti-plane problem such that the only non-vanishing displacement component is along the  $z$  axis and is denoted as  $w$ .

The constitutive equations and theoretical formulations for the anti-plane deformation of strain gradient materials are similar to those adopted by Vardoulakis et al. [1996] and Exadaktylos [1998]. There are two material length parameters that are responsible for material volumetric and surface strain gradient terms. These material constants are denoted as  $l$  and  $l'$ , respectively. This theory has been successfully employed to study the size effects in bending of micro-cantilever beams [Aifantis 2016], twisting of micro-wires [Aifantis 2011], and fracture [Giannakopoulos and Stamoulis 2007]. According to gradient elasticity theory, the stresses and double stresses derived from the constitutive equations of gradient elasticity with surface energy are given by the following equations (see [Chan et al. 2008; Paulino et al.

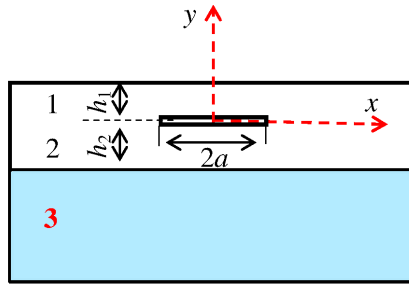


**Figure 1.** A crack in a strain gradient layer on a substrate: the strain gradient layer (1, 2) and the substrate (3).

2003; Vardoulakis et al. 1996], for example):

$$\tau_x = G \left[ \frac{\partial w}{\partial x} - l^2 \nabla^2 \frac{\partial w}{\partial x} \right], \quad \tau_y = G \left[ \frac{\partial w}{\partial y} - l^2 \nabla^2 \frac{\partial w}{\partial y} \right], \quad (1a)$$

$$\mu_{xx} = Gl^2 \frac{\partial^2 w}{\partial x^2}, \quad \mu_{xy} = Gl^2 \frac{\partial^2 w}{\partial x \partial y}, \quad (1b)$$

$$\mu_{yx} = G \left[ -l' \frac{\partial w}{\partial x} + l^2 \frac{\partial^2 w}{\partial x \partial y} \right], \quad \mu_{yy} = G \left[ -l' \frac{\partial w}{\partial y} + l^2 \frac{\partial^2 w}{\partial y^2} \right]. \quad (1c)$$

Here  $\nabla^2 = \partial^2/\partial x^2 + \partial^2/\partial y^2$ ,  $l$  and  $l^2$  are the volumetric and surface material characteristic lengths, respectively,  $G$  is the shear modulus,  $\tau$  is the stress tensor, and  $\mu$  is the double stress tensor,  $l$  and  $l^2$  are characteristic material lengths related to volume and surface energy, respectively, restricted (in order for the strain energy density to be positive definite) such that  $-1 < l'/l < 1$  [Exadaktylos et al. 1996; Vardoulakis et al. 1996]. This means that the surface length  $l'$  cannot exist alone (i.e.  $l' \neq 0$  and  $l = 0$  is not acceptable). When the surface energy  $l'$  is omitted, the closed form solution for an infinite medium with a crack has been obtained by Zhang et al. [1998].

The constitutive equations (1a) and (1b) show that the high order strains are considered however the high order stresses are ignored. The equilibrium equation remains the same as the classical one and is  $\partial \tau_x / \partial x + \partial \tau_y / \partial y = 0$ . This can be expressed in terms of the displacement component  $w$  with the help of (1a) as

$$\left[ \frac{\partial^2 w}{\partial x^2} + \frac{\partial^2 w}{\partial y^2} \right] - l^2 \left[ \frac{\partial^4 w}{\partial x^4} + 2 \frac{\partial^4 w}{\partial x^2 \partial y^2} + \frac{\partial^4 w}{\partial y^4} \right] = 0. \quad (2)$$

The general solution of the fourth order differential Equation (2) may be represented as  $w(x, y) = w^c(x, y) + w^s(x, y)$ , where  $w^c$  is the general solution of the harmonic equation  $\partial^2 w / \partial x^2 + \partial^2 w / \partial y^2 = 0$  and  $w^s$  is a particular solution of (2). The application of Fourier transform gives the solution of harmonic equation as

$$w^c(x, y) = \frac{1}{2\pi} \int_{-\infty}^{\infty} [A(s) e^{-|s|y} + C(s) e^{|s|y}] e^{-isx} ds. \quad (3a)$$

A particular solution of (2) can be given as

$$w^g(x, y) = \frac{1}{2\pi} \int_{-\infty}^{\infty} [B(s) e^{-|s_1|y} + D(s) e^{|s_1|y}] e^{-isx} ds, \quad (3b)$$

where  $|s_1| = \sqrt{s^2 + (1/l^2)}$ . Combining (3a) and (3b) gives the general solution of (2):

$$w(x, y) = \frac{1}{2\pi} \int_{-\infty}^{\infty} [A(s) e^{-|s|y} + B(s) e^{-|s_1|y} + C(s) e^{|s|y} + D(s) e^{|s_1|y}] e^{-isx} ds. \quad (4)$$

The constants  $A(s)$ ,  $B(s)$ ,  $C(s)$ , and  $D(s)$  are to be determined from the boundary conditions of the problem. For the purpose of the following analysis, the shear stress  $\tau_y(x, y)$  obtained from (1b) and (4) is written as

$$\tau_y(x, y) = -\frac{G}{2\pi} \int_{-\infty}^{\infty} |s| [A(s) e^{-|s|y} - C(s) e^{|s|y}] e^{-isx} ds, \quad (5)$$

and the double stress  $\mu_{yy}(x, y)$  obtained from (1c) and (4) is written as

$$\begin{aligned} \mu_{yy} = \frac{Gl'}{2\pi} \int_{-\infty}^{\infty} \left[ |s| A(s) e^{-|s|y} + |s_1| B(s) e^{-|s_1|y} \right] e^{-isx} ds \\ + \frac{Gl^2}{2\pi} \int_{-\infty}^{\infty} \left[ \begin{matrix} A(s) e^{-|s|y} s^2 + B(s) e^{-|s_1|y} s_1^2 \\ C(s) e^{|s|y} s^2 + D(s) e^{|s_1|y} s_1^2 \end{matrix} \right] e^{-isx} ds. \end{aligned} \quad (6)$$

In the following analysis, we will use the subscripts 1, 2 and 3 to distinguish the regions  $0 \leq y \leq h_1$ ,  $-h_2 \leq y \leq 0$ , and  $y \leq -h_2$ , respectively (see Figure 1). The crack is at the  $y = 0$  plane and the interface of the structure is at the  $y = -h_2$  plane. The displacement, stress and double stress of the substrate layer are, respectively

$$w_3(x, y) = \frac{1}{2\pi} \int_{-\infty}^{\infty} [C_3(s) e^{|s|y} + D_3(s) e^{|s_3|y}] e^{-isx} ds, \quad (7)$$

$$\tau_y(x, y) = \frac{G_s}{2\pi} \int_{-\infty}^{\infty} |s| C_3(s) e^{|s|y} e^{-isx} ds, \quad (8)$$

and

$$\begin{aligned} \mu_{3yy} = \frac{G_s l'_s}{2\pi} \int_{-\infty}^{\infty} [-|s| C_3(s) e^{|s|y} - |s_3| D_3(s) e^{|s_3|y}] e^{-isx} ds \\ + \frac{G_s l^2}{2\pi} \int_{-\infty}^{\infty} [C_3(s) e^{|s|y} s^2 + D_3(s) e^{|s_3|y} s_3^2] e^{-isx} ds, \end{aligned} \quad (9)$$

where  $|s_3| = \sqrt{s^2 + (1/l_3^2)}$ , and where  $l_3$  is the strain gradient parameter of the substrate layer.

### 3. The crack problem and its solution

The stress free conditions on the top surface requires that  $\tau_{1y}(x, h_1) = 0$  and  $\mu_{1yy}(x, h_1) = 0$ . The transmission conditions for ideal interface imply continuity of the stress, double stress, displacements and rotations [Piccolroaz et al. 2012]. Thus  $\tau_{1y}(x, 0) = \tau_{2y}(x, 0)$ ,  $\mu_{1yy}(x, 0) = \mu_{2yy}(x, 0)$ ,  $\partial w_1(x, 0)/\partial y =$

$\partial w_2(x, 0)/\partial y$ ,  $\tau_{2y}(x, -h_2) = \tau_{3y}(x, -h_2)$ ,  $\mu_{2yy}(x, -h_2) = \mu_{3yy}(x, -h_2)$ ,  $w_2(x, -h_2) = w_3(x, -h_2)$ . These represent the continuity conditions of the displacement and stress at the bonded region of the interfaces. As usually in the fracture mechanics analysis, the crack surfaces are assumed to be subjected to an applied anti-plane shear stress  $p(x)$  such that the following mixed boundary conditions on the  $y = 0$  plane hold (these boundary conditions were obtained from the variational principle and have been used by Paulino et al. [2003] and Chan et al. [2008])

$$\tau_y(x, 0) = -p(x), \quad |x| < a, \quad (10a)$$

$$w_1(x, 0) - w_2(x, 0) = 0, \quad |x| \leq a. \quad (10b)$$

In order to determine the full-field solution of the problem, we also introduce a discontinuity function  $g(x)$  along the cracked plane according to

$$g(x) = \frac{\partial[w_1(x, 0) - w_2(x, 0)]}{\partial x}. \quad (11)$$

By this definition, the continuity condition for the displacement on the  $y = 0$  plane requires that  $g(x) = 0$  for  $|x| \geq a$  and  $\int_{-a}^a g(x) dx = 0$ , which is the single-value condition.

Substituting (4) into (11) and with Fourier inversion, a relationship between  $A(s)$ ,  $B(s)$ ,  $C(s)$ , and  $D(s)$  can be obtained:

$$[A_1(s) + B_1(s) + C_1(s) + D_1(s)] - [A_2(s) + B_2(s) + C_2(s) + D_2(s)] = \frac{i}{2s} \int_{-a}^a g(r) e^{isr} dr. \quad (12)$$

As a result,  $A_i(s)$ ,  $B_i(s)$ ,  $C_i(s)$  and  $D_i(s)$  ( $i = 1, 2, 3$ ) can be expressed in terms of the single unknown function  $g(x)$ . Suppose the expressions for  $A_1(s)$  and  $C_1(s)$  are, respectively,

$$A_1(s) = \bar{A}(s) \frac{i}{2s} \int_{-a}^a g(r) e^{isr} dr, \quad (13a)$$

and

$$C_1(s) = \bar{C}(s) \frac{i}{2s} \int_{-a}^a g(r) e^{isr} dr. \quad (13b)$$

Then the shear stress on the cracked obtained with the submission of (13a) and (13b) into (5) is

$$\tau_y(x, 0) = G_1 \int_{-a}^a R(x, r) g(r) dr, \quad (14)$$

where the integral kernel  $R(x, r)$  is

$$R(x, r) = \lim_{y \rightarrow +0} \frac{i}{2\pi} \int_{-\infty}^{\infty} \frac{1}{2} \frac{|s|}{s} (-\bar{A}(s) e^{-|s|y} + \bar{C}(s) e^{|s|y}) e^{is(r-x)} ds, \quad (15)$$

or

$$R(x, r) = \lim_{y \rightarrow +0} \frac{1}{2\pi} \int_0^{\infty} (\bar{A}(s) e^{-|s|y} - \bar{C}(s) e^{|s|y}) \sin[s(r-x)] ds. \quad (16)$$

In order to identify the asymptotic behaviour of  $\bar{A}(s) - \bar{C}(s)$  for  $s$  at infinity, one can consider a crack of length  $2a$  at the infinite medium of the same material of the layer. This is, one considers  $h$  to be equal to infinity. After examining, it is found that for large values of  $s$ ,  $\bar{C}(s)$ , and  $\bar{D}(s)$  become

vanishing and  $\bar{A}(s)$  approaches to  $1 + l^2 s^2$ . This function is denoted as  $\Lambda_0(s)$  in the following analysis. The asymptotic analysis allowing splitting of the integral kernel  $R(x, r)$  into two parts so that the stress of (14) can be re-written as

$$\tau_y(x, 0) = G \int_{-a}^a \Omega(x, r) g(r) dr + G \int_{-a}^a R_\infty(x, r) g(r) dr, \quad (17)$$

where the regular kernel is

$$\Omega(x, r) = \frac{1}{2\pi} \int_0^\infty (\bar{A}(s) - \bar{C}(s) - \Lambda_0(s)) \sin[s(r - x)] ds, \quad (18)$$

and the singular kernel is

$$R_\infty(x, r) = \frac{1}{2\pi} \int_0^\infty [1 + l^2 s^2] \sin[s(r - x)] ds. \quad (19)$$

The regular kernel, Equation (18) can be evaluated by standard numerical integral technique. The singular kernel, Equation (19) can be evaluated by hypersingular integral equation technique of Paulino et al. [2003] and Chan et al. [2008]. As a result of such procedure, we get

$$\tau_y(x, 0) = -\frac{Gl^2}{\pi} \int_{-a}^a \frac{g(r)}{(r - x)^3} dr + \frac{G}{2\pi} \int_{-a}^a \frac{g(r)}{r - x} dr + G \int_{-a}^a \Omega(x, r) g(r) dr. \quad (20)$$

Equation (20) provides the expression for  $\tau_y(x, 0)$  outside as well as inside the crack. In the case of inside the crack, the crack face stress boundary condition gives

$$-\frac{(l/a)^2}{\pi} \int_{-1}^1 \frac{g(r)}{(\bar{r} - \bar{x})^3} d\bar{r} + \frac{1}{2\pi} \int_{-a}^a \frac{g(r)}{\bar{r} - \bar{x}} d\bar{r} + a \int_{-1}^1 \Omega(x, r) g(r) d\bar{r} = -\frac{P}{G}. \quad (21)$$

Here and in the following, the notations  $\bar{x} = x/a$  and  $\bar{r} = r/a$  will be used. Equation (21) is a hypersingular integral equation. According to Paulino et al. [2003] and Chan et al. [2008], the solution of  $g(r)$  can be expressed in the following form:

$$g(\bar{r}) = \sum_{m=1}^{\infty} C_m U_m(\bar{r}) \sqrt{1 - \bar{r}^2}, \quad (22)$$

in which  $U_m$  is the Chebyshev polynomial of the second kind  $U_m(\bar{x}) = \sin[(m + 1) \arccos(\bar{x})]/\sqrt{1 - \bar{x}^2}$ , and  $C_m$  are unknowns to be evaluated. It is observed that the single-value condition of  $g(x)$  is identically satisfied by (22). After substituting (22), truncated with the first  $M$  terms, into (21), and following the same procedure of Paulino et al. [2003] and Chan et al. [2008], and through expansions and integrals of Chebyshev polynomials given in Appendix, it can be seen that

$$-\frac{(l/a)^2}{4(1 - \bar{x}^2)} \sum_{m=1}^{\infty} C_m [m(m + 1) U_{m+1}(\bar{x}) - (m^2 + 3m + 2) U_{m-1}(\bar{x})] - \frac{1}{2} \sum_{m=1}^{\infty} C_m T_{m+1}(\bar{x}) + a \sum_{m=1}^{\infty} C_m V_m(\bar{x}) = -\frac{P}{G}, \quad (23)$$

where  $T_m$  is the Chebyshev polynomial of the first kind  $T_m(\bar{x}) = \cos[m \arccos(\bar{x})]$ , and  $V_m$  is

$$V_m(\bar{x}) = \int_{-1}^1 \Omega(x, r) U_m(\bar{r}) \sqrt{1 - \bar{r}^2} d\bar{r}. \quad (24)$$

For the case of infinite layer thickness, the regular integral kernel  $\Omega(x, r)$  vanishes and (23) becomes

$$-\frac{(l/a)^2}{4(1 - \bar{x}^2)} \sum_{m=1}^{\infty} C_m [m(m+1) U_{m+1}(\bar{x}) - (2m^2 + 3m + 2) U_{m-1}(\bar{x})] - \frac{1}{2} \sum_{m=1}^{\infty} C_m T_{m+1}(\bar{x}) = -\frac{p}{G}. \quad (25)$$

The simplest method for solving the functional (23) is using an appropriate collocation in  $x$ . After evaluating  $C_m$  from (23), the displacement field can be calculated from (4) since  $A(s)$ ,  $B(s)$ ,  $C(s)$ , and  $D(s)$  have been expressed in terms of  $g(x)$ . The associated stress can be obtained from the constitutive equations of (1a)–(1c). Thus, the full field solution is obtained.

Of particular interest are the crack opening displacement and the crack tip stress state. The displacement jump across the crack can be evaluated from  $\Delta w(x, 0) = \int_{-a}^x g(r) dr$ . With the substitution of (27), we get

$$\Delta w(x, 0) = a \sum_{m=1}^M C_m \left( \frac{\sin[(m+2) \arccos(x/a)]}{2(m+2)} - \frac{\sin[m \arccos(x/a)]}{2m} \right), \quad |x| < a. \quad (26)$$

Due to symmetry, the displacement on the upper surface of the crack  $w(x, 0)$  is half of  $\Delta w(x, 0)$ . The maximum crack face displacement appears at  $x = 0$  on the upper surface of the crack and is

$$w(0, 0) = \frac{\Delta w(0, 0)}{2} = -a \sum_{m=1}^M C_m \frac{\sin(m \pi/2)}{4} \left( \frac{1}{m+2} + \frac{1}{m} \right).$$

For gradient elasticity theory,  $\tau_y$  have a strong singularity, which can not be described by conventional linear elasticity fracture mechanics. Note that the expression for  $\tau_y(x, 0)$  is valid for  $|x| < a$  as well as  $|x| > a$ . Equation (20) provides the expression for  $\tau_y(x, 0)$  outside as well as inside the crack. With the substitution of the density function (22) and again through expansions of Chebyshev polynomials [Chan et al. 2003], the stress near the crack tip is found to be (neglect the secondary terms)

$$\begin{aligned} \tau_y(x, 0) = & -\frac{G}{2} \sum_{m=1}^{\infty} C_m \left( \bar{x} - \frac{|x|}{x} \sqrt{\bar{x}^2 - 1} \right)^{m+1} + \frac{G(l/a)^2}{2} \sum_{m=1}^{\infty} C_m (m+1) \left( \bar{x} - \frac{|x|}{x} \sqrt{\bar{x}^2 - 1} \right)^{m-1} \\ & \times \left[ m \left( 1 - \frac{|\bar{x}|}{\sqrt{\bar{x}^2 - 1}} \right)^2 + \frac{\bar{x} - \frac{|x|}{x} \sqrt{\bar{x}^2 - 1}}{(\sqrt{\bar{x}^2 - 1})^3} \right]. \quad (27) \end{aligned}$$

The highest singularity is  $(\bar{x} - 1)^{3/2}$ . This is totally different from the conventional linear elasticity fracture mechanics result, which gives  $(\bar{x} - 1)^{1/2}$  singularity.

The above formulation is general enough for consideration of a crack at any position in the film with or without substrate. For example, if we let  $G_s = 0$ , the problem will become a crack in a single layer. On the other hand, if we let  $G_s = \infty$ , the problem will correspond to a crack in a film on a rigid substrate. It can be seen that the value of  $l'$  does not appear in (21). Thus, the solution of the discontinuity function  $g(x)$  has no dependence on the material gradient parameter  $l'$  which is related to the surface energy. One can

also see that the shear stress  $\tau_y$  on the cracked plane also does not depend on  $l'$ . However, it is expected that the other stress components such as  $\tau_x$  should have a dependence on  $l'$ . The stress component  $\tau_y$  away from the cracked plane should also have relationship with  $l'$ . Karimipour and Fotuhi [2017] have also observed that the effect of the volumetric characteristic length  $l$  on the solution is more significant than that of the surface characteristic length  $l'$  and suggested that it is quite adequate if only the effect of  $l$  is studied.

4. Results and discussion

All results are given for the  $z$  direction displacement on the upper surface of the crack and the stress ahead of the crack tip on the cracked plane for a constant surface shear load  $\tau_y(x, 0) = -p_0$  on the crack faces. It is noticed from the calculations that the value of  $M$  required for a convergent result depends on the relative value of strain gradient  $l$  to the crack length parameter  $a$ . All calculations confirm that the results converge as the number of allocation points (the value of  $M$ ) increase.

In order to examine the influence of crack location, we consider a film on a substrate of the same material. This structure configuration can also be understood as a semi-infinite medium containing a crack at any location. Therefore, the effect of  $h_2$  is dropped out from the result. Some numerical results of crack surface displacement profiles for various values of  $h_1$  are shown in Figure 2 for  $l = 0.2a$ . The crack is considerably softened as it approaches the surface of the film. This fact can also be seen from Figure 3 which shows the influence of crack location on the stress ahead of the crack tip. As expected,

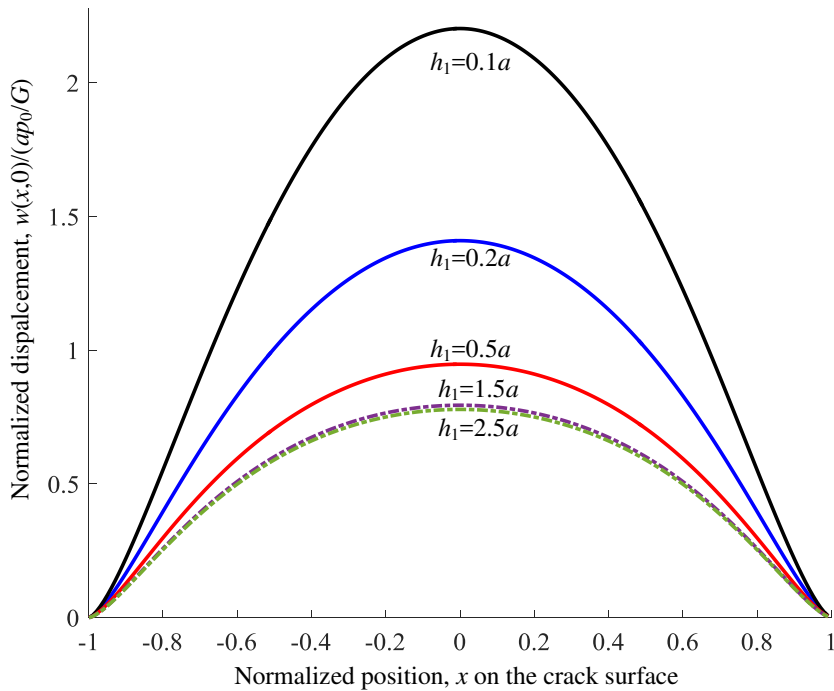


**Figure 2.** Crack surface displacement profiles for a film on the substrate of the same material with choice of  $l = 0.2a$ .



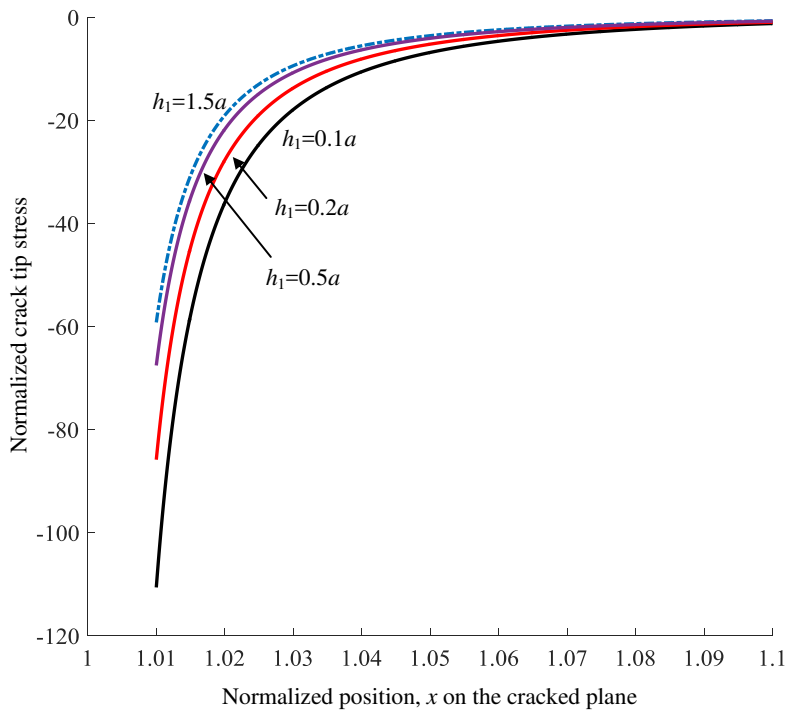


**Figure 3.** Normalized stress  $\tau_y(x, 0)/p_0$  near the right crack tip for a film on the substrate of the same material with choice of  $l = 0.2a$ .

the stress is significantly enhanced when  $h_1$  is smaller. Results for the value of  $h_1$  larger than  $1.5a$  are almost identical to those for a crack in an infinite medium. Basically, the effect of strain gradient on the crack in the finite layer is more significant than in the infinite layer. Generally, finite layer border tends to enhance the stress level near the crack tip.

Some numerical results for a crack at  $h_1 = 0.2a$  in a film on a substrate of the same material is plotted in Figure 4 to show the effect of the gradient parameter  $l$ . It can be seen that the displacement decreases considerably with the gradient parameter. Therefore, in comparison to the classical elasticity fracture mechanics, strain gradient effect will considerably stiffens the crack. As observed, when the gradient parameter become very small (in current case,  $l/a \leq 0.005$ ), the result is almost identical to the that obtained from the conventional linear elastic fracture mechanics analysis.

In order to further explore the strain gradient effect, it is necessary to know the stress near the crack tips and to evaluate the influence of the gradient parameter  $l$ . Therefore, in Figure 5, the normalized stresses near the right crack tip for a crack at  $h_1 = 0.2a$  in a film on the substrate of the same material are plotted for different values of  $l$ . The stresses at the left crack tip are same but with an opposite sign. It is obvious from Figure 5 that the magnitudes of the stress increase as  $l/a$  increases and vice versa. This suggests that the stresses in strain gradient fracture are significantly larger than those in the classical field. This trend observation is the same as that made by Zhang et al. [1998] based on the closed-form analysis of an infinite medium with an anti-plane crack. Another fact observed from Figure 5 is that for sufficiently small gradient parameter, the strain gradient solution can be reduced to that of

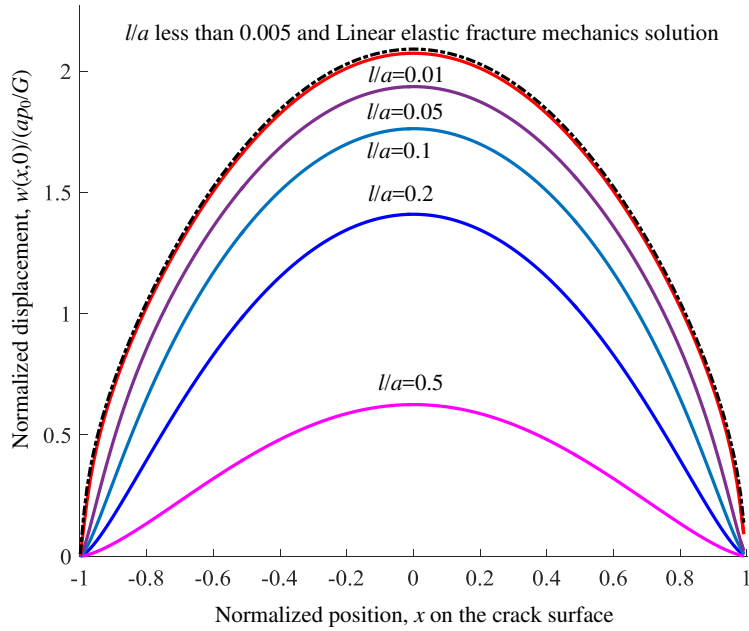


**Figure 4.** Crack (upper) surface displacement profiles for a crack at  $h_1 = 0.2a$ , in a film on the substrate of the same material for different values of  $l$ .

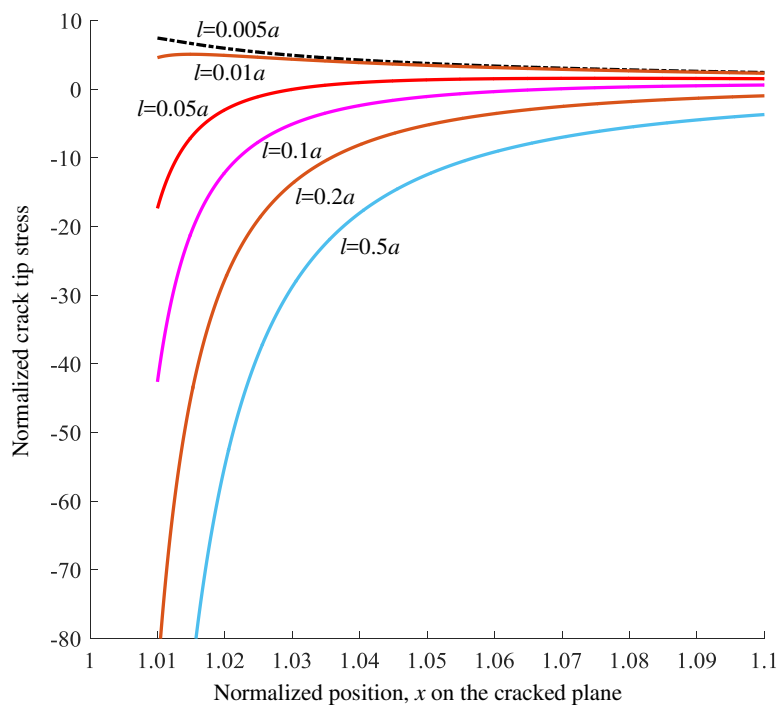


**Figure 5.** Normalized stress  $\tau_y(x, 0)/p_0$  near the right crack tip for a crack at  $h_1 = 0.2a$ , in a film on the substrate of the same material for different values of  $l$ .

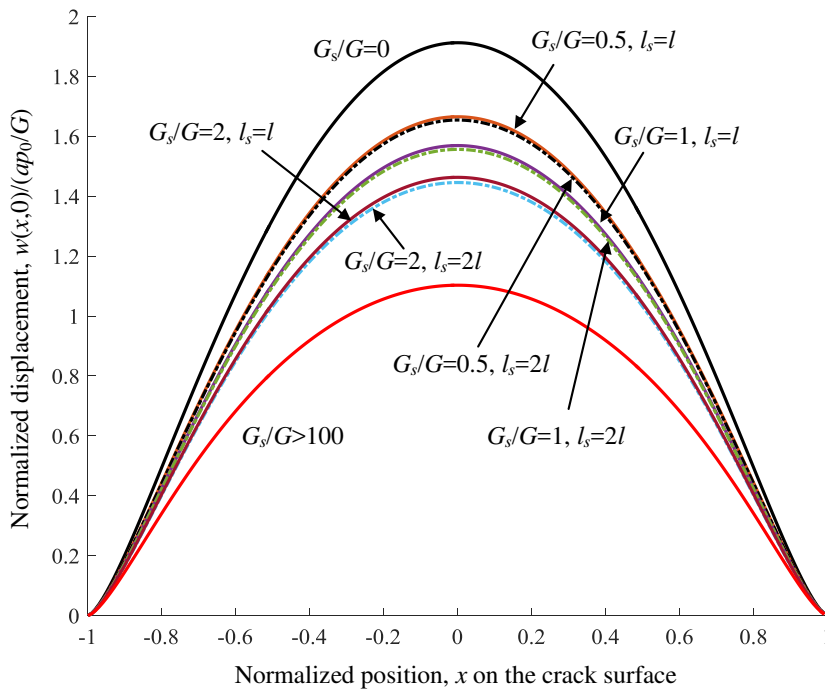


**Figure 6.** Crack surface displacement profiles in a film on a substrate of different stiffness and gradient parameter for  $h_1 = h_2 = 0.2a$  and  $l = 0.2a$ .

the conventional linear elastic fracture mechanics solution. However, the natures of the strain gradient solution and the conventional linear elastic fracture mechanics solution are totally different: the gradient solutions are always negative and with a higher magnitude of the stress level but the conventional linear elastic fracture mechanics solution is always positive and with a lower magnitude of the stress level.

Figure 6 displays variation of the crack surface displacement with the stiffness of the substrate for a crack at the center of the film with  $h_1 = h_2 = 0.2a$  and for  $l = 0.2a$ . As expected, the structure becomes stiffer and the crack surface displacement reduces when the shear modulus of the substrate layer increases. The zero substrate stiffness is related to a single layer with a crack. On the other hand, the infinite layer thickness corresponds to a single layer on a rigid substrate. From Figure 6 we can observe the influence of the gradient parameter of the substrate on the crack displacement. Generally, the gradient of the substrate reduces the crack face displacement. However, this effect is very small. Figure 7 shows variations of the stress at the right crack tip for  $h_1 = h_2 = 0.2a$ ,  $l = 0.2a$  and  $l_s = 2l$ . Apparently, the substrate provides a constraint to the film so that the crack tip stresses are reduced. The higher the value of the shear modulus of the substrate, the lower the crack tip stress. Since the influence of the gradient parameter of the substrate can not be observed when it is plotted in the figure, the results for other values of the substrate gradient parameters are not given in Figure 7.

Because the stresses are singular at the crack tips, it is necessary to study the intensity of the stress concentration near the crack front. For this, it is important to recognize that the stress at the crack tip has  $(x^2 - a)^{-3/2}$  singularity when  $x \rightarrow a^+$  or  $x \rightarrow -a^-$ . Paulino et al. [2003] defined the generalized

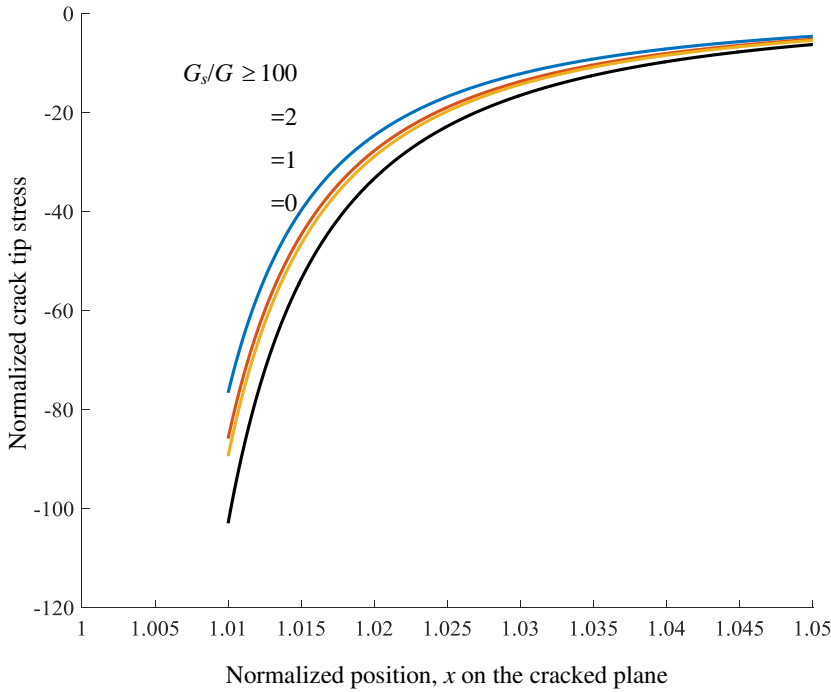


**Figure 7.** Normalized stress  $\tau_y(x, 0)/p_0$  near the right crack tip in a film on a substrate of different stiffness for  $h_1 = h_2 = 0.2a$ ,  $l = 0.2a$ , and  $l_s = 2l$ .

stress intensity factor  $K_{III}$  according to

$$lK_{III}(a) = \lim_{x \rightarrow a^+} 2\sqrt{2\pi(x-a)}(x-a)\tau_y(x, 0), \quad (28a)$$

$$lK_{III}(-a) = \lim_{x \rightarrow -a^-} 2\sqrt{2\pi(x+a)}(x+a)\tau_y(x, 0), \quad (28b)$$

and obtained the expressions as follows:

$$K_{III}(a) = \sqrt{\pi a} \frac{1}{2} \frac{l}{a} G \sum_{m=1}^{\infty} (m+1) A_m, \quad (29a)$$

$$K_{III}(-a) = \sqrt{\pi a} \frac{1}{2} \frac{l}{a} G \sum_{m=1}^{\infty} (-1)^m (m+1) A_m. \quad (29b)$$

The results of generalized stress intensity factor at the right crack tip, normalized with  $K_0 = p_0\sqrt{\pi a}$ , as functions of gradient parameters are plotted in [Figure 8](#) for various values of the substrate stiffness. The gradient parameters for the strain gradient layer and the substrate layer are same. It is observed that the magnitude of the normalized stress intensity factor reduces with the stiffness of the substrate material. Also observed is that the magnitude of the normalized stress intensity factor decreases with the gradient parameter. The same tendency has been observed by Paulino et al. [\[2003\]](#) and Karimipour and Fotuhi [\[2017\]](#).

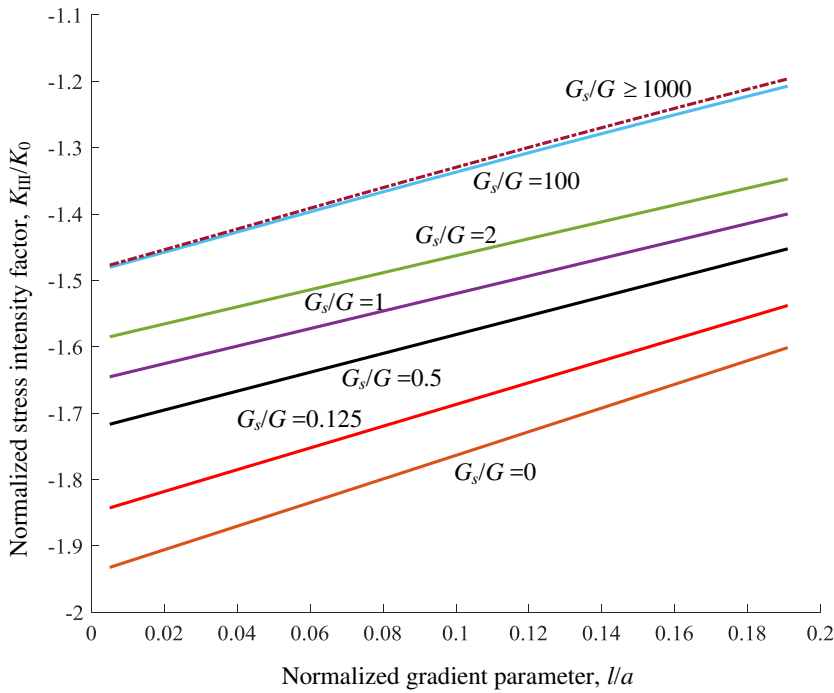


**Figure 8.** Normalized generalized stress intensity factor at the right crack tip for  $h_1 = h_2 = 0.2a$  and  $l_s = l$  where  $K_0 = p_0\sqrt{\pi a}$ . Due to symmetry,  $K_{III}$  at the left crack tip is opposite to these at the right crack tip.

## 5. Conclusion

A crack in a strain gradient layer on a substrate under anti-plane deformation has been studied. Both volumetric and surface strain gradient material constants are taken into consideration. The crack is parallel to the layer surface but is at any location in the strain gradient layer. The problem is governed by the solution of a hypersingular integral equation. It is found that when the gradient parameters are very small, results from the current strain gradient analysis reduce to the corresponding solutions of conventional linear fracture mechanics. Influences of strain gradient parameters, layer thickness and substrate stiffness have been conducted and are found to be very different from those of the conventional linear elastic fracture mechanics solutions.

## Acknowledgements

This research was supported by the National Science Foundation of China (Project No. 11502101, 11672084, 11372086), Research Innovation Foundation of Jinling Institute of Technology (Project No. jit-b-201515), and the Research Innovation Fund of Shenzhen City (Project No. JCYJ20170413104256729).

## Appendix

The following formulas [Paulino et al. 2003; Chan et al. 2008] have been used in deriving the hypersingular integral equations:

$$\frac{1}{\pi} \int_{-1}^1 \frac{U_m(r) \sqrt{1-r^2}}{(r-x)} dr = \begin{cases} -T_{m+1}(x), & m \geq 0, |x| < 1 \\ -[x - \frac{|x|}{x} \sqrt{x^2-1}]^{m+1}, & m \geq 0, |x| > 1 \end{cases}, \quad (\text{A1})$$

$$\begin{aligned} & \frac{1}{\pi} \int_{-1}^1 \frac{U_m(r) \sqrt{1-r^2}}{(r-x)^3} dr \\ &= \begin{cases} \frac{1}{[4(1-x^2)]} [(m^2+m) U_{m+1}(x) - (m^2+3m+2) U_{m-1}(x)], & m \geq 1, |x| < 1 \\ -\frac{1}{2}(m+1)[x - \frac{|x|}{x} \sqrt{x^2-1}]^{m-1} \left[ m \left(1 - \frac{|x|}{\sqrt{x^2-1}}\right)^2 + \frac{[x - \frac{|x|}{x} \sqrt{x^2-1}]}{(x^2-1)^{3/2}} \right], & m \geq 0, |x| > 1 \end{cases}. \quad (\text{A2}) \end{aligned}$$

## References

- [Aifantis 2011] E. C. Aifantis, “A note on gradient elasticity and nonsingular crack fields”, *J. Mech. Behav. Mater* **20** (2011), 103–105.
- [Aifantis 2016] E. C. Aifantis, “Chapter 1: Internal length gradient (ILG) material mechanics across scales and disciplines”, pp. 1–110 in *Advances in applied mechanics*, vol. 49, edited by S. P. A. Bordas and D. S. Balint, Elsevier, 2016.
- [Benvenuti and Simone 2013] E. Benvenuti and A. Simone, “One-dimensional nonlocal and gradient elasticity: closed-form solution and size effect”, *Mech. Res. Commun.* **48** (2013), 46–51.
- [Chan et al. 2003] Y.-S. Chan, A. C. Fannjiang, and H. Glaucio, “Integral equations with hypersingular kernels—theory and applications to fracture mechanics”, *Int. J. Eng. Sci.* **41**:7 (2003), 683–720.
- [Chan et al. 2008] Y.-S. Chan, G. H. Paulino, and A. C. Fannjiang, “Gradient elasticity theory for mode III fracture in functionally graded materials—part II: crack parallel to the material gradation”, *J. Appl. Mech. (ASME)* **75** (2008), 061015.
- [Exadaktylos 1998] G. Exadaktylos, “Gradient elasticity with surface energy: mode-I crack problem”, *Int. J. Solids Struct.* **35**:5-6 (1998), 421–456.
- [Exadaktylos and Vardoulakis 2001] G. E. Exadaktylos and I. Vardoulakis, “Microstructure in linear elasticity and scale effects: a reconsideration of basic rock mechanics and rock fracture mechanics”, *Tectonophysics* **335**:1-2 (2001), 81–109.
- [Exadaktylos et al. 1996] G. Exadaktylos, I. Vardoulakis, and E. Aifantis, “Cracks in gradient elastic bodies with surface energy”, *Int. J. Fract.* **79** (1996), 107–119.
- [Fannjiang et al. 2002] A. C. Fannjiang, G. H. Paulino, and Y.-S. Chan, “Strain gradient elasticity for antiplane shear cracks: a hypersingular integrodifferential equation approach”, *SIAM J. Appl. Math.* **62**:3 (2002), 1066–1091.
- [Fleck et al. 1994] N. A. Fleck, G. M. Muller, M. F. Ashby, and J. W. Hutchinson, “Strain gradient plasticity: theory and experiment”, *Acta Metall. Mater.* **42**:2 (1994), 475–487.
- [Giannakopoulos and Stamoulis 2007] A. E. Giannakopoulos and K. Stamoulis, “Structural analysis of gradient elastic components”, *Int. J. Solids Struct.* **44**:10 (2007), 3440–3451.
- [Grosskreutz and Mcneilt 1969] J. C. Grosskreutz and M. B. Mcneilt, “The fracture of surface coatings on a strained substrate”, *J. Appl. Phys.* **40** (1969), 355–359.
- [Hutchinson et al. 1987] J. W. Hutchinson, M. E. Mear, and J. R. Rice, “Crack paralleling an interface between dissimilar materials”, *J. Appl. Mech. (ASME)* **54**:4 (1987), 828–832.
- [Karimipour and Fotuhi 2017] I. Karimipour and A. R. Fotuhi, “Anti-plane analysis of an infinite plane with multiple cracks based on strain gradient theory”, *Acta Mech.* **228**:5 (2017), 1793–1817.
- [Kiang et al. 1998] C.-H. Kiang, M. Endo, P. M. Ajayan, G. Dresselhaus, and M. S. Dresselhaus, “Size effects in carbon nanotubes”, *Phys. Rev. Lett.* **81**:9 (1998), 1869–1872. also in arXiv:cond-mat/9811046.

- [Kim and Nairn 2000] S.-R. Kim and J. A. Nairn, “Fracture mechanics analysis of coating/substrate systems: part I: analysis of tensile and bending experiments”, *Eng. Fract. Mech.* **65**:5 (2000), 573–593.
- [Koiter 1964] W. Koiter, “Couple stresses in the theory of elasticity, I & II”, *Philos. Trans. Royal Soc. B* **67** (1964), 17–44.
- [Lam et al. 2003] D. C. C. Lam, F. Yang, A. C. M. Chong, J. Wang, and P. Tong, “Experiments and theory in strain gradient elasticity”, *J. Mech. Phys. Solids* **51**:8 (2003), 1477–1508.
- [Ma and Clarke 1995] Q. Ma and D. R. Clarke, “Size dependent hardness of silver single crystals”, *J. Mater. Res.* **10**:4 (1995), 853–863.
- [McElhaney et al. 1998] K. W. McElhaney, J. J. Vlassak, and W. D. Nix, “Determination of indenter tip geometry and indentation contact area for depth-sensing indentation experiments”, *J. Mater. Res.* **13**:5 (1998), 1300–1306.
- [McFarland and Colton 2005] A. W. McFarland and J. S. Colton, “Role of material microstructure in plate stiffness with relevance to microcantilever sensors”, *J. Micromech. Microeng.* **15**:5 (2005), 1060–1067.
- [Mindlin 1965] R. D. Mindlin, “Second gradient of strain and surface-tension in linear elasticity”, *Int. J. Solids Struct.* **1**:4 (1965), 417–438.
- [Mindlin and Eshel 1968] R. D. Mindlin and N. N. Eshel, “On first strain-gradient theories in linear elasticity”, *Int. J. Solids Struct.* **4**:1 (1968), 109–124.
- [Mindlin and Tiersten 1962] R. Mindlin and H. Tiersten, “Effects of couple-stresses in linear elasticity”, *Arch. Ration. Mech. Anal.* **11**:1 (1962), 415–448.
- [Mousavi and Aifantis 2005] S. M. Mousavi and E. Aifantis, “A note on dislocation-based mode III gradient elastic fracture mechanics”, *J. Mech. Behav. Mater.* **24**:3–4 (2005), 115–119.
- [Nix 1989] W. D. Nix, “Mechanical properties of thin films”, *Metall. Mater. Trans. A* **20** (1989), 2217.
- [Paulino et al. 2003] G. H. Paulino, A. C. Fannjiang, and Y.-S. Chan, “Gradient elasticity theory for mode III fracture in functionally graded materials—part I: crack perpendicular to the material gradation”, *J. Appl. Mech. (ASME)* **70**:4 (2003), 531–542.
- [Piccolroaz et al. 2012] A. Piccolroaz, G. Mishuris, and E. Radi, “Mode III interfacial crack in the presence of couple-stress elastic materials”, *Eng. Fract. Mech.* **80** (2012), 60–71.
- [Poole et al. 1996] W. J. Poole, M. F. Ashby, and N. A. Fleck, “Micro-hardness of annealed and work-hardened copper polycrystals”, *Scr. Mater.* **34**:4 (1996), 559–564.
- [Qiu et al. 2018] Y. Qiu, H. Wu, J. Wang, J. Lou, Z. Zhang, A. Liu, and G. Chai, “The enhanced piezoelectricity in compositionally graded ferroelectric thin films under electric field: a role of flexoelectric effect”, *J. Appl. Phys.* **123**:8 (2018), 084103.
- [Schulze and Erdogan 1998] G. W. Schulze and F. Erdogan, “Periodic cracking of elastic coatings”, *Int. J. Solids Struct.* **35**:28–29 (1998), 3615–3634.
- [Shi et al. 2014] M. Shi, H. Wu, L. Li, and G. Chai, “Calculation of stress intensity factors for functionally graded materials by using the weight functions derived by the virtual crack extension technique”, *Int. J. Mech. Mater. Des.* **10**:1 (2014), 65–77.
- [Stelmashenko et al. 1993] N. A. Stelmashenko, M. G. Walls, L. M. Brown, and Y. V. Milman, “Microindentations on W and Mo oriented single crystals: an STM study”, *Acta Metall. Mater.* **41**:10 (1993), 2855–2865.
- [Stolken 1997] J. S. Stolken, *The role of oxygen in nickel-sapphire interface fracture*, Ph.D. dissertation, University of California, Santa Barbara, 1997.
- [Toupin 1962] R. A. Toupin, “Elastic materials with couple-stresses”, *Arch. Ration. Mech. Anal.* **11**:1 (1962), 385–414.
- [Vardoulakis et al. 1996] I. Vardoulakis, G. Exadaktylos, and E. Aifantis, “Gradient elasticity with surface energy: mode-III crack problem”, *Int. J. Solids Struct.* **33**:30 (1996), 4531–4559.
- [Wu et al. 2016a] H. Wu, L. Li, G. Chai, F. Song, and T. Kitamura, “Three-dimensional thermal weight function method for the interface crack problems in bimaterial structures under a transient thermal loading”, *J. Therm. Stresses* **39**:4 (2016), 371–385.
- [Wu et al. 2016b] H. Wu, X. Ma, Z. Zhang, J. Zhu, J. Wang, and G. Chai, “Dielectric tunability of vertically aligned ferroelectric-metal oxide nanocomposite films controlled by out-of-plane misfit strain”, *J. Appl. Phys.* **119**:15 (2016), 154102.
- [Zhang et al. 1998] L. Zhang, Y. Huang, Y. J. Chen, and K. C. Hwang, “The mode III full-field solution in elastic materials with strain gradient effects”, *Int. J. Fract.* **92**:4 (1998), 325–348.

Received 18 Jun 2018. Revised 3 Oct 2018. Accepted 3 Oct 2018.

JINE LI: [lijine@jit.edu.cn](mailto:lijine@jit.edu.cn)

*School of Architectural Engineering, Jinling Institute of Technology, China*

BAOLIN WANG: [wangbl2001@hotmail.com](mailto:wangbl2001@hotmail.com)

*School of Science, Harbin Institute of Technology (Shenzhen), China*



# GROWTH-INDUCED INSTABILITIES OF AN ELASTIC FILM ON A VISCOELASTIC SUBSTRATE: ANALYTICAL SOLUTION AND COMPUTATIONAL APPROACH VIA EIGENVALUE ANALYSIS

IMAN VALIZADEH, PAUL STEINMANN AND ALI JAVILI

The objective of this contribution is to study for the first time the growth-induced instabilities of an elastic film on a viscoelastic substrate using an analytical approach as well as computational simulations via eigenvalue analysis. The growth-induced instabilities of a thin film on a substrate is of particular interest in modeling living tissues such as skin, brain, and airways. The analytical solution is based on Airy's stress function adopted to viscoelastic constitutive behavior. The computational simulations, on the other hand, are carried out using the finite deformation continuum theory accounting for growth via the multiplicative decomposition of the deformation gradient into elastic and growth parts. To capture the critical growth of elastic films and the associated folding pattern, eigenvalue analysis is utilized, in contrast to the commonly used perturbation strategy. The eigenvalue analysis provides accurate, reliable, and reproducible solutions as contrasted to the perturbation approach. The numerical results obtained from the finite element method show an excellent agreement between the computational simulations and the proposed analytical solution.

## 1. Introduction

Instabilities of bilayered structures consisting of a thin stiff film adhered to an infinite substrate are increasingly important due to their applications in biological tissues. Such structural instabilities in the form of wrinkles [Cao and Hutchinson 2012b; Budday et al. 2014], folds [Sun et al. 2012; Sultan and Boudaoud 2008], or creases [Cao and Hutchinson 2012a; Hong et al. 2009; Jin et al. 2015] have been studied recently. In many living systems, the formation of structural instabilities is critical to appropriate biological function of the system [Wyczalkowski et al. 2012]. Typical examples are wrinkling of skin [Tepole et al. 2011], villi formation in the intestine [Balbi and Ciarletta 2013], and folding of the developing brain [Xu et al. 2010; Budday et al. 2014; Budday and Steinmann 2018]. However, in some biological systems, the formation of structural instabilities can be an indication of a disease, e.g., the folding of the mucous membrane in asthmatic airways [Wiggs et al. 1997].

It is thus not surprising that the mathematical modeling of folding in tubular organs [Ciarletta and Ben Amar 2012], in particular the modeling of the folding mucous membrane [Moulton and Goriely 2011; Li et al. 2011; Xie et al. 2014], has attracted increasing scientific attention in the past decade. This problem (and variants thereof) has been widely studied lately [Budday et al. 2015; Cao and Hutchinson 2012b; Huang et al. 2005; Hutchinson 2013; Jin et al. 2011; Sun et al. 2012; Xu et al. 2014].

The concept of growth commonly has been modeled by continuum approaches via the multiplicative decomposition of the deformation gradient into an elastic and a growth part [Rodriguez et al. 1994] which

*Keywords:* growth-induced instabilities, viscoelasticity, wrinkling, finite element method.

pairs the growth to the kinematic level [Taber 1995]. This concept requires the introduction of an artificial intermediate configuration [Garikipati et al. 2004]. Additional details on the continuum theory of growth and its implications are discussed in [Ciarletta and Maugin 2011; Ciarletta et al. 2013; Dervaux and Ben Amar 2011; Dunlop et al. 2010; Epstein and Maugin 2000; Garikipati et al. 2004; Goriely et al. 2008; Kuhl et al. 2003; Li et al. 2011; Yavari 2010; Ben Amar and Goriely 2005; Javili et al. 2014], amongst others. Growth is commonly formulated within the framework of open-system thermodynamics [Kuhl and Steinmann 2003; Kuhl 2014] where the body is allowed to constantly exchange mass, momentum, and entropy with its environment through corresponding fluxes across its boundary; see also [Cowin and Hegedus 1976; Epstein and Maugin 2000; Javili et al. 2013].

Most of the contributions on the subject assume the compliant substrate to be elastic. This contribution for the first time studies the growth-induced instabilities of an elastic film on a *viscoelastic substrate* from both analytical and computational perspectives using eigenvalue analysis and, in particular, elaborates on the role of the relaxation time on the instability pattern as well as the critical growth; see also [Huang and Suo 2002; Huang 2005; Budday et al. 2014]. Key features of this contribution are:

- (1) to study the growth-induced instabilities of an elastic film on a viscoelastic substrate from both analytical and numerical perspectives,
- (2) to employ the eigenvalue analysis proposed in [Javili et al. 2015] for the numerical solution and not the common perturbation strategy, and
- (3) to illustrate an excellent agreement between the numerical and analytical solutions.

This manuscript is organized as follows. [Section 2](#) deals with the computational approach to study growth-induced instabilities of a thin film on a compliant viscoelastic substrate. Next, the analytical solution of the problem is derived in [Section 3](#) and its simplification to various classes of viscoelastic models are discussed. The results from the computational approach using the finite element method are compared against the analytical solution through a series of numerical examples in [Section 4](#) and it is found that the two strategies are in excellent agreement. Finally, [Section 5](#) concludes this work and provides further outlook.

## 2. Computational approach

The numerical solution of the problem is achieved by using the finite deformation theory in continuum mechanics to account for growth, whereby the deformation gradient is decomposed multiplicatively into an elastic and a growth part.

Let the continuum body  $\mathcal{B}_0$  occupy the material configuration at time  $t = 0$ , as shown in [Figure 1](#). The motion  $\boldsymbol{\varphi}$  maps the body  $\mathcal{B}_0$  to the spatial configuration  $\mathcal{B}_t$  at time  $t$ . The deformation gradient  $\boldsymbol{F}$  maps the line element  $d\mathbf{x}$  from  $\mathcal{B}_0$  to  $d\mathbf{x}$  in  $\mathcal{B}_t$  and is defined as  $\boldsymbol{F} := \text{Grad } \boldsymbol{\varphi}$ . The governing balance equations of finite deformation continuum mechanics consist of the balance of linear and angular momentum. The balance of linear momentum in material configuration, for body  $\mathcal{B}_0$  at time  $t = 0$  and a quasistatic process, reads

$$\text{Div } \boldsymbol{P} + \boldsymbol{b}_0 = \mathbf{0} \quad \text{in } \mathcal{B}_0 \text{ subject to } \boldsymbol{t} = \boldsymbol{t}_0 \text{ on } \partial\mathcal{B}_0 \text{ with } \boldsymbol{t} = \boldsymbol{P} \cdot \boldsymbol{N}, \quad (1)$$

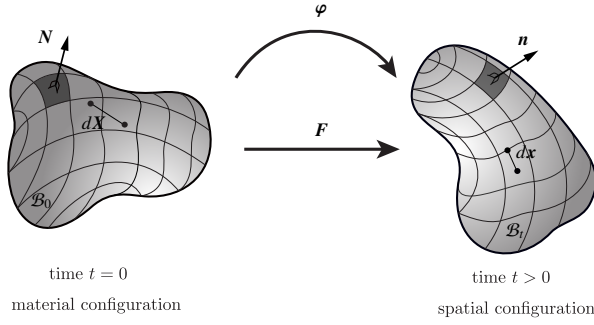


**Figure 1.** The material and spatial configurations of a continuum body with associated nonlinear deformation map  $\varphi$  and the linear tangent map  $\mathbf{F} := \text{Grad } \varphi$ .

where  $\mathbf{P}$  is Piola stress<sup>1</sup> and  $\mathbf{b}_0$  is the body force density in the material configuration. The balance of angular momentum leads to the symmetry of the Cauchy stress tensor  $\boldsymbol{\sigma} = \boldsymbol{\sigma}^t$  related to the Piola stress via  $\mathbf{P} = \boldsymbol{\sigma} \cdot \text{Cof } \mathbf{F}$ .

**2.1. Growing elastic film.** To model volumetric growth one can use the multiplicative decomposition of the deformation gradient  $\mathbf{F}$  into a growth part  $\mathbf{F}_g$  and an elastic part  $\mathbf{F}_e$  as

$$\mathbf{F} = \mathbf{F}_e \cdot \mathbf{F}_g \Rightarrow \mathbf{F}_e = \mathbf{F} \cdot \mathbf{F}_g^{-1} \quad \text{and} \quad J = J_e J_g, \quad J_e = \det \mathbf{F}_e, \quad J_g = \det \mathbf{F}_g, \quad (2)$$

where  $J$  is the Jacobian determinant of  $\mathbf{F}$  and indicates the volume change due to the deformation as  $J = dv/dV$ . In modeling growth, the growth part  $\mathbf{F}_g$  maps the body  $\mathcal{B}_0$  from the material configuration to an intermediate stress-free “configuration”, which may be incompatible. The elastic part of the deformation gradient  $\mathbf{F}_e$  maps the intermediate “configuration” to the compatible spatial configuration as shown in Figure 2. Here, growth is assumed to be morphogenetic and thus independent of the deformation itself. We consider anisotropic growth along the film such that it prevents growth in the lateral directions. Hence, the growth tensor can be described as  $\mathbf{F}_g = \mathbf{I} + g\mathbf{I}_{\text{ani}}$ , where  $\mathbf{I}_{\text{ani}} = \mathbf{I} - \mathbf{N} \otimes \mathbf{N}$  with  $\mathbf{N}$  being the unit normal vector to the film. Note that in the absence of growth, the growth tensor  $\mathbf{F}_g = \mathbf{I}$  and the deformation gradient  $\mathbf{F}$  is equal to the elastic part. The growth parameter  $g$  represents growth if  $g > 0$  and shrinkage or atrophy if  $g < 0$ .

The constitutive behavior of the film is identified via its free energy  $\psi$  depending on the growth part of the deformation gradient  $\mathbf{F}_g$  and  $\mathbf{F}$ , respectively. Therefore, the free energy  $\psi(\mathbf{F}, \mathbf{F}_g)$  renders the same value as the elastic free energy  $\psi_e(\mathbf{F}_e)$  as

$$\psi = \psi(\mathbf{F}, \mathbf{F}_g) = \psi_e(\mathbf{F}_e). \quad (3)$$

<sup>1</sup>The term Piola stress is adopted instead of the more commonly used first Piola–Kirchhoff stress. Nonetheless, it seems that the term *Piola stress* is more appropriate for this stress measure. Recall,  $\mathbf{P}$  is essentially the *Piola transform* of the Cauchy stress and ties perfectly to the *Piola identity*. Also historically, Kirchhoff (1824–1877) employed this stress measure after Piola (1794–1850); see also the discussion in [Podio-Guidugli 2000].

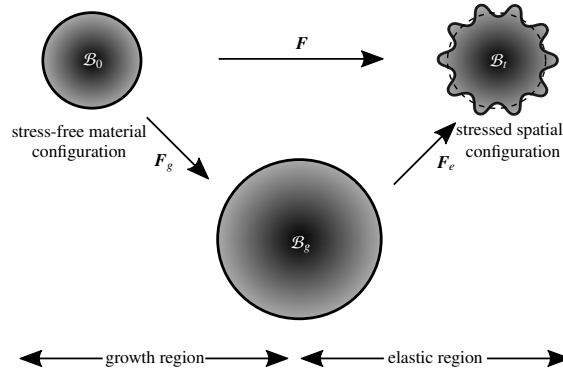


**Figure 2.** Kinematics of growth with multiplicative decomposition of the deformation gradient into elastic  $F_e$  and growth  $F_g$  parts. The intermediate configuration  $B_g$  is, in general, incompatible.

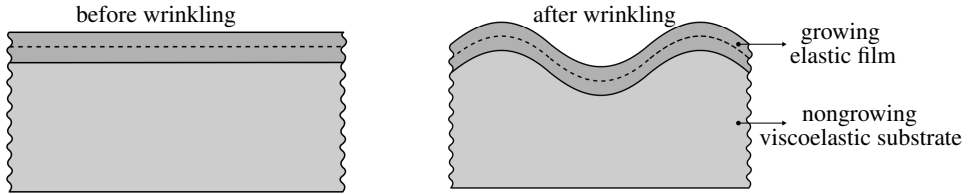


**Figure 3.** Geometry of elastic growing film on a viscoelastic substrate.

Due to the second law of thermodynamics and using the Coleman–Noll procedure, the Piola stress for a hyperelastic material reads

$$\mathbf{P} := \frac{\partial \psi}{\partial \mathbf{F}} = \frac{\partial \psi_e}{\partial \mathbf{F}_e} : \frac{\partial \mathbf{F}_e}{\partial \mathbf{F}} = \frac{\partial \psi_e}{\partial \mathbf{F}_e} : [\mathbf{I} \bar{\otimes} \mathbf{F}_g^{-t}] = \mathbf{P}_e \cdot \mathbf{F}_g^{-t} \quad \text{with} \quad \mathbf{P}_e := \frac{\partial \psi_e}{\partial \mathbf{F}_e}, \quad (4)$$

where the operator  $\bar{\otimes}$  denotes a nonstandard dyadic product with the index notation property  $[\mathbf{A} \bar{\otimes} \mathbf{B}]_{ijkl} = [\mathbf{A}]_{ik}[\mathbf{B}]_{jl}$  for two second-order tensors  $\mathbf{A}$  and  $\mathbf{B}$ .

**2.2. Viscoelastic substrate.** As the film grows, the stress in the film increases until the growth parameter reaches a critical value  $g_c$  at which point geometrical instabilities may occur in the form of wrinkles. Obviously, the corresponding deformed state is strongly dependent on the substrate beneath the film and thus the material behavior of the substrate plays an important role. In the problem of interest here, we consider an elastic growing film on a viscoelastic substrate as illustrated in Figure 3. The two sides are constrained in the horizontal direction and the bottom of the substrate is constrained in the vertical direction. The interface between the film and substrate is perfect and no debonding nor separation occurs throughout the process. This generalization shall be investigated in a future contribution.

The viscoelastic behavior of the substrate can be captured by introducing internal variables. For simplification, we consider the process to be isothermal and therefore neglect any temperature effects. Hence, the thermodynamic state of the body can be expressed merely by the deformation gradient and the internal variables. The free energy representing the viscoelastic material behavior of the substrate is

based on an additive decomposition of the energy into its *volumetric* and *isochoric* parts together with a dissipative contribution  $\psi^{\text{dis}}$  incorporating internal variables  $\alpha$  as

$$\psi(J, \bar{\mathbf{C}}) = \psi^{\text{vol}}(J) + \psi^{\text{iso}}(\bar{\mathbf{C}}) + \psi^{\text{dis}}(\alpha, \bar{\mathbf{C}}) \quad \text{with} \quad \bar{\mathbf{C}} = J^{-2/3} \mathbf{C}, \quad \mathbf{C} = \mathbf{F}^t \cdot \mathbf{F}. \quad (5)$$

The Piola–Kirchhoff stress  $\mathbf{S}$  can be determined as

$$\mathbf{S} = \mathbf{S}^{\text{vol}} + \mathbf{S}^{\text{iso}} + \mathbf{Q} \quad \text{with} \quad \mathbf{S}^{\text{vol}} = 2 \frac{\partial \psi^{\text{vol}}}{\partial \mathbf{C}}, \quad \mathbf{S}^{\text{iso}} = 2 \frac{\partial \psi^{\text{iso}}}{\partial \mathbf{C}}, \quad \text{and} \quad \mathbf{Q} = 2 \frac{\partial \psi^{\text{dis}}(\alpha, \bar{\mathbf{C}})}{\partial \mathbf{C}}, \quad (6)$$

from which the Piola stress is readily obtained by  $\mathbf{P} = \mathbf{F} \cdot \mathbf{S}$ . The evolution equation for  $\mathbf{Q}$  is assumed as

$$\dot{\mathbf{Q}} + \frac{1}{\tau} \mathbf{Q} = \frac{1}{\tau} \dot{\mathbf{S}}_{\text{iso}}, \quad (7)$$

where  $\tau$  denotes the *relaxation time* with the definition

$$\tau = \frac{\eta}{E}, \quad (8)$$

in which  $\eta$  and  $E$  are the viscosity and the elastic modulus of the material, respectively. For  $\mathbf{Q}$  the convolution representation, as proposed in [Holzapfel 2000; Simo and Hughes 1998], reads

$$\mathbf{Q} = \exp\left(-\frac{T}{\tau}\right) \mathbf{Q} + \int_{t=0}^{t=T} \frac{1}{\tau} \exp\left(-\frac{T-t}{\tau}\right) \dot{\mathbf{S}}_{\text{iso}} dt. \quad (9)$$

### 3. Analytical approach

Since we are only interested in the onset of instabilities, unlike the computational approach to this problem, the analytical solution is derived based on small strains instead of finite deformations. In the computational approach, it would be impossible to capture instabilities if geometrical nonlinearities were precluded. Nonetheless, the geometrical instabilities in the analytical approach are implicitly accounted for via a buckling analysis of the film. To study the viscoelastic behavior of the substrate at small strains, we choose a rheological model demonstrated in Figure 4 representing the (general) standard solid model to recover a wide range of material behaviors; see [Holzapfel 2000; Simo and Hughes 1998] for further details. As it will be clarified, the (general) standard solid model captures both the Maxwell model and the Kelvin model. The rheological model in Figure 4 consists of two spring elements with constants  $E$  and  $E_\infty$ , which represent the elastic response of the solid. The spring with constant  $E$  is connected in series with a dashpot with viscosity  $\eta$ . From a physical point of view, the constants  $E_\infty$ ,  $E$ , and  $\eta$  must be positive. The strains in both elements A and B are identical due to their parallel arrangement. The total stress  $\sigma$  prescribed in Figure 4 can be recovered as addition of the stress in A and B as

$$\sigma = \sigma^\infty + \sigma^\nu \quad \text{with} \quad \sigma^\infty = E_\infty \epsilon, \quad (10)$$

where  $\sigma^\infty$  is applied to the element B representing the stress of the rheological model as  $t \rightarrow \infty$  in a relaxation test and  $\sigma^\nu$  represents the viscous stress acting on the dashpot. From a mechanical point of view, the strain in the viscous element B is the addition of the elastic strain in the spring with constant  $E$  and the inelastic strain-like internal variable  $\alpha$  in the dashpot and thus

$$\sigma^\nu = E[\epsilon - \alpha] = \eta \dot{\alpha}. \quad (11)$$

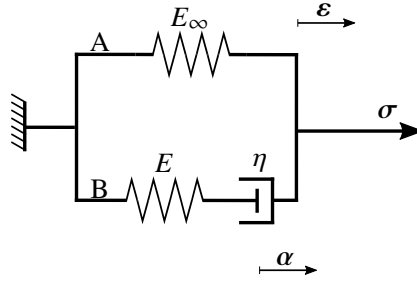


**Figure 4.** Illustration of the kinematics of the viscoelastic material with (general) standard solid element model. The rheological model is composed of two elements A and B. The subscript  $\infty$  denotes the elastic response of the solid for  $t \rightarrow \infty$  corresponding to the behavior of solid in a relaxation test after infinite time.

By considering the *initial modulus*  $E_0$  at  $t = 0$  with no strain in the dashpot, the rheological model in Figure 4 resembles a solid with two spring elements with constants  $E$  and  $E_\infty$  as instantaneous modulus  $E_0 = E_\infty + E$  and hence, (10) leads to

$$\sigma = E_0 \epsilon - E \alpha, \quad (12)$$

where the inelastic strain  $\alpha$  satisfies the evolution equation

$$\dot{\alpha} + \frac{1}{\tau} \alpha = \frac{1}{\tau} \epsilon \quad \text{with the condition} \quad \lim_{t \rightarrow -\infty} \alpha(t) = 0. \quad (13)$$

Additionally, there exists an alternative formulation by introducing a stress-like variable  $q = E[\epsilon - \alpha]$  acting on the dashpot, so that (12) transforms to  $\sigma = E_\infty \epsilon + q$  and thus the evolution equation (13) can be rewritten as

$$\dot{q} + \frac{1}{\tau} q = \frac{1}{\tau} E \epsilon \quad \text{with the condition} \quad \lim_{t \rightarrow -\infty} q(t) = 0. \quad (14)$$

To determine the critical growth of an elastic film on a viscoelastic substrate, we compute the critical growth by analyzing the buckling of the film on the substrate, Figure 5. In doing so, first we assume the substrate to be elastic and then we replace the elastic behavior of the substrate by its equivalent viscoelastic one. The whole analysis here is two-dimensional and corresponding to a plane-strain scenario. Let  $w$  denote the deflection of the film. The governing differential equation of a film adhered to an infinite half-space reads

$$\frac{1}{12} E_f h^3 \frac{d^4 w}{dx^4} + h \sigma \frac{d^2 w}{dx^2} = f_s, \quad (15)$$

where  $\sigma$  is the stress in the film,  $E_f$  is the film elastic modulus and  $h$  is the film thickness. The transverse force on the film from the substrate  $f_s$  reads [Allen 1969]

$$f_s = -\frac{2E_s}{[3 - \nu_s][1 + \nu_s]} n w, \quad (16)$$

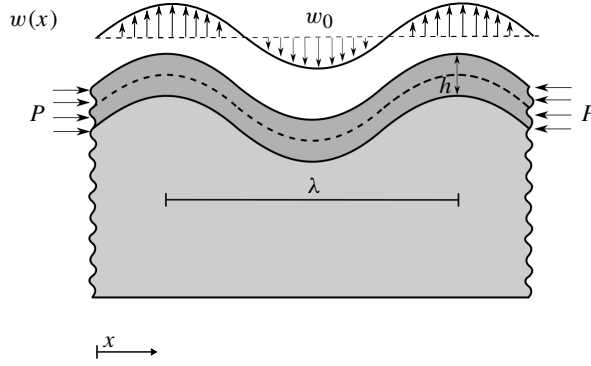


**Figure 5.** Analytical model of growing elastic film on a viscoelastic substrate. The film thickness is denoted  $h$  and  $\lambda$  is the wavelength. The amplitude of the sinusoidal wave on the substrate is denoted  $w_0$ . The lateral force  $P$  relates to the stress in the film via  $P = \sigma hb$  with  $b$  being the width of the domain in the direction normal to the plane.

where  $\nu_s$  is the Poisson's ratio of the substrate, with sinusoid  $w$  with the wavenumber  $n$  on its surface. By substituting  $f_s$  in (15) and solving for  $\sigma$ , we have

$$\sigma = \frac{1}{12} E_f h^2 n^2 + \frac{2E_s}{[3 - \nu_s][1 + \nu_s]hn}, \quad (17)$$

from which the critical wavenumber can be computed by minimizing with respect to  $\sigma$  as

$$n_c = \sqrt[3]{\frac{12E_s}{E_f[3 - \nu_s][1 + \nu_s]h^3}}, \quad (18)$$

from which the critical wavelength can be readily calculated. Inserting the critical wavenumber  $n_c$  into the stress equation (17) results in the critical stress  $\sigma_c$  and eventually the critical growth  $g_c$  is obtained as  $g_c \approx \varepsilon_c = \sigma_c/E_f$  for sufficiently small values of  $\varepsilon_c$ . A more accurate approximation for the critical growth reads  $g_c = \varepsilon_c/[1 - \varepsilon_c]$ . Nonetheless, the validity of this linear approach is questionable for larger  $\varepsilon_c$  corresponding to film-to-substrate stiffness ratios less than 10; see [Cao and Hutchinson 2012b].

Now, we generalize the elastic model to a viscoelastic one to study the effect of the viscoelastic material properties of the substrate on the critical growth of the film. To do so, by regarding  $E_s$  and  $\nu_s$  as the material constants of the substrate, the viscoelastic substrate model can be expressed solely by modifying the material constants of an elastic substrate model. First, by solving the internal variable in (14) in the linear viscoelastic regime, we have for the elastic modulus of the viscoelastic substrate

$$E_s = E_\infty + E \exp\left(-\frac{\Delta t}{\tau}\right). \quad (19)$$

It can be observed that for a large relaxation time  $\tau$  compared to the growth time  $\Delta t$ , the substrate elastic modulus results in  $E_s = E_\infty + E$ , where the substrate can be viewed as an elastic substrate. On the other hand, for relatively slowly growing film or alternatively small relaxation time, the exponential term tends to 0 resulting in the effective elastic modulus in substrate  $E_s = E_\infty$ . To formulate this in the governing

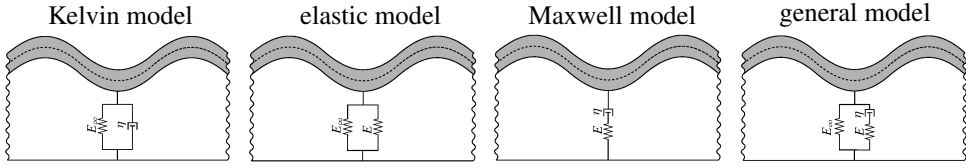


**Figure 6.** Illustration of four models for the substrate behavior. The standard solid model can recover Maxwell, Kelvin, and elastic models as three special cases.

equations of a growing film on a viscoelastic substrate, we introduce the effective substrate stiffness

$$E_s^{\text{eff}} = E_\infty + [E_s - E_\infty] \exp\left(-\frac{\Delta t}{\tau}\right), \quad (20)$$

and then by substituting (20) in (16) we obtain the viscoelastic substrate transverse force as

$$f_s = -\frac{2}{[3 - \nu_s][1 + \nu_s]} \left[ E_\infty + [E_s - E_\infty] \exp\left(-\frac{\Delta t}{\tau}\right) \right] n w(x), \quad (21)$$

and after substituting in (15) and solving for  $\sigma$  we have

$$\sigma = \frac{1}{12} E_f h^2 n^2 + \frac{2}{[3 - \nu_s][1 + \nu_s] h n} \left[ E_\infty + [E_s - E_\infty] \exp\left(-\frac{\Delta t}{\tau}\right) \right], \quad (22)$$

and consequently, the minimization with respect to  $\sigma$  yields the critical wavenumber

$$n_c = \sqrt[3]{\frac{12[E_\infty + [E_s - E_\infty] \exp(-\Delta t/\tau)]}{E_f h^3 [3 - \nu_s][1 + \nu_s]}}, \quad (23)$$

from which the critical stress  $\sigma_c$  and eventually the critical growth  $g_c$  can be calculated, as before.

Obviously, the standard solid model in viscoelastic material modeling can simplify to the Maxwell, Kelvin, and elastic models, as schematically illustrated in Figure 6. For instance, from Figure 6 it is obvious that a standard solid model reduces to the Maxwell model if  $E_\infty \rightarrow 0$ , and thus the effective stiffness of the substrate in this case reads

$$E_s = E \exp\left(-\frac{\Delta t}{\tau}\right), \quad (24)$$

and consequently

$$f_s = -\frac{2}{[3 - \nu_s][1 + \nu_s]} [E_s \exp\left(-\frac{\Delta t}{\tau}\right)] n w(x). \quad (25)$$

#### 4. Numerical examples

The purpose of this section is to illustrate the growth-induced instabilities in a bilayer system composed of a thin growing film on top of a viscoelastic substrate as shown in Figure 7. In particular, we study the influence of a viscoelastic substrate on the critical wavelength due to growth-induced buckling patterns as well as the critical growth. More importantly, the numerical results obtained from the computational simulations using the finite element method are compared against the proposed analytical solution.

For all examples, to omit further complexities in interpreting the results, it is assumed that the critical growth is reached at the same  $\Delta t$  independent of the stiffness ratio. Therefore, the relaxation time  $\tau$



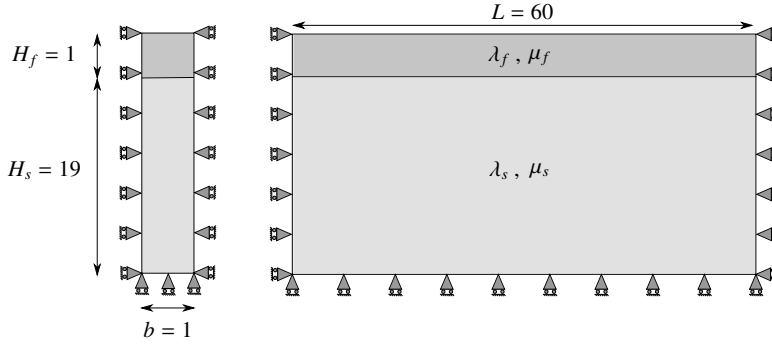


**Figure 7.** Geometry and dimensions of an elastic growing film on a viscoelastic substrate.

remains as the only independent parameter to study its effect instead of the ratio  $\Delta t/\tau$ . In order to extend the observations to a more general case with varying  $\Delta t$ , the dimensionless parameter  $\kappa = \Delta t/\tau$  is defined, thereby  $\kappa$  is essentially the ratio of the time for the film to reach the critical growth over the substrate relaxation time. For the problem of interest here, the neo-Hookean potential

$$\psi_e = \frac{1}{2}\mu[\mathbf{F}_e : \mathbf{F}_e - 2 - 2\ln J_e] + \frac{1}{2}\lambda\left[\frac{1}{2}[J_e^2 - 1] - \ln J_e\right] \quad \text{with} \quad J_e = \det \mathbf{F}_e \quad (26)$$

is used for the elastic response of the film and the substrate where  $\mu$  and  $\lambda$  are Lamé parameters. Furthermore, it is assumed that the film grows only along its length but not in the vertical direction. The film over substrate stiffness ratio is defined as  $\mu_f/\mu_s$  and the Poisson's ratio for both media is assumed as  $\nu_f = \nu_s = 0.45$ . Thus the larger the stiffness ratio, the more compliant is the substrate compared to the film. For the numerical simulations, the domain is discretized using biquadratic finite elements to achieve a better accuracy [Javili et al. 2015]. To compute critical growth of the film and folding pattern, the numerical approach based on the large deformation must be calculated. To this aim, first we weigh the strong form of the balance equations (1) with the test function  $\delta\boldsymbol{\varphi} \in \mathcal{H}_0^1(\mathcal{B}_0)$  with the definition  $\delta\boldsymbol{\varphi} = \mathbf{0}$  on  $\partial\mathcal{B}_0^\varphi$  and integrate over  $\mathcal{B}_0$ , yielding the following global weak form:

$$\mathbf{r}^\varphi(\boldsymbol{\varphi}(\mathbf{x}, t)) = \int_{\mathcal{B}_0} \text{Grad } X \delta\boldsymbol{\varphi} : \mathbf{P} \, dV - \int_{\mathcal{B}_0} \delta\boldsymbol{\varphi} \cdot \mathbf{b}_0 \, dV - \int_{\partial\mathcal{B}_0} \delta\boldsymbol{\varphi} \cdot \mathbf{t}_0 \, dA = \mathbf{0}. \quad (27)$$

In the frame of finite element analysis, the goal is to solve (27) by vanishing the residual  $\mathbf{r}^\varphi(\boldsymbol{\varphi}(\mathbf{x}, t))$ . To obtain this, and find  $\boldsymbol{\varphi}$  such that the residuum vanishes, the Newton–Raphson scheme can be used:

$$\mathbf{r}(\boldsymbol{\varphi}_{m+1}) = \mathbf{r}(\boldsymbol{\varphi}_m) + \frac{\partial \mathbf{r}}{\partial \boldsymbol{\varphi}} \cdot \Delta\boldsymbol{\varphi}, \quad (28)$$

where index  $m$  denotes the iteration number. The derivative of the residual with respect to  $\boldsymbol{\varphi}$  can be described as the stiffness matrix  $\mathbf{K} = \partial \mathbf{r} / \partial \boldsymbol{\varphi}$ : the eigenvalue representation for diagonalizable matrices [Javili et al. 2015] of a stiffness matrix for a system with  $n$  degrees of freedom is

$$\mathbf{K}_{n \times n} = K_1 \boldsymbol{\lambda}_1 \otimes \boldsymbol{\lambda}_1 + K_2 \boldsymbol{\lambda}_2 \otimes \boldsymbol{\lambda}_2 + \cdots + K_i \boldsymbol{\lambda}_i \otimes \boldsymbol{\lambda}_i + \cdots + K_n \boldsymbol{\lambda}_n \otimes \boldsymbol{\lambda}_n = \sum_{i=1}^n K_i \boldsymbol{\lambda}_i \otimes \boldsymbol{\lambda}_i, \quad (29)$$

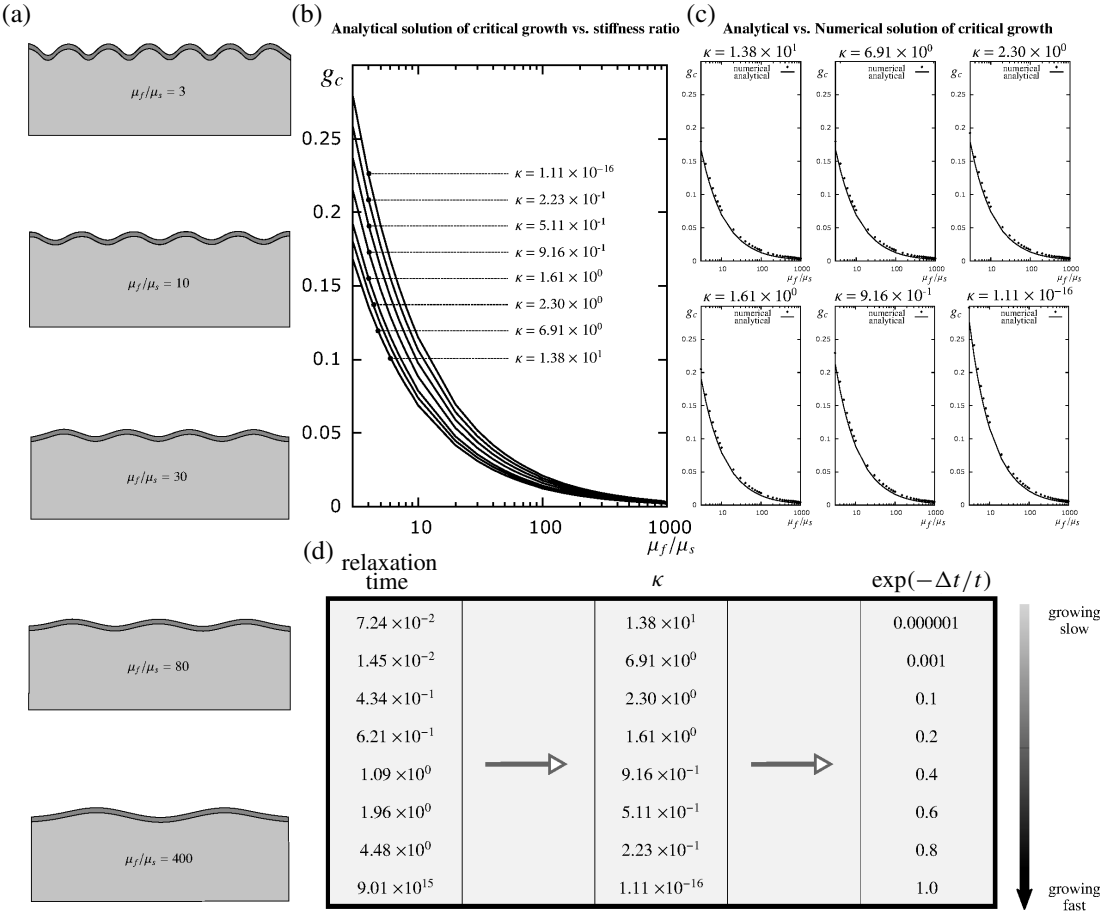


**Figure 8.** Instability study of growing elastic film with thickness 1 on a viscoelastic substrate by using various relaxation times to examine the viscous substrate effects on the critical growth of the elastic film. The standard solid model is chosen to capture viscoelastic effects. The relation of growth time to relaxation time is  $\kappa = \Delta t/\tau$ . The stiffness ratio is  $\mu_f/\mu_s$  and the Poisson’s ratio for both the film and substrate is  $\nu_f = \nu_s = 0.45$ . The variation of relaxation times occurs by changing the viscosity  $\eta$  of the material. This effect could have identical results by holding viscosity constant and changing growth time. The right growing time line shows this parallel impact.

in which  $K_i$  represents the eigenvalue and  $\lambda_i$  the associated unit eigenvector for  $i = 1, \dots, n$ . In the sense of studying growth instability, the negative eigenvalue of stiffness matrices represents the growth instability and the associated unit eigenvector represents the folding pattern. To obtain the critical value of growth, the growth is increased until one of the eigenvalues becomes negative. Then, the associated growth is the critical growth of the system. More computational details are explained in the [Appendix](#).

Figure 8 gathers the analytical results and numerical simulations using eigenvalue analysis. The critical growth  $g_c$  in Figure 8, b and c, and corresponding folding pattern in Figure 8a are illustrated for different

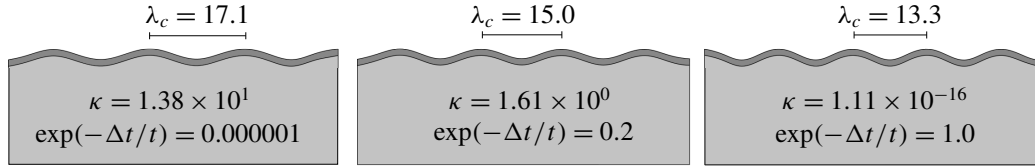


**Figure 9.** Folding of growing film with thickness 1 on a viscoelastic substrate for some  $\kappa = \Delta t/\tau$  with stiffness ratio  $\mu_f/\mu_s = 40$ . The Poisson's ratio for both the film and substrate is  $\nu_f = \nu_s = 0.45$ . The critical wavelength is denoted  $\lambda_c = 2\pi/n_c$ , where the critical wavenumber  $n_c$  can be calculated from (23).

stiffness ratios  $\mu_f/\mu_s$  for various  $\kappa$  in Figure 8d to study the effect of relaxation time on the critical growth  $g_c$  and wavelength. First, we see that for a given  $\tau$  in Figure 8b, the critical growth decreases by increasing the stiffness ratio. Second, it is observed that the critical growth  $g_c$  increases by decreasing  $\kappa$  or alternatively increasing the relaxation time  $\tau$ . This can be justified by the first observation. That is, for a given  $\mu_f/\mu_s$ , a larger relaxation time  $\tau$  leads to an increased effective stiffness of the substrate and hence resembles an overall smaller film-to-substrate stiffness ratio which in turn results in a larger critical growth. Third, there is excellent agreement between the numerical results in Figure 8c using the finite element method via eigenvalue analysis and the proposed analytical solution. So much so that the points corresponding to the numerical results are shown on separate graphs for a better visualization. The numerical results from the finite element method consistently overestimate the analytical solution only and provide an overall stiffer response, as expected. Furthermore, for a given relaxation time, e.g.,  $\tau = 0.0724$ , the deformation is illustrated for various stiffness ratios on the left. Increasing the stiffness ratio results in a larger wavelength and thus less waves for a given length of the domain according to (23). Finally, the folding patterns for a given stiffness ratio of  $\mu_f/\mu_s = 40$  but for varying relaxation time  $\tau$  are illustrated in Figure 9 and it is obvious that increasing the relaxation time decreases the wavelength. This can again be justified by the fact that increasing the relaxation time is effectively decreasing the stiffness ratio and hence the wavelength.

## 5. Conclusion

Biological growth in living systems can lead to geometric instabilities in the form of folding and wrinkling, thus understanding these phenomenon is of crucial importance. Growth-induced instabilities are often studied in bilayer systems where both the thin film and the underlying compliant substrate behave elastically. Nonetheless, due to its relevance for living tissues, the substrate in this contribution is considered to be viscoelastic. This problem is carefully analyzed using both an analytical approach as well as computational simulations using the finite element method whereby eigenvalue analysis is utilized to capture the instabilities. The results obtained from both methods are compared for a wide range of parameters and show an excellent agreement between the computational simulations and the proposed analytical solution. It is observed that the viscoelastic influence of the substrate can be interpreted and eventually replaced by an “effective” elastic model. Our next immediate extension of this contribution is to replace the perfect bonding between the substrate and the film by a general interface model [Javili et al. 2017; Javili 2018] and study its implications.

---

```

read data: geometrical data, material parameters, and boundary conditions
initialization: set degrees of freedom, quadrature points, and shape functions
while eigenvalues > 0 do
    calculate Neumann, Dirichlet, and loads for this time step
    while Newton loop do
        initialize global tangent stiffness matrix, residuum, volume, surface, and internal forces
        for element loop do
            determine DOFs, displacement, and coordinates belonging to the current element
            for integration loop do
                evaluate shape function and its gradient at the current quadrature point
                calculate deformation gradient  $\mathbf{F}$ 
                if film element then
                    | elasticity material box( $\mathbf{F}$ , state variables)
                else
                    | viscoelasticity material box( $\mathbf{F}$ , state variables)
                end
                for node loop do
                    | assemble element stiffness matrix  $\mathbf{K}$ 
                end
            end
            assemble global stiffness matrix, volume, surface, and internal forces
        end
        calculate residual  $\mathbf{r}^\varphi(\boldsymbol{\varphi}(\mathbf{X}, t))$ 
    end
    eigenvalue analysis
    if eigenvalue < 0 then
        |  $g = g_{cr}$ 
        | calculate eigenvector
        | break while loop
    else
        | growth increment  $g_{\text{new}} = g_{\text{old}} + \Delta g$ 
    end
end

```

---

**Algorithm 1.** The incremental nonlinear finite element method with eigenvalue analysis to capture geometrical instabilities.

### Appendix: Computational aspects

The geometry in Figure 7 consists of a rectangular domain which is meshed with 560 quadratic quadrilateral elements with 3578 DOFs. Computations are carried out using our in-house nonlinear finite element code; to have a proper numerical solution we use the finite element method algorithm 1, which explains the finite element structure using eigenvalue analysis. Algorithm 2 is an elastic material box used to model growth of elastic film and Algorithm 3 is a viscoelastic material box to model the substrate behavior.

---

**Input:** deformation gradient ( $F$ ), state variables  
**Update configurations**  $J_{n+1} := \det[F_{n+1}]$ ,  $C_{n+1} = F_{n+1}^t F_{n+1}$   
**Decompose  $F$  to  $F_e$  and  $F_g$**   
**Calculate growth part  $F_g$**   
**Compute  $P$ ,  $\mathbb{C}$**   
**Output:** Piola stress and algorithmic tangent moduli

---

**Algorithm 2.** Elastic material box to calculate growth in living materials.

---

**Input:** deformation gradient ( $F$ ), state variables  
**Update configurations**  $J_{n+1} := \det[F_{n+1}]$ ,  $C_{n+1} = F_{n+1}^t F_{n+1}$ ,  $\bar{F}_{n+1} = J_{n+1}^{-1/3} F_{n+1}$ ,  $\bar{C}_{n+1} = J_{n+1}^{-2/3} C_{n+1}$   
     calculate the second Piola–Kirchhoff stress  $S_{n+1}$  and internal variable  $Q_{n+1}$   
**Compute  $P$ ,  $\mathbb{C}$**   
**Output:** Piola stress, algorithmic tangent moduli

---

**Algorithm 3.** Viscoelasticity material box to calculate viscoelastic effects of substrate.

## References

- [Allen 1969] H. G. Allen, *Analysis and design of structural sandwich panels*, Pergamon, Oxford, 1969.
- [Balbi and Ciarletta 2013] V. Balbi and P. Ciarletta, “Morpho-elasticity of intestinal villi”, *J. R. Soc. Interface* **10**:82 (2013), art. id. 20130109.
- [Ben Amar and Goriely 2005] M. Ben Amar and A. Goriely, “Growth and instability in elastic tissues”, *J. Mech. Phys. Solids* **53**:10 (2005), 2284–2319.
- [Budday and Steinmann 2018] S. Budday and P. Steinmann, “On the influence of inhomogeneous stiffness and growth on mechanical instabilities in the developing brain”, *Int. J. Solids Struct.* **132–133** (2018), 31–41.
- [Budday et al. 2014] S. Budday, P. Steinmann, and E. Kuhl, “The role of mechanics during brain development”, *J. Mech. Phys. Solids* **72** (2014), 75–92.
- [Budday et al. 2015] S. Budday, E. Kuhl, and J. W. Hutchinson, “Period-doubling and period-tripling in growing bilayered systems”, *Philos. Mag.* **95**:28–30 (2015), 3208–3224.
- [Cao and Hutchinson 2012a] Y. Cao and J. W. Hutchinson, “From wrinkles to creases in elastomers: the instability and imperfection-sensitivity of wrinkling”, *Proc. R. Soc. Lond. A* **468**:2137 (2012), 94–115.
- [Cao and Hutchinson 2012b] Y. Cao and J. W. Hutchinson, “Wrinkling phenomena in neo-Hookean film/substrate bilayers”, *J. Appl. Mech.* **79**:3 (2012), art. id. 031019.
- [Ciarletta and Ben Amar 2012] P. Ciarletta and M. Ben Amar, “Growth instabilities and folding in tubular organs: a variational method in non-linear elasticity”, *Int. J. Non-Linear Mech.* **47**:2 (2012), 248–257.
- [Ciarletta and Maugin 2011] P. Ciarletta and G. A. Maugin, “Elements of a finite strain-gradient thermomechanical theory for material growth and remodeling”, *Int. J. Non-Linear Mech.* **46**:10 (2011), 1341–1346.
- [Ciarletta et al. 2013] P. Ciarletta, L. Preziosi, and G. A. Maugin, “Mechanobiology of interfacial growth”, *J. Mech. Phys. Solids* **61**:3 (2013), 852–872.
- [Cowin and Hegedus 1976] S. C. Cowin and D. H. Hegedus, “Bone remodeling, I: Theory of adaptive elasticity”, *J. Elasticity* **6**:3 (1976), 313–326.
- [Dervaux and Ben Amar 2011] J. Dervaux and M. Ben Amar, “Buckling condensation in constrained growth”, *J. Mech. Phys. Solids* **59**:3 (2011), 538–560.

- [Dunlop et al. 2010] J. W. C. Dunlop, F. D. Fischer, E. Gamsjäger, and P. Fratzl, “A theoretical model for tissue growth in confined geometries”, *J. Mech. Phys. Solids* **58**:8 (2010), 1073–1087.
- [Epstein and Maugin 2000] M. Epstein and G. A. Maugin, “Thermomechanics of volumetric growth in uniform bodies”, *Int. J. Plast.* **16**:7-8 (2000), 951–978.
- [Garikipati et al. 2004] K. Garikipati, E. M. Arruda, K. Grosh, H. Narayanan, and S. Calve, “A continuum treatment of growth in biological tissue: the coupling of mass transport and mechanics”, *J. Mech. Phys. Solids* **52**:7 (2004), 1595–1625.
- [Goriely et al. 2008] A. Goriely, M. Robertson-Tessi, M. Tabor, and R. Vandiver, “Elastic growth models”, pp. 1–44 in *Mathematical modelling of biosystems*, edited by R. P. Mondaini and P. M. Pardalos, Appl. Optim. **102**, Springer, 2008.
- [Holzapfel 2000] G. A. Holzapfel, *Nonlinear solid mechanics: a continuum approach for engineering*, Wiley, Chichester, England, 2000.
- [Hong et al. 2009] W. Hong, X. Zhao, and Z. Suo, “Formation of creases on the surfaces of elastomers and gels”, *Appl. Phys. Lett.* **95**:11 (2009), art. id. 111901.
- [Huang 2005] R. Huang, “Kinetic wrinkling of an elastic film on a viscoelastic substrate”, *J. Mech. Phys. Solids* **53**:1 (2005), 63–89.
- [Huang and Suo 2002] R. Huang and Z. Suo, “Instability of a compressed elastic film on a viscous layer”, *Int. J. Solids Struct.* **39**:7 (2002), 1791–1802.
- [Huang et al. 2005] Z. Y. Huang, W. Hong, and Z. Suo, “Nonlinear analyses of wrinkles in a film bonded to a compliant substrate”, *J. Mech. Phys. Solids* **53**:9 (2005), 2101–2118.
- [Hutchinson 2013] J. W. Hutchinson, “The role of nonlinear substrate elasticity in the wrinkling of thin films”, *Phil. Trans. R. Soc. A* **371**:1993 (2013), art. id. 20120422.
- [Javili 2018] A. Javili, “Variational formulation of generalized interfaces for finite deformation elasticity”, *Math. Mech. Solids* **23**:9 (2018), 1303–1322.
- [Javili et al. 2013] A. Javili, A. McBride, and P. Steinmann, “Thermomechanics of solids with lower-dimensional energetics: on the importance of surface, interface, and curve structures at the nanoscale”, *Appl. Mech. Rev.* **65**:1 (2013), art. id. 010802.
- [Javili et al. 2014] A. Javili, P. Steinmann, and E. Kuhl, “A novel strategy to identify the critical conditions for growth-induced instabilities”, *J. Mech. Behav. Biomed. Mater.* **29** (2014), 20–32.
- [Javili et al. 2015] A. Javili, B. Dortdivanlioglu, E. Kuhl, and C. Linder, “Computational aspects of growth-induced instabilities through eigenvalue analysis”, *Comput. Mech.* **56**:3 (2015), 405–420.
- [Javili et al. 2017] A. Javili, P. Steinmann, and J. Mosler, “Micro-to-macro transition accounting for general imperfect interfaces”, *Comput. Methods Appl. Mech. Eng.* **317** (2017), 274–317.
- [Jin et al. 2011] L. Jin, S. Cai, and Z. Suo, “Creases in soft tissues generated by growth”, *Europhys. Lett.* **95**:6 (2011), art. id. 64002.
- [Jin et al. 2015] L. Jin, A. Auguste, R. C. Hayward, and Z. Suo, “Bifurcation diagrams for the formation of wrinkles or creases in soft bilayers”, *J. Appl. Mech.* **82**:6 (2015), art. id. 061008.
- [Kuhl 2014] E. Kuhl, “Growing matter: a review of growth in living systems”, *J. Mech. Behav. Biomed. Mater.* **29** (2014), 529–543.
- [Kuhl and Steinmann 2003] E. Kuhl and P. Steinmann, “Mass- and volume-specific views on thermodynamics for open systems”, *Proc. R. Soc. Lond. A* **459**:2038 (2003), 2547–2568.
- [Kuhl et al. 2003] E. Kuhl, A. Menzel, and P. Steinmann, “Computational modeling of growth”, *Comput. Mech.* **32**:1-2 (2003), 71–88.
- [Li et al. 2011] B. Li, Y.-P. Cao, X.-Q. Feng, and H. Gao, “Surface wrinkling of mucosa induced by volumetric growth: theory, simulation and experiment”, *J. Mech. Phys. Solids* **59**:4 (2011), 758–774.
- [Moulton and Goriely 2011] D. E. Moulton and A. Goriely, “Circumferential buckling instability of a growing cylindrical tube”, *J. Mech. Phys. Solids* **59**:3 (2011), 525–537.
- [Podio-Guidugli 2000] P. Podio-Guidugli, “A primer in elasticity”, *J. Elasticity* **58**:1 (2000), 1–104.
- [Rodriguez et al. 1994] E. K. Rodriguez, A. Hoger, and A. D. McCulloch, “Stress-dependent finite growth in soft elastic tissues”, *J. Biomech.* **27**:4 (1994), 455–467.

- [Simo and Hughes 1998] J. C. Simo and T. J. R. Hughes, *Computational inelasticity*, Interdisc. Applied Math. **7**, Springer, 1998.
- [Sultan and Boudaoud 2008] E. Sultan and A. Boudaoud, “The buckling of a swollen thin gel layer bound to a compliant substrate”, *J. Appl. Mech.* **75**:5 (2008), art. id. 051002.
- [Sun et al. 2012] J.-Y. Sun, S. Xia, M.-W. Moon, K. H. Oh, and K.-S. Kim, “Folding wrinkles of a thin stiff layer on a soft substrate”, *Proc. R. Soc. Lond. A* **468**:2140 (2012), 932–953.
- [Taber 1995] L. A. Taber, “Biomechanics of growth, remodeling, and morphogenesis”, *Appl. Mech. Rev.* **48**:8 (1995), 487–545.
- [Tepole et al. 2011] A. B. Tepole, C. J. Ploch, J. Wong, A. K. Gosain, and E. Kuhl, “Growing skin: a computational model for skin expansion in reconstructive surgery”, *J. Mech. Phys. Solids* **59**:10 (2011), 2177–2190.
- [Wiggs et al. 1997] B. R. Wiggs, C. A. Hrousis, J. M. Drazen, and R. D. Kamm, “On the mechanism of mucosal folding in normal and asthmatic airways”, *J. Appl. Physiol.* **83**:6 (1997), 1814–1821.
- [Wyczalkowski et al. 2012] M. A. Wyczalkowski, Z. Chen, B. A. Filas, V. D. Varner, and L. A. Taber, “Computational models for mechanics of morphogenesis”, *Birth Defects Res. C Embryo Today* **96**:2 (2012), 132–152.
- [Xie et al. 2014] W.-H. Xie, B. Li, Y.-P. Cao, and X.-Q. Feng, “Effects of internal pressure and surface tension on the growth-induced wrinkling of mucosae”, *J. Mech. Behav. Biomed. Mater.* **29** (2014), 594–601.
- [Xu et al. 2010] G. Xu, A. K. Knutsen, K. Dikranian, C. D. Kroenke, P. V. Bayly, and L. A. Taber, “Axons pull on the brain, but tension does not drive cortical folding”, *J. Biomech. Eng. (ASME)* **132**:7 (2010), art. id. 071013.
- [Xu et al. 2014] F. Xu, M. Potier-Ferry, S. Belouettar, and Y. Cong, “3D finite element modeling for instabilities in thin films on soft substrates”, *Int. J. Solids Struct.* **51**:21-22 (2014), 3619–3632.
- [Yavari 2010] A. Yavari, “A geometric theory of growth mechanics”, *J. Nonlinear Sci.* **20**:6 (2010), 781–830.

Received 3 Aug 2018. Revised 2 Sep 2018. Accepted 9 Sep 2018.

IMAN VALIZADEH: [iman.valizadeh@udo.edu](mailto:iman.valizadeh@udo.edu)

Department of Mechanical Engineering, TU-Dortmund, Dortmund, Germany

PAUL STEINMANN: [paul.steinmann@fau.de](mailto:paul.steinmann@fau.de)

Chair of Applied Mechanics, Universität Erlangen-Nürnberg, Erlangen, Germany

and

Glasgow Computational Engineering Centre, School of Engineering, University of Glasgow, Glasgow, UK

ALI JAVILI: [ajavili@bilkent.edu.tr](mailto:ajavili@bilkent.edu.tr)

Department of Mechanical Engineering, Bilkent University, Ankara, Turkey





# APPLICATION OF THE HYBRID COMPLEX VARIABLE METHOD TO THE ANALYSIS OF A CRACK AT A PIEZOELECTRIC-METAL INTERFACE

VOLODYMYR GOVORUKHA AND MARC KAMLAH

A plane strain problem for an electrically conducting interface crack between linear transversely isotropic piezoelectric and isotropic elastic conductor materials under remote mechanical loading is considered. The attention is focused on a hybrid complex variable method which combines the Stroh formalism for piezoelectric materials with the Muskhelishvili formalism for conducting isotropic elastic materials. This method is illustrated in detail for the open crack model and the contact zone crack model. Using special presentations of mechanical quantities via sectionally analytic functions, a combined Dirichlet–Riemann and Hilbert boundary value problem is formulated and solved analytically. Stress intensity factors as well as the crack tip energy release rate are found in a clear analytical form. Furthermore, transcendental equations for the determination of the realistic contact zone length and the location of the first interpenetration point have been obtained. A significant influence of the external mechanical loading on the crack opening and the stresses as well as the contact zone and interpenetration region lengths is observed. The dependencies of the mentioned values on the intensities of the mechanical loading are presented in tables and associated diagrams.

## 1. Introduction

With the rapid development of modern industry, piezoelectric-metal composites have been widely used in various electromechanical devices. Due to excellent piezoelectric effects as well as good mechanical properties, these composites have become attractive candidates for use in transducers and actuators for vibration control and biomedical imaging applications [Pritchard et al. 2001]. What is even more common, piezoelectric-metal bimetals have an apparent application in any kind of piezoelectric sensors and transducers, where metal electrodes are always placed on piezoelectric material surfaces to introduce high applied electric fields. However, various defects may occur on the interface of the metal and piezoelectric phases due to flaws during manufacturing, impact, cooling or other unexpected reasons. These defects cause geometric, electric and mechanical discontinuities and thus induce strong stress and electric field concentrations, which may induce crack initiation and crack growth, eventually causing fracture and failure. Therefore, it is important to understand and be able to analyze the fracture characteristics of piezoelectric-metal structures so that reliable service life predictions of the pertinent devices can be conducted.

The earliest research on this topic appears to have been done by Kudriavtsev et al. [1975a; 1975b], who modeled an interface crack between a piezoelectric ceramic and an elastic isotropic conductor as rectilinear and axisymmetric, respectively. Liu and Hsia [2003] provided a result for a double edged crack in such a bimaterial under in-plane electric loading. Based on the integral transformation technique,

*Keywords:* Piezoelectric-metal joint, complex variable method, electrically conducting interface crack, contact zone.

Parton [1976] and Bakirov [2004] studied the plane problem of a crack on a piezoelectric-metal interface, in which the axis of axisymmetry of the transversely isotropic piezoelectric materials is normal to the interface and a normal homogeneous tensile loading is applied at infinity. As presented by Bakirov and Kim [2009], the plane strain problem of a crack on an interface between an isotropic elastic conductor and a transversely isotropic piezoelectric material was reduced to the boundary equations on the interface, which make it possible to calculate the crack tip energy release rate with respect to the distribution of the loading applied to the crack surfaces. A more detailed review of the interface crack problem investigation in piezoelectric-metal composites was presented in the review paper by Govorukha et al. [2016].

Since piezoelectric ceramics and metals are two different kinds of solids, especially concerning electronic transport, it is quite difficult to combine their constitutive equations in an interface crack analysis. For convenience, Ou and Chen [2004] and Li and Chen [2007; 2009] assumed that the metal phase could be considered as a special piezoelectric material with extremely large permittivity and extremely small piezoelectricity and in this way used the extended Stroh formalism to treat this interface crack problem. Although a nonpiezoelectric isotropic elastic material can be treated as a special case of piezoelectric materials with vanishing piezoelectric constants, the well-known Stroh formalism, on which almost all of the existing works on interface cracks in piezoelectric media have been based, breaks down or becomes complicated in the degenerate case of isotropic elastic materials due to the appearance of multiple eigenvalues [Ting and Chou 1981]. In order to eliminate this discrepancy, a hybrid complex variable method was proposed by Ru [2008], in which the isotropic elastic material was handled with the convenient and powerful Muskhelishvili formalism while the piezoelectric material was analyzed with the Stroh formalism. This method was illustrated for an insulating interface crack between a piezoelectric half-plane and an isotropic elastic half-plane.

It should be noted that most of the above-mentioned solutions for interface cracks in piezoelectric-metal composites have oscillatory singularities, as in the case of elasticity [Williams 1959], which causes the overlapping of crack faces, a physically unreasonable phenomenon. To correct this shortcoming, Comninou [1977] developed a contact zone model for a crack between two nonpiezoelectric materials. On the basis of this model, a numerical analysis of an interface crack between a piezoelectric ceramic and an elastic isotropic conductor has been performed by Govorukha and Loboda [2000]. However an analytical investigation of an interface crack with contact zones in a piezoelectric-metal bimaterial is unknown, at least to the authors of this paper.

In the present paper a closed-form solution for a conducting interface crack between a piezoelectric half-plane and a conducting isotropic elastic half-plane is obtained with the use of hybrid complex variable method. The open crack model and the contact zone crack model are utilized. A significant influence of the external mechanical loading on the crack opening, stresses as well as the contact zone and interpenetration region lengths is demonstrated.

## 2. Basic equations

The constitutive and equilibrium equations for a linear piezoelectric material in the absence of body forces and free charges can be represented in the form [Pak 1992]

$$\prod_{mJ} = E_{mJKl} V_{K,l}, \quad (1)$$

$$\prod_{mJ,m} = 0, \quad (2)$$

where

$$V_K = \begin{cases} u_k, & K = 1, 2, 3, \\ \varphi, & K = 4, \end{cases} \quad \prod_{mJ} = \begin{cases} \sigma_{mj}, & m, J = 1, 2, 3, \\ D_m, & m = 1, 2, 3; J = 4, \end{cases}$$

$$E_{mJKl} = \begin{cases} c_{mjkl}, & m, J, K, l = 1, 2, 3, \\ e_{lmj}, & m, J, l = 1, 2, 3; K = 4, \\ e_{mkl}, & m, K, l = 1, 2, 3; J = 4, \\ -\varepsilon_{ml}, & m, l = 1, 2, 3; J, K = 4. \end{cases}$$

Here,  $u_k$ ,  $\varphi$ ,  $\sigma_{mj}$ , and  $D_m$  are the elastic displacements, electric potential, stresses, and electric displacements, while  $c_{mjkl}$ ,  $e_{mjkl}$ , and  $\varepsilon_{mj}$  are the elastic, piezoelectric, and dielectric constants, respectively. Lower case subscripts range from 1 to 3, upper case subscripts range from 1 to 4, and summation over repeated subscripts is implied. The subscript comma denotes partial derivative with respect to the Cartesian coordinates. In addition, the electric field  $E_m$  is related to the electric potential  $\varphi$  by

$$E_m = -\varphi_{,m}.$$

For a two-dimensional problems in which  $u_k$  and  $\varphi$  depend on  $x_1$  and  $x_3$  only, a general solution of (1), (2) according to the method originally proposed by Eshelby et al. [1953] and used by Stroh [1958] can be written as

$$V = A f(z) + \bar{A} \overline{f(z)}, \quad (3)$$

$$t = B f'(z) + \bar{B} \overline{f'(z)}, \quad (4)$$

where  $V = [u_1, u_2, u_3, \varphi]^T$ ,  $t = [\sigma_{13}, \sigma_{23}, \sigma_{33}, D_3]^T$ , and  $f(z)$  consists of four arbitrary analytic functions of the respective variables  $z_\alpha = x_1 + p_\alpha x_3$  ( $\alpha = 1, 2, 3, 4$ ) as

$$f(z) = [f_1(z), f_2(z_2), f_3(z_3), f_4(z_4)]^T.$$

Matrices  $A$  and  $B$  are defined by the material constants, and  $p_\alpha$  are four distinct complex roots with positive imaginary parts of the characteristic equation described by Suo et al. [1992]. Here and afterwards, the superscript  $T$  denotes transposition and the overbar stands for the complex conjugate.

In this paper, we consider transversely isotropic piezoelectric materials poled in the  $x_3$ -direction. In this case, the displacement  $u_2$  decouples in the  $(x_1, x_3)$ -plane from  $(u_1, u_3, \varphi)$ . Because of the simplicity of the  $u_2$ -determination our attention will be devoted to the in-plane problem which is characterized by the displacements  $u_1, u_3$  and the electric potential  $\varphi$ . Thus, the second row and the second column will be deleted from all matrices in (3) and (4).

In the case of the plane problems for the isotropic elastic materials, the stresses and associated elastic displacements can be expressed in terms of the Muskhelishvili complex potentials [1953]  $\phi(z)$  and  $\psi(z)$ :

$$2\mu(u_1 - iu_3) = \kappa \overline{\phi(z)} - \bar{z} \phi'(z) - \psi(z),$$

$$\sigma_{33} + i\sigma_{13} = \phi'(z) + \overline{\phi'(z)} + \bar{z} \phi''(z) + \psi'(z),$$

where  $\kappa = 3 - 4\nu$  for plane strain and  $\kappa = (3 - \nu)/(1 + \nu)$  for plane stress, and  $\mu$  and  $\nu$  are the shear modulus and Poisson's ratio, respectively.

Introducing new analytic functions by the formulas

$$\Psi(z) = \bar{z}\phi''(z) + \psi'(z), \quad \Phi(z) = \phi'(z),$$

one can write,

$$2\mu(u'_1 - iu'_3) = \kappa\overline{\Phi(z)} - \Phi(z) - \Psi(z), \quad (5)$$

$$\sigma_{33} + i\sigma_{13} = \Phi(z) + \overline{\Phi(z)} + \Psi(z). \quad (6)$$

The attention is focused in the following on a hybrid complex variable method which combines the Stroh formalism of the piezoelectric materials with the Muskhelishvili formalism of the conducting isotropic elastic materials (such as metal).

### 3. Complex function representation for the stresses and displacement jumps at the interface

In this section, we develop as a major novelty expressions by which the solution of various mixed boundary conditions at the interface, i.e., different models for cracks between a piezoelectric and a metal, can be obtained. Consider a bimaterial composition, where the piezoelectric phase occupies the upper half-plane ( $x_3 \geq 0$ ) and the metal phase occupies the lower half-plane ( $x_3 \leq 0$ ). We assume, that the stresses and the tangential component of the electric field are continuous across the whole bimaterial interface. The part of the interface which is mechanically bounded is denoted by  $L$ . Then, the boundary conditions at the interface  $x_3 = 0$  are

$$E_1^\pm(x_1, 0) = 0 \quad \text{for } x_1 \in (-\infty, \infty), \quad (7)$$

$$\sigma_{33}^+(x_1, 0) + i\sigma_{13}^+(x_1, 0) = \sigma_{33}^-(x_1, 0) + i\sigma_{13}^-(x_1, 0) \quad \text{for } x_1 \in (-\infty, \infty), \quad (8)$$

$$u_1^+(x_1, 0) - iu_3^+(x_1, 0) = u_1^-(x_1, 0) - iu_3^-(x_1, 0) \quad \text{for } x_1 \in L, \quad (9)$$

where the superscripts “+” and “−” indicate the limit values takes from the upper and the lower half-planes, respectively.

It should be noted that, due to the compatibility conditions at the bonded interface, the respective uniform remote loadings given in the two half-planes must be compatible, in order to give rise to uniform stress and electric fields in the absence of the interface crack. In particular, the component  $E_1^\infty$  of remote uniform electric field parallel to the interface in the upper half-plane must be zero, because it must be compatible with the vanishing tangential electric field of the lower half-plane along the bonded interface.

The electro-elastic field in the upper half-plane is described by the Stroh formalism and given in terms of the three functions  $f_k(z_k)$  of the respective variables  $z_k$  ( $k = 1, 3, 4$ ), while the elastic field in the lower half-plane is described by the Muskhelishvili formalism and given in terms of the two functions  $\Phi(z)$  and  $\Psi(z)$  of the single complex variable  $z$ . Thus, the problem is to determine the three analytic functions  $f_k(z_k)$  in the upper half-plane and two analytic functions  $\Phi(z)$  and  $\Psi(z)$  in the lower half-plane.

Let us define three analytic functions of the single complex variable  $z$  in the upper half-plane, in terms of the functions  $f_k(z_k)$  as

$$g(z) = Af'(z), \quad (10)$$

where  $\mathbf{g}(z) = [g_1(z), g_3(z), g_4(z)]^T$ .

Using relation (10), the expressions (3) and (4) can be represented in the form

$$\mathbf{V}' = \mathbf{g}(z) + \overline{\mathbf{g}(z)}, \quad (11)$$

$$\mathbf{t} = \mathbf{D}\mathbf{g}(z) + \overline{\mathbf{D}}\overline{\mathbf{g}(z)}, \quad (12)$$

where  $\mathbf{D} = i\mathbf{Y}^{-1}$ ,  $\mathbf{Y} = i\mathbf{A}\mathbf{B}^{-1}$ .

In this paper, as defined before, we consider transversely isotropic piezoelectric materials of the symmetry class 6 mm poled in the  $x_3$ -direction which have an essential practical significance. For this case, the matrix  $\mathbf{D}$  has the form

$$\mathbf{D} = \begin{bmatrix} id_{11} & d_{13} & d_{14} \\ d_{31} & id_{33} & id_{34} \\ d_{41} & id_{43} & id_{44} \end{bmatrix},$$

where all  $d_{ij}$  are real and  $d_{31} = -d_{13}$ ,  $d_{41} = -d_{14}$ ,  $d_{43} = d_{34}$  hold true.

Further, the boundary condition (7) along the whole bimaterial interface and the condition  $E_1^\infty = 0$  at infinity give

$$g_4(z) \equiv 0, \quad x_3 \geq 0.$$

In view of the interface conditions (8) and the relations (6) and (12), the continuity of mechanical tractions along the whole real axis gives

$$q_{11}g_1^+(x_1) + q_{12}\overline{g_1^+(x_1)} + iq_{21}g_3^+(x_1) + iq_{22}\overline{g_3^+(x_1)} = \Phi^-(x_1) + \overline{\Phi^-(x_1)} + \Psi^-(x_1),$$

which can be rewritten as

$$q_{11}g_1^+(x_1) + iq_{21}g_3^+(x_1) - \overline{\Phi^+}(x_1) = \Phi^-(x_1) + \Psi^-(x_1) - q_{12}\overline{g_1^+}(x_1) - iq_{22}\overline{g_3^+}(x_1), \quad x_1 \in (-\infty, \infty), \quad (13)$$

where  $q_{11} = d_{31} - d_{11}$ ,  $q_{12} = d_{31} + d_{11}$ ,  $q_{21} = d_{13} + d_{33}$ ,  $q_{22} = d_{13} - d_{33}$ .

The left-hand side of (13) is the boundary value of a function analytic in the upper half-plane, and the right-hand side is the boundary value of another function analytic in the lower half-plane. Hence, both functions are equal to a function defined as

$$M(z) = \begin{cases} q_{11}g_1(z) + iq_{21}g_3(z) - \overline{\Phi}(z) & \text{for } x_3 > 0, \\ \Phi(z) + \Psi(z) - q_{12}\overline{g_1}(z) - iq_{22}\overline{g_3}(z) & \text{for } x_3 < 0, \end{cases} \quad (14)$$

which is analytic in the whole plane.

Taking into account that the stresses are bounded at infinity, it follows that  $M(z)|_{z \rightarrow \infty} = M^{(0)} = \text{const.}$  But according to Liouville's theorem, this means that  $M(z) = M^{(0)}$  holds true in the whole plane. Because  $g_1(z)$ ,  $g_3(z)$ ,  $\Phi(z)$ , and  $\Psi(z)$  are arbitrary functions, without loss of generality, one can choose  $M^{(0)} = 0$ . Thus, Equation (14) leads to

$$q_{11}g_1(z) + iq_{21}g_3(z) - \overline{\Phi}(z) = 0, \quad x_3 > 0,$$

$$\Phi(z) + \Psi(z) - q_{12}\overline{g_1}(z) - iq_{22}\overline{g_3}(z) = 0, \quad x_3 < 0,$$

and then

$$\begin{aligned} iq_{21}g_3(z) &= -q_{11}g_1(z) + \overline{\Phi}(z), & x_3 > 0, \\ q_{21}\Psi(z) &= (q_{12}q_{21} + q_{11}q_{22})\overline{g_1}(z) - (q_{21} + q_{22})\Phi(z), & x_3 < 0. \end{aligned} \quad (15)$$

Hence, the problem is reduced to the determination of the two functions:  $g_1(z)$  in the upper half-plane and  $\Phi(z)$  in the lower half-plane.

Now taking the derivatives of both sides in the interface condition (9) and using the relations (5) and (11) we obtain

$$g_1^+(x_1) - i g_3^+(x_1) - \frac{\kappa}{2\mu} \bar{\Phi}^+(x_1) = -\bar{g}_1^-(x_1) + i \bar{g}_3^-(x_1) - \frac{1}{2\mu} \Phi^-(x_1) - \frac{1}{2\mu} \Psi^-(x_1), \quad x_1 \in L. \quad (16)$$

Continuity of the displacement across the bonded interface, as inferred from (16), implies that a function defined as

$$\Omega(z) = \begin{cases} g_1(z) - i g_3(z) - (\kappa/2\mu) \bar{\Phi}(z) & \text{for } x_3 > 0, \\ -\bar{g}_1(z) + i \bar{g}_3(z) - (1/2\mu) \Phi(z) - (1/2\mu) \Psi(z) & \text{for } x_3 < 0, \end{cases}$$

is analytic in the whole plane with a cut along  $(-\infty, \infty) \setminus L$  and tends to a constant as  $|z| \rightarrow \infty$ .

Thus,  $g_1(z)$  and  $\Phi(z)$  can be expressed via  $\Omega(z)$  as

$$g_1(z) = p_{11}\Omega(z) + p_{12}\bar{\Phi}(z), \quad x_3 > 0, \quad \Phi(z) = p_{21}\Omega(z) + p_{22}\bar{\Phi}(z), \quad x_3 < 0, \quad (17)$$

where

$$p_{11} = \frac{2\mu}{\Delta}(q_{22} - 2\mu), \quad p_{12} = \frac{2\mu}{\Delta}(2\mu + \kappa q_{21}), \quad p_{21} = \frac{4\mu^2}{\Delta}(q_{11} + q_{21}), \\ p_{22} = \frac{2\mu}{\Delta}[2\mu(q_{21} - q_{11}) + q_{12}q_{21} + q_{11}q_{22}], \quad \Delta = (2\mu - \kappa q_{11})(q_{22} - 2\mu) - (2\mu + \kappa q_{21})(q_{12} + 2\mu).$$

Substituting (15) and (17) into (6), we may express the stresses on the whole interface in terms of the single function  $\Phi(z)$ :

$$\begin{aligned} \sigma_{33}(x_1, 0) + i\sigma_{13}(x_1, 0) &= s_{11}\Omega^+(x_1) + s_{12}\bar{\Phi}^+(x_1) + s_{21}\Omega^-(x_1) + s_{22}\bar{\Phi}^-(x_1), \\ \sigma_{33}(x_1, 0) - i\sigma_{13}(x_1, 0) &= s_{11}\bar{\Phi}^-(x_1) + s_{12}\Omega^-(x_1) + s_{21}\bar{\Phi}^+(x_1) + s_{22}\Omega^+(x_1), \end{aligned} \quad (18)$$

where  $s_{11} = p_{22}$ ,  $s_{12} = p_{21}$ ,  $s_{21} = p_{12}q_{12} + q_{22}(p_{12}q_{11} - p_{21})/q_{21}$ ,  $s_{22} = p_{21}$ . It should be noted that the same expressions of the stresses can be found from relation (12).

Similarly, using (5) and (11), we may evaluate the derivatives of the displacement jumps and find

$$\begin{aligned} \langle u_1'(x_1) \rangle - i \langle u_3'(x_1) \rangle &= \Omega^+(x_1) - \Omega^-(x_1), \\ \langle u_1'(x) \rangle + i \langle u_3'(x_1) \rangle &= \bar{\Phi}^-(x_1) - \bar{\Phi}^+(x_1). \end{aligned} \quad (19)$$

Here and afterwards the brackets  $\langle \dots \rangle$  denote the jump of the corresponding function over bimaterial interface.

Introducing the new functions

$$F_j(z) = \frac{s_{11} + \alpha_j s_{22}}{s_{11} - s_{12} + \alpha_j (s_{22} - s_{21})} \left\{ \Omega(z) + \frac{s_{12} + \alpha_j s_{21}}{s_{11} + \alpha_j s_{22}} \bar{\Phi}(z) \right\}, \quad (20)$$

having the same properties as  $\Phi(z)$ , and combining the first and second equation of (18) one can write

$$\sigma_{33}(x_1, 0) + im_j \sigma_{13}(x_1, 0) = t_j [F_j^+(x_1) + \gamma_j F_j^-(x_1)], \quad (21)$$

where  $\alpha_j$  are the roots of the quadratic equation

$$\frac{s_{12} + \alpha s_{21}}{s_{11} + \alpha s_{22}} = \frac{s_{22} + \alpha s_{11}}{s_{21} + \alpha s_{12}},$$

and

$$m_j = \frac{1 - \alpha_j}{1 + \alpha_j}, \quad \gamma_j = \frac{s_{21} + \alpha_j s_{12}}{s_{11} + \alpha_j s_{22}}, \quad t_j = \frac{s_{11} - s_{12} + \alpha_j (s_{22} - s_{21})}{1 + \alpha_j}, \quad j = 1, 2.$$

On the other hand, (19) and (20) lead to the expression for the derivatives of the displacement jumps

$$\langle u'_1(x_1) \rangle + i s_j \langle u'_3(x_1) \rangle = F_j^+(x_1) - F_j^-(x_1), \quad (22)$$

where  $s_{1,2} = -m_{1,2}$ . Numerical analysis shows that the constants  $\alpha_j$ ,  $m_j$ ,  $\gamma_j$ ,  $t_j$  are real, and besides  $\gamma_2 = 1/\gamma_1$  holds true.

The expressions (21) and (22) play an important role in the following analysis because by means of these expressions the problems of linear relationship for various mixed boundary conditions at the interface can be formulated.

#### 4. Open crack model

Consider now the same bimaterial as in the previous chapter and assume that an electrically conducting interface crack is situated in the region  $-b \leq x_1 \leq b$ ,  $x_3 = 0$  (Figure 1). Taking into account that the stress intensity factors and the energy release rate for an electrically conducting interface crack depend on the material properties and the applied mechanical loads, but not on the applied electric loads [Zhang and Gao 2004], we pay our attention to the influence of the external mechanical loading only. Therefore, it is assumed that the half-planes are loaded at infinity with uniform stresses  $\sigma_{33}^{(j)} = \sigma_{33}^\infty$ ,  $\sigma_{13}^{(j)} = \sigma_{13}^\infty$ , and  $\sigma_{11}^{(j)} = (\sigma_{11}^\infty)_j$  which satisfy the continuity conditions at the interface ( $j = 1$  stands for the upper half-plane and  $j = 2$  for the lower one). Because the load does not depend on the coordinate  $x_2$ , the plane strain problem in the  $(x_1, x_3)$ -plane can be considered. The open crack model based upon the initial assumption that the crack is completely open is employed in the following analysis.

For a traction- and charge-free electrically conducting crack, the continuity and boundary conditions at the interface  $x_3 = 0$  are

$$\langle \sigma_{13}(x_1) \rangle = 0, \quad \langle \sigma_{33}(x_1) \rangle = 0, \quad E_1^\pm(x_1, 0) = 0 \quad \text{for } x_1 \in (-\infty, \infty), \quad (23)$$

$$\langle u_1(x_1) \rangle = 0, \quad \langle u_3(x_1) \rangle = 0 \quad \text{for } x_1 \notin (-b, b), \quad (24)$$

$$\sigma_{13}^\pm(x_1, 0) = 0, \quad \sigma_{33}^\pm(x_1, 0) = 0 \quad \text{for } x_1 \in (-b, b). \quad (25)$$

The stress components and the derivatives of the displacement jumps at the bimaterial interface can be represented by means of the expressions (21) and (22), respectively. Due to the method of construction of these expressions, they automatically satisfy the boundary conditions (23) and (24). To satisfy additionally the boundary conditions (25), the homogeneous Hilbert problem

$$F_j^+(x_1) + \gamma_j F_j^-(x_1) = 0, \quad x_1 \in (-b, b), \quad (26)$$

by using expression (21) arises [Muskhelishvili 1953]. Taking into account that for  $x_1 \notin (-b, b)$  the relation  $F_j^+(x_1) = F_j^-(x_1)$  is valid, by use of (21) and the prescribed remote mechanical loads the

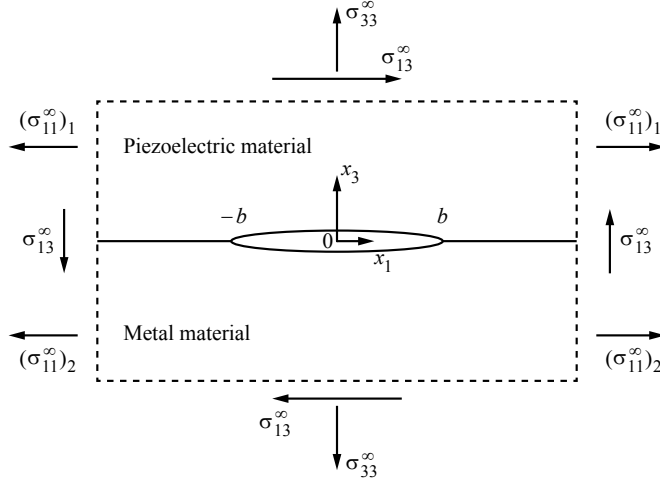


**Figure 1.** An open interface crack subject to remote uniform mechanical loading.

conditions at infinity for the functions  $F_j(z)$  can be written as

$$F_j(z)|_{z \rightarrow \infty} = \frac{\sigma_{33}^{\infty} + im_j \sigma_{13}^{\infty}}{t_j(1 + \gamma_j)}. \quad (27)$$

By applying the relation  $\gamma_2 = 1/\gamma_1$ , the solution of this problem for  $j = 2$  can be obtained from the associated solution for  $j = 1$ . Therefore, in the following our attention will be focused only to the case  $j = 1$ . According to the results by Muskhelishvili [1953] the most general solution of the homogeneous Hilbert problem (26), analytic at infinity, has the form

$$F_1(z) = (z + b)^{-1/2 + i\varepsilon_1} (z - b)^{-1/2 - i\varepsilon_1} P(z),$$

where  $\varepsilon_1 = (\ln \gamma_1)/2\pi$ ,  $P(z) = C_1 z + C_0$ , and  $C_0, C_1$  are arbitrary constants.

Further, by means of the condition at infinity (27) and the condition of the single-valuedness of the displacements, which due to (22) can be written as

$$\int_{-b}^b \{F_1^+(x_1) - F_1^-(x_1)\} dx_1 = 0,$$

the expressions

$$C_0 = \frac{-il\varepsilon_1(\sigma_{33}^{\infty} + im_1\sigma_{13}^{\infty})}{t_1(1 + \gamma_1)}, \quad C_1 = \frac{\sigma_{33}^{\infty} + im_1\sigma_{13}^{\infty}}{t_1(1 + \gamma_1)}$$

for the unknown coefficients of the polynomial  $P(z)$  are found and the function  $F_1(z)$  can be represented in the form

$$F_1(z) = \frac{\sigma_{33}^{\infty} + im_1\sigma_{13}^{\infty}}{t_1(1 + \gamma_1)} (z + b)^{-1/2 + i\varepsilon_1} (z - b)^{-1/2 - i\varepsilon_1} (z - il\varepsilon_1), \quad (28)$$

where  $l = 2b$  is the crack length.



Substituting (28) into (21), we get the expressions

$$\sigma_{33}(x_1, 0) + im_1\sigma_{13}(x_1, 0) = \frac{\sigma_{33}^\infty + im_1\sigma_{13}^\infty}{\sqrt{(x_1 + b)(x_1 - b)}}(x_1 - il\varepsilon_1) \left[ \frac{x_1 + b}{x_1 - b} \right]^{i\varepsilon_1} \quad (29)$$

for the stresses at the bonded part  $x_1 > b$  of the bimaterial interface. Substituting (28) into (22), the expressions for the derivatives of the crack face's displacement jumps can be written as

$$\langle u_1'(x_1) \rangle + is_1 \langle u_3'(x_1) \rangle = \frac{\sigma_{33}^\infty + im_1\sigma_{13}^\infty}{it_1\sqrt{\gamma_1}(x_1 + b)(b - x_1)}(x_1 - il\varepsilon_1) \left[ \frac{x_1 + b}{b - x_1} \right]^{i\varepsilon_1}. \quad (30)$$

Integrating the last expression, one obtains

$$\langle u_1(x_1) \rangle + is_1 \langle u_3(x_1) \rangle = \frac{i(\sigma_{33}^\infty + im_1\sigma_{13}^\infty)}{t_1\sqrt{\gamma_1}} \sqrt{(x_1 + b)(b - x_1)} \left[ \frac{x_1 + b}{b - x_1} \right]^{i\varepsilon_1}. \quad (31)$$

Introducing similarly to Rice [1988] the complex stress intensity factor (SIF) is

$$K_1 + im_1K_2 = \lim_{x_1 \rightarrow b+0} \sqrt{2\pi(x_1 - b)} [\sigma_{33}(x_1, 0) + im_1\sigma_{13}(x_1, 0)](x_1 - b)^{i\varepsilon_1} l^{-i\varepsilon_1}$$

at the right crack tip, associated to the crack length and using (29) one arrives at the expression for the conjugating SIF:

$$K_1 - im_1K_2 = \sqrt{\frac{1}{2}\pi l}(1 + 2i\varepsilon_1)(\sigma_{33}^\infty - im_1\sigma_{13}^\infty). \quad (32)$$

The crack-tip field of an interface crack is uniquely determined by the complex SIF (32) or by its real and imaginary parts, respectively. Employing a polar coordinate system  $(\rho, \theta)$  with the origin at the right crack tip, the near-tip tractions along the bonded interface part ( $\theta = 0$ ) are expressed as

$$\sigma_{33}(\rho, 0) - im_1\sigma_{13}(\rho, 0) = \frac{K_1 - im_1K_2}{\sqrt{2\pi\rho}}(\rho/l)^{i\varepsilon_1} \quad \text{for } \rho \rightarrow 0. \quad (33)$$

The corresponding near-tip expression for the discontinuity in displacement across the crack ( $\theta = \pi$ ) is

$$\langle u_3(\rho) \rangle + \frac{i}{s_1} \langle u_1(\rho) \rangle = \frac{2}{s_1 t_1 \sqrt{\gamma_1}} \frac{K_1 - im_1K_2}{1 + 2i\varepsilon_1} \sqrt{\frac{\rho}{2\pi}} (\rho/l)^{i\varepsilon_1} \quad \text{for } \rho \rightarrow 0. \quad (34)$$

Using

$$(\rho/l)^{i\varepsilon_1} = \cos[\varepsilon_1 \ln(\rho/l)] + i \sin[\varepsilon_1 \ln(\rho/l)],$$

it can be seen that the asymptotic fields (33) and (34) change their sign an infinite number of times in a small neighboring area of the crack tip. This means that for the open crack model the well-known oscillating singularity is observed [Williams 1959]. It is characterized by physically unrealistic interpenetration of the two materials along the crack faces. The degree of oscillation is determined by parameter  $\varepsilon_1$ , which depends on the ratio of the stiffness characteristics of the two materials. With the definitions employed for  $\gamma_1$  and  $\varepsilon_1$ ,  $\gamma_1 > 1$  implies  $\varepsilon_1 > 0$ . For identical materials it holds that  $\gamma_1 = 1$  and  $\varepsilon_1 = 0$ . It should also be noticed that transposition of the half-planes yields a change in the sign of  $\varepsilon_1$ .

Defining the phase angle of the complex SIF as  $\psi_K = \arg(K_1 - im_1K_2)$  and taking into account that

$$K_1 - im_1K_2 = |K_1 - im_1K_2| e^{i\psi_K}, \quad 1 + 2i\varepsilon_1 = \sqrt{1 + 4\varepsilon_1^2} e^{i \arctan(2\varepsilon_1)},$$

hold true and separating real and imaginary parts of the expression (34), we have

$$\langle u_3(\rho) \rangle = \frac{2}{s_1 t_1 \sqrt{\gamma_1}} \frac{|K_1 - i m_1 K_2|}{\sqrt{1 + 4\varepsilon_1^2}} \sqrt{\frac{\rho}{2\pi}} \cos[\psi_u(\rho)] \quad \text{for } \rho \rightarrow 0, \quad (35)$$

with

$$\psi_u(\rho) = \psi_K + \varepsilon_1 \ln(\rho/l) - \arctan(2\varepsilon_1). \quad (36)$$

As the opening of the crack,  $\langle u_3(\rho) \rangle$ , oscillates, an infinite number of interpenetration zones exists, in which  $\langle u_3(\rho) \rangle < 0$ . By means of the expression (35), we can estimate the length of the interpenetration region at the crack tip. For this purpose, we identify the location of the first interpenetration point  $\rho_I$  where the crack opening  $\langle u_3(\rho) \rangle$  due to the oscillation becomes zero for the first time. As pointed out by Hills and Barber [1993], imposing  $\langle u_3(\rho) \rangle < 0$  in (35), interpenetration zones are defined by the condition  $\cos[\psi_u(\rho)] < 0$ , which results in the intervals

$$(2n - \frac{3}{2})\pi < \psi_u(\rho) < (2n - \frac{1}{2})\pi,$$

with  $n$  being any integer. Therefore, in view of (36), the interpenetration zones are characterized by the intervals

$$\rho_L < \rho < \rho_R, \quad (37)$$

where

$$\rho_L = l \exp\left\{\frac{1}{\varepsilon_1}[(2n - \frac{3}{2})\pi - \psi_K + \arctan(2\varepsilon_1)]\right\}, \quad \rho_R = l \exp\left\{\frac{1}{\varepsilon_1}[(2n - \frac{1}{2})\pi - \psi_K + \arctan(2\varepsilon_1)]\right\}.$$

Equation (37) defines an infinite sequence of interpenetration zones as  $n$  takes all integer values, positive and negative. Hills and Barber [1993] concluded that the location of the first interpenetration point  $\rho_I$  can be obtained as the largest value of  $\rho_R$  which is lower than the crack length, i.e.,

$$\rho_I = l \exp\left\{\frac{1}{\varepsilon_1}[(2n - \frac{1}{2})\pi - \psi_K + \arctan(2\varepsilon_1)]\right\}. \quad (38)$$

It is worth reminding that the relation (38) is valid for  $\varepsilon_1 > 0$  only. In the case  $\varepsilon_1 < 0$ , the inequalities (37) must be reversed, and therefore the location of the first interpenetration point is defined by the largest value of  $\rho_L$  which is lower than the crack length [Graciani et al. 2007].

For the open crack model, the energy release rate (ERR) at the right crack tip is defined as [Parton and Kudryavtsev 1988]

$$G = \lim_{\Delta l \rightarrow 0} \frac{1}{2\Delta l} \int_b^{b+\Delta l} \sigma_{33}(\tau, 0) \langle u_3(\tau - \Delta l) \rangle + \sigma_{13}(\tau, 0) \langle u_1(\tau - \Delta l) \rangle d\tau. \quad (39)$$

The electrical component of the energy release rate is missing since the drop of electric potential for an electrically conducting crack is zero along the entire material interface.

Substituting expressions (33) and (34) into (39), we get

$$G = -\frac{K_1^2 + m_1^2 K_2^2}{2m_1 t_1 (1 + \gamma_1)}. \quad (40)$$

In deriving (40), the identity

$$\int_0^{\Delta l} \left( \frac{\Delta l - \tau}{\tau} \right)^{(1/2)+i\varepsilon_1} d\tau = \frac{1}{2}\pi \Delta l (1 + 2i\varepsilon_1) \operatorname{sech}(\pi \varepsilon_1),$$

has been used with  $\varepsilon_1 > 0$  and  $\Delta l > 0$ .

## 5. Contact zone model

Considering the same type of loadings at infinity, following Comninou [1977], we introduce a frictionless contact zone  $a < x_1 < b$  at the right crack tip to avoid an oscillating singularity, where the position of the point  $a$  is chosen arbitrarily for the time being (Figure 2). For a such an arbitrary position of point  $a$ , we have an artificial contact zone model, which is not physically justified, but from this model the specific value of  $a$  for the realistic contact zone length in the sense of Comninou will be found. Taking into consideration only the right contact zone is justified by the fact that the left contact zone under considered loading is extremely short and its influence upon the longer right contact zone is negligibly small [Dundurs and Gautesen 1988].

The boundary conditions at the crack faces for the considered model can be written as

$$\sigma_{13}^{\pm}(x_1, 0) = 0, \quad \sigma_{33}^{\pm}(x_1, 0) = 0 \quad \text{for } x_1 \in (-b, a), \quad (41)$$

$$\sigma_{13}^{\pm}(x_1, 0) = 0, \quad \langle u_3(x_1) \rangle = 0 \quad \text{for } x_1 \in (a, b). \quad (42)$$

Satisfying conditions (41), (42) by means of the expressions (21), (22) leads to the homogeneous combined Dirichlet–Riemann boundary value problem

$$F_1^+(x_1) + \gamma_1 F_1^-(x_1) = 0, \quad x_1 \in (-b, a), \quad \operatorname{Im} F_1^{\pm}(x_1) = 0, \quad x_1 \in (a, b). \quad (43)$$

The behavior of the function  $F_1(z)$  at infinity is determined by (27).

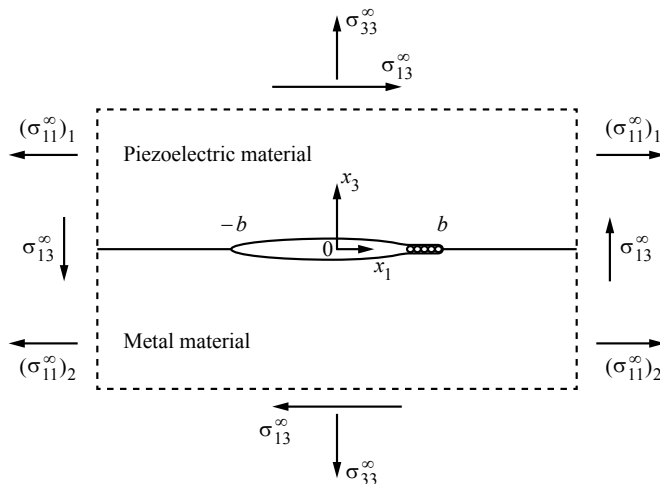


**Figure 2.** An interface crack with one contact zone subject to remote uniform mechanical loading.

Following Nakhmein and Nuller [1986] and Herrmann and Loboda [2000], the general solution of the problem (43) can be represented in the form

$$F_1(z) = P(z)X_1(z) + Q(z)X_2(z), \quad (44)$$

where

$$X_1(z) = \frac{ie^{i\theta(z)}}{\sqrt{(z+b)(z-b)}}, \quad X_2(z) = \frac{e^{i\theta(z)}}{\sqrt{(z+b)(z-a)}}, \quad \theta(z) = 2\varepsilon_1 \ln \frac{\sqrt{(b-a)(z+b)}}{\sqrt{l(z-a)} + \sqrt{(a+b)(z-b)}},$$

and  $P(z) = C_1z + C_0$ ,  $Q(z) = D_1z + D_0$  are polynomials with arbitrary real coefficients. Constants  $C_0$ ,  $C_1$ ,  $D_0$ ,  $D_1$  can be found from the condition (27) at infinity in the form

$$\begin{aligned} C_0 &= -\beta_1 D_1, & D_0 &= \beta_1 C_1 - \frac{a-b}{2} D_1, \\ C_1 &= \frac{m_1 \sigma_{13}^\infty \cos \beta - \sigma_{33}^\infty \sin \beta}{t_1(1+\gamma_1)}, & D_1 &= \frac{\sigma_{33}^\infty \cos \beta + m_1 \sigma_{13}^\infty \sin \beta}{t_1(1+\gamma_1)}, \end{aligned}$$

where

$$\beta = \varepsilon_1 \ln \frac{\lambda}{2(1+\sqrt{1-\lambda})-\lambda}, \quad \beta_1 = \varepsilon_1 \sqrt{l(a+b)}.$$

The parameter  $\lambda = (b-a)/l$  defines the relative length of the contact zone of the crack faces and will be found later.

Substituting the formula (44) into (21), (22) and taking into account that  $F_1^+(x_1) = F_1^-(x_1)$  for  $x_1 > b$  and  $F_1^-(x_1) = -F_1^+(x_1)/\gamma_1$  for  $x_1 \in (-b, a)$ , the following expressions are obtained for the stresses and the derivatives of the displacement jumps at the material interface for  $x_1 > b$ :

$$\sigma_{33}(x_1, 0) + im_1 \sigma_{13}(x_1, 0) = \frac{t_1(1+\gamma_1)e^{i\theta(x_1)}}{\sqrt{x_1+b}} \left[ \frac{Q(x_1)}{\sqrt{x_1-a}} + i \frac{P(x_1)}{\sqrt{x_1-b}} \right], \quad (45)$$

for  $x_1 \in (-b, a)$ ,

$$\langle u_1'(x_1) \rangle + is_1 \langle u_3'(x_1) \rangle = \frac{(1+\gamma_1)e^{i\theta^*(x_1)}}{\sqrt{\gamma(x_1+b)}} \left[ \frac{P(x_1)}{\sqrt{b-x_1}} - i \frac{Q(x_1)}{\sqrt{a-x_1}} \right]; \quad (46)$$

for  $x_1 \in (a, b)$ ,

$$\begin{aligned} \sigma_{33}(x_1, 0) &= \frac{t_1(1+\gamma_1)P(x_1)}{\sqrt{(x_1+b)(b-x_1)}} \left[ \sinh \tilde{\theta}(x_1) + \frac{1-\gamma_1}{1+\gamma_1} \cosh \tilde{\theta}(x_1) \right] \\ &\quad + \frac{t_1(1+\gamma_1)Q(x_1)}{\sqrt{(x_1+b)(x_1-a)}} \left[ \cosh \tilde{\theta}(x_1) + \frac{1-\gamma_1}{1+\gamma_1} \sinh \tilde{\theta}(x_1) \right], \end{aligned} \quad (47)$$

$$\langle u_1'(x_1) \rangle = \frac{2}{\sqrt{x_1+b}} \left[ \frac{P(x_1)}{\sqrt{b-x_1}} \cosh \tilde{\theta}(x_1) + \frac{Q(x_1)}{\sqrt{x_1-a}} \sinh \tilde{\theta}(x_1) \right], \quad (48)$$

where

$$\theta^*(x_1) = 2\varepsilon_1 \ln \frac{\sqrt{(b-a)(x_1+b)}}{\sqrt{l(a-x_1)} + \sqrt{(a+b)(b-x_1)}}, \quad \tilde{\theta}(x_1) = 2\varepsilon_1 \arctan \sqrt{\frac{(a+b)(b-x_1)}{l(x_1-a)}}.$$

As it follows from the analysis of the formulas (45) and (47) the normal stress is limited for  $x_1 \rightarrow b + 0$ . On the other hand, the shear stress is singular for  $x_1 \rightarrow b + 0$  as well as the normal stress for  $x_1 \rightarrow a + 0$ . The stress intensity factors are introduced to characterize these singularities:

$$k_1 = \lim_{x_1 \rightarrow a+0} \sqrt{2\pi(x_1 - a)} \sigma_{33}(x_1, 0), \quad k_2 = \lim_{x_1 \rightarrow b+0} \sqrt{2\pi(x_1 - b)} \sigma_{13}(x_1, 0).$$

Using relations (45) and (47) leads to the expressions

$$\begin{aligned} k_1 &= \frac{\sqrt{2\pi l \gamma_1}}{1 + \gamma_1} [\sqrt{1 - \gamma} (\sigma_{33}^\infty \cos \beta + m_1 \sigma_{13}^\infty \sin \beta) - 2\varepsilon_1 (\sigma_{33}^\infty \sin \beta - m_1 \sigma_{13}^\infty \cos \beta)], \\ k_2 &= -\frac{1}{m_1} \sqrt{\frac{1}{2}\pi l} [\sigma_{33}^\infty \sin \beta - m_1 \sigma_{13}^\infty \cos \beta + 2\varepsilon_1 \sqrt{1 - \lambda} (\sigma_{33}^\infty \cos \beta + m_1 \sigma_{13}^\infty \sin \beta)]. \end{aligned} \quad (49)$$

We define the energy release rate near the right crack tip as [Parton and Kudryavtsev 1988]

$$G = \lim_{\Delta l \rightarrow 0} \frac{1}{2\Delta l} \left\{ \int_a^{a+\Delta l} \sigma_{33}(x_1, 0) \langle u_3(x_1 - \Delta l) \rangle dx_1 + \int_b^{b+\Delta l} \sigma_{13}(x_1, 0) \langle u_1(x_1 - \Delta l) \rangle dx_1 \right\}. \quad (50)$$

Substituting the asymptotic formulas for the stresses and the displacement jumps in the vicinity of the points  $a$  and  $b$  into (50) and calculating the corresponding integrals, we get

$$G = \frac{1}{2t_1} \left( \frac{1 + \gamma_1}{4s_1\gamma_1} k_1^2 - \frac{m_1}{1 + \gamma_1} k_2^2 \right). \quad (51)$$

The obtained solution is mathematically correct for any position of the point  $a$ , and the associated interface crack model was called an artificial contact zone model [Herrmann and Loboda 2000]. However, it is physically justified if the inequalities

$$\sigma_{33}(x_1, 0) \leq 0, \quad x_1 \in (a, b), \quad \langle u_3(x_1) \rangle \geq 0, \quad x_1 \in (-b, a), \quad (52)$$

are valid. The first inequality ensures that the crack faces are closing on  $(a, b)$ , and the second one excludes their interpenetration on  $(-b, a)$  (it violates only in a very small area near the left crack tip because of oscillation, but it does not significantly influence in the vicinity of the right crack tip, as mentioned before). In this case a realistic contact zone in the sense of Comninou [1977] is present at the crack tip.

The inequalities in (52) are satisfied simultaneously in the case of a smooth closing of the crack at the point  $a$ , i.e., when  $k_1 = 0$  [Loboda 1993]. The latter condition is a necessary one for the satisfaction of the inequalities in (52) and, from (49), it leads to the transcendental equation

$$\tan \beta = \frac{\sqrt{1 - \lambda} \sigma_{33}^\infty + 2\varepsilon_1 m_1 \sigma_{13}^\infty}{2\varepsilon_1 \sigma_{33}^\infty - \sqrt{1 - \lambda} m_1 \sigma_{13}^\infty}, \quad (53)$$

with respect to the parameter  $\lambda$ . Usually (53) is solved numerically and the maximum root  $\lambda = \lambda_0$  from interval  $(0, 1)$  should be selected. For small values of  $\lambda$ , assuming  $\sqrt{1 - \lambda} \approx 1$ , we get the asymptotic formula

$$\lambda_0 = 4 \exp \left\{ -\frac{1}{\varepsilon_1} \left[ \arctan(2\varepsilon_1) - \arctan \left( \frac{m_1 \sigma_{13}^\infty}{\sigma_{33}^\infty} \right) - \pi(n - 0, 5) \right] \right\}, \quad (54)$$

where the integer  $n$  is chosen to provide  $\lambda_0$  as the maximum root of (54) in the interval  $(0, 1)$ .

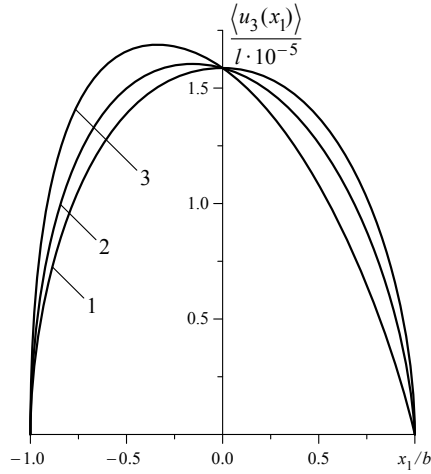


**Figure 3.** The variation of the normalized crack opening along the crack region for  $\sigma_{33}^{\infty} = 1$  MPa and  $\sigma_{13}^{\infty}/\sigma_{33}^{\infty} = -1$  (line 1),  $\sigma_{13}^{\infty}/\sigma_{33}^{\infty} = -20$  (line 2),  $\sigma_{13}^{\infty}/\sigma_{33}^{\infty} = -50$  (line 3).

## 6. Numerical results and discussion

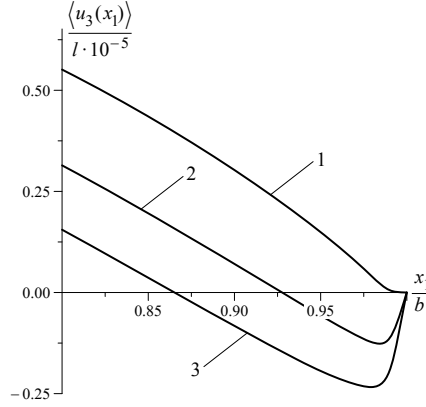
We pay our attention to the influence of the external mechanical loading on the crack opening and the stresses as well as the contact zone and interpenetration region lengths. The bimaterial consisting of piezoceramic PZT-4 [Pak 1992] (the upper material) and steel (Young's modulus  $E = 21.0 \times 10^{10}$  N/m<sup>2</sup> and Poisson's ratio  $\nu = 0.3$ ) (the lower one) is chosen for the numerical calculations. In the SI system of units, matrix  $\mathbf{D}$  for the piezoceramic PZT-4 has the form

$$\begin{bmatrix} 4.69302 \cdot 10^{10} i & 5.80012 \cdot 10^9 & 11.5642 \\ -5.80012 \cdot 10^9 & 4.39991 \cdot 10^{10} i & 12.3926 i \\ -11.5642 & 12.3926 i & -5.81112 \cdot 10^{-9} i \end{bmatrix}.$$

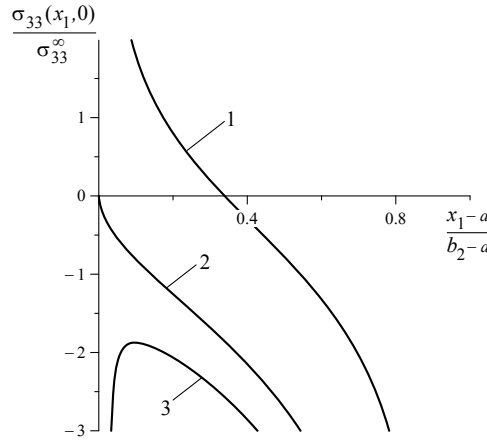
At the beginning, the variation of the normalized normal crack displacement jump (crack opening) along the crack region for the open crack model is shown in Figure 3. The graphs are presented for different shear loads  $\sigma_{13}^{\infty} = -1$  MPa (line 1),  $\sigma_{13}^{\infty} = -20$  MPa (line 2), and  $\sigma_{13}^{\infty} = -50$  MPa (line 3) with fixed  $\sigma_{33}^{\infty} = 1$  MPa. The obtained results confirm the essential influence of normal-shear loading coefficient on the crack opening.

Figure 4 shows the graph of the normalized displacement jump at the right crack tip for the open crack model. Curves 1, 2, and 3 in this figure correspond to the values  $\sigma_{13}^{\infty}/\sigma_{33}^{\infty} = -50$ ,  $\sigma_{13}^{\infty}/\sigma_{33}^{\infty} = -80$ , and  $\sigma_{13}^{\infty}/\sigma_{33}^{\infty} = -100$ , respectively. It follows from the analysis of these graphs that crack opening is negative in some areas, i.e., a physically impossible overlapping of the crack faces is observed there. If  $\sigma_{13}^{\infty}/\sigma_{33}^{\infty} = -50$  this overlapping is invisibly small although it takes place, but for  $\sigma_{13}^{\infty}/\sigma_{33}^{\infty} = -80$  it is quite noticeable and for  $\sigma_{13}^{\infty}/\sigma_{33}^{\infty} = -100$  the overlapping covers one tenth of the crack length. It is clear that in such cases the open crack model is not adequate to reality and the contact zone model should be used.

The distribution of the normalized normal stress  $\sigma_{33}(x_1, 0)/\sigma_{33}^{\infty}$  in the contact zone  $x_1 \in (a, b)$  for  $\sigma_{33}^{\infty} = 1$  MPa,  $\sigma_{13}^{\infty}/\sigma_{33}^{\infty} = -70$  and different values of the relative contact zone length  $\lambda$  is shown in



**Figure 4.** The variation of the normalized crack opening along the near-crack tip region for  $\sigma_{33}^\infty = 1$  MPa and  $\sigma_{13}^\infty/\sigma_{33}^\infty = -50$  (line 1),  $\sigma_{13}^\infty/\sigma_{33}^\infty = -80$  (line 2),  $\sigma_{13}^\infty/\sigma_{33}^\infty = -100$  (line 3).



**Figure 5.** Variation of the normalized normal stress  $\sigma_{33}(x_1, 0)/\sigma_{33}^\infty$  in the contact zone  $(a, b)$  for  $\sigma_{33}^\infty = 1$  MPa,  $\sigma_{13}^\infty/\sigma_{33}^\infty = -70$ , and  $\lambda = 0.03$  (line 1),  $\lambda = \lambda_0 \approx 0.01238$  (line 2),  $\lambda = 0.001$  (line 3).

**Figure 5.** Curve 1 corresponds to  $\lambda = 0.03$  ( $\lambda > \lambda_0$ ), curve 2 to  $\lambda = \lambda_0 \approx 0.01238$ , and curve 3 to  $\lambda = 0.01$  ( $\lambda < \lambda_0$ ). It is seen that for  $\lambda > \lambda_0$ , normal stress is tensile in most parts of the interval  $(a, b)$  and is compressive only near the point  $b$ . A decrease of  $\lambda$  leads to an increase of the compressive stress field zone. For  $\lambda \leq \lambda_0$ , the normal stress becomes negative throughout the interval  $(a, b)$ . Only for  $\lambda = \lambda_0$  the stress  $\sigma_{33}(x_1, 0)$  at the point  $a$  becomes equal to zero. This means that for  $\lambda = \lambda_0$ , the crack faces are compressed against each other in the entire interval  $(a, b)$  and their closure in point  $a$  is smooth.

**Figure 6** shows the normalized crack opening  $\langle u_3(x_1) \rangle/l$  in the left neighboring area of the point  $a$  for the same materials and loads, as in **Figure 5**. Curve 1 corresponds to  $\lambda = 0.03$  ( $\lambda > \lambda_0$ ), curve 2 to  $\lambda = \lambda_0 \approx 0.01238$ , and curve 3 to  $\lambda = 0.001$  ( $\lambda < \lambda_0$ ). It follows from the analysis of the above results that for  $\lambda \geq \lambda_0$  the second inequality in (52) is satisfied for all  $x_1 \in (-b, a)$ , except  $\lim_{x_1 \rightarrow a-0} \langle u_3'(x_1) \rangle \rightarrow 0$ ,

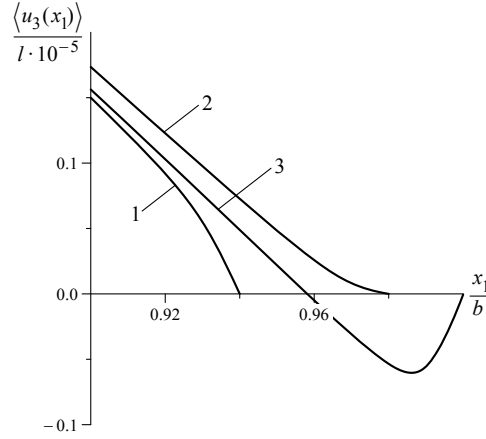


**Figure 6.** Variation of the normalized crack opening  $\langle u_3(x_1) \rangle / l$  in the left neighboring area of the point  $a$  for  $\sigma_{33}^\infty = 1$  MPa,  $\sigma_{13}^\infty / \sigma_{33}^\infty = -70$ , and  $\lambda = 0.03$  (line 1),  $\lambda = \lambda_0 \approx 0.01238$  (line 2),  $\lambda = 0.001$  (line 3).

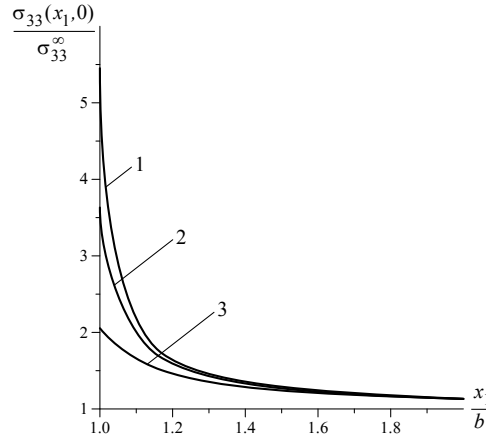


**Figure 7.** Variation of the normalized normal stress  $\sigma_{33}(x_1, 0) / \sigma_{33}^\infty$  for the contact zone model at the crack continuation for  $\sigma_{33}^\infty = 1$  MPa and  $\sigma_{13}^\infty / \sigma_{33}^\infty = -40$  (line 1),  $\sigma_{13}^\infty / \sigma_{33}^\infty = -50$  (line 2),  $\sigma_{13}^\infty / \sigma_{33}^\infty = -80$  (line 3).

and equality  $\langle u'_3(a) \rangle = 0$  holds true only for  $\lambda = \lambda_0$ . On the other hand, if  $\lambda < \lambda_0$ , physically incorrect overlapping of the crack faces is observed, which increases with  $\lambda$  decreasing. Thus, the results presented in Figure 5 and Figure 6 numerically confirm the fact that the inequalities in (52) are satisfied only for  $\lambda = \lambda_0$ .

The results of the calculations of the normalized normal stress  $\sigma_{33}(x_1, 0) / \sigma_{33}^\infty$  at the crack continuations are shown in Figure 7. Curves 1, 2, and 3 in this figure correspond to the values  $\sigma_{13}^\infty / \sigma_{33}^\infty = -40$ ,  $\sigma_{13}^\infty / \sigma_{33}^\infty = -50$ , and  $\sigma_{13}^\infty / \sigma_{33}^\infty = -80$ , respectively. These results demonstrate that, although the normal stress  $\sigma_{33}(x_1, 0)$  is not singular in the right neighborhood of the point  $b$ , its value remains very high in this region and can contribute crack propagation.



$\sigma_{13}^{\infty}/\sigma_{33}^{\infty}$	$\rho_I/l$	$\lambda_0$	$G/(l\sigma_{33}^{\infty})$
-10	$4.08058 \cdot 10^{-12}$	$2.20907 \cdot 10^{-12}$	$1.20334 \cdot 10^{-3}$
-20	$1.95214 \cdot 10^{-6}$	$1.05682 \cdot 10^{-6}$	$4.77593 \cdot 10^{-3}$
-30	$1.55536 \cdot 10^{-4}$	$8.41908 \cdot 10^{-5}$	$1.07303 \cdot 10^{-2}$
-40	$1.39120 \cdot 10^{-3}$	$7.52293 \cdot 10^{-4}$	$1.90663 \cdot 10^{-2}$
-50	$5.18241 \cdot 10^{-3}$	$2.79381 \cdot 10^{-3}$	$2.97841 \cdot 10^{-2}$
-60	$1.24555 \cdot 10^{-2}$	$6.67549 \cdot 10^{-3}$	$4.28836 \cdot 10^{-2}$
-70	$2.33029 \cdot 10^{-2}$	$1.23814 \cdot 10^{-2}$	$5.83648 \cdot 10^{-2}$
-80	$3.72787 \cdot 10^{-2}$	$1.95898 \cdot 10^{-2}$	$7.62278 \cdot 10^{-2}$

**Table 1.** The variation of the relative interpenetration region length  $\rho_I/l$ , the relative contact zone length  $\lambda_0$ , and the normalized energy release rate  $G/(l\sigma_{33}^{\infty})$  with respect to different shear loads  $\sigma_{13}^{\infty}/\sigma_{33}^{\infty}$  for  $\sigma_{33}^{\infty} = 1$  MPa.

In Table 1, the magnitudes of the relative interpenetration region length  $\rho_I/l$ , the relative contact zone length  $\lambda_0$  and the energy release rate  $G$  for different values of the shear loads are presented. It can be seen that all these values increase with the increase of magnitude of the applied shear load. In the absence of shear stress, the contact zone and interpenetration region lengths for piezoelectric-metal structures are several orders less than the characteristic size of the crack. However, for an essential shear field they become longer and even comparable with the crack length.

Comparing the results shown in Table 1, we can note that under the same loads the relative length of the material interpenetration region is always longer than the relative length of the realistic contact zone. This finding can be useful for the prediction of the first approximation for the realistic contact zone length, which can be refined later by an iterative procedure.

Carrying out a similar analysis for  $\sigma_{13}(x_1, 0)$  for  $x_1 \rightarrow b+0$ , one can see that the size of the area in the vicinity of the crack tip, where the stress changes its sign an infinite number of times, is approximately equal to  $\rho_I$ .

## 7. Conclusion

An interface crack between a piezoelectric material and a conducting isotropic elastic material under the action of a mechanical loading has been considered. By using a hybrid complex variable method which combines the Stroh formalism of piezoelectric materials with the Muskhelishvili formalism of isotropic elastic materials, the stresses and the derivatives of the displacement jumps via sectionally holomorphic functions have been presented. On the base of these representations, the exact analytical solutions for two interface crack models—the open crack one and the contact zone one—have been found. Furthermore, the explicit expressions of the crack tip ERR and the crack tip SIF have been obtained when the piezoelectric-metal bimaterial is subjected to the mechanical loading at infinity.

The present investigation shows that the structure of the singular fields near the conducting interface crack tip within the framework of the open crack model consists of an oscillating singularity, which is similar to that in the linear elastic dissimilar anisotropic materials but quite different from that under the impermeable crack assumption. It can be concluded that the electric boundary condition along

an interface crack in piezoelectric-metal bimetals exerts significant influence on the structure of the singularity of the near-tip fields. An oscillating singularity is characterized by physically unrealistic interpenetration of the two materials along the crack faces. The degree of oscillation is determined by parameter  $\varepsilon_1$ , which depends on the ratio of the stiffness characteristics of the two materials. The zone of crack face interpenetrations at the crack tip has been investigated and, in particular, the distance between the point of first interpenetration and the crack tip in the open crack model solution has been estimated.

The contact zone model in Comninou's sense has been derived as a particular case of the obtained solution within the framework of the artificial contact zone model. A simple transcendental equation and corresponding asymptotic formulas have been found for the determination of the realistic contact zone length. It is shown that at the same loads the relative length of the material interpenetration region is always longer than the relative length of the realistic contact area. This finding can be useful for the prediction of the first approximation for the realistic contact zone length, which can be refined later by an iterative procedure.

### Acknowledgments

Part of this work was executed during a stay of Govorukha at Karlsruhe Institute of Technology (KIT). The authors gratefully acknowledge the support from KIT by funding a guest stay of Govorukha.

### References

- [Bakirov 2004] V. F. Bakirov, "Integral relations for the problem of a crack on a piezoelectric-conductor interface", *Mech. Solids* **39**:6 (2004), 99–115.
- [Bakirov and Kim 2009] V. F. Bakirov and T.-W. Kim, "Analysis of a crack at the piezoceramic-metal interface and estimates of adhesion fracture energy", *Int. J. Eng. Sci.* **47**:7-8 (2009), 793–804.
- [Comninou 1977] M. Comninou, "The interface crack", *J. Appl. Mech. (ASME)* **44**:4 (1977), 631–636.
- [Dundurs and Gautesen 1988] J. Dundurs and A. K. Gautesen, "An opportunistic analysis of the interface crack", *Int. J. Fract.* **36**:2 (1988), 151–159.
- [Eshelby et al. 1953] J. D. Eshelby, W. T. Read, and W. Shockley, "Anisotropic elasticity with applications to dislocation theory", *Acta Metall.* **1**:3 (1953), 251–259.
- [Govorukha and Loboda 2000] V. B. Govorukha and V. V. Loboda, "Contact zone models for an interface crack in a piezoelectric material", *Acta Mech.* **140**:3-4 (2000), 233–246.
- [Govorukha et al. 2016] V. Govorukha, M. Kamlah, V. Loboda, and Y. Lapusta, "Interface cracks in piezoelectric materials", *Smart Mater. Struct.* **25**:2 (2016), 023001.
- [Graciani et al. 2007] E. Graciani, V. Mantič, and F. Paris, "On the estimation of the first interpenetration point in the open model of interface cracks", *Int. J. Fract.* **143**:3 (2007), 287–290.
- [Herrmann and Loboda 2000] K. P. Herrmann and V. V. Loboda, "Fracture-mechanical assessment of electrically permeable interface cracks in piezoelectric bimetals by considerations of various contact zone models", *Arch. Appl. Mech.* **70**:1-3 (2000), 127–143.
- [Hills and Barber 1993] D. A. Hills and J. R. Barber, "Interface cracks", *Int. J. Mech. Sci.* **35**:1 (1993), 27–37.
- [Kudriavtsev et al. 1975a] B. A. Kudriavtsev, V. Z. Parton, and V. I. Rakitin, "Fracture mechanics of piezoelectric materials: axisymmetric crack on the boundary with a conductor", *J. Appl. Math. Mech.* **39**:2 (1975), 328–338.
- [Kudriavtsev et al. 1975b] B. A. Kudriavtsev, V. Z. Parton, and V. I. Rakitin, "Fracture mechanics of piezoelectric materials: rectilinear tunnel crack on the boundary with a conductor", *J. Appl. Math. Mech.* **39**:1 (1975), 136–146.
- [Li and Chen 2007] Q. Li and Y. Chen, "Analysis of crack-tip singularities for an interfacial permeable crack in metal/piezoelectric bimetals", *Acta Mech. Solida Sin.* **20**:3 (2007), 247–257.

- [Li and Chen 2009] Q. Li and Y. H. Chen, “The Coulombic traction on the surfaces of an interface crack in dielectric/piezoelectric or metal/piezoelectric bimetals”, *Acta Mech.* **202**:1-4 (2009), 111–126.
- [Liu and Hsia 2003] M. Liu and K. J. Hsia, “Interfacial cracks between piezoelectric and elastic materials under in-plane electric loading”, *J. Mech. Phys. Solids* **51**:5 (2003), 921–944.
- [Loboda 1993] V. V. Loboda, “The quasi-invariant in the theory of interface crack”, *Eng. Fract. Mech.* **44**:4 (1993), 573–580.
- [Muskhelishvili 1953] N. I. Muskhelishvili, *Some basic problems of mathematical theory of elasticity*, Noordhoff Publishers, Groningen, 1953.
- [Nakhmein and Nuller 1986] E. L. Nakhmein and B. M. Nuller, “Contact between an elastic half-plane and a partly separated stamp”, *J. Appl. Math. Mech.* **50**:4 (1986), 507–515.
- [Ou and Chen 2004] Z. C. Ou and Y. H. Chen, “Near-tip stress fields and intensity factors for an interface crack in metal/piezoelectric bimetals”, *Int. J. Eng. Sci.* **42**:13-14 (2004), 1407–1438.
- [Pak 1992] Y. E. Pak, “Linear electro-elastic fracture mechanics of piezoelectric materials”, *Int. J. Fract.* **54**:1 (1992), 79–100.
- [Parton 1976] V. Z. Parton, “Fracture mechanics of piezoelectric materials”, *Acta Astronaut.* **3**:9-10 (1976), 671–683.
- [Parton and Kudryavtsev 1988] V. Z. Parton and B. A. Kudryavtsev, *Electromagnetoelasticity*, Gordon and Breach Science Publishers, New York, 1988.
- [Pritchard et al. 2001] J. Pritchard, C. R. Bowen, and F. Lowrie, “Multilayer actuators: review”, *Br. Ceram. Trans.* **100**:6 (2001), 265–273.
- [Rice 1988] J. R. Rice, “Elastic fracture mechanics concepts for interfacial cracks”, *J. Appl. Mech. (ASME)* **55**:1 (1988), 98–103.
- [Ru 2008] C. Q. Ru, “A hybrid complex-variable solution for piezoelectric/isotropic elastic interfacial cracks”, *Int. J. Fract.* **152**:2 (2008), 169–178.
- [Stroh 1958] A. N. Stroh, “Dislocation and crack in anisotropic elasticity”, *Phil. Mag.* **3**:30 (1958), 625–646.
- [Suo et al. 1992] Z. Suo, C.-M. Kuo, D. M. Barnett, and J. R. Willis, “Fracture mechanics for piezoelectric ceramics”, *J. Mech. Phys. Solids* **40**:4 (1992), 739–765.
- [Ting and Chou 1981] T. C. T. Ting and S. C. Chou, “Edge singularities in anisotropic composites”, *Int. J. Solids Struct.* **17**:11 (1981), 1057–1068.
- [Williams 1959] M. L. Williams, “The stresses around a fault or cracks in dissimilar media”, *Bull. Seismol. Soc. Am.* **49**:2 (1959), 199–204.
- [Zhang and Gao 2004] T. Y. Zhang and C. F. Gao, “Fracture behaviors of piezoelectric materials”, *Theor. Appl. Fract. Mech.* **41**:1-3 (2004), 339–379.

Received 7 Aug 2018. Revised 9 Nov 2018. Accepted 15 Nov 2018.

VOLODYMYR GOVORUKHA: [govorukhavb@yahoo.com](mailto:govorukhavb@yahoo.com)

Department of Computational Mathematics, Oles Honchar Dnipro National University, Dnipro, Ukraine

MARC KAMLAH: [marc.kamlah@kit.edu](mailto:marc.kamlah@kit.edu)

Institute of Applied Materials, Karlsruhe Institute of Technology, Eggenstein-Leopoldshafen, Germany



# SUBMISSION GUIDELINES

## ORIGINALITY

Authors may submit manuscripts in PDF format online at the Submissions page. Submission of a manuscript acknowledges that the manuscript is original and has neither previously, nor simultaneously, in whole or in part, been submitted elsewhere. Information regarding the preparation of manuscripts is provided below. Correspondence by email is requested for convenience and speed. For further information, write to [contact@msp.org](mailto:contact@msp.org).

## LANGUAGE

Manuscripts must be in English. A brief abstract of about 150 words or less must be included. The abstract should be self-contained and not make any reference to the bibliography. Also required are keywords and subject classification for the article, and, for each author, postal address, affiliation (if appropriate), and email address if available. A home-page URL is optional.

## FORMAT

Authors can use their preferred manuscript-preparation software, including for example Microsoft Word or any variant of  $\text{\LaTeX}$ . The journal itself is produced in  $\text{\LaTeX}$ , so accepted articles prepared using other software will be converted to  $\text{\LaTeX}$  at production time. Authors wishing to prepare their document in  $\text{\LaTeX}$  can follow the example file at [www.jomms.net](http://www.jomms.net) (but the use of other class files is acceptable). At submission time only a PDF file is required. After acceptance, authors must submit all source material (see especially Figures below).

## REFERENCES

Bibliographical references should be complete, including article titles and page ranges. All references in the bibliography should be cited in the text. The use of Bib $\text{\TeX}$  is preferred but not required. Tags will be converted to the house format (see a current issue for examples); however, for submission you may use the format of your choice. Links will be provided to all literature with known web locations; authors can supply their own links in addition to those provided by the editorial process.

## FIGURES

Figures must be of publication quality. After acceptance, you will need to submit the original source files in vector format for all diagrams and graphs in your manuscript: vector EPS or vector PDF files are the most useful. (EPS stands for Encapsulated PostScript.)

Most drawing and graphing packages—Mathematica, Adobe Illustrator, Corel Draw, MATLAB, etc.—allow the user to save files in one of these formats. Make sure that what you’re saving is vector graphics and not a bitmap. If you need help, please write to [graphics@msp.org](mailto:graphics@msp.org) with as many details as you can about how your graphics were generated.

Please also include the original data for any plots. This is particularly important if you are unable to save Excel-generated plots in vector format. Saving them as bitmaps is not useful; please send the Excel (.xls) spreadsheets instead. Bundle your figure files into a single archive (using zip, tar, rar or other format of your choice) and upload on the link you been given at acceptance time.

Each figure should be captioned and numbered so that it can float. Small figures occupying no more than three lines of vertical space can be kept in the text (“the curve looks like this:”). It is acceptable to submit a manuscript with all figures at the end, if their placement is specified in the text by means of comments such as “Place Figure 1 here”. The same considerations apply to tables.

## WHITE SPACE

Forced line breaks or page breaks should not be inserted in the document. There is no point in your trying to optimize line and page breaks in the original manuscript. The manuscript will be reformatted to use the journal’s preferred fonts and layout.

## PROOFS

Page proofs will be made available to authors (or to the designated corresponding author) at a Web site in PDF format. Failure to acknowledge the receipt of proofs or to return corrections within the requested deadline may cause publication to be postponed.

<b>Prediction of springback and residual stress of a beam/plate subjected to three-point bending</b>	<b>QUANG KHOA DANG, PEI-LUN CHANG, SHIH-KANG KUO and DUNG-AN WANG</b>	<b>421</b>
<b>Characterization of CNT properties using space-frame structure</b>	<b>MUHAMMAD ARIF and JACOB MUTHU</b>	<b>443</b>
<b>Analytical approach to the problem of an auxetic layer under a spatially periodic load</b>	<b>HENRYK KAMIŃSKI and PAWEŁ FRITZKOWSKI</b>	<b>463</b>
<b>Stability and nonplanar postbuckling behavior of current-carrying microwires in a longitudinal magnetic field</b>	<b>YUANZHUO HONG, LIN WANG and HU-LIANG DAI</b>	<b>481</b>
<b>Three-dimensional Trefftz computational grains for the micromechanical modeling of heterogeneous media with coated spherical inclusions</b>	<b>GUANNAN WANG, LEITING DONG, JUNBO WANG and SATYA N. ATLURI</b>	<b>505</b>
<b>Uniform stress resultants inside two nonelliptical inhomogeneities in isotropic laminated plates</b>	<b>XU WANG, LIANG CHEN and PETER SCHIAVONE</b>	<b>531</b>
<b>An analytical solution for heat flux distribution of cylindrically orthotropic fiber reinforced composites with surface effect</b>	<b>JUNHUA XIAO, YAOLING XU and FUCHENG ZHANG</b>	<b>543</b>
<b>Strain gradient fracture of a mode III crack in an elastic layer on a substrate</b>	<b>JINE LI and BAOLIN WANG</b>	<b>555</b>
<b>Growth-induced instabilities of an elastic film on a viscoelastic substrate: analytical solution and computational approach via eigenvalue analysis</b>	<b>IMAN VALIZADEH, PAUL STEINMANN and ALI JAVILI</b>	<b>571</b>
<b>Application of the hybrid complex variable method to the analysis of a crack at a piezoelectric-metal interface</b>	<b>VOLODYMYR GOVORUKHA and MARC KAMLAH</b>	<b>587</b>